

## PHD THESIS



# MOLECULAR PROCESSES AFFECTING THE MACROSCOPIC TRIBOLOGICAL BEHAVIOR OF SURFACES

conducted at the  
Institut für Angewandte Physik  
of the Vienna University of Technology

supervised by  
Ao.Univ.Prof. Dr.techn. Wolfgang WERNER  
Ao.Univ.Prof. Dipl.-Ing. Dr.techn. Friedrich FRANEK  
Ao.Univ.Prof. Dr.phil. Herbert STÖRI

written by  
AGNIESZKA MARIA TOMALA

Vienna, May 2011



The work presented in this thesis has been supported by the EC, Sixth Framework Programme, Marie Curie Action (*WEMESURF* research project entitled: "*Characterization of wear mechanisms and surface functionalities with regard to life time prediction and quality criteria-from the micro to the nano range*" under contract MRTN CT 2006 035589).

Agnieszka Maria Tomala, Matrikelnummer 0727729: *MOLECULAR PROCESSES AFFECTING THE MACROSCOPIC TRIBOLOGICAL BEHAVIOR OF SURFACES* ausgeführt zum Zwecke der Erlangung des akademischen Grades eines Doktors der technischen Wissenschaften unter der Leitung von Ao.Univ.Prof. Dr.techn. WOLFGANG WERNER, May 2011.

This Thesis is Dedicated to My Family  
Pracę tę Poświęcam Mojej Rodzinie  
- Agnieszka

I am among those who think that science has great beauty. A scientist in his laboratory is not only a technician: he is also a child placed before natural phenomena which impress him like a fairy tale.  
Maria Skłodowska Curie (1867 - 1934)



# ABSTRACT

The purpose of this study was to investigate the influence of various additives on the tribological properties of a system in the macro and nanoscale, as well as clarify lubricant interactions with surfaces and materials. To accomplish that a wide range of lubricants and additives were considered. Moreover, a detail chemical analysis was carried out, in order to explain the effect on the friction coefficient, wear mechanisms and corrosion process in lubricated tribosystems.

This research was mainly focused on additives for water based lubricants. Solutions of anti-corrosion and anti-foaming agents - amines, friction modifiers - glycols and amines derivatives with longer hydrocarbon chains were investigated. The results showed that the additives build chemisorbed mono-molecular films on surfaces, what was verified by AFM, AR-XPS and AES analysis, and compared with SESSA simulation. Investigated tribo-films affect the friction coefficient in nanoscale, however during tribological test in the macroscale, they showed different results depending on contact situation (rolling and/or sliding). The conclusion states that the differences in tribological behavior might be due to the orientation of amine and hydroxyl groups on the surfaces.

Furthermore, lubricants for rolling bearing elements such as polar and non polar oils with zinc dialkyldithiophosphate (ZDDP) additives were studied. The results demonstrated that a reaction layer formation is strongly dependent on the molecular polarity of the oils and additives. The evolution of the topography and mechanical properties of the ZDDP-derived tribo-layer with rubbing time showed that initially a thin and soft ZDDP reaction layer develops very quick.

The second part of this work was addressed on chemical vapor deposited (CVD) diamond films and transition metal dichalcogenides (TMD) in consideration of desired properties for micro electro mechanical systems (MEMS). The main scientific goal of this part of the work was to evaluate the influence of surface morphologies on the micro- and nanomechanical properties. Keeping nanotribological application in mind, a comparative AFM analysis were carried out and the influence of carbon content on the mechanical behavior of such a coatings was evaluated.



# Contents

|          |   |           |
|----------|---|-----------|
| <b>1</b> | <b>INTRODUCTION</b>   | <b>9</b>  |
| 1.1      | Motivation . . . . .  | 11        |
| 1.2      | Tasks . . . . .   | 13        |
| 1.3      | Organization of the thesis . . . . .                            | 14        |
| <b>2</b> | <b>TRIBOLOGY FUNDAMENTALS</b>                                   | <b>18</b> |
| 2.1      | Water Based Lubrication . . . . .                               | 22        |
| 2.2      | Effect of ZDDP Additives on Rolling Bearings . . . . .          | 26        |
| 2.3      | Hard Coatings . . . . .   | 27        |
| <b>3</b> | <b>MATERIALS</b>  | <b>31</b> |
| 3.1      | Mating Materials/Surfaces . . . . .                             | 31        |
| 3.1.1    | 100Cr6 Steel . . . . .  | 31        |
| 3.1.2    | Copper Sputtered on Silicon Wafer . . . . .                     | 31        |
| 3.1.3    | Transition Metal Dichalcogenides (TMD) . . . . .                | 32        |
| 3.1.4    | Diamond Films . . . . .   | 32        |
| 3.2      | Additives . . . . .   | 32        |
| 3.2.1    | Amines and Glycols for Water Based Lubricants . . . . .         | 33        |
| 3.2.2    | Zinc Dialkyl-Dithio-Phosphate (ZDDP) in oil solutions . . . . . | 35        |
| <b>4</b> | <b>EXPERIMENTAL METHODOLOGY</b>                                 | <b>36</b> |
| 4.1      | Atomic Force Microscopy . . . . .                               | 36        |
| 4.1.1    | Operation principle . . . . .                                   | 37        |
| 4.1.2    | Cantilever . . . . .  | 38        |
| 4.1.3    | Scanning modes . . . . .  | 39        |
| 4.1.4    | Closed Fluid Cell . . . . .                                     | 40        |
| 4.1.5    | Application in Tribology . . . . .                              | 41        |
| 4.1.6    | Force Distance Curves . . . . .                                 | 42        |
| 4.1.7    | Friction Measurements . . . . .                                 | 43        |
| 4.1.8    | Surface roughness parameters . . . . .                          | 45        |

|          |   |            |
|----------|---|------------|
| 4.2      | Tribology Methods . . . . .   | 49         |
| 4.2.1    | Microtribometer . . . . .   | 49         |
| 4.2.2    | Mini Traction Machine (MTM) . . . . .   | 49         |
| 4.2.3    | TOG Tribometer . . . . .  | 50         |
| 4.3      | Spectroscopy Methods . . . . .  | 51         |
| 4.3.1    | X-Ray Photoelectron Spectroscopy (XPS) . . . . .  | 51         |
| 4.3.2    | Spectrometer Components . . . . .   | 52         |
| 4.3.3    | Adsorption experiment . . . . .   | 56         |
| 4.3.4    | Angle Resolved X-ray Photoelectron Spectroscopy (AR-XPS) . . . . .                                    | 57         |
| 4.3.5    | Auger Electron Spectroscopy (AES) . . . . .   | 66         |
| 4.4      | Optical Methods . . . . .   | 67         |
| 4.4.1    | Wyko - Optical Profilometer . . . . .   | 67         |
| 4.4.2    | Optical Microscopy . . . . .  | 68         |
| <b>5</b> | <b>RESULTS AND DISCUSSION</b>   | <b>69</b>  |
| 5.1      | Additives for Water Based Lubricants . . . . .  | 69         |
| 5.1.1    | Oligomer specific lubrication . . . . .   | 69         |
| 5.1.2    | Tribochemistry of monomolecular lubricant films of ethanolamine oligomers . . . . .                   | 80         |
| 5.1.3    | Tribological properties of additives for water-based lubricants . . . . .                             | 93         |
| 5.1.4    | Behavior of corrosion inhibitors under different tribological contact . . . . .                       | 103        |
| 5.2      | Effect of ZDDP Additives on Rolling Bearings . . . . .  | 122        |
| 5.2.1    | Effect of Base Oil Polarity on Micro and Nano Friction Behavior of Base Oil + ZDDP Solution . . . . . | 122        |
| 5.2.2    | Evolution of ZDDP-derived reaction layer morphology with rubbing time . . . . .                       | 136        |
| 5.3      | Solid Lubrication . . . . .   | 152        |
| 5.3.1    | Micro- and Nanomechanical Properties of Diamond Films with Various Surface Morphologies . . . . .     | 152        |
| 5.3.2    | Nanotribology of Mo-Se-C Films . . . . .  | 168        |
| <b>6</b> | <b>SUMMARY</b>  | <b>186</b> |
| <b>7</b> | <b>CONCLUSION</b>   | <b>190</b> |
| <b>7</b> | <b>REFERENCES</b>   | <b>191</b> |
| <b>8</b> | <b>ACKNOWLEDGMENT</b>   | <b>213</b> |

# 1 INTRODUCTION

The work presented in this thesis has been supported by the EC, Sixth Framework Programme, Marie Curie Action (*WEMESURF* research project entitled: "*Characterization of wear mechanisms and surface functionalities with regard to life time prediction and quality criteria- from the micro to the nano range*" under contract MRTN CT 2006 035589).

Within the WEMESURF network 12 partners studied physical and tribochemical phenomena that occur at micro and nano-scales in a sliding contact between two counterparts covered by a lubricant film. Investigate of novel lubricants and additives and their chemical interaction with common used surfaces. The specific tasks of the work packages are:

- Improved 3D-analysis-methods for determination of wear and chemical changes on advanced functional surfaces and coatings.
- Improved physical/chemical analysis methods to describe chemical and metallurgical interactions between advanced lubricants and functional surfaces.
- Set up a theoretical parameter and criteria model for wear characterization in sub micro- metre and nano-metre scale.
- Development of an improved micro-nano-simulation-model to describe the surface and advanced lubricant relevant interactions and wear mechanisms.
- Economical impact of improved wear mechanisms understanding and ecological impact of wear reduction/prevention.

This work is dedicated to specific tasks in 1<sup>st</sup>, 2<sup>nd</sup>, 3<sup>rd</sup> and 4<sup>th</sup> work packages. Partner TU Wien contributed in WP1 to the tasks:

T1.1 by performing nanometer surface topography measurements applying AFM and interference microscopy, thus delivering an extensive database of results of the surface and wear zone characterization.

T1.2 by carrying out chemical element and molecule analysis of surfaces with methods such as X-ray Photoelectron Spectroscopy and Auger Electrons Spectroscopy. The contribution to WP2 comprises:

T2.1 investigating chemical interactions between the surface, the additive and the lubricant, to understand changes of these interactions during tribological processes.

T2.3 together with another partner developing a novel measuring method for low wear rate and particle distribution for model tribo-tests.

The contribution to WP3 comprises:

T3.2 comparing different experimental tools and measuring devices to improve reliability.

The contribution to WP4 comprises:

T4.3 by performing simulation of electron spectra and comparing with experimental lubricant analysis.

General objectives of this work are presented in Table. 1.1. Methodology and research path are graphically illustrated in Fig. 1.1.

Table 1.1: Main Objectives

| Molecular processes affecting the macroscopic tribological behavior of surfaces   |   |
|---|---|
| Mechanisms of how individual additives and lubricants influence tribological performance (friction, wear, tribo-corrosion, failure) in macro and nanoscale. | Lubricant interactions with surfaces - chemical bonding and their effect on the surface properties. |

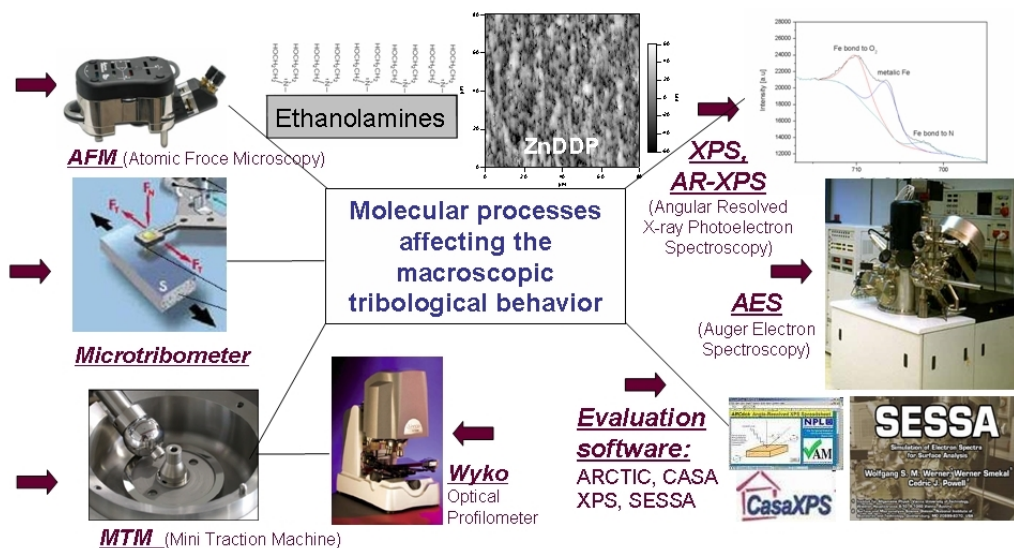


Figure 1.1: Objectives and methodology used in this research work.

## 1.1 Motivation

The physical and chemical composition of surfaces determine many important properties of the solids such as corrosion rates, adhesive properties, frictional properties, catalytic activity, wettability, contact potential, and finally and most importantly, the failure mechanism. At a fundamental level, friction, adhesion and wear need to be understood in terms of the behavior of lubricant molecules at the interface during tribological processes. At applied loads, wear and tribocorrosion processes leading to fracture of many atomic bonds, displacement and creation of dislocations and debris particles, are important.

In this study a wide range of lubricants and additives are considered.

The focus is mostly on additives for water based lubricants. Fully formulated water based lubricants have been thoroughly described in the literature. However, the influence of individual additives on tribological properties of these compositions is still not fully clear. Previous studies showed that additives such as amines and glycols used in fully formulated fluids, can reduce tribocorrosion, wear and friction of water lubricated systems. Thus solutions of anti-corrosion, anti-foaming and anti-microbial agents were investigated: - amines (Ethanolamine oligomers, Ethylamine oligomers), friction modifiers - glycols (monoethylene glycol, 1,4-butylene glycol) and amine derivatives with longer hydrocarbon chains (3-amino-1-propanol, 4-amino-1-butanol). Furthermore, lubricants for rolling bearing elements like polar and non polar oil with zinc dialkyldithiophosphate (ZDDP) solutions. The scientific goals and milestones of this work were:

- To establish how various individual additives influence the tribological properties of a system on the macro and nanoscale, and to select the best compounds and concentrations for this purpose.
- To clarify lubricant interactions with surfaces and materials - analyze the chemical bonding and explain their effect on the tribological performance of surfaces. In particular, the effect on the friction coefficient, wear mechanisms and corrosion processes in lubricated tribosystems.

The second part of this work addressed chemical vapor deposited (CVD) diamond films and transition metal dichalcogenides (TMD) in consideration of desired properties for micro electro mechanical systems (MEMS). The main scientific goal for this part of the work was:

- To evaluate the influence of surface morphologies such as faceted, fine ballas

and coarse ballas on the micro- and nanomechanical properties of microcrystalline diamond film.

- To carry out a comparative AFM investigations of co-sputtered Mo-Se-C and W-S-C films keeping nanotribological application in mind. To analyze the influence of carbon content on the nanotribological behavior of such coatings.

## 1.2 Tasks

To reach the milestones denoted in the motivation section the following specific tasks were designated:

- to develop a method and perform nanotribological studies in liquid and ambient environment using Atomic Force Microscopy (AFM)
- to achieve fast and robust method to measure friction coefficient versus applied load and scanning speed and to measure nanowear rate of hard coatings and cantilever blunt level
- to complete chemical analysis of additive molecules on tribological surfaces with X-Ray Photoelectron Spectroscopy (XPS) and Auger Electron Spectroscopy (AES)
- to adapt an XPS spectrometer and achieve Angle Resolved X-Ray Photoelectron Spectroscopy (AR-XPS) depth profiles of molecules on copper and steel substrates
- to perform a variety of macrotribological test (translatory oscillating test machine (TOG), microtribometer, ball on disc, Mini Traction Machine (MTM)) on copper and steel surfaces using miscellaneous lubricants (polar and non-polar based oils, water) and additives (ethanolamines, ethylamines, glycols, ZDDP)
- to measure wear volume and estimate a corrosion factor for tribotested specimens
- to analyze wear tracks of tribotested specimens by means of XPS
- to compare AR-XPS experimental results with simulations performed with Simulation of Electron Spectra for Surface Analysis (SESSA) software

## 1.3 Organization of the thesis

This thesis consists of five major chapters. The Introduction section (**Chapter 1**) presents the motivation, the milestones and the tasks of this research. Fundamental principles in tribology with literature review are introduced in **Chapter 2**. These concerns three main subjects of this work: additives for water lubrication, the effect of ZDDP additives on rolling bearing and solid lubrication. Although these three branches concern different functionalities of tribosystems, a common concept of boundary lubrication has been used. Materials section (**Chapter 3**) specifies tribological surfaces and type of additives used within this research. Experimental methodology - **Chapter 4** familiarizes with nano and macro tribological test equipments. It explains the principle of friction coefficient measurements with such systems. Special attention is put on the importance of using Atomic Force Microscopy in tribology to understand friction origins and adhesion effect on it, to investigate interrelation phenomena and to adequately describe surface roughness. Spectroscopy methods subsection summarizes the work which has been done to adjust the spectrometer to perform studies on molecular mechanisms. A brief physical principles of operation, the components and setup instructions are also described. An optical methods used for inspection of specimens after tribotests are specified.

**Chapter 5** contains composition of publications written within three years of my PhD studies. Various research in this work showed that molecular processes, especially chemical bondings between lubricants, additives and surfaces strongly affect performance of tribological systems. Presented publications in this section support this statement in three main subjects:

- Additives for Water Based Lubricants. This part describes the influence of amine based corrosion inhibitors on tribo-corrosion behavior of surfaces in micro and macro scales. General conclusion states that the way how the additives bond to the substrate and how the molecules behave under different tribo-contact situation affect friction, wear and corrosion rates.
- Effect of ZDDP additives on rolling bearings. In this section functionality of anti-wear additives in polar and non-polar oil environment were studied. The results demonstrated that a reaction layer formation is strongly dependent on the molecular polarity of the oils and additives. The evolution of the topography and mechanical properties of the ZDDP-derived tribo-layer

with rubbing time showed that initially a thin and soft ZDDP reaction layer develops very quick.

- Solid Lubrication. This part of work was addressed on chemical vapor deposited (CVD) diamond films and transition metal dichalcogenides (TMD) in consideration of desired properties for micro electro mechanical systems (MEMS). The main scientific goal of this part of the work was to evaluate the influence of surface morphologies on the micro- and nanomechanical properties. Keeping nanotribological application in mind, a comparative AFM analysis were carried out and the influence of carbon content on the mechanical behavior of such a coatings was evaluated.

**Additives for Water Based Lubricants** includes four manuscripts:

*"Oligomer specific lubrication"* [1] reports on nanoscale tribological investigations on ethanolamine oligomers in aqueous solutions investigated with an AFM closed fluid cell. The friction measurements under nano Newton load range and calculations carried out to characterize behavior of the additives in aqueous media are presented.

*"Tribiochemistry of monomolecular lubricant films of ethanolamine oligomers"* [2] explains the influence of hydroxyl groups and nitrogen containing ethanolamine oligomers on the nano and macroscale tribological behavior. AR-XPS results were analyzed and molecular mechanisms leading to the macroscopic lubricity was illustrated.

*"Tribological properties of additives for water-based lubricants"* [3] compares the friction, wear and corrosion performance in rolling/sliding tribological contact of additives for water lubricants with similar chemical structure such as ethanolamines, ethylamines and glycols. These studies established the mechanism how various individual additives influence tribological properties of the water system and selected the best compounds and concentrations for this purpose. XPS chemical analysis was performed before and after tribotesting to understand how the structure of the molecular film influences macroscopic tribological performance and how it changes under mechanical loading.

*"Behavior of corrosion inhibitors under different tribological contact"* presents the performance comparison of the additives for water lubricants in different tribological contact situations - rolling/sliding and severe pure sliding conditions.

In this manuscript ethanolamines, ethylamines and glycols were investigated under static corrosion and tribologically induced corrosion conditions. A wide range of rolling and sliding tribocontact parameters was tested to show differences in behaviors. At the same time molecular processes which affect macrotribological performance were explained and graphically illustrated.

**Effect of ZDDP additives on rolling bearings:** Work presented in this subsection is based on collaboration with SKF - the market leading bearing company in particular with Engineering and Research Center engaged in research on improvements of the bearing performance.

*"Effect of Base Oil Polarity on Micro and Nano Friction Behavior of Base Oil + ZDDP Solution"* [4] presents the effect of base oil polarity on the ZDDP molecular behavior (boundary film formation) and friction performance of steel-steel contacts lubricated with two reference base oils (hexadecane - non polar and diethylenglycol - polar) blended with different concentrations of the ZDDP (zinc dialkyldithiophosphate).

*"Evolution of ZDDP-derived reaction layer morphology with rubbing time"* [5] reports on growth of tribological film within tribotesting time until reaching a limiting thickness. The tribotests were conducted with a low polarity commercial base oil, poly- $\alpha$ -olefin (PAO), blended with C<sub>4</sub> Zinc Dialkyl DithioPhosphates (ZDDP). An adapted in-situ interferometry technique was continuously used to monitor the additive derived reaction layer formation. The evolution of the topography and mechanical properties of the ZDDP-derived reaction layer with rubbing time were studied using Atomic Force Microscopy.

**Solid Lubrication** includes two manuscripts. Work presented in this subsection is based on collaboration with AC<sup>2</sup>T Austrian Center of Competence for Tribology. Nanotribological investigations of miscellaneous hard coatings with variance properties were carried out in order to find the best structure desired for application in microelectromechanical systems (MEMS).

*"Micro- and Nanomechanical Properties of Diamond Films with Various Surface Morphologies"* [6] concerns the influence of the morphologies of chemically vapour deposited (CVD) diamond films on their micro- and nanomechanical properties. Diamond films having coarse ballas, fine ballas and faceted morphologies

were characterized with the help of Scanning Electron Microscopy (SEM) and Raman spectroscopy. Hardness of the films was evaluated using nano indenter. Force spectroscopy, topographies and lateral force values of these films were estimated by means of Atomic Force Microscopy (AFM).

*"Nanotribology of Mo-Se-C Films"* [7] examines topography, lateral force and pull off force of transition metal dichalcogenides film at an applied load in the range of nanonewton. The effect of carbon content, applied load and scanning speed on the friction coefficient was evaluated. Observed nanotribological behavior of these films was analyzed in the light of their nanohardness. Chemical analysis showed that these films consist of very fine MoSe<sub>2</sub> grains embedded in a carbon matrix.

In Conclusion (**Chapter 6**) and Summary section (**Chapter 7**), the main conclusion of this thesis, general summary, some recommendations for future work and open questions are presented.

## 2 TRIBOLOGY FUNDAMENTALS

Tribology is the science and technology related with processes between interacting surfaces under relative movement. Moreover, it concerns effects and processes between such surfaces during the transition from standstill to motion (acceleration) and vice versa (deceleration). Tribology covers the fields of friction, wear and lubrication. Tribological processes concern mechanically-dynamic effects (in relative motion), thus they are mostly highly transient. The first signs of tribology came from wall paintings from 2400 B.C. where ancient Egyptians wrestled with transporting heavy statues. There are evidences that they had developed a number of sophisticated tribological devices. For example wheeled carriages and potters wheel and each of these requires some basic bearings. Leonardo da Vinci showed in 1490 in his experiments that the friction increases with increasing load, but is independent of the contact area. His notebooks show many designs for moving parts and machines that show a remarkable similarity to those in use today as shown in Fig. 2.1. [8]

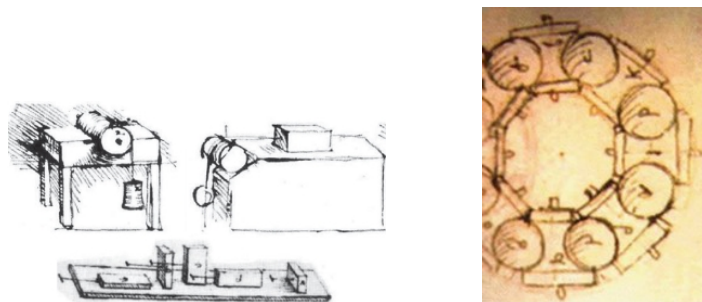


Figure 2.1: Sketches from da Vinci's notebook, demonstrating some of his notable friction experiments.

Two hundred years later Amonton's law, also called the friction law, was formulated (Amonton Guillaume, 1699), which postulates:

I) proportion for the quotient between the friction force  $F$  and the applied load  $L$ .

$$\mu = \frac{F}{L} \quad (2.1)$$

where:  $\mu$ - friction coefficient

II) disproportion from geometrical contact area

III) disproportion from sliding speed Most people assume that Amonton's work was for dry contacts. In fact he put used pork fat on the surfaces he was rubbing together.

In 1785 Coulomb verified three Amonton's laws and additionally showed that a more accurate friction formula should also contain a load-independent term  $C$  [8]:

$$F = \mu * L + C \quad (2.2)$$

This two-term friction equation reflects that dry friction arises from two effects:

- Adhesion between the contacting asperities of the sliding surfaces (based on the real area of contact  $A_c$  of the asperities), ( $\mu * L$ )
- Interlocking (later ploughing) by asperities in the opposing surface (cohesion of molecules of the two sliding surfaces), ( $C$ )

In the 1950s, Bowden and Tabor developed an important friction model based on solid/solid adhesion [9]. According to their model, as rough surfaces approach, the initial contacting asperities deform plastically and adhere until the real area of contact,  $A_c$ , is just enough to support the load Fig. 2.2

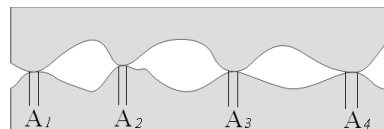


Figure 2.2: Approach of two rough surfaces. Real area of contact is  $A_c = A_1 + A_2 + \dots$

For fully plastic deformation, the real area of contact is proportional to the applied load:

$$L = A_c H \quad (2.3)$$

where  $H$  is effective surface hardness. The force needed to shear these junctions will be proportional to the real area of contact:

$$F = A_c \tau_f \quad (2.4)$$

where  $\tau_f$  is effective shear strength of the junctions. Therefore, assuming friction arises only from adhesion at contact asperities, the friction coefficient is:

$$\mu = \frac{F}{L} = \frac{\tau_f}{H} \quad (2.5)$$

When asperities adhere and a shearing force is applied, the junctions can grow plastically, since both the normal force and the shear force will couple to produce deformation. This will result in an increase in real contact area and thus in friction coefficient [10]. Tabor used this thought to extend his simple model to equation:

$$\mu = \frac{1}{\delta^{1/2}(f^{-2} - 1)^{1/2}} \quad (2.6)$$

where  $f = \tau_f/p_y$  is the ratio of the shear strength of the film to the yield stress of the bulk deformation material, and the  $\delta$  is constant with value of  $\approx 9$  (assuming that hardness=3 x yield stress), this finally gives:

$$\mu = \frac{1}{((H/\tau_f)^2 - 9)^{1/2}} \quad (2.7)$$

As it was shown above, Bowden and Tabor's model explains Amonton's first two laws on the basis of small real contact area  $A_c$ , which is proportional to the applied load and independent of the geometrical area. Since the friction is proportional to the contact area  $A_c$ , friction is proportional to load  $L$ . However the described model is relevant for plastic deformation of asperities. In practice, applied load is also supported by elastic deformation of asperities. Archard in 1957 and subsequently Greenwood and Williamson in 1966, confirm that even for elastic asperity deformation, a statistically-distributed, rough surface will result in  $A_c \propto L$  [11]. This means that Amonton's Laws of friction results from adhesion of plastically deformed asperities (Tabor's theory), even if elastic deformation also occurs. In all above presented friction models, the ratio of interfacial shear strength  $\tau_i$  to solid yield strength or hardness is a crucial parameter in determining adhesive friction. To obtain a low adhesive friction coefficient between rubbing rough surfaces in contact we need low surface shear strength  $\tau_i$  and/or high hardness,  $H$ . These requirements are incompatible for clean metals but can be met if a thin low shear strength layer is formed on a hard metal substrate. Such a layer has to be thin enough not to bend significantly and so increase  $A_c$ . This concept, of using a very thin, weak layer on a much harder substrate to reduce friction is the basis of boundary lubrication and will be used throughout this thesis.

Boundary films can be formed by several processes: physisorption, chemisorption and chemical reactions, as shown schematically in Fig. 2.3. In the case of

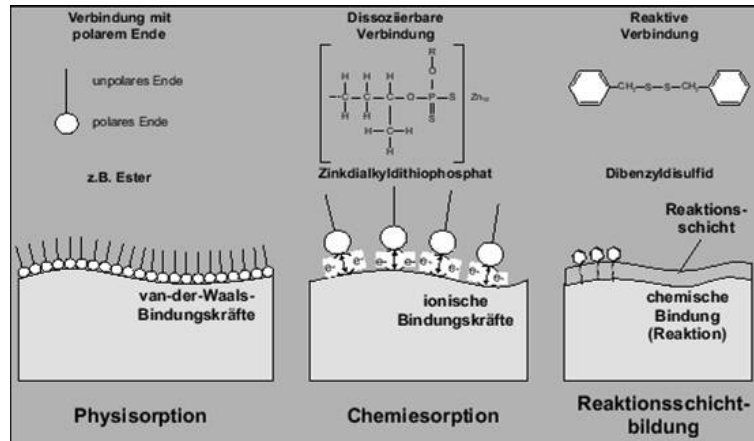


Figure 2.3: Formation of boundary films by 1. physisorption (polar ending connected with surface - van der Waals forces) 2. chemisorption (exchange of electrons- covalent bonding) 3. chemical reactions (chemical reactions of the surface with the environment) [12]

physisorption no exchange of electrons takes place between the lubricant molecule and the surface - this process involves weak van der Waals forces. Chemisorption means the sharing of electrons and electron interchange between chemisorbed species and the solid surface resulting in the formation of chemical bonds. Finally, chemical reactions comprise the formation of surface layers with considerable chemical alteration of both additive and surface. The stability and durability of surface films decrease in the following order: chemical reaction layers (thick films), chemisorbed films (with monomolecular thickness), physisorbed films (monolayers or multilayers) [13].

So called Stribeck curve in Fig. 2.4 represents different regimes of lubrication [14]. The hydrodynamic or elastohydrodynamic lubrication is present when a full lubricant film separates rubbing solid surfaces in contact. Well known example of elastohydrodynamic lubrication is when a thin water film separates the tire and the road. When the film becomes thin the applied load is carried partly by the fluid film and partly by pressure at asperity conjunctions. This is the mixed lubrication regime. At some point, the fluid film thickness becomes so thin that practically all of the load is carried at asperity conjunctions, protected by adsorbed molecules of the lubricant and a thin layer of oxides. The contact is then operating in boundary conditions. Dry contact is excluded from boundary lubrication.

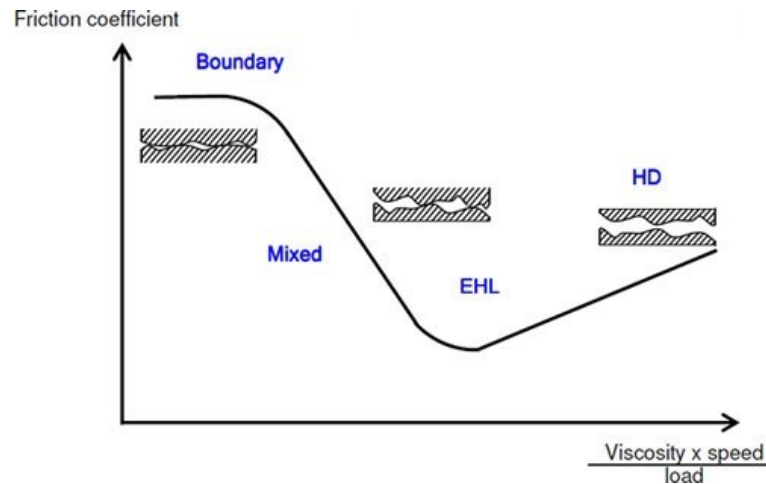


Figure 2.4: Typical Stribeck curve shows how friction varies with the viscosity, speed and load. When the speed and/or viscosity are high (hydrodynamic HD and elastohydrodynamic EHL lubrication regimes), the surfaces in contact are fully separated by the lubricant film. As the speed and/or viscosity decreases, the film thickness decreases and the contact enters the mixed lubrication regime, where surface asperities are only separated by thin surface boundary films [14].

## 2.1 Water Based Lubrication

Water is a low cost lubricant with high cooling capacity but its low viscosity and corrosive properties make it unacceptable for most tribological applications. In order to adjust the performance and improve properties of water-based lubricants, high quality additives are used, such as surface/interface active molecules [15]. The application of water based lubricants include steady-state processes like cooling or rolling operations and non-steady-state processes like metalworking (metalforming and metalcutting mechanisms) [16]. Metalworking or cutting fluids are usually used to reduce cutting force and friction, lower cutting temperature, prolong tool life and enhance machining efficiency.

There are three major types of metalworking lubricant formulations: oils (commonly consist of a petroleum oil), emulsions (mineral oil in the form of suspended droplets) and water-based products (only water and water soluble chemicals). In the past the oil-based lubricants have been used in most practical applications. However they have some fatal disadvantages such as low heat dissipation efficiency, high fire risk, poor biodegradability and non-renewability. Recently more research is focused on water-based lubricants due to advantages such as good heat-sinking capacity, tractability and low toxicity. Thus water-based lubricants are consider as an alternative substitute in oil based metalworking fluids and other fields [17–19].

All three types of lubricants are compounded with additives of various types. Additives are a chemical component or blend used at a specific treat rate to provide one or more functions in the fluid. There are many types of additives:

- Boundary additives enhance the lubricity of the fluid by adsorbing on the surface of the metal to form a film, reducing metal-to-metal contact. These additives typically have a polar group that interfaces with metal and a tail that is compatible with mineral oil or water.
- Extreme pressure additives are a special type of boundary additives that react with the metal surface, instead of adsorbing on the surface. They form a physical barrier between the tool and the workpiece under severe metalworking conditions, thus reducing friction, wear and damage. Examples are chlorinated paraffins, sulfurized lard oils, phosphate esters and overbased calcium sulfonates. These additives have different temperatures of activation.
- Corrosion inhibitors prevent the fluid from corroding the metal workpiece, cutting tool and machine tool. They perform by either forming a protective coating on the metal surface or by neutralizing corrosive contaminants in the fluid. Examples are overbased sulfonates (some of these also can act as extreme-pressure additives), alkanolamides, aminoborates and aminocarboxylates.
- Reserve alkalinity additives maintain the fluid's corrosion protection by neutralizing acidic contaminants and by maintaining the pH in a suitable range. These additives also can act as form emulsifiers with other components to stabilize the fluid. Examples are alkanolamines like monoethanolamine, triethanolamine, aminomethylpropanol and 2(2-aminoethoxy) ethanol.
- Emulsifiers stabilize oil-soluble additives in waterdilutable metalworking fluids by reducing interfacial tension between incompatible components by forming micelles (a submicroscopic aggregation of molecules, as a droplet in a colloidal system). These droplets then can remain suspended in the fluid. In metalworking fluids, examples of emulsifiers are sodium petroleum sulfonate and alkanolamine salts of fatty acids

There are also less important additives such as: metal deactivators, couplers, chelating agents (also known as water softeners or conditioners), antimist, dyes [20]. That is quite a list of multi functional additives, but mixing some of them, which separately give very good results, can cause the opposite outcome [20, 21].

In general sulfur, phosphorus and nitrogen are considered as "active elements" for ferrous-based equipment. Additives with these elements are investigated by many researchers to minimized friction, wear and corrosion in water lubricated systems [22]. Tokarzewski et al. synthesized phosphoryl tris(diethanolamide) DAP as a water-soluble additive, and found that the additive was suitable for non-flammable hydraulic fluid lubricants for mining and machining industry [23]. Zhang et al. investigated the friction and wear behaviors of a (Ca, Mg)-sialon/SAE 52100 steel pair under the lubrication of various polyols in water and found that the friction coefficient was much lower than that of pure water [24]. Lei et al. studied tribological behavior of fullerene-styrene sulfonic acid copolymer as water-based lubricant additive, and found that it can improve wear resistance, load carrying capacity and anti-friction ability [25]. Kajdas in his review on additives for metalworking lubricants enumerate many corrosion inhibitors based on amines. They improve corrosion resistance and can be removed from metal parts by aqueous methods. Additionally nitrites are used to prevent anodic corrosion in electrolytic phenomena [16]. Mango et al. found that amine salts of monoalkylene dicarboxylic acids such as ethanolamine salts of N-ethanolanilidomaleic acid are rust inhibitors agents for aqueous lubricants used in machining metals [26]. Huan et al. reports about improvement of load carrying capacity and friction reducing properties for S-(carboxylpropyl)-N-dialkyl dithiocarbamic acid in water-based fluids [27]. Mori et al. reports about good lubrication properties of TR Gel-Lube which is based on amide and alkyl group additives [28].

In most tribological systems lubricated with water, materials forming the tribological contact are exposed to a very corrosive environment and therefore they are subjected to both mechanical and chemical devastation. Typical examples are orthopedic implants, chemical pumps, mining equipment, or well-known problem of erosion corrosion of pumps and pipes carrying slurries. Corrosive wear is defined as the degradation of materials in which both corrosion and wear mechanisms are involved. The combined effects of wear and corrosion can result in total material losses that are much greater than the effects of each process taken alone, which indicates synergism between the two processes [29]. Corrosion and wear damage to materials, both directly and indirectly, costs hundreds of billions of dollars annually. Although corrosion can often occur in the absence of mechanical wear, the converse is rarely true. Under such a conditions the rate of degradation of a tribological contact cannot be predicted simply from knowledge of the wear resistance in the absence of corrosion or from the corrosion resistance in the absence of friction. The reason is that in tribocorrosion systems the chemical and me-

mechanical degradation mechanism are not independent of each other and synergistic effects can result in accelerated material removal. In other words, tribocorrosion affects the friction, wear and lubrication behavior of the tribosystems and vice versa [30]. Normally, tribocorrosion leads to degradation of the material, but in some applications tribocorrosion can be useful for example chemical-mechanical polishing (CMP) for surface planarization and smoothing. [31] Materials degradation due to simultaneous chemical and mechanical effects may occur under a variety of conditions as shown schematically in Fig. 2.5.

**TYPE OF CONTACT:**

**Sliding**

*corrosive wear  
wear accelerated corrosion  
chemo-mechanical polishing*

**Fretting**

*fretting corrosion*

**Rolling**

*corrosive wear*

**Impingement**

*erosion corrosion  
impingement attack*

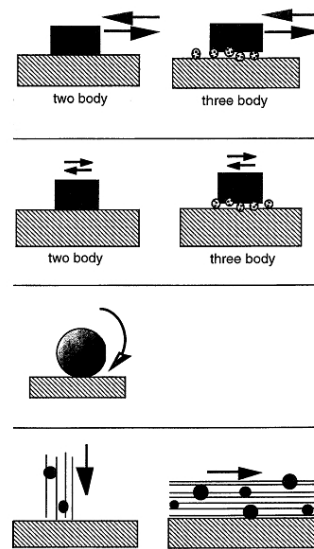


Figure 2.5: Different types of tribological contacts involving simultaneous mechanical and chemical effects

Two body contact involves workpiece and mating materials, whereas three body contact involves separated particles from both materials. Two or three body contact between sliding surfaces can be unidirectional such as in pin-on-disc apparatus or it can be reciprocating. Fretting is special type of tribological contact involving a reciprocating motion of small amplitude. Tribocorrosion is also observed in rolling contacts typical for ball bearings. Particle impact can result in a combined mechanical and chemical attack of the material. From physical point of view tribocorrosion includes variety of mechanical and chemical degradation phenomena referred to variability in the literature as corrosive wear, wear accelerated corrosion, erosion corrosion, oxidative wear, fretting corrosion and impingement attack [30]. In this work tribocorrosion in both sliding and rolling contacts will be discussed.

## 2.2 Effect of ZDDP Additives on Rolling Bearings

Commercially available lubricants are formulated products composed of a base oil (mineral or synthetic) and a functional additive package designed to achieve a required performance for a specific application [32]. For rolling bearings additive package must contain antioxidants and corrosion inhibitors since highly-finished bearing surfaces are susceptible to rust pitting which initiates fatigue. Zinc dialkyldithiophosphates ("ZnDTP", "ZDTP", "ZDDP", "ZDP") have been widely used in the past decades as additives in engine lubrication oil. ZDDP was initially used as an antioxidant, but their excellent antiwear properties were quickly recognized. They can also act as mild extreme pressure agents and corrosion inhibitors. ZDDP additives have also been the object of a great deal of research due to their multifunctional performance and the complexity of the mechanisms that lead to it. The antiwear properties of ZDDP additives arise from their ability to interact chemically with rubbing metal surfaces to form a protective layer. It protects the surface under conditions where elastohydrodynamic lubrication breaks down. In order to perform effectively, films of this kind must possess a shear strength that is sufficiently low to ensure that the shear plane resist within protective layer itself, while being high enough to maintain layer integrity [32].

A variety of mechanisms have been proposed for the formation of the ZDDP derived reaction layers, involving oxidative (by reaction with hydroperoxides or peroxy radicals) [33], catalytic (chemisorption on metal, hydrolytic [34]), and thermal [35] decomposition of the ZDDP. Some of the existing theories suggest that E.P additive also function by a modified form of adsorption. The weak interaction of the molecules with steel surface starts through initial adsorption at room temperatures [36]. ZDDP starts to catalytically decompose around 50°C in the presence of iron oxide substrate [37]. An increase in loads, sliding speeds or operating temperatures causes the adsorbed additives to decompose on the worn surface. Decomposition products react to generate a 50-150 nm thick layer [32], [38]. The resulting reaction layers have a heterogeneous composition with the chemical structure of the starting materials dictating their chemical composition. The structure and chemical composition of the layer has been analyzed using advanced spectroscopy techniques such as X-ray photoelectron spectroscopy (XPS), Auger electron spectroscopy (AES), and X-ray absorption near-edge spectroscopy and found to be dependent on temperature and tribological conditions [39]. The layers are composed of a mixture of short- and long- polyphosphates with the presence of sulfides and oxides in the in the layer bulk [40]. A two-layer structure for the

ZDDP-derived reaction layers has also been proposed, where a thin long-chain zinc poly(thio)phosphate layer is superimposed on a thicker short-chain mixed Fe/Zn polyphosphate layer, containing embedded nanocrystallites of ZnO and ZnS [41]. However several studies have proved that ZDDP have detrimental effects on wear under certain operation conditions, and to enhance friction when the system is operating in mixed and boundary lubrication regimes [42].

The anti wear films produce particularly by ZDDP are highly uneven [43]. Sheasby and Nisenholz [44] detected the existence of 20  $\mu\text{m}$  diameter "pads" of ZDDP-derived anti-wear films by means of SEM. Graham et al. [45] found that ZDDP indeed yielded 10-20  $\mu\text{m}$  pads with flattened tops, elongated in the sliding direction and surrounded by lower smaller pads. They also measure mechanical properties of these pads, and found that at the center of the large pads indentation modulus values were as high as 209 GPa (compared to 220GPa for the substrate 52100 steel!). Canning et al. [46] showed that alkyl-ZDDP films formulate large pads consist of long-chain polyphosphates, whereas smaller pads contain short-chain phosphates. They also proved that aryl-ZDDP-derived films were homogeneously distributed on surface and did not display such high indentation moduli, what consequently gives inferior wear resistance. This suggests that an agglomeration of large long pads of polyphosphate chains perform as sacrificing load carrying "platforms" [32]

## 2.3 Hard Coatings

In the past 50 years, during the industrial revolution solid tribological materials and coatings have continued to play important roles in many engineering areas, mainly because mechanical systems rely on them for high performance, durability, and efficiency. Recent developments in deposition technologies have provided the flexibility needed for design and development of multifunctional coatings. The use of thin surface coatings (such as diamond, diamond-like carbon, molybdenum disulfide, nitrides, carbides, and their composites and dopants) afford low friction and long wear life of rolling, rotating, or sliding mechanical parts and components in recent years [47]. Application of the thin coatings on solid surfaces ensure that premature failures due to thermal, mechanical, or chemical incompatibility are nonexistent. In this field, there are almost unlimited numbers of material combinations, surface parameters, and application conditions that one can manipulate to a achieve better performance and longer durability.

In this work solid lubricants and self-lubricating films such as transition-metal

dichalcogenides (TMD), diamond, diamond-like carbon, and composites have been used.

Solid lubricants are used when service conditions are very severe (i.e., very high or low temperatures, vacuum, radiation, etc.) and liquid or grease lubricant fail. Solid lubricants owe their lubricity to a unique layered crystal structure an example are transition-metal dichalcogenides  $MX_2$  (where M is molybdenum, tungsten, or niobium, and X is sulfur, selenium, or tellurium). In Fig. 2.6 the crystal structure of these solids is shown. It can be observed that while the atoms lying on the same layer are closely packed and strongly bonded to each other, the layers themselves are relatively far apart, and the forces that bond them (e.g., van der Waals) are weak. When present between sliding surfaces, these layers can align themselves parallel to the direction of relative motion and slide over one another with relative ease, thus providing low friction. In addition, strong interatomic bonding and packing in each layer is thought to help reduce wear damage.

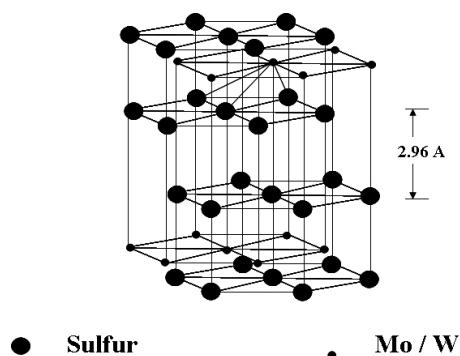


Figure 2.6: Schematic illustration of layered crystal structures of molybdenum disulfide (representing transition metal dichalcogenides) [47]

Solid lubricants are typically deposited on surfaces by advanced vacuum deposition processes (e.g., sputtering, ion plating, and ion-beam-assisted deposition) to achieve strong bonding, dense microstructure, uniform thickness, and long wear life [48]. Ion-beam deposition and mixing can also be used to enhance the durability of solid lubricant coatings [49]. Nowadays magnetron sputtering, PVD and CVD deposition techniques let to the synthesis of adaptive, self-lubricating coatings with composite or multilayer architectures [50]. These are based on layers of a self-lubricating dichalcogenide (e.g.,  $MoS_2$ ,  $WS_2$ , etc.) and a soft metallic or hard ceramic layer, and work extremely well under demanding tribological conditions. It is also known that properties of solid lubricants depends on sputtering method. For example  $MoS_2$  films deposited by conventional sputtering methods exhibit higher friction and shorter wear lives than films produced by ion-beam-

assisted deposition. However films deposited by magnetron sputtering techniques can have near-perfect stoichiometry, purity, and basal plane orientation parallel to the substrate [51]. It is also noted that WS<sub>2</sub> and MoSe co-sputtered with carbon significantly improved tribological properties compared to pure WS<sub>2</sub> and MoSe [52]. Radio-frequency (r.f.) magnetron sputtering of MoSe<sub>2</sub> or WS<sub>2</sub> films alloyed with C can be seen in Fig. 2.7.

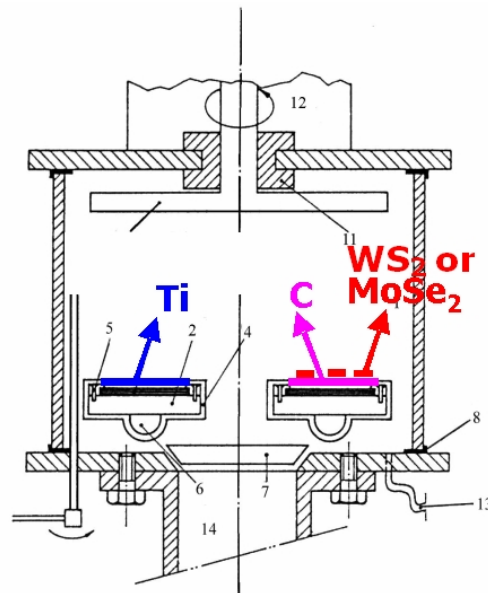


Figure 2.7: Principle of radio-frequency magnetron sputtering from a carbon target embedded with WS<sub>2</sub>/MoSe<sub>2</sub> pallets [53].

Diamond, diamond-like carbon (DLC), and other related coatings (such as carbon nitride and cubic boron nitride) are some of the hardest tribomaterials known having the lowest friction and wear coefficients under dry sliding conditions. Applications of diamond-like carbon coatings include rolling and sliding bearings, machining, mechanical seals, biomedical implants, microelectromechanical systems (magnetic rigid disks and metal evaporated tapes used in magnetic storage devices) [54], [55].

Diamond is chemically inert, and it exhibits poor adhesion with other solids with consequent low friction and wear. Its high thermal conductivity allows dissipation of frictional heat during sliding and protects the interface, and the dangling carbon bonds on the surface react with the environment to form hydrocarbons that act as good lubrication films. These are some of the reasons for low friction and wear of the diamond [56].

Natural diamond is rarely used for tribological purposes however, synthetic polycrystalline diamonds (PCDs) have been available for more than 30 years and they

are widely used in many industrial applications. The DLC films exhibit a wide range of structure, composition, and attractive mechanical, optical, electrical, chemical, and tribological properties depending on deposition technique. The film structure and properties are determined by the H content and the relative ratio of the two sp<sup>2</sup> and sp<sup>3</sup> carbon hybridizations, the sp<sup>1</sup> C hybridization being negligible. The amorphous carbon coatings can be prepared by a variety of deposition techniques: DC, RF or ion beam sputtering, RF or DC plasma-enhanced chemical vapor deposition (PECVD), electron cyclotron resonance chemical vapor deposition (ECR-CVD), direct ion beam deposition, pulsed laser vaporization and vacuum arc from a variety of carbon-bearing solids or gaseous source materials.

In our work microwave plasma CVD apparatus was used to deposit DLC film with faceted, fine ballas and coarse ballas morphologies.

# 3 MATERIALS

## 3.1 Mating Materials/Surfaces

### 3.1.1 100Cr6 Steel

All the tribological test were performed on 100Cr6 steel balls and disc.

**WAM tests** The steel balls (20 mm diameter) were of AISI 52100 steel with hardness 59-66 HRC and an average roughness (Ra) of 10 nm. The rings were washers (WS 81212) from SKF Cylindrical Thrust Roller Bearings (CTRB) of AISI 52100 steel with hardness 59-66 HRC and Ra=100 nm. The specimens were cleaned prior to testing by successive immersion first in an ultrasonic bath of petroleum ether for 10 min and then acetone for 10 min.

**MTM tests** Specimens used for MTM tribotests were made of AISI 52100 steel (PCS instruments, London, UK). The initial disc and ball roughness was Ra=0.01  $\mu\text{m}$ , and their diameters were 46 mm and 19.05 mm respectively. The specimens were cleaned in an ultrasonic bath of toluene for 10 min and then in ethanol for 10 min.

**Adsorption test** The samples for adsorption tests were cut from SKF standard roller bearing with cutting machine. The final size of the samples was 0.8 x 10 x 3 mm<sup>3</sup> and slightly exceed the size of XPS sample holders. The sheets were grounded with silicon carbide abrasive paper with grid size from 150 to 4000 on a Struers LaboPol-4 grinding machine. Afterwards the sheets were polished with DP-Spray containing polycrystalline diamond grains with size of 1  $\mu\text{m}$ . Afterwards the samples were cleaned in ultrasonic bath with toluene for 10 min and than with ethanol for 10 min.

### 3.1.2 Copper Sputtered on Silicon Wafer

Silicons wafers from Institute of Electronic Materials Technology (Warsaw), one side polished, with thickness 280  $\mu\text{m}$  were cut into 1 x 1 cm<sup>2</sup> pieces. Copper sputtering was performed in the Institute for Solid State Physics, Vienna University of Technology.

### 3.1.3 Transition Metal Dichalcogenides (TMD)

All TMD coatings have been deposited on 100Cr6 polished steel samples, with hardness close to 5 GPa. Co-sputtered Mo-Se-C and W-S-C films were alloyed at approximately 55% carbon. Coatings were deposited by radio-frequency magnetron sputtering of a carbon target with pellets of MoSe<sub>2</sub> and WS<sub>2</sub> in a basic ESM 100 Edwards unit in an argon atmosphere. The pellets (99.8% pure) with dimensions of 1.5 x 3 x 4 mm<sup>3</sup> were distributed uniformly in the circular erosion zone of the carbon target, their number varied between 16 and 72. For W-S-C films WS<sub>2</sub> pellets were used and for Mo-Se-C films MoSe<sub>2</sub> pellets. Before deposition, the substrates were cleaned for 30 min by establishing the plasma close to the substrate electrode. The discharge pressure and the power density were 0.75 Pa and 8 Wcm<sup>-2</sup> respectively. The deposition time was 1 h giving rise to a final thickness of the coatings in the range of 1 μm. No substrate bias was applied during the deposition.

### 3.1.4 Diamond Films

Diamond films were deposited using an ASTEX microwave plasma CVD apparatus. The system has a stainless steel chamber and it operates at 2.45 GHz, 1.5 kW. It is equipped with a heated graphite substrate holder. Silicon (100) substrates scratched with diamond powders were used for deposition of film. Si was scratched with 0.25 mm diamond powders for 30 min and then cleaned ultrasonically. The substrate temperatures were measured with the help of an optical pyrometer. Deposition parameters such as gas pressure, gas flow and microwave power were kept constant. The ratio of CH<sub>4</sub> to H<sub>2</sub>, substrate temperature and deposition time were varied.

## 3.2 Additives

Basically, liquids are good lubricants when they contain polar compounds and thus are able to adsorb on solid surfaces. Such polar compounds contain reactive functional groups with low ionization potential, or functional groups with high polarizability. Furthermore, boundary lubrication properties of lubricants depend on molecular conformation and lubricant spreading [56].

Most of commercial packages of lubricant additives or corrosion inhibitors have organic polar molecules that adsorb on the surface and form a protective film barrier. For better results the organic additives must be chemisorbed on surface

to be effective. It is usually the pendant chain, which anchors to the surface [57]. Monomolecular lubricant layers on solid surfaces may reduce friction, wear, and rust. In the case of dispersions, they have the ability to stabilize emulsions, foams, and solid dispersions [58].

### 3.2.1 Amines and Glycols for Water Based Lubricants

Ethanolamines or aminoethanols are known as multidentate ligands with the possibility to form chelates with metals via their amino, hydroxyl and deprotonated hydroxyl groups. The total formula of these water soluble compounds is  $NH_3 - nRn$  ( $R = CH_2CH_2OH, n = 1 - 3$ ). Ethanolamines appear as three different oligomers: monoethanolamine (MEA), diethanolamine (DEA) and triethanolamine (TEA) as shown in Fig. 3.1

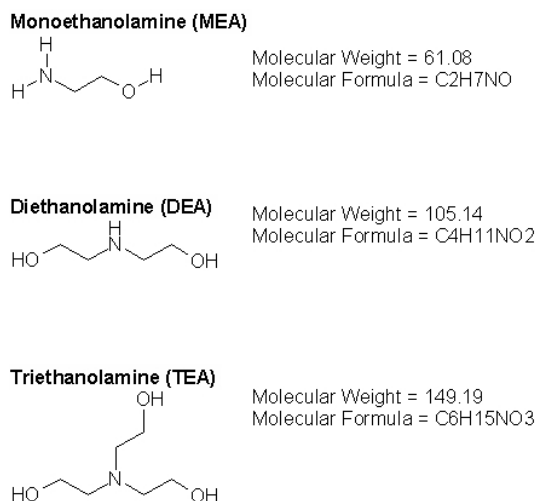


Figure 3.1: Structural formula of mono-, di- and triethanolamine

MEA, DEA and TEA were at least of 98% purity (GC) and used as obtained. Some ethanolamine derivatives with longer hydrocarbon chains (3-amino-1-propanol, 4-amino-1-butanol) were also used in tribotest to examine influence of the length of carbon chain on performance. Chemical structures of ethanolamine derivatives are shown in Fig.3.2

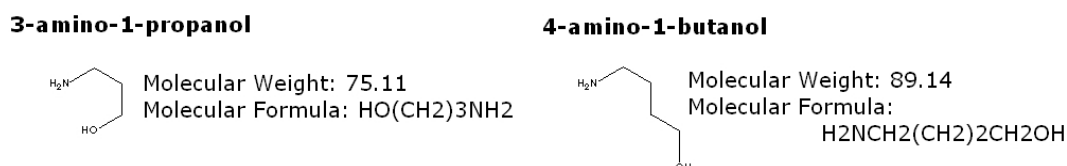


Figure 3.2: Structural formula of 3-amino-1-propanol and 4-amino-1-butanol

Ethylamines are organic water soluble compounds with the total formula  $NH_2-nRn$  ( $R = CH_2CH_3, n = 1-3$ ). Ethylamines are widely used in chemical industry and organic synthesis. In this work diethylamine, triethylamine and some derivatives with longer carbon chain such as propylamine and dipropylamine were tested. Their chemical formulas with molecular weight are shown in Fig.3.3

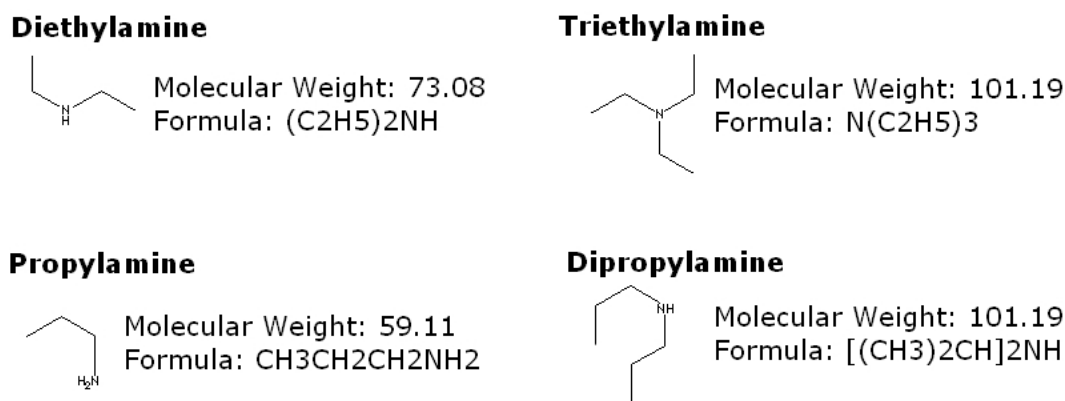


Figure 3.3: Structural formula of diethylamine, triethylamine, propylamine and dipropylamine

Glycols in this work have been used as known friction modifier as a reference additive. Glycols are organic chemicals characterized by having separate two hydroxyl (-OH) groups, contribute to high water solubility, hygroscopicity and reactivity with many organic compounds. Chemical structural formulas of Monoethylene glycol and 1,4-Butylene glycol are shown on Fig.3.4

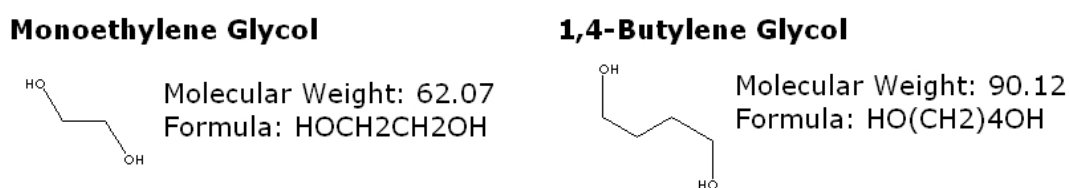


Figure 3.4: Structural formula of monoethylene glycol and 1,4-butylene glycol

Each of the ethanolamines, ethylamines and glycols were dissolved in double distilled water with a concentration of 250 ppm (parts per million), 500 ppm and 1000 ppm. The chosen concentration of these additives was significantly below saturation concentration to prevent growth of additive crystals on the surfaces. To achieve such a small target concentration, 20  $\mu\text{L}$  of each pure ethanolamine and ethylamine have been injected by pipette into 80 mL of double distilled water. Additionally calculation of molecular concentration have been performed, to be sure that all water solution have the same molar content. That means that number

of mole have to be the same for all additive molecules.

$$m_s = \rho \cdot V \quad (3.1)$$

$$C_m = \frac{m_s}{m_r} \cdot 100\% \quad (3.2)$$

$$n = \frac{m_s}{MW_s} \quad (3.3)$$

where  $m_s$  is a mass of substance,  $m_r$  is a mass of solvent,  $\rho$  is a density,  $V$  is a volume,  $C_m$  is a molecular concentration,  $n$  is a number of mole and  $MW$  is a molecular weight. One calculation example is shown for Monoethanolamine oligomer and its derivative structure 3-amino-1-propanol:

Double distilled water:  $m_r = 80$  mL,  $V = 80$  g

Monoethanolamine:  $\rho = 1.022$  g/mL,  $MW = 61.08$ ,  $V = 20\mu\text{L} = 0.02\text{mL}$ ,

$m_s = 1.022$  g/mL $\cdot$ 0.02mL = 0.02044g

$$\begin{aligned} C_m &= \frac{0.02044\text{g}}{80\text{g}} = 0.02555 = 255.5\text{ppm} \\ n &= \frac{0.02044}{61.08} = 0.000334643 \end{aligned} \quad (3.4)$$

The same molar concentration as monoethanolamine must have 3-amino-1-propanol:  $\rho = 0.982$  g/mL,  $MW = 75.11$ ,  $m_s = 0.000334643 \cdot 75.11 = 0.025135\text{g}$ ,  $V = 0.025135\text{g}/0.982\text{g/mL} = 0.02556\text{mL} = 25.6 \mu\text{L}$ . This means that for 3-amino-1-propanol to obtain same molar concentration as monoethanolamines  $V=25.6 \mu\text{L}$  has to be introduced to  $80\mu\text{L}$  of double distilled water. The same calculations have been performed for all the additives and their derivative structures.

### 3.2.2 Zinc Dialkyl-Dithio-Phosphate (ZDDP) in oil solutions

In order to study the influence of base oil polarity on tribological performance two low-viscosity model base oils were selected: one polar oil, diethylenglycol diethyleter (DEG) and one non polar oil, n-hexadecane (HeD), both by Acros Organics, NJ, USA. Iso-C<sub>4</sub>butyl-zinc dithiophosphate (ZDDP), 99% purity by A&S Chemie, Tübingen, Germany, was employed in simple solution in both base oils without other additives present.

The lubricant selected for investigation of ZDDP derived reaction layer evaluation was the base oil poly- $\alpha$ -olefin (PAO), a synthetic non-polar oil. PAO was chosen over mineral oil due to its purity, as mineral oil has a relatively high concentration of sulfur which might interfere with the additives.

# 4 EXPERIMENTAL METHODOLOGY

Good Working Practices:

If in doubt don't.

If in doubt ask.

Don't panic.

When handling solvents wear apron, mask, gloves and only in ventilated area.

When handling or decanting mineral oils wear protective clothing.

Aerosols of mineral oils, can be hazardous and an exhaust is recommended.

Before attempting to service electrical apparatus, isolate from the mains.

Treat all unknown substances as hazardous.

Dispose of substances in an appropriate manner.

Use the correct tool for the job.

Wear protective clothing and glasses when using liquid nitrogen.

Always keep protective screens on if using an X-ray source.

Always make sure you understand a procedure well before attempting it for the first time and so on ...

## 4.1 Atomic Force Microscopy

The invention of the scanning tunneling microscope (STM) by Binnig and Rohrer in 1981 opened the gate to the fascinating area of studying the topographic and physical properties of surfaces at a nano scale. As acknowledged by Binnig, such a powerful technique has its origins in the stylus profiler (invented by Schmalz already in 1929) [59]. In 1971 Russell Young demonstrated a noncontact type of stylus profiler, called the Topographiner. Young used the fact that the electron field emission current between a sharp metal probe and a surface is very dependent on the probe sample distance for electrically conductive samples. The resolution of Young's instrument was controlled by the instrument's vibrations [60]. Binnig and Rohrer demonstrated that by controlling the vibrations of an instrument

very similar to Young's Topographiner, it was possible to monitor the electron tunnelling current between a sharp probe and a sample. Since electron tunnelling is much more sensitive than field emission, the probe could be used to scan very close to the surface. The results were astounding: Binnig and Rohrer were able to see individual silicon atoms on a surface. Although the STM was considered a fundamental advancement for scientific research, it had limited applications, because it worked only on electrically conductive samples[61]. Atomic Force Microscopy (AFM) was for the first time introduced by Binnig and co-workers in 1986. Instead of measuring the tunneling current, a new physical quantity could be investigated: the force between the tip and the sample surface [62]. Sample conductivity was no longer a requirement, and measurements on new classes of materials like insulators and large band-gap semiconductors by atomic-scale scanning probe microscope become feasible.

### 4.1.1 Operation principle

Measurements were performed with an AFM MFP-3D atomic force microscopy (by Asylum Research, Santa Barbara, CA). The operation principle of the AFM is very easy, it measures ultra small forces ( $\leq 1$  nN) between an AFM tip and a sample surface. The AFM can measure a variety of forces used for imaging surface properties, including van-der-Waals-forces, electrostatic forces, magnetic forces, adhesion forces and friction forces. There are also techniques for measuring electrical, mechanical and chemical properties of a sample.

The AFM can measure the lateral and horizontal deflection of the cantilever with nanometer resolution. This is due to application of an optical lever: a light beam, emitted by a diode laser, usually 5 mW max peak output at 670 nm (infrared), forms a spot on the back of the cantilever which gets reflected to the screen. The screen itself is a position sensitive detector, which is divided into four quadrants and converts the spot position into an electrical signal (see Fig. 4.1). Upper and lower parts of screen give the height distribution (topographic imaging), left and right parts of this screen give the lateral distribution (friction imaging). When the tip is scanning over the sample surface, the deflection of the cantilever can be recorded as an image, which represents the three dimensional shape of the sample surface.

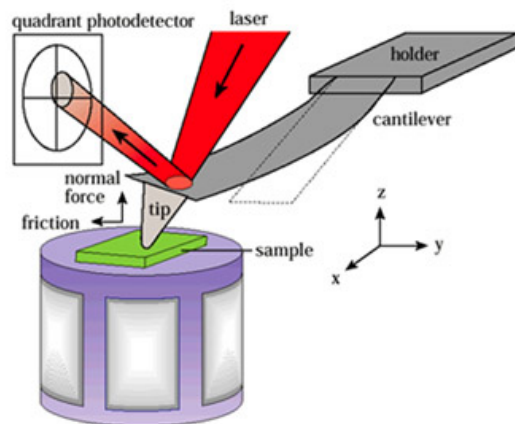


Figure 4.1: Schematic diagram of atomic force microscope [63]

The sample is placed on AFM sample stage, which can move the sample in  $x$  and  $y$  direction and a scanner in  $z$ -direction using piezos. Piezoelectric materials have the property to change their crystal structure when a voltage is applied, this causes an expansion or a retraction of the crystal. In the case of our AFM (MFP-3D, by Asylum Research, Santa Barbara, CA) the piezos used are so called stacks, which can move only in one dimension. This solves the problem of coupling the motion in  $x$ - and  $y$ -direction and even in  $z$ -direction, when piezo tubes were applied in different systems. A stack can expand about  $45\ \mu\text{m}$  with an enormous force. This is very important to push the tiny springs of the sample holder and therefore move the sample table. If a voltage is applied on the piezo stack it expands and pushes the metal bar. The metal bars flexes and pulls on the central stage. The central stage is held on the rest of the sample table by little springs and so the movement of the  $x$ -axis and the  $y$ -axis is completely independent [63].

The position of the piezo is determined by using LVDTs (Linear Variable Differential Transformer). A LVDT is a sensor, which can detect changes of capacities and inductivities. With this information, drift effects and hysteresis effects are compensated. The linear variable differential transformer is a type of electrical transformer used for measuring linear displacement. LVDTs are often used for position feedback. They are sensitive enough to digitize the movements on a nanoscale.

### 4.1.2 Cantilever

Typically AFM probe contains one to five cantilevers ( $100\text{-}200\ \mu\text{m}$  long), with a sharp tip located at the end (a few microns long and less than  $100\ \text{\AA}$  in diameter). Each of the flexible cantilevers has a different spring constant, that allows the cantilever to bend and respond to the forces between the tip and the sample sur-

face. Cantilevers operate at a certain resonance frequency, ranging from 5-300 kHz, depending on the geometry and the spring constant, available in a range from 0.01 to 100 N/m [64]. The resonant frequency of cantilever  $\varpi_0$  depends on its spring constant  $k_c$  and effective mass, and is given by:

$$\varpi_0 = \sqrt{k_c/m} \quad (4.1)$$

On this basis smaller cantilevers with high spring constant give higher speed performance and allow lower noise sensitivity.

The deflection of the cantilever can be described by Hook's law, stating that the force affecting the cantilever is proportional to its displacement:

$$F_c = -k_c \cdot d \quad (4.2)$$

Where  $F_c$  is the force acting on the cantilever,  $k_c$  is spring constant, and  $d$  is its deflection. Depending on the type of measurement and sample different cantilevers have to be chosen.

Parameters for imaging such as scanning mode, scanning speed, resonant frequency and spring constant are all cantilever dependent. Those parameters together with the quality and stability of cantilever tips have a major influence on the imaging quality. The shape of the tip has the influence on the topography of a sample surface. The obtained image sometimes is an interference of the shape of the tip and sample surface topography as illustrated in Fig. 4.2. Also the chemical properties of the tip have an influence on the obtained image or pull-off force, due to the interactions between tip and probe [58].

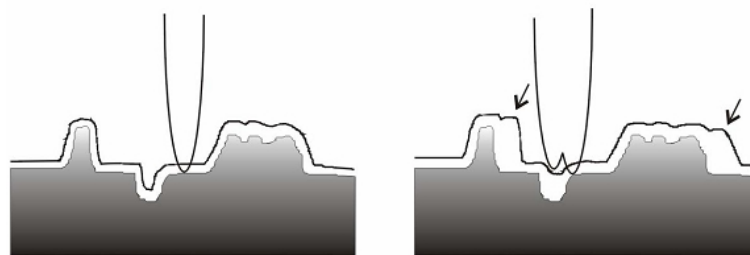


Figure 4.2: Effect of tip shape on topography image

### 4.1.3 Scanning modes

There are two main imaging modes using AFM: contact mode and dynamic mode (tapping, AC mode).

In contact mode, the cantilever tip is in close contact with the surface of the sample. During the first contact, the atoms of the cantilever tip sense a repulsive force, which is caused by the overlap of the electronic orbitals of the atoms of the sample surface with the tip. While scanning, the tip is in contact with the sample surface, this causes a movement of the cantilever in z-direction and so changes of the deflection signal. Set point is the user preset value of deflection. DC feedback amplifier compares the actual and preset value, and if the deflection value is different from the preset value, the feedback amplifier applies a voltage to the piezo to raise or lower the cantilever tip relative to the sample surface in order to restore the preset value of deflection. So the voltage to the piezo is directly related to the cantilever movement and yields the topography of the sample surface. Because the tip is in hard contact with the surface, the stiffness of the cantilever needs to be less than the effective spring constant holding atoms together, which is on the order of 1-10 nN/nm. Most contact mode levers have a spring constant of  $< 1\text{N/m}$ .

In dynamic mode the distance between the tip of the cantilever and the sample surface is constant. The tip hovers 5 - 15 nm above the sample surface and attractive Van der Waals' forces between the tip and the sample are detected. Since the attractive forces from the sample are substantially weaker than the forces used in contact mode, the tip must be given a small oscillation at its resonant frequency so that detection methods can be used to detect the small forces between the tip and the sample by measuring the change in amplitude, phase, or frequency of the oscillating cantilever in response to force gradients from the sample.

#### 4.1.4 Closed Fluid Cell

Part of this work was performed in fluid environment in a closed fluid cell. The fluid cell is a chamber consisting of two halves (Fig. 4.3a) screwed together mechanically: The samples were glued onto glass on the lower part of the closed fluid cell while the upper half basically consisted of the electronic interface, the cantilever and a flexible membrane. After screwing together both halves, the fluid cell was flooded with double distilled water (Fig. 4.3b). Two channels of the cell were used to inject fluid into the cell and to drain it, respectively. In the next step, the fluid cell was attached to the head of the AFM. After placing the head with the cell onto the moving table the head was lowered until the cell attached to the table (Fig. 4.3c). The reference scans in double distilled water environment were carried out when the mounting and calibration procedure of the system was completed. The lateral trace and retrace data were recorded. Then, the ethanolamine oligomer solutions

were injected into the cell with a syringe and the AFM experiments were performed analogously to the reference measurements. For reproducibility of the results it is very important that all parts of the fluid cell have to be properly clean with isopropanol and the cantilever and tubes have to be completely replaced after every contact with ethanolamine solution.

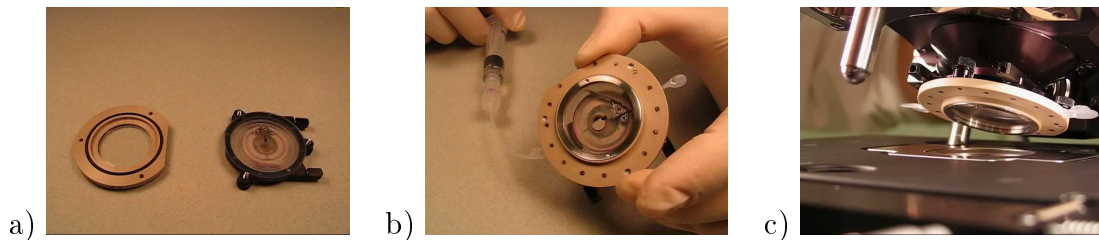


Figure 4.3: Assembling Closed Fluid Cell a) Sealing the cell and mounting the appropriate tubes to the four inlet/outlet ports b) Filling the cell with fluid and performing a leak test c) Putting the closed cell assembly onto the head and setting-up the tube-clamp

#### 4.1.5 Application in Tribology

Micro/nanotribological studies are needed to develop a fundamental understanding of interfacial phenomena on a small scale. These investigations of interfacial phenomena also involve ultra thin films and micro/nanostructures - both currently being used in magnetic storage systems, micro/nanomechanical systems (MEMS/NEMS) and other industrial applications. Probe-based microscopes, e.g. the atomic force microscope (AFM), and the surface force apparatus are widely used for such micro/nanotribological studies [56], [58]. AFM is suitable to study engineering surfaces under dry or wet conditions with atomic resolution. One of the most notable extension of AFM capabilities was the possibility to measure lateral forces between the tip and the sample. Thus, the atomic-scale origins of friction could be observed with this technique, usually described as lateral or friction force microscopy (LFM or FFM). This fact established the AFM as an important tool in the emerging field of nanotribology: the study of the atomic-scale interactions between surfaces in relative motion, such as friction, adhesion, lubrication and wear. Moreover, the gap between this atomic-scale understanding and macroscopic application will need to be bridged. Transition from single (nanoscale) asperity to multiple asperity contacts hold the promise to predict tribological behavior. Hence much effort has been invested to resolve and quantify tribological phenomena also on nanometer scales. AFM techniques for quantitative, fundamental nanotribology

are in a nascent stage, still some key issues as force calibration, tip characterization or effects of the environment are neither fully resolved nor standardized.

#### 4.1.6 Force Distance Curves

Force plots are often used to measure the interaction forces between the tip and the surface. This is done by pushing the tip against the surface, and then separating the tip and surface. From this data, a number of things can be studied, such as adhesion, indentation or tribolayer elasticity. There are different force regimes in which forces can be measured with the AFM. Fig. 4.4 describes in detail the normal force typically experienced by the tip when it is brought towards a sample surface.

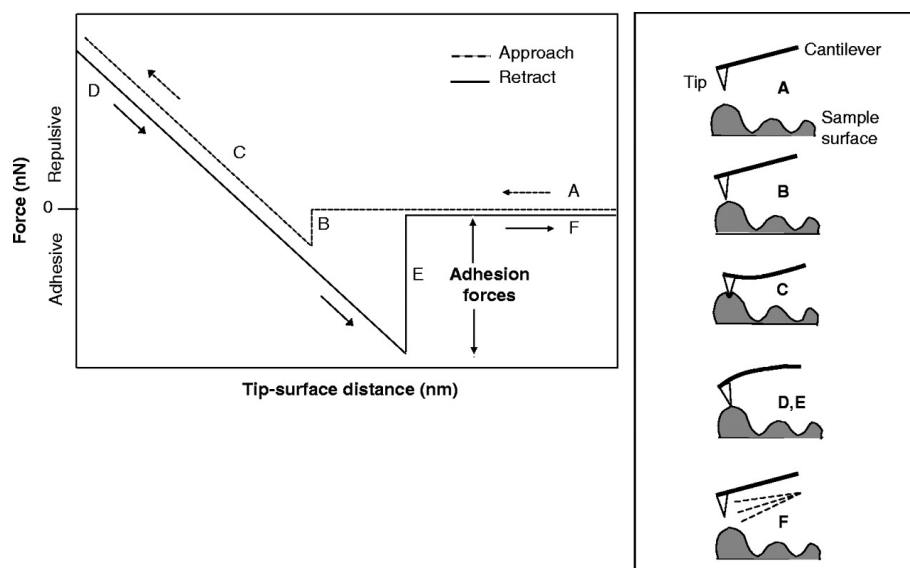


Figure 4.4: An "approach curve" or "force distance" curve displays the vertical cantilever bending vs cantilever-sample displacement [65].

In the Fig. 4.4: a - The cantilever and sample are initially far apart and no forces act. B - As the cantilever is brought close to the sample, the tip senses attractive forces (van der Waals and electrostatic), when their gradient exceed the spring constant of the cantilever then the tip snaps into contact with the sample. C - The lever-sample displacement continue to be reduce, the lever is pressed downwards. D, E - The motion is reversed, the tip is pulled off. Adhesion between the tip and sample maintains the contact although there is negative load applied. F - Finally the load overcomes the adhesion and tip snaps out of a contact with the sample. Force distance curves are capable of providing information about the lateral variations of probe-sample interactions. The lateral force needs to be cali-

brated by the determination of the slope of deflection vs. LVDT. The calibration delivers an accurate value of the inverse optical lever sensitivity (InvOLS) describing the sensitivity of the detector-cantilever combination. With the knowledge of the accurate value of InvOLS and spring constant of the cantilever, it is possible to calibrate the units commonly used in AFM Volt into Newton.

### 4.1.7 Friction Measurements

A reliable quantification of the surface morphology based on any AFM lateral image requires determination of the friction coefficient (lateral force dependent on normal forces). However quantitative determination of friction forces is a challenge, due to difficulties with the calibration of the instrument and cantilever. Typically this calibration involves the conversion of the lateral force signal (also named output voltage signal) of the sector area-sensitive photodiode to values of absolute lateral force using (a) the torsional spring constant of the cantilever and (b) the lateral sensitivity of the photodiode. Many existing methods provide calibration approaches with large errors (30-50%) and suffer from poor reproducibility [66, 67].

Bhushan introduced two methods to measure the friction in AFM experiments [56]. For the presented measurements, the lateral force technique has been chosen since it is described as more reliable and objective: the sample is scanned perpendicularly to the long axis of the cantilever beam, i.e. scanning along the arrow directions, to record the lateral force signals in trace and retrace (LT, LRT). Using this arrangement, the friction force between tip and surface will cause the cantilever to twist as soon as the sample moves under the tip. Therefore, the signal intensity between the left and the right detectors will vary as:

$$FFM = (L - R)/(L + R) \quad (4.3)$$

Where FFM denotes the friction force signal. This signal can be related to the degree of twisting, hence to the magnitude of friction force. By changing the set point parameter in the feedback loop, the normal force applied between probing tip and sample surface can be changed. The scan area was  $5 \times 5 \mu\text{m}$  consisting of 512 scan lines with each 512 scan points. First, the average values of all 512 lines with 512 points for lateral trace (LTV<sub>avg</sub>) and lateral retrace (LRTV<sub>avg</sub>) from every scan were calculated. To obtain the friction force value (FFV), these two mean values have to be subtracted from each other, and divided by two:

$$FFV = \frac{|LTV_{avg} - LRTV_{avg}|}{2} \quad (4.4)$$

The measurements of the friction force values were repeated ten times in every environment (water, water + oligomer) to obtain representative and repeatable results. Assuming that the friction in the nanoscale follows Amonton's law, the friction force is given by:

$$FFV = \mu(SP + F_0) \quad (4.5)$$

Where  $\mu$  is the friction coefficient, the set point (SP) is the applied load and  $F_0$  is a force constant. Following the procedure suggested by Beake et al.[68], the force constant is nearly equal to the pull-off force determined from the force distance curves. Usually, the FFV and SP values are given in [V] Volts as acquired from lateral force measurements. However, the results can be easily compared with each other because findings in Volts are connected with the forces between tip and surface. In order to obtain commonly used units ([N] Newton), the lateral force needs to be calibrated by the determination of the slope of deflection vs. LVDT. The calibration delivers an accurate value of the inverse optical lever sensitivity (InvOLS) describing the sensitivity of the detector-cantilever combination. With the knowledge of the accurate value of InvOLS, it is possible to calculate FFV and SP in Newton:

$$FFV[V] \times InvOLS[nm/V] \times springconstantk[nN/nm] = FFV[nN] \quad (4.6)$$

$$SP[V] \times InvOLS[nm/V] \times springconstant[nN/nm] = SP[nN] \quad (4.7)$$

Another solution for calibrating the lateral force signal is the wedge calibration method, introduced by D.F. Ogletree et.al [69] and improved after by E.Tocha et.al [70], which gives an error in the calibration factors of about 5%. The "wedge" method of force calibration is an *in situ* method and it is applicable for a wide range of cantilevers and materials. This method is based on comparing lateral force signals on surfaces with different well-defined slopes. The known geometrical contribution to the total lateral force gives a different calibration of lateral force response in terms of normal force response. If the normal force constant is known a quantitative friction measurement can be performed. If it is not known the ratio of normal to lateral forces (the friction coefficient) can be determined. An experimental force calibration is made by sliding the tip across a surface of known slope (grating) and measuring the lateral force signal as a function of applied load. In this work silicon calibration gratings *MikroMash* test structure TGG01 (Tallin, Estonia) was used. It is a 1-D array of triangular steps having precise linear and angular dimensions defined by the crystallography of Silicon (111) planes. The

edges of the triangular steps have curvature radii of less than 10 nm.

Using the wedge calibration method, we experimentally measured the voltage output from the lateral force transducer LTo where  $\alpha LTo = LT$  (here the subscript "o" indicates that the value is measured in Volts, LT is lateral signal). If we can find  $\alpha$  (Newtons per Volt) we have a direct calibration of the lateral force response to the FFV signal. The calibration constant  $\alpha$  is the product of all the factors of the experiment: the lever lateral force constant, the deflection of the reflected laser as a function of cantilever displacement and the photodiode angular sensitivity.

### 4.1.8 Surface roughness parameters

To adequately describe the roughness of a surface, at least two quantities are needed, one is the height of the asperities (e.g. root mean square (RMS) roughness, maximum peak to valley height, mean peak height,  $R_a$ ) and the other to describe their distribution in the plane of the surface (e.g. correlation length, peak density, average wavelength).

- Selected Height Parameters (insufficient in tribology, however typically used in industrial applications due to standardization):
  - **$R_a$  or Centre Line Average (CLA)** is the arithmetic mean of the departure  $z$  of the profile from the centre line:

$$R_a = \frac{1}{L} \int_0^L |z| dx \quad (4.8)$$

It is the standard height parameter used to describe the roughness of a machined surface, and is available in most surface-measuring instruments.

- **$R_q$  or Root Mean Square (RMS)** is obtained by squaring each value over the evaluation length or area, then taking the square root of the mean.

$$R_q = \sqrt{\frac{1}{L} \int_0^L z^2 dx} \quad (4.9)$$

RMS is more statistical parameter, compared to  $R_a$  it emphasizes values of the height distribution.

- **$R_p$**  is the distance from the mean height to the highest asperity.
- **$R_z$**  is the average height difference between the five highest and the five lowest measured peaks within a sampling length  $L$ .  $R_z$  is useful when

only a short distance can be measured, particularly when the presence of peaks or valleys is of functional significance.

Obviously, these parameters characterize only the variation of  $z$ -height about the surface mean. These single classical roughness parameters don't characterize surfaces from a tribological point of view, thus the more appropriate way is to calculate  $R_p/R_z$  values. Nevertheless by plotting the height distribution one can obtain a much more detail picture of how the surface heights vary, thus introduction of spatial distribution in the plane is necessary.

- Spatial Characteristics:

- **Average Wavelength  $\lambda_a$  and  $\lambda_q$**  both measure the spacing between local peaks and valleys, based on their amplitude and slopes.  $\lambda_a$  is based on  $R_a$  and  $\lambda_q$  is based on RMS.

$$\lambda_a = 2\pi \frac{R_a}{\Delta a} \quad \lambda_q = 2\pi \frac{R_q}{\Delta q} \quad (4.10)$$

Where  $\Delta a$  is the mean absolute slope of the profile and  $\Delta q$  is the root mean square of the slope distribution of the profile.

- **Autocorrelation Function  $R$**  the quantities  $\Delta a$  and  $\Delta q$  as described above, are just single value descriptions of spacing. A distribution function can be obtained by subjecting the measured profile to "correlation analysis", which compares surface heights at different distances points apart along the surface. The autocorrelation function is a plot of  $R$  versus  $\lambda$ , and full description of roughness spacing, analogous to the height distribution for roughness height.

Most of the scattering methods yield intensity distributions that are the convolution of an instrument function with the Fourier transform of the autocorrelation function of the interface. The autocorrelation function (also called height-height correlation function), can be obtained from the measured intensity of a scattering experiment by deconvolution and inverse Fourier transformation. To analyze this function one has to distinguish between crystalline surfaces resulting in a diffraction pattern and continuous surface causing a diffuse intensity in a scattering experiment [71]. AFM scans are of discrete nature, typically containing  $N \times N$  equidistant pixels, that is why we consider only discrete approximations of the functions. Surface morphology can be described by function  $z_{ij}$ , that assigns to each point  $x_i, y_j$

a height  $z(x_i, y_j) = z(\vec{r})$ , in Cartesian coordinates, the 2D height-height correlation function is defined as

$$C(\vec{r}) = \langle [z(\vec{r}_0 + \vec{r}) - \langle z \rangle][z(\vec{r}_0) - \langle z \rangle] \rangle \quad (4.11)$$

where  $\langle \dots \rangle$  means the average over all possible pairs in the matrix that are separated by  $\vec{r} = x\vec{e}_x + y\vec{e}_y$ . The  $z$  values are deviations from the average height  $\langle z \rangle$ .

Different rough surfaces have different statistical parameters. An important task in characterization of rough surfaces consist of classification into random (absence of long-range order) and fractal ones. Nowadays high developed technologies, which allow processing and control of high-quality surfaces (including electron or atomic-force microscopy) put in evidence that a fractal model of surface structure is quite adequate in many instances. There are also opinions that commonly used rough surfaces, such as glass surfaces processed with abrasive, may be described with traditional statistical model and the fractal model within different ranges of heights [71]. The idea of fractal geometry is associated with the property of invariance under a change of scale. A self-similar fractal objects looks statistically the same when the space it occupies is stretched uniformly by a factor  $\epsilon$ . Another useful concept for describing surface morphology is the self-affine fractal (it looks the same after an affine transformation). Usually the surface morphology during thin film growth/etching process shows self-affine fractal behavior because the height fluctuations are much smaller than the lateral dimensions [72]. For a surface that shows a self-affine fractal behavior on a short length scale and that is smooth on a long length scale, the height-height correlation function can be written as Eq. 4.12 [73]

$$C(\vec{r}) = \sigma^2 \exp[-(|\vec{r}|/\xi)^{2\alpha}] \quad (4.12)$$

Where  $\sigma$  is the root mean square of the deviations of the surface from the average height level  $\langle z \rangle$  or interface roughness. It is commonly called RMS or  $R_q$  roughness and is already described in Eq. 4.9.  $\sigma$  can be simply calculated from  $z_{ij}$ :

$$\sigma = \sqrt{\frac{1}{N^2} \sum_{i=1}^N \sum_{j=1}^N [z(x_i, y_j) - \langle z \rangle]^2} \quad (4.13)$$

It can be seen from Eq. 4.11 and Eq. 4.13 that  $C(\vec{0}) = \sigma^2$ . The parameter  $\xi$  in Eq. 4.12 is called lateral correlation length, and denotes the average length for which the heights between two surface points are correlated.  $\xi$  is a measure for the lateral fluctuations of the roughness. The third parameter in Eq. 4.12 is the

roughness exponent  $\alpha$ , also called Hurst parameter, which is related to the local fractal dimension  $d$  of the surface through  $\alpha = 3 - d$ . It tells how jagged a surface with a given RMS roughness and lateral correlation length is.  $\alpha$  usually ranges between 0.5 (exponential decay of  $C(\vec{r})$ -more jagged surface) and 1 (Gaussian  $C(\vec{r})$ -less jagged) [72]. There are easy ways to determine these three roughness parameters from a given morphology as can be seen in Fig. 4.5

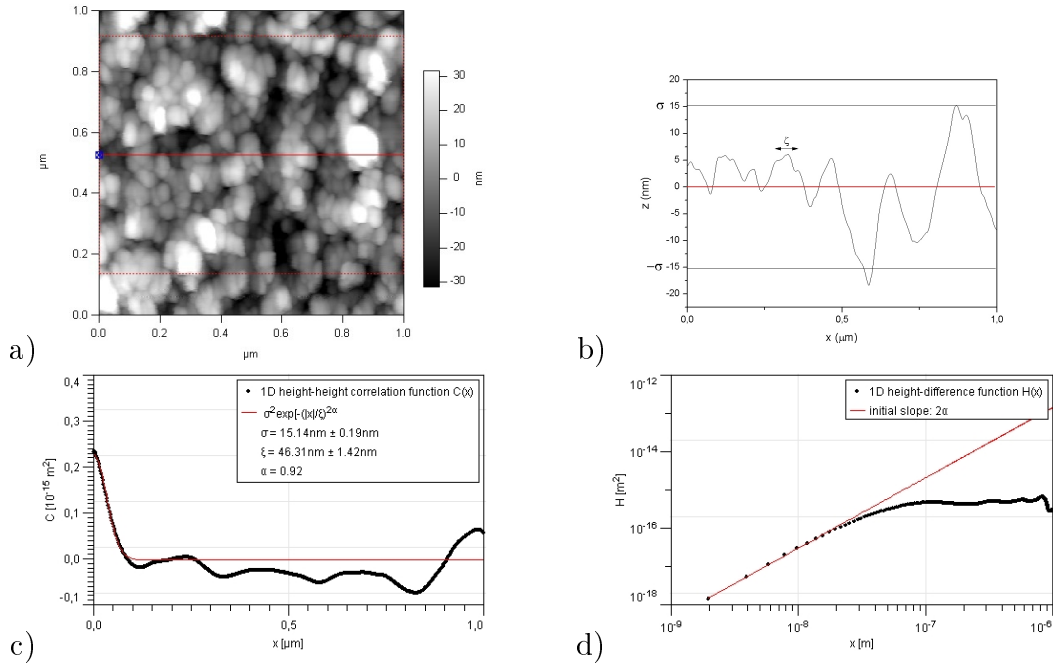


Figure 4.5: Example how the roughness parameter for self-affine fractal surface can be deduced from an AFM image by calculating the correlation function (a)  $1\mu\text{m} \times 1\mu\text{m}$  AFM image (b) 1D cross section along the line indicated in (a)(c) 1D height-height correlation function  $C(x)$  averaged over all scan lines. The lateral correlation length  $\xi$  is determined by the  $1/e$  fall-off of  $C(x)$ . The red curve is calculated from Eq. 4.12, the deviations for large  $x$  values are due to insufficient statistics (d) 1D height-difference function  $H(x)$  averaged over all scan lines. The roughness exponent  $\alpha$  is obtained from the initial slope of the log-log plot of the height-difference function in the short range scale

These three parameters  $\sigma, \alpha, \zeta$  are independent from each other and sufficiently characterize a self-affine surface. They vary according to the process by which the surface morphology is formed.

## 4.2 Tribology Methods

### 4.2.1 Microtribometer

The microtribometer FALEX-MUST 2D-FM working in reciprocating mode was used for copper sputtered silicon wafers to apply small loads from 1 mN to 1 N in order to prevent the silicon wafers from breaking. As counter body a steel ball mounted on a 2D force transducer was used. The normal force  $F_N$  (orthogonal to the surface), the tangential force  $F_T$  (parallel to the surface of the test sample and opposing the relative velocity) and the moving distance  $s$  were recorded over time  $t$  while the sample (copper coated silicon wafer) was moved in reciprocating mode. Fig. 4.6 depicts the functional principle of this micro-tribometer. The FALEX-MUST 2D-FM special force transducer consists of a cantilever based on a parallel spring system, two mirrors fixed on a moving part of the cantilever and a mechanical carrier. The cantilever is fixed on the mechanical carrier and helps to change the measurement mode of the force transducer. The two mirrors positioned orthogonally to each other are used as reflective surface for the fibre optic sensors (FOS). FOS is for the measurement of the deflection of the force transducer and the positioning of the piezo drives.

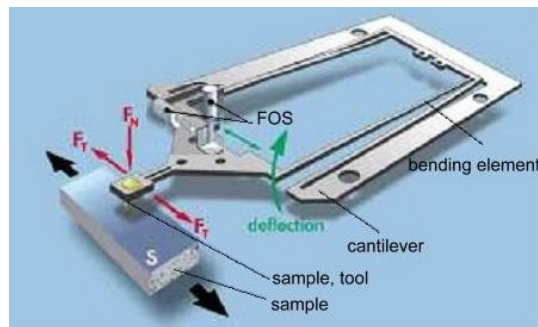


Figure 4.6: Functional principle of the force transducer in microtribometer [74]

### 4.2.2 Mini Traction Machine (MTM)

Mini-Traction Machine (MTM) allows to measure friction in mixed rolling/sliding contact between a test ball and a disc [75]. The frictional force between the ball and disc is measured by a force transducer. Additional sensors measure the applied load, the lubricant temperature and (optionally) the electrical contact resistance between the specimens and the relative wear between them. Fig. 4.7 shows a schematic illustration of an MTM.

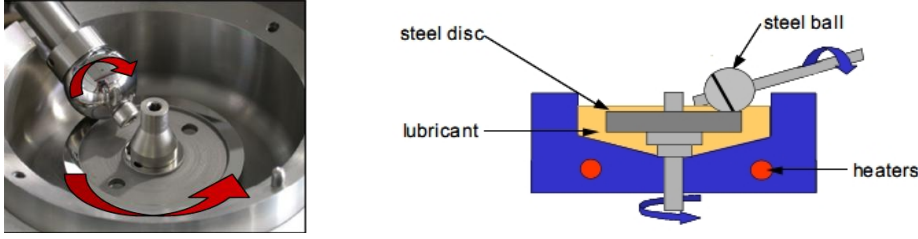


Figure 4.7: Schematic of MTM [75]

An MTM provides a mixed sliding/rolling contact through the independent control of the ball and disc velocities. The slide/roll ratio, SRR, is defined as the percentage ratio of the difference and the mean of the ball track velocity ( $v_{ball}$ ) and disc velocity ( $v_{disc}$ ) [75]:

$$SRR = \frac{|v_{ball} - v_{disc}|}{\left(\frac{v_{ball} + v_{disc}}{2}\right)} \times 100\% \quad (4.14)$$

Thus,  $SRR = 0\%$  ( $v_{ball} = v_{disc}$ ), represent pure rolling contact, and  $SRR = 200\%$  (either  $v_{ball} = 0$  or  $v_{disc} = 0$ ), represent pure sliding contact, while the values between 0 and 200% represent a mixed sliding/rolling contact.

### 4.2.3 TOG Tribometer

A translatorily oscillating test machine (TOG), as shown in Fig. 4.8, was chosen for investigation of lubricity on a macroscopic scale on steel samples. TOGs are widely used for the study of the tribological behavior of tribo-partners with translatory relative movement to evaluate material combinations in a dry or wet lubrication regime. The TOG tribometer is based on a steel cylinder which is loaded against the steel sample. The sample was mounted on a special sample holder, which is constructed for tribotesting in lubricants. During the measuring process the cylinder oscillates at a certain frequency and is in constant contact with the sample (see Fig. 4.8). The 12N load was applied to the upper specimen holder where the cylinder was mounted to press on a sample. For reference substances the tests were carried out only once.

The tribometer sample holder for testing in lubricants itself was screwed to a plate, which was fixed on the carriage. The carriage resides on a roller bearing and is driven by pneumatics. If the lever system is adjusted in a way that the levers are parallel to the surface of the sample during tribotesting, the friction force can be easily calculated from the stress measured by a resistance strain gauge, the load applied and the dimensions of the tribometer.

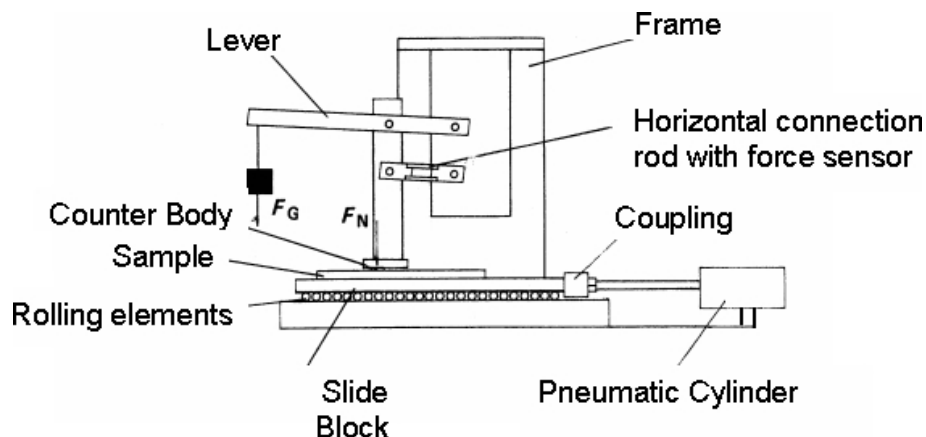


Figure 4.8: Sketch of the TOG tribometer [76]

## 4.3 Spectroscopy Methods

### 4.3.1 X-Ray Photoelectron Spectroscopy (XPS)

X-Ray Photoelectron Spectroscopy (XPS) also known by its former acronym as ESCA (Electron Spectroscopy for Chemical Analysis) was developed in the 1960ies by Kai Siegbahn and his research group at the University of Uppsala, Sweden. It became commercially available in 1969. Surface analysis by XPS is accomplished by irradiating a sample with soft x-rays and analyzing the energy of the emitted electrons. Usually Mg  $K\alpha$  (1253.6 eV) and Al  $K\alpha$  (1486.6 eV) x-rays are used. They interact with atoms in the surface, causing electrons to be emitted by the photoelectric effect, explained by Einstein in 1905. The binding energy (BE) of the atomic orbital from which the electron originates is given by:

$$BE = h\nu - KE - W \quad (4.15)$$

where  $h\nu$  is the energy of the photon, KE is the kinetic energy of the emitted electron and  $W$  is the spectrometer work function. The binding energy is the energy difference between initial and final state after the photoelectron has left the atom. There is variety of possible final states of the ions for each type of the atom, and for each final state there is a different probability for ionization (cross-section). Because each element has a unique set of binding energies, XPS is used for elements identification and to determine the concentration of elements in the surface region. Variations in the XPS elemental binding energies (the chemical shifts) arise from differences of chemical potential and the polarizability of compounds. These informations are used to identify the chemical state of the materials being analyzed. The process of photoemission is schematically shown in Fig. 4.9, where an electron

from the K shell is ejected from the atom (a 1s photoelectron). The photoelectron spectrum reproduces accurately the electronic structure of an element because all electrons with a binding energy less than the photon energy contribute to the spectrum. a typical photoelectron spectrum contains: characteristic peaks of electrons which exit and escape without energy loss and a background due to electron inelastic scattering and energy loss. Once a photoelectron has been emitted, the ionized atom relaxes. The relaxation process can be achieved by emission of an X-ray photon (known as X-ray fluorescence) or an Auger electron. Thus photoelectron spectra also contain Auger peaks (section 4.3.5 on page 66).

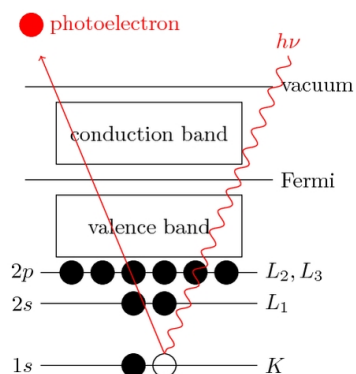


Figure 4.9: Schematic diagram for the XPS emission process, showing photoionization of an atom by ejection of an 1s electron [77]

### 4.3.2 Spectrometer Components

All XPS measurements were conducted in a Vacuum Generators MicroLab MKII. The spectrometer was adopted several times in order to extend its capabilities. Most of the changes apply to sample preparation and the valve system to an extended chamber. The spectrometer consists of four chambers:

1. Load Lock (where the sample is introduced into the system),
2. Preparation chamber (where preparation procedures like sample cleaving, thermal coating or sample cleaning by Argon ion sputtering is performed),
3. Analysis chamber (where the XPS measurement takes place).
4. a chamber for electrochemical and adsorption experiments [78].

The experiments are carried out in Ultra Height Vacuum (UHV) environment because XPS technique is surface sensitive due to limited mean free path of electrons. Surface contamination is critical in XPS analysis, lifetimes of clean surfaces

are limited by adsorption of residual gas atoms and molecules. a monolayer of oxide is adsorbed on the clean surface after 6 s at a pressure of  $10^{-6}$  mbar and after  $6 \times 10^3$  s = 1.5 hour at  $10^{-9}$  mbar [77].

The spectrometer is equipped with four pumping systems to obtain sufficient UHV and keep it in the same level:

1. Rotary Vane Pump - used to pump the load lock to vacuum down to  $1 \times 10^{-3}$  mbar. These pumps are a pre-pumping system for the turbomolecular pump.
2. Turbomolecular Pump - pumps the load lock to vacuum of less than  $1 \times 10^{-9}$  mbar.
3. Ion Getter Pump - used in the preparation and analysis chamber to keep the vacuum between  $1 \times 10^{-8}$  mbar and  $1 \times 10^{-10}$  mbar.
4. Additionally, a Titanium Sublimation Pump is used with an LN2 (liquid nitrogen) cryo baffle to further reduce the pressure.

The pressure in the chambers is monitored using various pressure gauges. ESCA is also equipped with a quadrupole mass spectrometer to study the composition of the residual gas.

The essential components for MKII XPS spectrometer are: X-ray source; Energy Analyzer; Electron Detector; Data Recording, processing and output system.

**The X-ray source** consists of a twin anode with two different targets for the electron beam emitted by a filament. One target is made of aluminum, which allows measurements with Al  $K\alpha$  radiation at 1486.6 eV, and the second consists of magnesium used for measurements using Mg  $K\alpha$  radiation at 1253.6 eV. Those targets are placed on a copper block, which is cooled by water.

By applying a high voltage to the anode the electrons are accelerated. Emission from the filament takes place by heating it with a current (thermionic effect). The acceleration voltage is usually 15 kV in order to reduce Bremsstrahlung at energies near the characteristic X-ray line, to maximize the cross section of the electrons impinging on the target, and to avoid flashover between the filament and the anode. The current between the filament and the anode can be adjusted to 5, 10, 20, 34, 40 and 53 mA, it is very important while starting/shutting-down the X-ray source to increase/reduce the voltage and current gradually. The maximum power allowed for continuous measurement is 300 W for magnesium and 600 W for aluminum.

**The Energy Analyzer** disperses the emitted electrons from the sample according to their energies. The MKII ESCA in IAP lab uses a Concentric Hemispherical Analyzer (CHA). It consists of two concentric hemispheres of inner radius  $r_1$  and outer radius  $r_2$  as shown in Fig. 4.10. The hemispheres are at different potentials  $dV$  ( $V_1 > 0$  and  $V_2 < 0$ ), so the trajectories of the electrons are influenced by the electrical field. Between the spheres there is an equipotential surface of radius  $r_0$ . At the entry and exit of analyzer there are two slits. The entry and exit slits lie on a diameter  $w$  (can be adjusted to 20, 3, 2, 1 and 0.5 mm) and are centered at the distance  $r_0$  from the center of curvature. In front of the electrostatic lens is placed an aperture which allows to change the opening angle  $\alpha$  of the analyzer within  $0^\circ$  and  $22^\circ$ . The energy resolution  $\Delta E$  of CHA is given by:

$$\frac{\Delta E}{E} = \frac{w}{r_0} + \alpha^2 \quad (4.16)$$

where  $\alpha$  is the entrance angle into the CHA,  $w$  is the width of the slit and  $E$  is the energy of electrons. Generally, a large entrance angle increases sensitivity, however to compromise sensitivity and resolution it is common practice to choose  $\alpha$  such that  $\alpha = w/2r_0$  [79].

The analyzer can be operated in two modes: Constant Analyzer Energy (CAE) (usually used for XPS measurements) and Constant Retard Ratio (CRR) mode (usually used for AES measurement). In CAE mode electrons are accelerated or retarded by applying a voltage to the grids (V). The voltage difference between the hemispheres ( $dV$ ) is constant and equal to pass energy, which corresponds to the energy electrons must have after they passed the parallel grid in order to reach the channeltrons. The selected pass energy is proportional to resolution and inversely proportional to the transmission of the analyzer. After acquisition the areas of the peaks need to be corrected by the transmission function of the analyzer for quantification.

In CRR mode the ratio of the pass energy and the kinetic energy is kept constant. In this mode the pass energy is proportional to the kinetic energy (user defined range), that means that the resolution also changes with pass energy. The transmission increases with increasing kinetic energy, which has the effect on low kinetic energy (high binding energy) end of the spectrum, thus usually an Auger electron spectra is collected in the CRR mode. Quantification of XPS spectra is done in the CAE mode as the resolution and transmission of the analyzer remains constant.

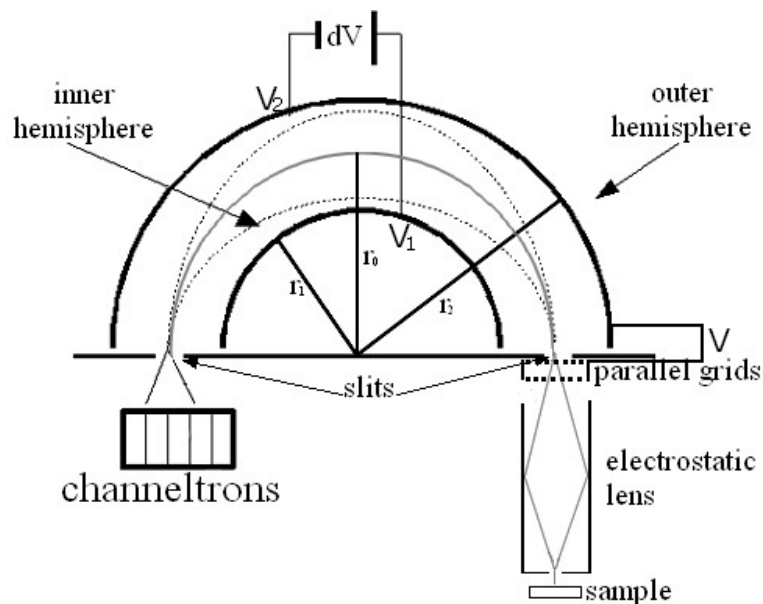


Figure 4.10: Cross-sectional schematic view of the CHA with input lens. The dashed lines indicates trajectories followed by the emitted electrons. The central gray line represents an equipotential surface. The electrostatic lens subsequently focuses the electrons as they are ejected from the sample on the enhance slit. The parallel grids accelerate the electrons such that their energy matches the pass energy of the analyzer which is determined by the potential of the inner and outer hemisphere. The electrons are guided through the hemispheres to reach the output plane of the analyzer where five detectors (channeltrons) are placed. Each of the detectors collects electrons of a slightly different energy.

The function of **Energy Detector** in our XPS system is performed by Channel Electron Multipliers (CEMs). It is an electrostatic device that uses a continuous dynode surface (a thin-film insulating layer on the inside of the channel). a dynode has the property of emitting secondary electrons when primary particles bombard it via secondary electron emission. The secondary electrons are accelerated by a positive bias, until they strike the surface again and produce further secondary electrons. This process is repeated until the electron cloud contains approximately  $10^8$  electrons. The output of this detector consist of a series of pulses that are fed into a pulse amplifier/discriminator which are then led into a computer. The advantage of a CEM is that it can be exposed to air, it has also efficient electron count rate even for electrons with small kinetic energy. The drawback is that at high countrate a saturation effect occurs.

### 4.3.3 Adsorption experiment

Two types of tribological surfaces Copper sputtered on silicon wafer and *Fe100Cr6* steel were used to investigate the chemical behavior of additives (detailed descriptions can be found in Materials chapter 3.1 on page 31). The samples were mounted on custom made a 45°-slanted sample holder (figure 4.11) with conductive glue, an additional point of conductive silver was in lower and upper sample/holder border.



Figure 4.11: The sample holder used for angle resolved XPS measurements. It was turned from a stainless steel rod, which was cut at an angle of 45° with respect to its axis.

Specimen was introduced into the XPS load lock, and after that into the preparation chamber, where they were cleaned by argon ion sputtering until the XPS spectra showed no peaks of contamination. It was experimentally proven that for steel *Fe100Cr6* surfaces 40 min of sputtering with  $Ar^{2+}$  ion at  $20 \mu A$  current is needed to remove contamination. Nevertheless for a Cu sample only 5 min are needed. Afterwards the samples were transfered to the electrochemical chamber,

and positioned upside-down with the surface adjusted horizontally. Then the valve to the turbomolecular pump was closed and chamber was filled with noble gas until the pressure was in the same range as atmospheric pressure. At the same time preparation of the electrochemical setup was done.

**The Electrochemical setup** consists of two supply reservoirs (one with solvent-water, and another one with a chemical solution), Dreschel bottles attached to supply reservoirs, one waste reservoir, the adsorption cell, a gas distributor and rubber pipes between vessels. Fig. 4.12 shows a detailed sketch and description of the installation.

All the experiments were carried using He 6.0 as noble gas and double distilled water as solvent. During this procedure the whole electrochemical equipment was kept under a slight overpressure of noble gas to keep air out of the setup. Distilled water was not only used to prepare the chemical solutions but also to rinse the samples and clean the equipment. The next step after the adsorption procedure was to introduce the sample back to the electrochemical chamber and preparation chamber and finally position it in the analysis chamber for AR-XPS measurement. Rotating the sample during AR-XPS measurements was done automatically using the FoldMonkey program.

#### 4.3.4 Angle Resolved X-ray Photoelectron Spectroscopy (AR-XPS)

In order to obtain detailed information about the elemental composition, chemical bonds, structure and morphology of a surface, analytical methods such as X-ray photoelectron spectroscopy (XPS) and Auger Electron Spectroscopy (AES) are favorable candidates. To get in-depth information, depth profiling using ion sputtering is typically used. However for very thin films (like monomolecular thin films of additives on surface) the XPS/AES methodology using sputter depth profiling has got its limitations. Because the ion sputtering process is always accompanied by energy impact, various processes in the analyzing region occur, e.g. atomic mixing, phase changes or roughening [80], [81].

One way to achieve quantitative results on the near-surface structure of the material is to vary the detection angle in electron spectroscopy for depth dependent analysis. Due to the finite mean free path of electrons within the solid the information depth in XPS analysis is in the order of a few nanometers if the electrons are detected at a direction normal to the sample surface. If the electrons are detected at a different angle to the normal then the information depth is reduced by

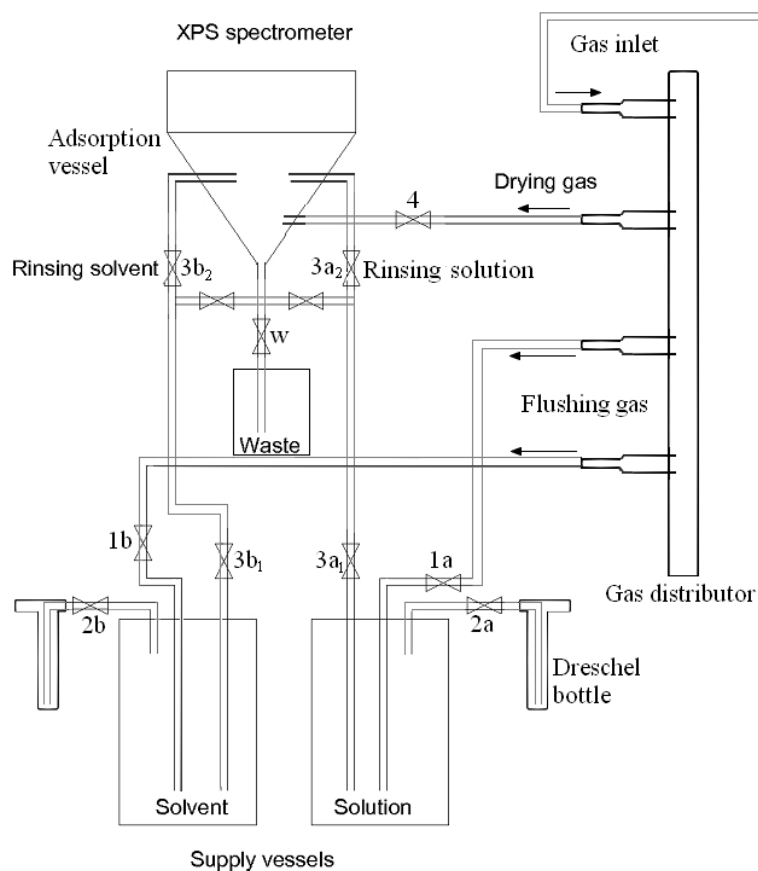


Figure 4.12: Sketch of the electrochemical device used for adsorption of the additives. The stop cocks marked from  $1a - 3a$  shows the order of opening and closing valves for the solution and  $1b - 3b$  for the solvent. Before starting the experiment the solvent and the chemical solution were flushed for 20 min with noble gas to expel the solved gases like oxygen and nitrogen ( $1a, 1b, 2a, 2b$  open). The Dreschel bottles were used as bubblers. Afterwards the gas outlets to the Dreschel bottles ( $2a$  and  $2b$ ) were closed, and both valves between the chemical solution reservoir and the adsorption cell was opened ( $3a_1, 3a_2$ ), thus the liquid from the supply vessels was pressed to the adsorption vessel by applying an overpressure. The sample was dipped in the solution for 20 min. Afterwards chemical solution was outflow by closing  $3a_2$  and opening the  $w$  stop cock. After the adsorption process, sample was rinsed with solvent (valves  $1b, 3b_1, 3b_2$  opened) and blown dry with noble gas (valve 4 opened).

an amount equal to the cosine of the angle between the surface normal and the analysis direction (emission angle), as shown in Fig. 4.13a. This is the basis for the powerful analysis technique angle resolved XPS (ARXPS). The instrumental geometry of angle-resolved XPS for the microlab instrument MKII is shown in Fig. 4.13b. On the sketch the emission angle  $\theta$  refers to the angle between surface normal and analyzer. In the geometry of our spectrometer the angle  $\eta$  between z-axis and analyzer is  $60^\circ$  and angle  $\gamma$  between the X-ray source and the analyzer is also  $60^\circ$ . The sample holder used in experiments has a slant angle  $\chi$  equal to  $45^\circ$ . The stage in the analysis chamber can be moved in x-, y-, z- directions. Additionally the sample can be tilted and rotated. Before the AR-XPS experiments the stage was positioned in such a way that the analyzer axis was pointing directly at the center of the samples (as shown in Fig. 4.13b). This adjustment was performed by moving a copper sample with a centered silver point of 2 mm in diameter along the x-, y-, z-axis of the spectrometer. First adjustment in y-axis was performed in such way that a maximum in the signal intensity was achieved, afterwards positioning in the x-direction was performed. 2 revolutions of the stepper motor controller correspond to 0.14 mm. After every step spectra of copper and silver photoelectron regions were recorded. The same procedure was repeated in the z-direction. The position of the stage where the intensity of the silver peak reached a maximum was saved as absolute position. Every time when successive samples were introduced to the analysis chamber for the ARXPS measurements the stage was moved back to this absolute position. For ARXPS measurements in our spectrometer the emission angle  $\theta$  was varied by rotating the sample around the z-axis by 2 revolutions of a step motor controller, that corresponds to rotations over an angle of  $20^\circ$ . The corresponding emission angles can be calculated from the geometric factors as presented below. [78]

The rotation matrix for a vector in three dimensions  $\mathfrak{R}^3$ , clockwise rotation by  $\phi$  with z-axis as rotation axis and  $\xi$  as x-axis as rotation axis is presented below:

$$\mathfrak{R}_z = \begin{pmatrix} \cos(\phi) & \sin(\phi) & 0 \\ -\sin(\phi) & \cos(\phi) & 0 \\ 0 & 0 & 1 \end{pmatrix} \quad (4.17)$$

$$\mathfrak{R}_x = \begin{pmatrix} 1 & 0 & 0 \\ 0 & \cos(\xi) & \sin(\xi) \\ 0 & -\sin(\xi) & \cos(\xi) \end{pmatrix} \quad (4.18)$$

The z-axis is parallel to the back plane and normal to the bottom of the sample

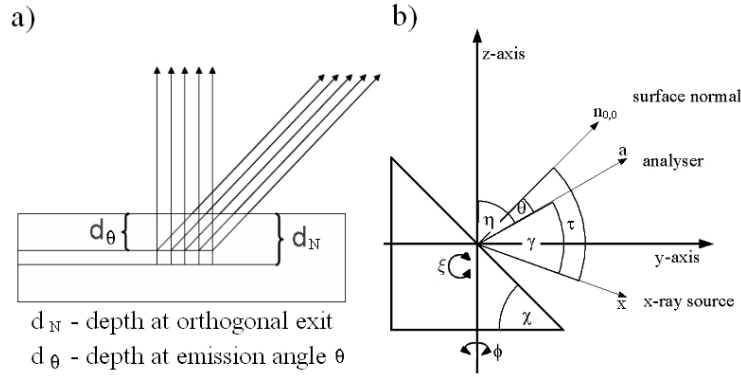


Figure 4.13: Geometry of angle-resolved XPS used in calculations a) information depth at normal to the sample surface (orthogonal) and at emission angle  $\theta$  b) instrumental and sample geometry used in the AR-XPS measurements.

holder. Therefore the angle between z-axis and the surface normal is equal to  $\chi$ . The the unit vector of the surface normal  $\vec{n}_{0,0}$  is defined as:

$$\vec{n}_{0,0} = \vec{n}(\phi = 0) = \begin{pmatrix} 0 \\ \sin(\chi) \\ \cos(\chi) \end{pmatrix} \quad (4.19)$$

where  $\chi$  is the base angle of sample holder. The unit vector in the direction of the analyser is:

$$\vec{a} = \begin{pmatrix} 0 \\ \sin(\eta) \\ \cos(\eta) \end{pmatrix} \quad (4.20)$$

The vector of the surface normal after rotation around the z-axis by  $\phi$  is calculated by multiplying Eq. 4.17 and Eq. 4.19 and given by:

$$\vec{n}_z = \vec{n}_{0,0} \cdot \mathfrak{R}_z = \begin{pmatrix} \sin(\chi) \sin(\phi) \\ \sin(\chi) \cos(\phi) \\ \cos(\chi) \end{pmatrix} \quad (4.21)$$

The vector of the surface normal after rotation around the x-axis is given by:

$$\vec{n} = \vec{n}_z \cdot \mathfrak{R}_x = \begin{pmatrix} \sin(\chi) \sin(\phi) \\ \cos(\xi) \sin(\chi) \cos(\phi) + \sin(\xi) \cos(\chi) \\ -\sin(\xi) \sin(\chi) \cos(\phi) + \cos(\xi) \cos(\chi) \end{pmatrix} \quad (4.22)$$

The cosine of the angle  $\theta$  between the surface normal vector  $\vec{n}_{0,0}$  after rotation

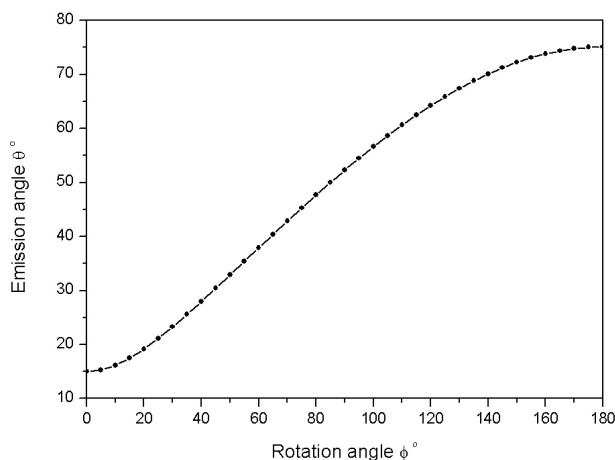


Figure 4.14: Plot of dependency on emission angle  $\theta$  between the sample normal and the analyzer and the sample rotation angle  $\phi$ .

and the vector  $\vec{a}$  in direction to analyzer can be calculated by a normal projection of the unit  $\vec{n}$  (Eq. 4.22) onto the unit vector  $\vec{a}$  (Eq. 4.20), which corresponds to the scalar product of these vectors:

$$\begin{aligned} \cos(\theta) &= \vec{n} \cdot \vec{a} = \\ &= \cos(\phi) \sin(\chi) [\cos(\xi) \sin(\eta) - \sin(\xi) \cos(\eta)] + \\ &+ \cos(\chi) [\sin(\xi) \sin(\eta) + \cos(\xi) \cos(\eta)] \end{aligned}$$

Taking into account the geometry of our spectrometer - the angle  $\eta$  between the z-axis and the analyzer is  $60^\circ$  and the sample holder used in these experiments has the angle  $\chi$  equal  $45^\circ$  - gives us result presented in Fig. 4.14, where the emission angle  $\theta$  is plotted as a function of the rotation angle  $\phi$ . Therefore for measurements taken at rotation angles  $0^\circ$ ,  $20^\circ$ ,  $40^\circ$ ,  $60^\circ$ ,  $80^\circ$  the emission angles calculated for the geometries used in experiment were  $15^\circ$ ,  $22^\circ$ ,  $35^\circ$ ,  $49^\circ$ ,  $63^\circ$ .

A thin overlayer on the sample leads to a characteristic angle distribution predicted by the Beer-Lambert expression. The intensity of electrons ( $I$ ) emitted at an angle  $\theta$  relative to the surface normal (emission angle) from depth greater than  $d$  is given by the Beer-Lambert relationship:

$$I = I_0 \exp(-d/\lambda \cdot \cos \theta) \quad (4.23)$$

where  $\lambda$  is the attenuation length of the electrons (which is related to the Inelastic Mean Free Path (IMFP))- the distance covered by an electron between two

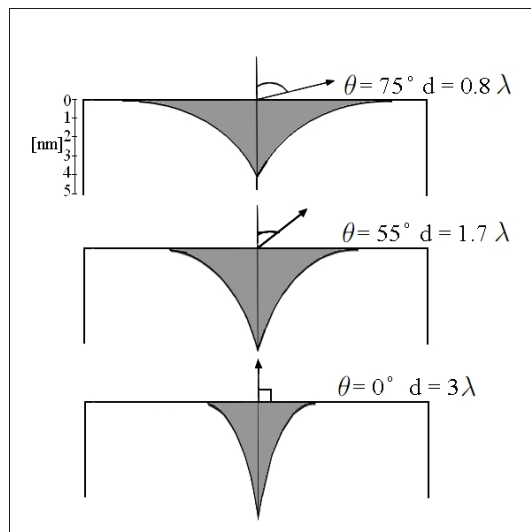


Figure 4.15: Angular electron emission: sampling depth as a function of electron take-off angle  $\theta$ . The width of shaded area represent the proportion of the detected electrons emitted as function of depth [77]

inelastic collisions. Considering Eq. 4.23, it is clear that the depth of analysis is dependent on the electron angle of emission. By recording XPS spectra for high  $\theta$ , extreme surface sensitivity can be achieved, and at normal electron emission ( $\theta = 0^\circ$ ) analysis depth has its maximum at depth  $\approx 3\lambda$ . The variation of electron intensity with depth is shown and relative sampling depths at different take off angles are illustrated in Fig. 4.15. The Beer-Lambert equation can be manipulated in a variety of ways to provide information about the overlayer thickness and quantification of ARXPS spectra.

### Thickness of uniform layer

If we consider a thin layer with a thickness  $d$  of a material a on a substrate B, the Beer-Lambert Eq. 4.23 must be integrated from 0 to  $d$  to obtain an expression for the signal from A:

$$I_A = I_A^\infty [1 - \exp(-d/(\lambda_{A,A} \cdot \cos\theta))] \quad (4.24)$$

where  $I_A$  is the signal intensity coming from the overlayer and  $\lambda_{A,A}$  is the attenuation length in layer a for electrons emitted from layer A. The signal from B arriving at the B-A interface is  $I_B^\infty$ , assuming that layer B is thick ( $> 100$  nm). This signal is then attenuated by passing through the layer A, and finally giving:

$$I_B = I_B^\infty \exp(-d/(\lambda_{B,A} \cdot \cos\theta)) \quad (4.25)$$

where  $I_B$  is the signal intensity from the substrate and  $\lambda_{B,A}$  is the attenuation length in layer a for electrons emitted in layer B. If we take the ratio of these

signals we get:

$$\frac{I_A}{I_B} = R = R^\infty \left[ \exp\left(\frac{d}{\lambda_{B,A} \cdot \cos\theta}\right) - \exp\left(\frac{d}{\cos\theta} \left[ \frac{1}{\lambda_{B,A}} - \frac{1}{\lambda_{A,A}} \right] \right) \right] \quad (4.26)$$

where  $R^\infty = I_A^\infty / I_B^\infty$ .

We assume that  $\lambda_{A,A} = \lambda_{B,A} = \lambda$ . This is only true when the intensities of photoelectron peaks from the substrate are measured together with peak from the same element in overlayer since then these photoelectrons have almost the same energy thus almost identical attenuation length when passing through the overlayer. After rearranging and taking the logarithm Eq. 4.26 becomes:

$$d = \lambda \cos\theta \ln[1 + R/R^\infty] \quad (4.27)$$

This is the so called Hill equation [82].

### Quantification of ARXPS spectra

The intensity of photoelectron peaks can be calculated according to the straight line approximation (SLA), which neglect elastic scattering of the electrons

$$I(\theta) = S \cdot \int_0^\infty C(z) \exp^{-\frac{z}{\lambda \cos\theta}} dz \quad (4.28)$$

where  $z$  is the depth,  $S$  is the sensitivity factor and  $C(z)$  is the concentration depth profile (atomic density of an elements in depth  $z$ ). Eq. 4.28 is a simplification of a much more complicated formula, which take into account instrumental factors, X-ray flux, transmission of analyzer, detection probability, etc. In the Hill equation Eq. 4.27 the value for  $R^\infty$  is the ratio of the intensities of the appropriate peaks from thick overlayers ( $>100$  nm). For thin overlayers ( $<5$  nm) the factors mentioned above cancel out, thus the Hill equation can be presented as:

$$d = \lambda \cos\theta \ln\left[1 + \frac{I_o/s_o}{I_s/s_s}\right] \quad (4.29)$$

where  $I_o, s_o$  and  $I_s, s_s$  are intensities and sensitivity factors from overlayer and substrate respectively.

One of the methods to quantify ARXPS spectra is the stratification method, which is extremely powerful, because it provides information of the depth and relative amount of each element in each layer. The principle is based on transforming the 'single-angle' Hill equation from Eq. 4.29 to 'two-angles'. We assume that molecules on the surface are composed of an  $n$ -atomically-flat layers, each

containing a particular element in different n states, resolvable in the XPS spectra due chemical shift in the peaks. The ratio of the peak intensity at an emission angle  $\theta$  ( $I_n(\theta)$ ) to intensity at normal emission angle ( $I_n(0)$ ) is given by:

$$\frac{I_n(\theta)}{I_n(0)} = k(\theta) \left[ \frac{1 - e^{-\frac{t_n}{\lambda_n \cos \theta}}}{1 - e^{-\frac{t_n}{\lambda_n}}} \right] \frac{e^{-\frac{d_n}{\lambda_n \cos \theta}}}{e^{-\frac{d_n}{\lambda_n}}} \quad (4.30)$$

where  $t_n$  and  $d_n$  are the thickness and the mean depth of the  $n^{th}$  layer respectively, and  $k(\theta)$  is an instrumental function (which contains a number of geometrical factors, for example, describing the area of analysis with an emission angle). To estimate the  $k(\theta)$  factor the ratio of background intensities at an emission angle  $\theta$  ( $I_b(\theta)$ ) to background intensity at normal emission angle ( $I_b(0)$ ) has to be determined as:

$$k(\theta) = \frac{I_b(\theta)}{I_b(0)} \quad (4.31)$$

To calculate the average depth and the relative quantity of material in each layer new parameters like *characteristic depth parameter*  $Z_n$  and *relative amount*  $A_n$  are now introduced. The characteristic depth parameter gives the average depth of the layer in units of the attenuation length  $\lambda_n$ :

$$Z_n = \frac{\ln \left[ \frac{I_i(\theta) I_b(0)}{I_i(0) I_b(\theta)} \right] - \ln(\sec \theta)}{1 - \sec \theta} \quad (4.32)$$

The relative amount  $A_n$  is a measure of the total amount of the species in that layer relative to all other layers quantified [82]. If we consider that there is no inelastic scattering in the specimen, then the peak intensities at any emission angle would be proportional to the amount of each layer (in fact the attenuation length describes how the peak intensity is reduced with depth). If the observed intensity from each layer is scaled by  $e^{Z_n}$  then the relative amount  $A_n$  of species in each layer is given by Eq. 4.33 [82].

$$A_n = \frac{I_n(0)}{S_n} e^{Z_n} \quad (4.33)$$

where  $S_n$  is the relative sensitivity factor.

Using the ARCTic software [83] it is possible to do stratification, simply by filling the excel spreadsheet, where above described equations 4.32 and 4.33 described above are implemented. For each species just two measurements are needed at normal and large emission angles as shown in Fig. 4.16

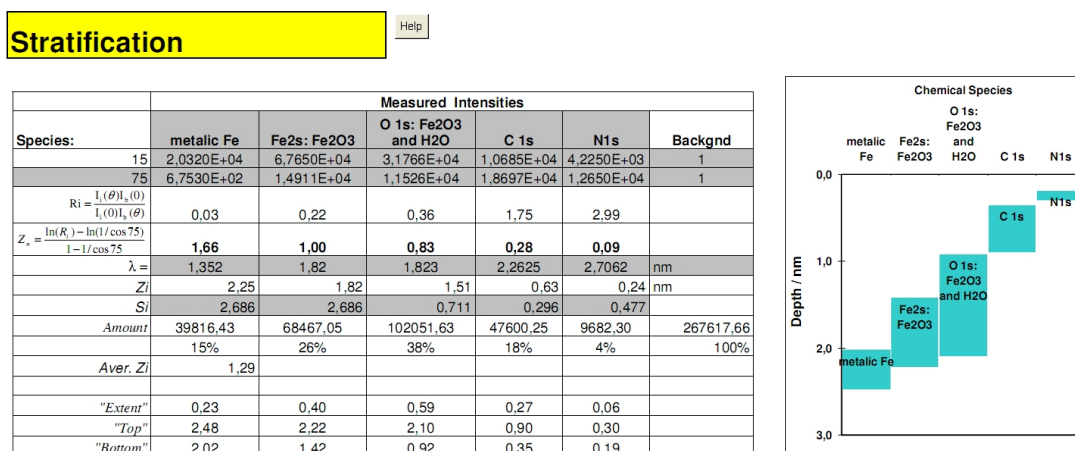


Figure 4.16: Stratification method using ARCTic software. Coloured bars tells the average depth of each layer, while the area of each bar tells the relative quantity of each species.

**SESSA simulation** The AR-XPS experimental results were compared with simulations performed with the SESSA software (Simulation of Electron Spectra for Surface Analysis), which was developed at our institute [84]. The objective of SESSA is to help with the interpretation of AES and XPS electron spectra, and to improve the accuracy in quantification in analysis. In a first step users specify the sample composition, spectrometer settings and excitation source. Then SESSA finds the relevant peaks, which are listed in "Sample/Peaks" menu, the user can adjust the number of simulated peaks, the position or FWHM (Full Width Half Maximum). When a given element is present in more than one chemical state, each peak is added to the peak list, accordingly labeled. After the peaks have been established, the parameters describing the signal and surface sensitivity are obtained from corresponding databases. When all parameters are known, a simulation can be performed with SESSA which provides an expected XPS spectra. The simulation algorithm is based on partial intensity approach for electron-solid interaction. Partial intensities describe the number of electrons arriving at the detector, which participated in a number of inelastic collisions before leaving the sample surface. In SESSA, the partial intensities are calculated with Monte-Carlo simulations based on trajectory reversal algorithm [84].

### 4.3.5 Auger Electron Spectroscopy (AES)

Auger Electron Spectrometer, model VG Microlab 310F, with an EX05 ion gun system was used to perform chemical analysis, distribution of additives on surface and depth profiles.

Emission of Auger electrons takes place when a sample is bombarded with a finely focused electron beam. This is applied in Auger Electron Spectroscopy (AES). The relaxation process of an ionized atom and the emission of an Auger electron is presented in Fig. 4.17.

The kinetic energy of an  $KL_{2,3}L_{2,3}$  Auger electron is approximately equal to the difference between the energy of the core hole and the energy levels of the two outer electrons  $E_{L_{2,3}}$  but it also includes the coupling in the final state that occurs between two unfilled shells. The calculation of the energy of an Auger electron transition is complex. However there is a rough approximation empirical approach given in Eq. 4.34 which considers the energies of the atomic levels involved and those of the next element in the periodic table (thus the atomic number  $Z$  is taken into account) [77].

$$E_{KL_1L_{2,3}}(Z) = E_K(Z) - 1/2[E_{L_1}(Z) + E_{L_1}(Z + 1)] - 1/2[E_{L_{2,3}}(Z) + E_{L_{2,3}}(Z + 1)] \quad (4.34)$$

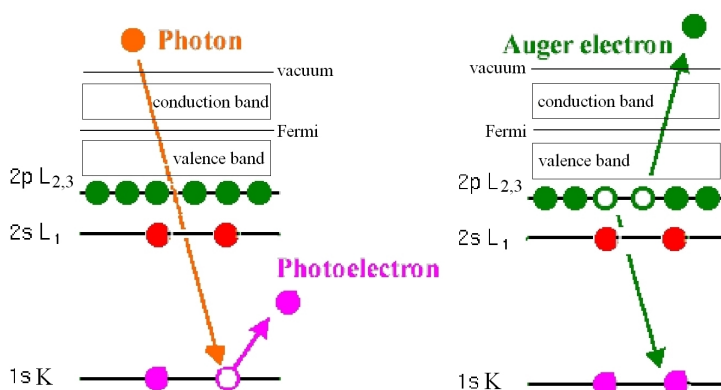


Figure 4.17: Schematic diagram for the relaxation process, showing the emission of an  $KL_{2,3}L_{2,3}$  Auger electron [77].

AES Spectroscopy has a high surface sensitivity, which is due to the limited mean free path of electrons in the kinetic energy range of 20 to 3000 eV. Auger Electrons, which loose energy through plasmon losses, core excitations or interband transitions are removed from the observed Auger peaks and contribute to the background on which Auger peaks are superimposed. The incident electron beam penetrates the sample and ionizes atoms in 1-2  $\mu m$  in depth (dependent on the density of the

material). The sensitivity to Auger electrons is greater in the outer surface layer, than from subsurface layers because of strong inelastic scattering between signal electrons and solid state electrons. Quantitative AES analysis usually involves the use of elemental sensitivity factors. The atomic concentration ( $C$ ) of an element  $x$  is given by:

$$C_x = \frac{I_x/S_x}{\sum(I_i/S_i)} \quad (4.35)$$

where  $I_x$  is the intensity of the Auger signal and  $S_i$  is the relative sensitivity of element  $i$ .

Depth profiling is one of the most important applications of AES, it allows to analyze the in-depth composition of the surface layers, but it is a destructive technique. In this method the sample is eroded by ion sputtering. The sample is bombarded with Ar ions accelerated in an ion gun, the ion beam is rastered over the surface for a defined time to remove an uniform layer, then the surface is analyzed by AES finally giving the depth distribution of different species.

## 4.4 Optical Methods

### 4.4.1 Wyko - Optical Profilometer

The Veeco Wyko NT9100 Optical Profiler was used to analyze the samples after tribological test and to measure the wear volume. The Wyko is an optical profiler providing three-dimensional surface topography measurement without contact. The operation principle is similar to a typical interferometer, the white-light beam emitted from the light source is divided by a beam splitter into two beams, one is reflected from the reference mirror and the other one from the sample. These two beams are recombined by the beamsplitter to interfere, and create bright and dark bands called fringes, which represent the topography of the object (Fig. 4.18) [85]. Next, the imaging lenses image the interferogram onto a CCD camera that registers it and forwards the frame to the computer for processing using interferometric phase-mapping programs.

There are two working modes available in Wyko: VSI (Vertical Shift Interference) and PSI (Phase Shift Interference). The VSI mode, based on white light vertical scanning interferometry, is dedicated for very rough surfaces with a maximum measurable topography step up to 1 mm. The PSI mode, based on optical phase-shifting, is dedicated to roughness measurements for rather smooth surfaces, with small steps (maximum 150 nm pick to valley topography).

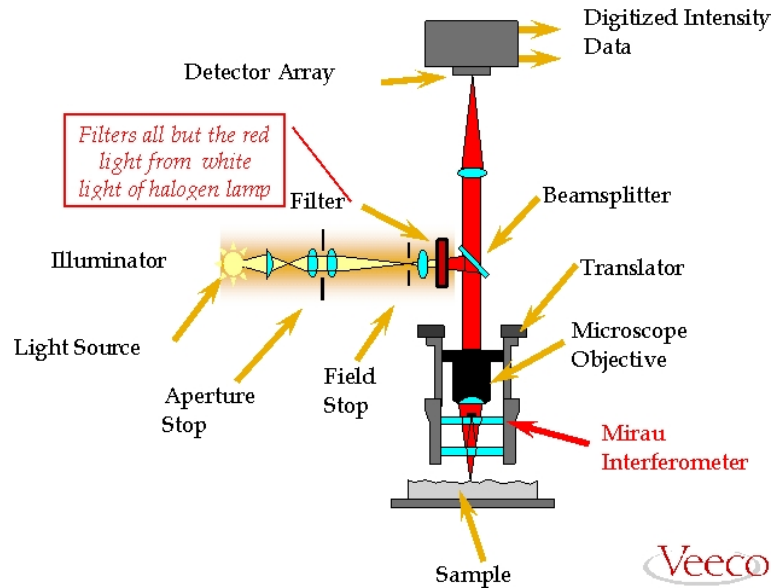


Figure 4.18: Operation principle of a typical microscope-based interferometer. Veeco Wyko is equipped with a Mirau-type interferometric objective, typically for magnification up to 50x [85].

#### 4.4.2 Optical Microscopy

Optical Microscopy was used to analyze wear track after tribological tests.

A traditional optical microscope *Zeiss Axioskop* was coupled with *CoolSNAP-Pro of Color* camera to output images to computer, afterwards *Image-Pro Express v. 4.5.1.3* software was used to process the data. Images in three different magnifications 2.5x, 10x, 50x were acquired. The width of the wear track and corrosion factor was estimated from microscopy images.

# 5 RESULTS AND DISCUSSION

Various research in this work showed that molecular processes, especially chemical bondings between lubricants, additives and surfaces strongly affect performance of tribological systems. Presented publications in this chapter were written within three years of my PhD studies. The references in this chapter will continuously follow numeration according previous part. Additional comments raised by thesis reviewers will be incorporated in the form of footnotes in the published manuscripts.

## 5.1 Additives for Water Based Lubricants

### 5.1.1 Oligomer specific lubrication

*"Oligomer specific lubrication"* [1] reports on nanoscale tribological investigations on ethanolamine oligomers in aqueous solutions investigated with an AFM closed fluid cell. The friction measurements under nano Newton load range and calculations carried out to characterize behavior of the additives in aqueous media are presented. This work showed oligomer specific lubrication: the most efficient additive reduced friction by 76% with respect to reference friction measurements performed in double distilled water. Thus further studies were needed to confirm the performance on the macroscale.

#### OLIGOMER SPECIFIC LUBRICATION

A. Tomala<sup>1</sup>, I.C. Gebeshuber<sup>1,2</sup>, C.A. Vasko<sup>1</sup>, N. Doerr<sup>2</sup>, H. Stoeri<sup>1</sup>

<sup>1</sup> Institut für Angewandte Physik, Vienna University of Technology, Wiedner  
Hauptstrasse 8-10/134, 1040 Wien

<sup>2</sup> AC <sup>2</sup>T research GmbH, Austrian Center of Competence for Tribology, Viktor  
Kaplan-Strasse 2, 2700 Wiener Neustadt, Austria

Under evaluation in TRIBOLOGY INTERNATIONAL.

## ABSTRACT

Ethanolamines or aminoethanols are known as multidentate ligands with the possibility to form chelates with metals via their amino, hydroxyl and deprotonated hydroxyl groups. The total formula of these water soluble compounds is  $NH_{3-n}R_n$  ( $R = CH_2CH_2OH$ ,  $n = 1 - 3$ ). Ethanolamines are widely used as cleaning agents. In the field of lubrication, they are utilized as additives in metalworking lubricants.

Understanding the lubrication properties of the first chemisorbed layer of additives on work pieces yields important information for the optimization of lubrication in aqueous and non-aqueous solutions, in particular with regard to the type of additive, oligomer and amount needed.

Chemisorbed layers of the mono-, di- and triethanolamine oligomer were studied with atomic force microscopic methods to reveal differences in their lubrication properties in the nanoscale. Therefore, the ethanolamines were dissolved in double distilled water. Copper sputtered silicon wafers served as substrates.

The research work showed oligomer specific lubrication: The monoethanolamine oligomer reduced friction most efficiently by 76% and the diethanolamine enabled a reduction of friction by 65%. Finally, triethanolamine oligomer allowed a decrease of just 35% in respect to reference friction measurements performed in double distilled water.

## INTRODUCTION

The main goal of research in tribology is the minimization and elimination of losses resulting from friction and wear at all levels of technology where interactions of surfaces in relative motion are involved.

Micro/nanotribological studies are needed to develop a fundamental understanding of interfacial phenomena on a small scale. These investigations of interfacial phenomena also involve ultra thin films and micro/nanostructures - both currently being used in magnetic storage systems, micro/nanomechanical systems (MEMS/NEMS) and other industrial applications. Probe-based microscopes, e.g. the atomic force microscope (AFM), and the surface force apparatus are widely used for such micro/nanotribological studies [58] [56].

AFM relies on a scanning technique to produce images of sample surfaces with a very high resolution. The AFM records ultra small forces ( $\leq 1$  nN) occurring between the AFM tip surface and the sample surface. These small forces are gathered by measuring the deflection of a very flexible cantilever beam [62]. AFM is suitable to study engineering surfaces under dry or wet conditions with atomic resolution.

Monomolecular lubricant layers on solid surfaces may reduce friction, wear, and rust. In the case of dispersions, they have the ability to stabilize emulsions, foams, and solid dispersions [58].

Basically, liquids are good lubricants when they contain polar compounds and thus are able to adsorb on solid surfaces. Such polar compounds contain reactive functional groups with low ionization potential, or functional groups with high polarizability. Furthermore, boundary lubrication properties of lubricants depend on molecular conformation and lubricant spreading [56].

Boundary films can be formed by several processes: Physisorption, chemisorption and chemical reactions. In the case of physisorption no exchange of electrons takes place between the lubricant molecule and the surface - this process involves weak van der Waals forces. Chemisorption means the sharing of electrons and electron interchange between chemisorbed species and the solid surface resulting in the formation of chemical bonds. Finally, chemical reactions comprise the formation of surface layers with considerable chemical alteration of both additive and surface. The stability and durability of surface films decrease in following order: chemical reaction layers (thick films), chemisorbed films (with monomolecular thickness), physisorbed films (monolayers or multilayers) [56].

Ethanolamines or aminoethanols are known as multidentate ligands with the possibility to form chelates with metals via their amino, hydroxyl and deprotonated hydroxyl groups. The total formula of these water soluble compounds is  $NH_{3-n}R_n$  ( $R = CH_2CH_2OH$ ,  $n = 1 - 3$ ). Ethanolamines appear as three different oligomers: monoethanolamine (MEA), diethanolamine (DEA) and triethanolamine (TEA) as shown in Fig. 5.1.

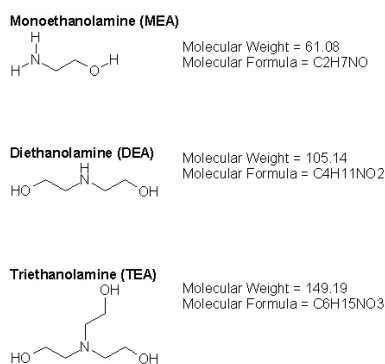


Figure 5.1: Structural formula of mono-, di- and triethanolamine

Ethanolamines can be found in a broad spectrum of applications, e.g. as cleaning agents, due to the joint properties of amines and alcohols with the unique capability to undergo reactions common to both groups. In the field of lubrication,

they are utilized as additives in metalworking lubricants. In this publication, the authors report on experiments on ethanolamines in aqueous solutions investigated for oligomer specific lubricating properties in the nanoscale using AFM.

## MATERIALS AND METHODS

### Preparation of ethanolamine oligomer solutions

MEA, DEA and TEA were at least of 98% purity (GC) and used as obtained. Each of the ethanolamine oligomers was dissolved in double distilled water with a concentration of 250 ppm (parts per million). The chosen concentration of these additives was significantly below saturation concentration to prevent growth of additive crystals on the copper surface. To achieve such a small target concentration, 20  $\mu\text{L}$  of each pure ethanolamine oligomers have been injected by pipette into 80 mL of double distilled water.

### Sample preparation and AFM data acquisition

Measurements were performed with an AFM MFP-3D atomic force microscopy (by Asylum Research, Santa Barbara, CA) in a closed fluid cell using non conductive silicon nitride cantilevers with a spring constant  $k = 0.01 \text{ N/m}$  and a resonant frequency  $f_0 = 4 - 10 \text{ kHz}$  (Veeco). The main measurement parameters were: a scan size of  $5 \times 5 \mu\text{m}^2$  (512 scan points and 512 scan lines), a scan rate of 2 Hz, scan angle of  $90^\circ$ , and a set point of 3.3 nN in contact mode. The recorded data was each trace/retrace of height, deflection, and lateral force.

Copper sputtered silicon wafers were used as specimens and were provided by the Institute for Solid State Physics, Vienna University of Technology. The fluid cell was a chamber consisting of two halves screwed together mechanically: The samples were glued onto glass on the lower part of the closed fluid cell while the upper half basically consisted of the electronic interface, the cantilever and a flexible membrane. After screwing together both halves, the fluid cell was flooded with double distilled water. Two channels of the cell were used to inject fluid into the cell and to drain it, respectively. In the next step, the fluid cell was attached to the head of the AFM. After placing the head with the cell onto the moving table the head was lowered until the cell attached to the table. The reference scans in double distilled water environment were carried out when the mounting and calibration procedure of the system was completed. The lateral trace and retrace data were recorded. Then, the ethanolamine oligomer solutions were injected into the cell with a syringe and the AFM experiments were performed analogously to the reference measurements.

### Friction measurements

Bhushan introduced two methods to measure the friction in AFM experiments [56]. For the presented measurements, the lateral force technique has been chosen since it is described as more reliable and objective: the sample is scanned perpendicularly to the long axis of the cantilever beam, i.e. scanning along the arrow directions as shown in Fig. 5.2, to record the lateral force signals in trace and retrace (LT, LRT).

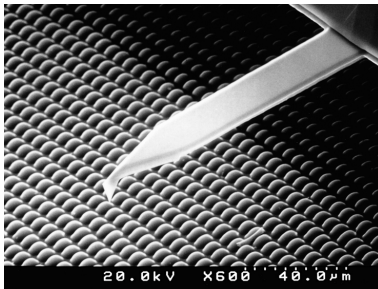


Figure 5.2: Definition of the x-directions relative to the cantilever, and sample traveling direction in friction force measurements [86]

Using this arrangement, the friction force between tip and surface will cause the cantilever to twist as soon as the sample moves under the tip. Therefore, the signal intensity between the left and the right detectors will vary denoted as FFM signal:

$$FFM = (L - R)/(L + R) \quad (5.1)$$

This signal can be related to the degree of twisting, hence to the magnitude of friction force. By changing the set point parameter in the feedback loop, the normal force applied between probing tip and sample surface can be changed. The scan area was  $5 \times 5 \mu\text{m}$  consisting of 512 scan lines with each 512 scan points. First, the average values of all 512 lines with 512 points for lateral trace (LTV<sub>avg</sub>) and lateral retrace (LRTV<sub>avg</sub>) from every scan were calculated. To obtain the friction force value (FFV), these two mean values have to be subtracted from each other, and divided by two.

$$FFV = \frac{|LTV_{avg} - LRTV_{avg}|}{2} \quad (5.2)$$

The measurements of the friction force values were repeated ten times in every environment (water, water + oligomer) to obtain representative and repeatable results. Assuming that the friction in the nanoscale follows Amonton's law, the friction force is given by:

$$FFV = \mu(SP + F_0) \quad (5.3)$$

Where  $\mu$  is the friction coefficient, the set point (SP) is the applied load and  $F_0$  is a force constant. Following the procedure suggested by Beake et al.[68], the force constant is nearly equal to the pull off force determined from the force distance curves. Usually, the FFV and SP values are given in [V] Volts as acquired from lateral force measurements. However, the results can be easily compared with each other because findings in Volts are connected with the forces between tip and surface. In order to obtain commonly used units ([N] Newton), the lateral force needs to be calibrated by the determination of the slope of deflection vs. LVDT. The calibration delivers an accurate value of the inverse optical lever sensitivity (InvOLS) describing the sensitivity of the detector-cantilever combination. With the knowledge of the accurate value of InvOLS, it is possible to calculate FFV and SP in Newton:

$$FFV[V] \times InvOLS[nm/V] \times springconstantk[nN/nm] = FFV[nN] \quad (5.4)$$

$$SP[V] \times InvOLS[nm/V] \times springconstant[nN/nm] = SP[nN] \quad (5.5)$$

## RESULTS AND DISCUSSION

The friction force values and friction coefficient of the virgin surfaces were determined. Then the additives were introduced into the fluid cell and the measurements were repeated with the lubricant present.

Representative three dimensional topographies of the ethanolamine films are displayed in Fig. 5.3-5.5 with section graphs and the Root Mean Square (RMS) parameter.

In the case of monoethanolamine the surface roughness and RMS parameter were significantly lower compared to pure double distilled water (Fig. 5.3). In the case of triethanolamine corrosion pits were observed (Fig. 5.5), being the reason why friction coefficient and roughness were much higher then for other oligomers.

In a next step, force spectroscopy was performed on the surfaces as depicted in Fig. 5.6. Blue lines indicate the cantilever tip approaching the surface and red dashed lines represent the tip retracting. The vertical separation between point A, where the tip is touching the film, and point B, where the tip is pulled off the film, yields the pull off force [87].

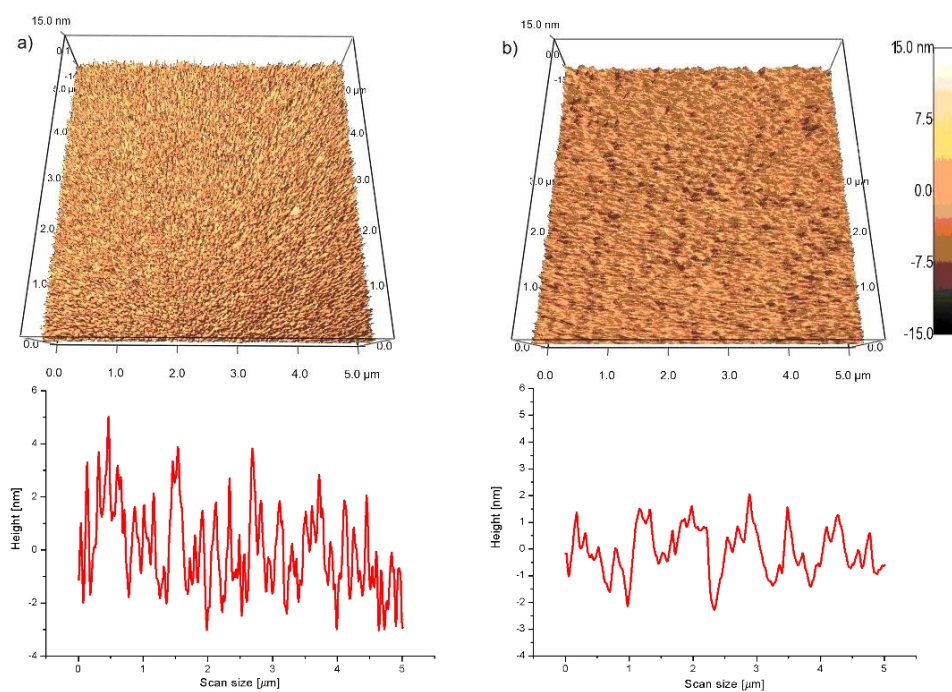


Figure 5.3: Topography images a) copper sample in double distilled water,  $RMS=3.59nm \pm 1.97nm$ , b) copper sample with double distilled water + MEA,  $RMS=0.89nm \pm 0.58nm$

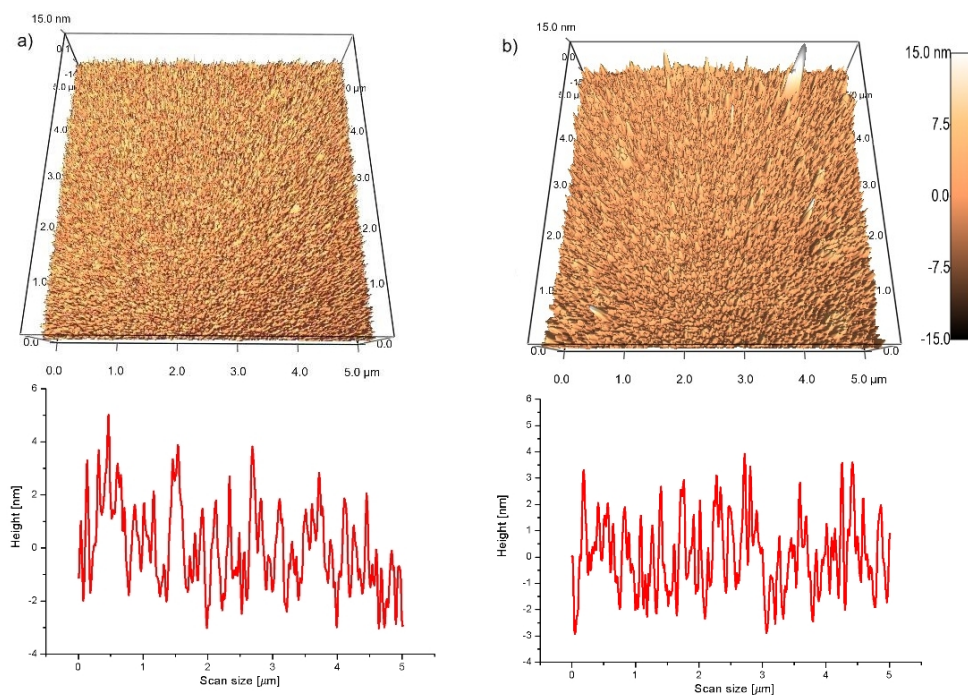


Figure 5.4: Topography images a) copper sample in double distilled water,  $RMS=3.59nm \pm 1.97nm$  b) copper sample with double distilled water + DEA,  $RMS = 7.85nm \pm 6.71nm$

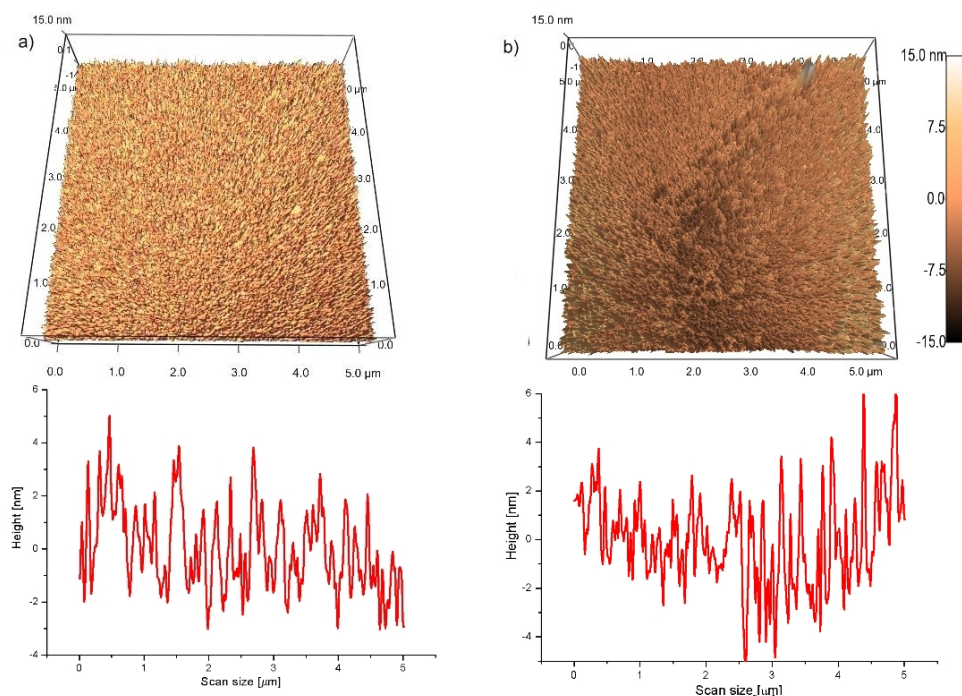


Figure 5.5: Topography images a) copper sample in double distilled water  $RMS=3.59nm \pm 1.97nm$ , b) copper sample with double distilled water + TEA,  $RMS=6.68nm \pm 4.91 nm$ .

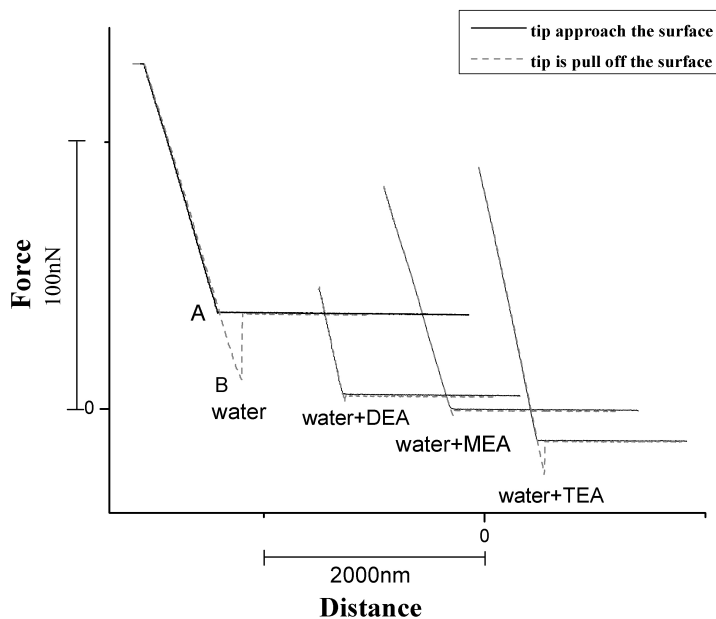


Figure 5.6: Force distance curves of the investigated monolayers.

It can clearly be seen that pull off forces for double distilled water without any additives are larger than pull of forces for water with ethanolamines. For water with monoethanolamine oligomer the pull of force is smaller than for water with diethanolamine and triethanolamine oligomers. This fact may be related to an increase of surface energy due to the additives. The hydroxyl groups, being components of ethanolamine oligomers, increase the surface energy and the increased surface energy in turn increases the pull off forces.

Future studies have been done with X-ray photoelectron spectroscopy (XPS) to obtain insight into the molecular mechanisms leading to the macroscopic lubricity. The solution with a concentration of 250 ppm ethanolamine oligomers in double distilled water was transferred into the adsorption device, which is an extension of the spectrometer. The structure of the molecular film is elucidated using angular resolved X-ray photoelectron spectroscopy [88]. The results indicate that while oxygen and carbon were located on top, copper and nitrogen were beneath. Therefore it was deduced that the molecules stand upright on the surface, bound to the same by the nitrogen atom [2].

The results show a significant drop in the friction force value after 10 minutes after introducing ethanolamine oligomer to the solvent. For the other oligomers investigated similar drops in friction occurred (Table 5.1, Fig. 5.7).

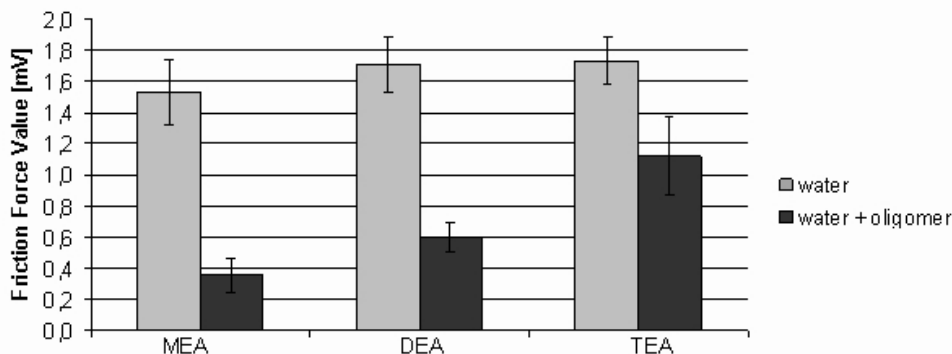


Figure 5.7: FFV of double distilled water and decrease of FFV after the addition of solutions with 0.025% ethanolamine oligomer

| Oligomer         | Reference value for pure double distilled water [mV] | Double distilled water with 0.025% ethanolamine oligomer [mV] | Reduction of FFV |
|------------------|--|---|------------------|
| Monoethanolamine | $1.53 \pm 0.2$                                       | $0.35 \pm 0.11$   | 76 %             |
| Diethanolamine   | $1.71 \pm 0.18$                                      | $0.59 \pm 0.09$   | 65 %             |
| Triethanolamine  | $1.73 \pm 0.15$                                      | $1.12 \pm 0.25$   | 35 %             |

Table 5.1: FFV of double distilled water and solutions with 250 ppm ethanolamine oligomer, relative reduction of FFV due to the addition of ethanolamines

## CONCLUSION AND OUTLOOK

For the first time, oligomer specific lubrication of mono-, di- and tri-ethanolamines has been demonstrated. In this work we present friction behavior investigated with Atomic Force Microscopy, additionally X-ray photoelectron spectroscopy (XPS) was used to obtain insight into molecular mechanisms leading to the macroscopic lubricity.

The results show that ethanolamine oligomers dissolved in water lower the friction at a concentration of 0.025% introduction to the closed fluid cell. The reproducibility of lateral friction measurements in pure water and aqueous solutions proves that the experimental setup is suitable for such investigations. Monoethanolamine, diethanolamine and triethanolamine reduce the friction in statistically relevant amounts: from 1.53 mV in pure water to 0.35, 0.59 and 1.12 nN, respectively, in the aqueous solutions of the ethanolamines. The relative reduction of friction forces of MEA, DEA and TEA comes to 76%, 65% and 35%, respectively, relative to pure water.

Basically, these properties can be explained by the functional groups - amine and hydroxyl - of the ethanolamine oligomers. In detail, XPS measurements gave that the hydroxyl group(s) are rather located on the top of monomolecular lubricant film while the amine group rather bonds to copper. Although ethanolamines are at least bidentate ligands, the results suggest only monodentate sorption to the copper surface. Usually, increasing degree of oligomerisation causes increasing sterical hindrance. Consequently, the relatively poor reduction of friction with triethanolamine may be explained by a less efficient bonding to the copper surface in comparison to mono- and diethanolamine.

Corrosive pits observed for triethanolamine oligomer are result of high basicity of this compounds, and to avoid it the concentration of additives have to be reduce.

The promising results from the oligomer dependent interaction of ethanolamines with copper surfaces and silicon nitride of the AFM tips give rise to future research in this field. Future work is plan with angular resolved X-ray photoelectron spec-

trosopy to have insight look into molecular structure and characterize the bonding of the molecules to the surface of the adsorbents. The tests are plan for other metals, e.g. iron and in different temperature rate to elucidation of the lubrication mechanism.

#### **ACKNOWLEDGMENTS**

The authors are grateful to Christoph Eisenmenger-Sittner from the Institute for Solid State Physics, Vienna University of Technology, for the supply of the Cu-sputtered silicon samples. The work presented in this paper has been supported by the EC, Sixth Framework Programme, Marie Curie Action (WEMESURF research project entitled: "Characterization of wear mechanisms and surface functionalities with regard to life time prediction and quality criteria-from micro to nano range" under contract MRTN CT 2006 035589).

### 5.1.2 Tribochemistry of monomolecular lubricant films of ethanolamine oligomers

*"Tribochemistry of monomolecular lubricant films of ethanolamine oligomers"* [2] explains the influence of hydroxyl groups and nitrogen containing ethanolamine oligomers on the nano and macroscale tribological behavior. AR-XPS results were analyzed and molecular mechanisms leading to the macroscopic lubricity was illustrated. This manuscript concludes that for the investigated additives, a comparable tribological performance was observed for a wide range of loads (nano and micro Newtons). The results showed that the differences in tribological behavior might be due to the orientation of amine and hydroxyl groups on the surface. It was deduced that ethanolamine molecules stand upright on the surface, bound to it by the nitrogen atom. The number of hydroxyl groups in a chemical compound have an influence on friction and compromise on the top layer of the film.

#### TRIBOCHEMISTRY OF MONOMOLECULAR LUBRICANT FILMS OF ETHANOLAMINE OLIGOMERS

A. Tomala<sup>1</sup>, W.S.M. Werner<sup>1</sup>, I.C. Gebeshuber<sup>1,2</sup>, N. Doerr<sup>2</sup>, H. Stoeri<sup>1</sup>

<sup>1</sup> Institut für Angewandte Physik, Vienna University of Technology, Wiedner Hauptstrasse 8-10/134, 1040 Wien

<sup>2</sup> AC <sup>2</sup>T research GmbH, Austrian Center of Competence for Tribology, Wiktorkaplan-Strasse 2, 2700 Wiener Neustadt, Austria

TRIBOLOGY INTERNATIONAL

Volume 42, Issue 10, October 2009, Pages 1513-1518

Special Issue: NORDTRIB 2008

#### ABSTRACT

The aim of present study was to find out the influence of oxygen and nitrogen containing ethanolamine oligomers on the tribological behavior. X-ray photoelectron spectroscopy (XPS) was used to obtain insight into the molecular mechanisms leading to the macroscopic lubricity. Monomolecular lubricant films were deposited onto ultra thin copper films sputtered onto silicon wafers. Surfaces covered with the three ethanolamine oligomers were investigated by XPS before and after tribological tests, performed with the translatorily oscillating test machine and Falex micro-tribometer.

The structure of the molecular film is elucidated using angular resolved X-ray photoelectron spectroscopy with a prototype preparation chamber, permitting the transfer of samples from liquid to the analysis chamber under Helium protective gas preventing exposure to ambient conditions. Solutions with a concentration of 250 ppm of the respective ethanolamine oligomers in double distilled water were transferred into the adsorption device, which is an extension of the spectrometer. Results show that compounds bond to copper and steel surface by N atom present in ammonia group and hydroxyl group are oriented on the top layer of tribofilm, this highest group influence lubricity properties.

## INTRODUCTION

Additives are of crucial importance in lubrication technology. Additive molecules physisorbed or chemisorbed onto surfaces form lubricating films fundamentally influencing wear and friction properties of two rubbing surfaces.

Earlier experiments in the macroscale as well as in the nanoscale showed that the three different oligomers of ethanolamine have different lubrication properties on 100Cr6 steel and copper [1], respectively. Ethanolamines act as multidentate ligands on the base of amino, hydroxyl and deprotonated hydroxyl groups of the total formula  $NH_{3-n}R_n$  ( $R = CH_2CH_2OH$ ,  $n = 1 - 3$ ). Mono-, di- and triethanolamine are readily soluble in water and are utilised as additives in metal-working fluids. The understanding of the lubrication mechanisms of the additive layer chemisorbed on the specimens measured yields important information regarding lubrication optimisation in term of the type of additive, type of isomer or oligomer and amount.

One of an unexplained mechanism are different lubrication properties of oligomers of ethanolamines. Whereas mono- and diethanolamine oligomer exhibit good lubrication properties triethanolamine oligomer do not and increase surface roughness by corrosive pit into the copper surface [1].

To ensure the reliability of micro- and nano-devices as well as of magnetic storage devices, the application of lubricant film is required for the protection of the sliding surfaces from wear. Ideally, these films should be in the range of monomolecular layers because of small clearances in such devices and to minimize adhesion of sliding partners and to reduce wear and friction.

The classical approach to lubrication of micro- and nano-devices uses multi-molecular layers of liquid lubricants. Boundary films are formed by

- Physisorption without exchange of electrons between the molecules of the adsorbate and adsorbent - this process involves weak Van der Waals forces).

- Chemisorption were electrons shear and electron interchange between chemisorbed species and the solid surface by formation of covalent bonds.
- Chemical reaction where films are formed by chemical reaction of the solid surface with the environment, the additive and the solid surface.

The stability and durability of the above surface films decrease in the following order: chemically reacted films (large film thickness), chemisorbed films (monomolecular layers), physisorbed films (monomolecular to multimolecular layers).

Sub-monomolecular films with a thickness in the order of a few nanometers, may be discontinuous and may deposit in an island form of non uniform thickness with lateral resolution in the nanometer scale [56].

A film fully covered with one layer of additive, often referred to as a monolayer, may reduce friction, wear, and rust, or may stabilize emulsions, foams, and solid dispersions. In this study, we investigated so-called ethanolamines which have three different oligomers: monoethanolamine (MEA), diethanolamine (DEA) and triethanolamine (TEA). The chemical structures are depicted in Fig. 5.8. Ehanolamines are multidentate ligands through amino, hydroxyl, and deprotonated hydroxyl groups, with the total formula  $NH_{3-n}R_n$  ( $R = CH_2CH_2OH$ ,  $n = 1 - 3$ ).

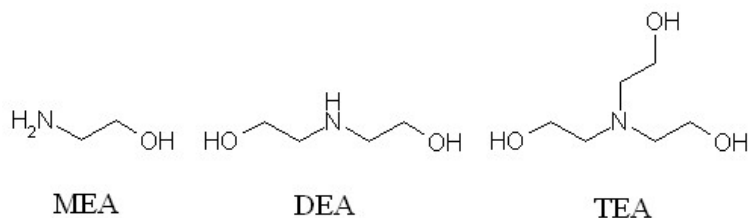


Figure 5.8: Three oligomers of ethanolamine [1].

Ethanolamines have a broad spectrum of applications, because they combine properties of amines and alcohols. Thus, they exhibit a unique capability of undergoing reactions common to both groups.

In order to acquire knowledge of the tribological behavior of the oligomers at the interface between solids, a fundamental research work on the interaction of additive molecules with the surface is necessary.

XPS is the appropriate analytical method for the chemical analysis of adsorbents on surfaces. This technique is capable of characterizing the binding of the molecules to the surface as well as of providing concentration depth profiles of organic compounds adsorbed to solid surfaces. The chemical shift of the photoelectron peaks provides information about the atoms bound to the surface and

is an indicator for the strength of the interaction between surface and additive. Angle resolved XPS is capable of determining the depth distribution of elements in each particular oxidation state in the first atomic layers. Moreover, the surface coverage can be deduced from the intensity dependent on the take-off angle of the photoelectrons. Finally, quantitative information about the composition can be gathered and quantitative concentration depth profiles are available [89].

## **MATERIALS AND METHODS**

### **Sample preparation**

Silicon wafers of  $10 \times 10 \text{ mm}^2$  were cut from  $5 \times 5 \text{ cm}^2$  sheets, and coated with 200 nm of copper by sputtering. The surface roughness of these coated slides was determined with an atomic force microscope (AFM MFP-3D, Asylum Research Santa Barbara, CA) in contact mode in air, and it turned out that the samples were almost flat at the atomic level, and not exceed 5 nm.

Investigations by X-ray photoelectron spectroscopy (XPS) were performed using a VG ESCALAB Mk III equipment with a prototype preparation chamber permitting the transfer of samples from liquid to the analysis chamber under Helium protective gas preventing exposure to ambient conditions. The samples were transferred from the load lock chamber into the preparation chamber ( $5 \times 10^{-9}$  mbar) of the XPS. It is well known that polluted sample surfaces change their properties [90]. For this reason, the specimens have been cleaned by argon ion sputtering until the XPS spectra of samples showed no peaks of contamination. 100Cr6 steel samples were prepared from sheets of  $8 \times 12 \text{ mm}^2$ , which were cut from roll from roller bearing. Then these samples were ground with abrasive paper down to  $4000 \mu\text{m}$ , and then with DP-Spray P containing crystalline diamond with a grain size of  $1 \mu\text{m}$ . The average roughnesses (RMS) of the samples were checked by AFM and gave values of approximately 20 nm.

### **Preparation of ethanolamine oligomer solutions**

Each ethanolamine oligomer (MEA - monoethanolamine oligomer, DEA - diethanolamine oligomer, TEA - triethanolamine oligomer) was dissolved in double distilled water to a concentration of 250 ppm. All water solutions had the same molar content (molecular concentration). Concentrations of the additives were significantly below saturation concentration, to prevent growth of additive crystals on the copper surface.

For the experiments, the solutions were then transferred into the electrochemical device consisting of two supply reservoirs, one was used as storage of double distilled water for rinsing the samples and the other contained the additive solution of the absorbents. A pressure line, which was filled with He 6.0 provided

the pressure to transport the liquids into the adsorption vessel. In the adsorption vessel the samples were prepared. Bubblers were used to release the pressure and to keep air out of the system. Thus, the entire device was permanent under a slight overpressure of He. Furthermore, the He flow was used to flush the solutions in the storage supply in order to degas the solution [91].

The clean copper sheets were transferred from the preparation chamber of the XPS spectrometer directly into the adsorption vessel of the electrochemical device. There, they were dipped in 0.025 % solutions of the adsorbates for 10 minutes at room temperature. Afterwards, the samples were rinsed with double distilled water, blown dry with He and transferred directly without exposing them to environment into the preparation chamber of the XPS [92].

### **Data acquisition**

For XPS spectra, the samples were transferred from the preparation into the analysis chamber ( $< 5 \cdot 10^{-10}$  mbar, except for sputtering). In angle resolved measurements (ARXPS), the angle between the sample surface and the analyzer, which is called emission angle, was altered by rotating the samples around the x-axis. This corresponded to rotations at angles of  $0^\circ$  and  $80^\circ$ . The emission angle was calculated from the geometric factors. Therefore, the emission angles calculated for the geometries used in the experiments were  $15^\circ$  and  $63^\circ$ . All XPS measurements were performed using aluminum  $K\alpha$  radiation. The energy covered a range from 0 eV to 1400 eV binding energy. Spectra of C 1s, O 1s, N 1s and Cu 2p for silicon samples with copper layer and Fe 2p for steel samples were recorded.

### **Tribological experiments**

A translatorily oscillating test machine (TOG), as shown in Fig. 5.9, was chosen for the investigation of lubricity on a macroscopic scale on steel samples. TOG is widely used for the study of the tribological behavior of tribo-partners with translatory relative movement to evaluate material combinations in a dry or wet lubrication regime. The TOG tribometer is based on a steel cylinder which is loaded against the steel sample. The sample was mounted on a special sample holder, which had been constructed for tribotesting in lubricants. During the measuring process the cylinder was oscillating in certain frequency and was in constant contact with the sample (see figure 2). The 12N load was applied to the upper specimen holder where the cylinder was mounted to press on a sample. For substances the test were carried only once.

The tribometer sample holder for testing in lubricants itself was screwed to a plate, which was fixed on the carriage. The carriage resides on a roller bearing and is driven by pneumatics. If the parallel lever system is adjusted in a way that

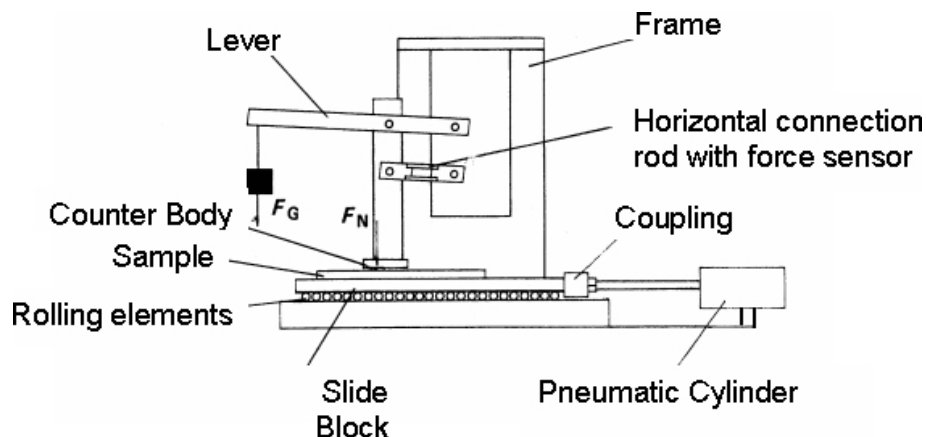


Figure 5.9: Sketch of the TOG tribometer [76]

the levers are parallel to the surface of the sample during tribotesting, friction force can be easily calculated from the stress measured by resistance strain gauge and the load applied and the dimensions of the tribometer.

#### Micro-tribometer FALEX-MUST 2D-FM

The tribometer FALEX-MUST 2D-FM working in reciprocating mode was used for copper sputtered silicon wafers to apply small loads from 1 mN to 1 N in order to prevent the silicon wafers from breaking. As counter body a steel ball mounted on a 2D force transducer was used. The normal force  $F_N$  (orthogonal to the surface), the tangential force  $F_T$  (parallel to the surface of the test sample and opposing the relative velocity) and the moving distance  $s$  were recorded over time  $t$  while the sample (copper coated silicon wafer) was moved in reciprocating mode.

Fig. 5.10 depicts the functional principle of this micro-tribometer. The FALEX-MUST 2D-FM special force transducer consists of a cantilever based on parallel spring system, two mirrors fixed on a moving part of the cantilever and a mechanical carrier. The cantilever is fixed on the mechanical carrier and helps to change the measurement mode of the force transducer. The two mirrors positioned orthogonally to each other are used as reflective surface for the fibre optic sensors (FOS). FOS is for the measurement of the deflection of the force transducer and the positioning of the piezo drives.

In this tribological experiment, the steel ball was loaded against the copper coated silicon wafer. The chosen test parameters are listed in Tab.5.2.

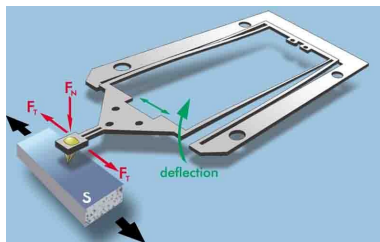


Figure 5.10: Functional principle of the force transducer in microtribometer [74]

|                            |                   |
|----------------------------|-------------------|
| Counter material           | 100Cr6 steel ball |
| Target force               | 30 mN             |
| Stroke length              | 7 mm              |
| Scan speed                 | 5 mm/s            |
| number of cycles per track | 10                |

Table 5.2: Test parameters for copper coated silicon wafers sliding against steel balls in micro-tribometer FALEX-MUST 2D-FM

## RESULTS

### Micro-tribometer

The results obtained with micro-tribometer show that ethanolamine oligomers dissolved in water lower the friction at a concentration of 250 ppm. Monoethanolamine oligomer reduce friction by 63% and this was the lowest observed friction. Diethanolamine reduce friction coefficient by 25% and triethanolamine by 44% (Fig. 5.11).

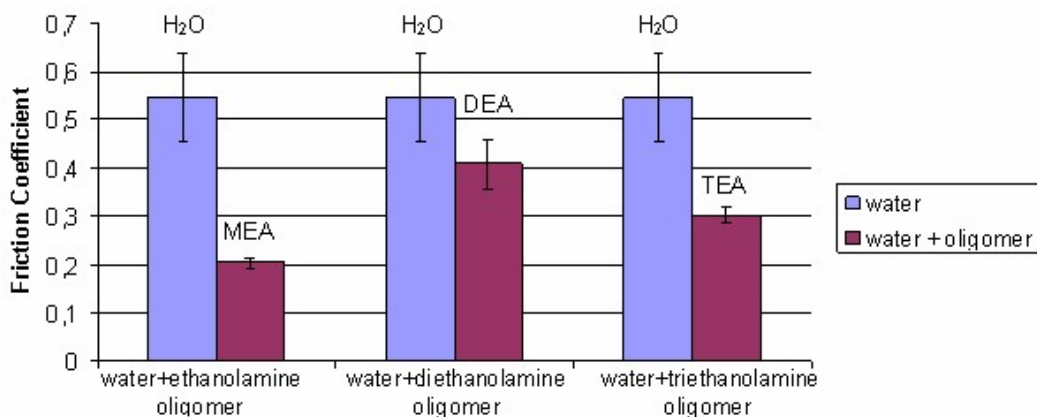


Figure 5.11: Microtribometer results showing drop of friction coefficient for three oligomers of ethanolamines compare to double distilled water

**TOG** The results show that ethanolamine oligomers dissolved in water lower the friction at a concentration of 250 ppm. Monoethanolamine and diethanolamine oligomer reduce friction the mostly by 58% and 37%, whereas triethanolamine only by 11% (Fig. 5.12).

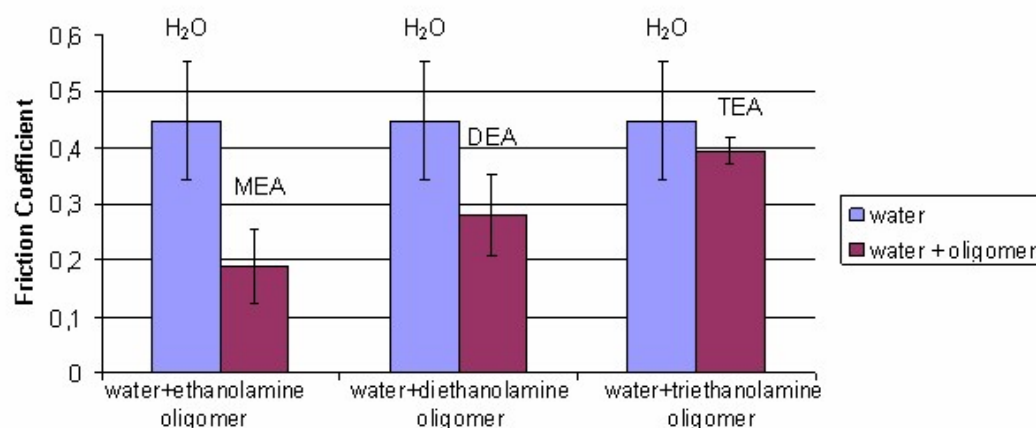


Figure 5.12: TOG results showing drop of friction coefficient for three oligomers of ethanolamines compared to double distilled water

In previous work [1] the Atomic Force microscopy studies with nano-Newton resolution were performed with a MFP-3D from Asylum Research. Set point - applied load on the sample by cantilever was 3.3 nN. The results showed the same tribological behavior of ethanolamines as in macroscale, that the lowest friction coefficient was observed for monoethanolamine oligomer. The differences in tribological behavior were observed by AFM with 3.3 nN load, microtribometer with 30 mN load and with TOG tribometer with 12 N load. Results show that monoethanolamine oligomer and diethanolamine oligomer have an excellent behavior regarding all tested parameters. Triethanolamine oligomer increases surface roughness by corrosive pit into the copper surface.

### XPS results

#### Copper surface

The survey spectra of all copper samples showed only peaks of copper, oxygen, nitrogen and carbon as expected. The position of photoelectron peaks was determined using Casa XPS, and a combination of Gaussian and Lorentzian peak was used for fit. The adsorption of ethanolamine oligomers onto atomically flat surface of copper layer takes only 10 minutes. The survey spectra shows that after this time surface adsorb measurable amount of the oligomers. The quantification

of the O1s and C1s showed that there was an equal amount of both oxygen and carbon in the adsorbed films. The C1s peak was in the region typical for alcohols and organic compounds containing nitrogen. The Cu 2p photoelectron region of diethanolamine showed different intensity ratio of the copper peak on clean surface and the copper peak with DEA film. The loss in intensity of iron peak was due to the coverage of the surface with the adsorbed diethanolamine. At emission angle  $63^\circ$  the Cu peak almost vanished in the spectra recorded from samples with diethanolamine film (Fig. 5.13).

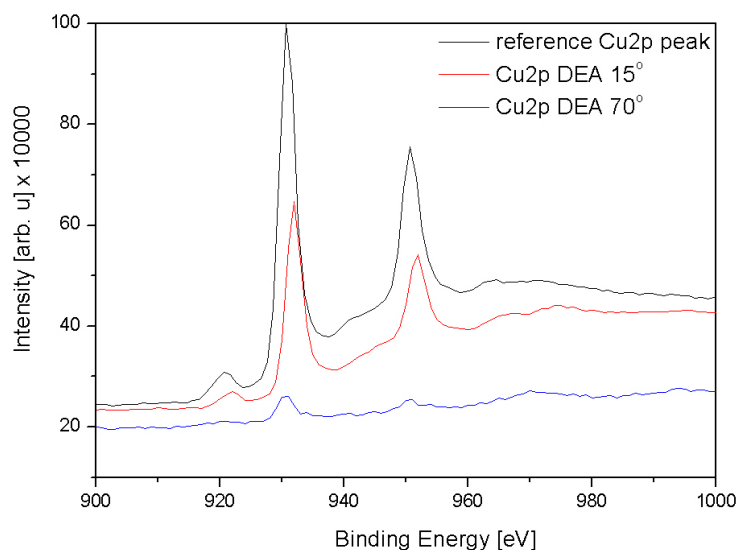


Figure 5.13: Cu2p region of monolayer of DEA on copper surface. The spectra are shown for two different electron take off angles. For comparison the spectra of clean copper are also shown.

Results obtained for diethanolamine and monoethanolamine present clearly the orientation of the molecules on the surface. The intensity of oxygen peak O1s and carbon peak C1s increase with increasing analyzer angle, and copper peak 2p<sub>1/2</sub> and 2p<sub>3/2</sub> and nitrogen N1s peak decreasing with emission angle (Fig. 5.14). This results indicates that oxygen and carbon was located on top, copper and nitrogen were beneath. Therefore it was deduced that the molecules stand upright on the surface, bound to it by the nitrogen atom.

In Fig. 5.14, can be clearly seen that the intensity of copper continuously declines, therefore the whole surface is covered with molecules of diethanolamine. Angular resolved measurements showed that three oxygen species were situated in different heights. The one located on the top appear to increase with emission angle - this correspond to oxygen from hydroxyl group (HO-CH<sub>2</sub> bonding). The

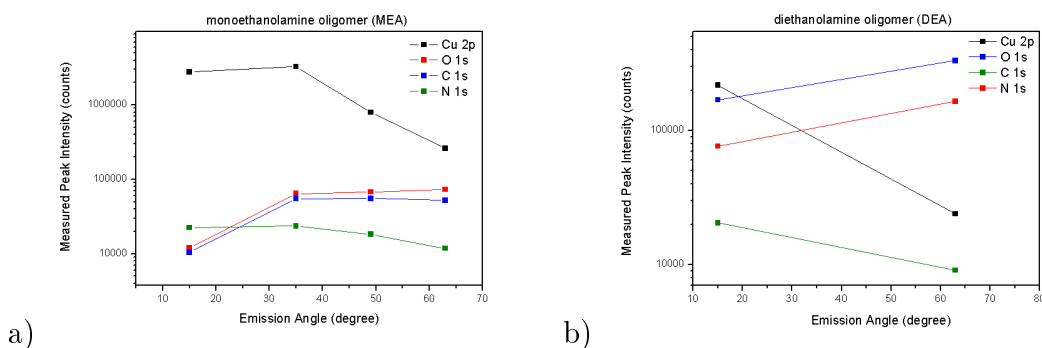


Figure 5.14: Intensity ratios of a) monoethanolamine oligomer and b) diethanolamine oligomer XPS peaks depending on the take off angle (with the surface normal)

depth distribution of the underlying one correspond to copper oxide. The last to oxygen from water used to blow up sample after deposition monolayer.

### Polish steel surface

For 100Cr6 steel sample with deposited diethanolamine oligomer monomolecular layer AR-XPS measurements showed slightly different behavior. The Fe photoelectron region of diethanolamine showed a completely different intensity ratio of the iron and the iron oxide peak (Fig. 5.15). The loss in intensity of iron peak was due to the coverage of the surface with the chemisorbed diethanolamine oligomer film. At emission angle  $63^\circ$  the Fe metal peak almost vanished in the spectra recorded from samples with diethanolamine film.

Angular resolved measurements showed that Fe 2p peak contain three iron species situated in different heights (Fig. 5.16). The peak at 706.5 eV was attributed to pure iron, and the one at 710 eV to iron oxide [93], [94]. Other peak at about 702.3 eV may result from Fe bond to nitrogen as assigned by Riviere and co-workers [95], [96].

The C1s peak as well as the O1s peak consist of three peaks. The positions of O1s peaks are: 529.2 eV attributed to iron oxides [93], [94], 531.6 eV to oxygen from water used as solvent [93], 525.6 eV to oxygen in hydroxyl group [97]. The N1s peak was found on both steel and copper samples after deposition DEA film. In both cases N1s peak consist of 2 species (Fig. 5.17). On 100Cr6 steel surface positions of N1s peaks are 398.838 eV correspond to N bond to Fe [95], [96], and 395.038 eV reported as NH-CH<sub>2</sub> [98]. Interesting is the fact that with emission angle peak intensity of NH-CH<sub>2</sub> increase, and N bond to Fe corresponding peak decrease as it is shown on Fig. 5.17.

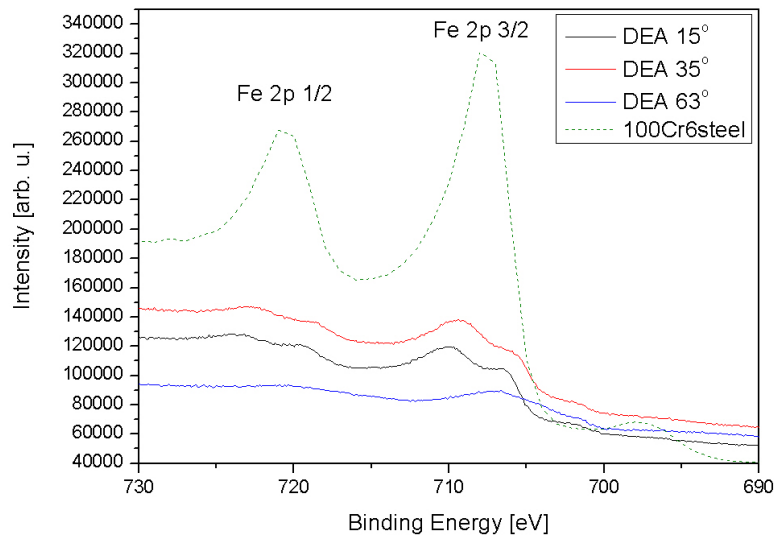


Figure 5.15: Fe 2p region of monolayers of DEA on 100Cr6 steel steel. The spectra are shown for three different electron take off angles. For comparison the spectra of clean 100Cr6 steel is also shown.

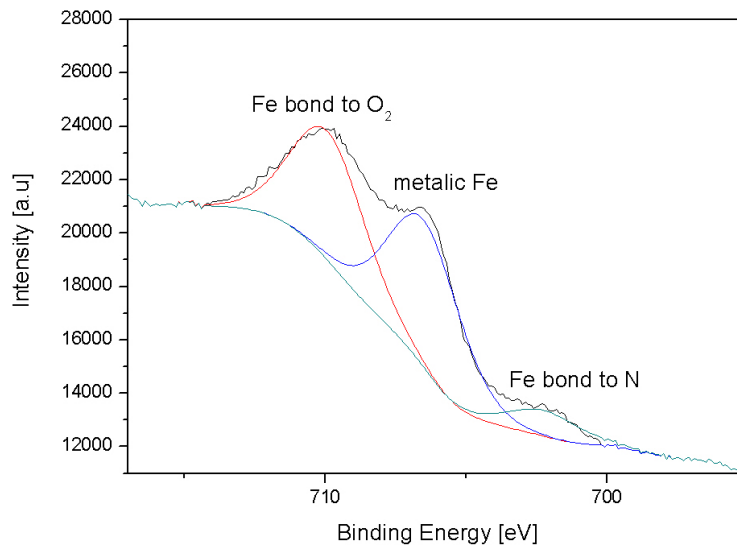


Figure 5.16: Fe 2p region of monolayers of DEA on 100Cr6 steel with emission angle  $15^\circ$ .

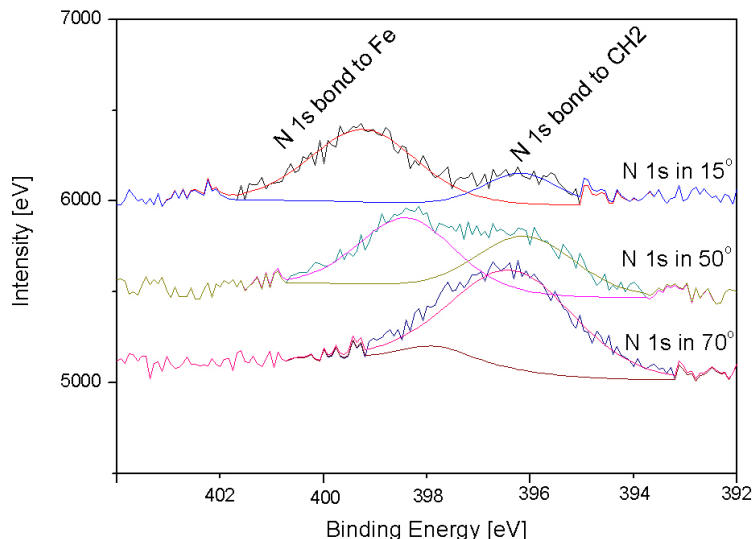


Figure 5.17: N1s region of monolayers of DEA on 100Cr6 steel. The spectra are shown for three different electron take off angles.

In case of N1s on copper surface two composites also have been observed at binding energy: 402 eV correspond to as NH-CH<sub>2</sub> as it was observed for DEA molecules [98] and 396.1 eV, this peak could not be definitely assigned. It may be result from Cu bond to nitrogen, but there was no confirmation in Cu2p peak.

Detail analysis of angular resolved measurements of peaks Cu, Fe, O, C and N confirm our theory that the molecules of diethanolamine oligomer stand upright on the surface, bound to it by the nitrogen atom.

Multi point acquisition perform with Auger Electron Spectroscopy confirm obtained results, show that the whole surface is covered by homogeneous layer of tribofilm, and Auger spectra showed C1s, N1s and O1s peaks which are the elements of ethanolamines. In the case of triethanolamine multi point acquisition performed with Auger Electron Spectroscopy and Scanning Electron Microscopy, the image shows that not a whole surface is covered by uniform layer of ethanolamine oligomer. Auger spectra in different positions showed different amounts of additives. Additionally, depth profiles were recorded with Ar ions in Auger Electron Spectroscopy. For three cases of ethanolamine oligomers, the film created on the surface was very thin and was between 1 and 2 nm. The nitrogen, carbon and oxygen peak was observed only in the first layer (see Fig. 5.18) .

Future angle resolved XPS measurements on mono and triethanolamine on copper and steel surfaces are planned, to prove chemical bonding between copper with

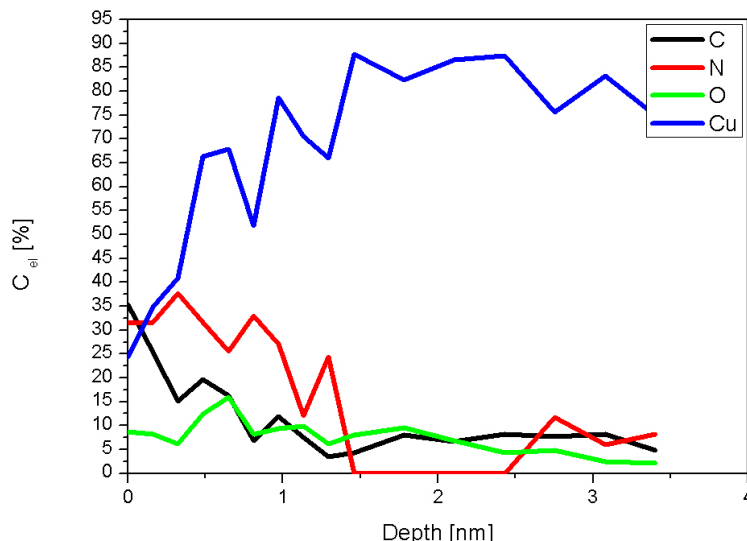


Figure 5.18: Diethanolamine oligomer film depth profile with Ar ions on AES.

nitrogen and steel with nitrogen. Future studies are needed to check chemisorption of ethanolamine oligomers on other surfaces.

### DISCUSSION, CONCLUSION AND OUTLOOK

In this paper, oligomer specific lubrication was studied. Differences in tribological behavior of the oligomers of ethanolamine have been observed by AFM, microtribometer and TOG tribometer and the chemical structure of the film by XPS. Very interesting is the fact that for copper surface is observed the same behavior of the friction coefficient for a wide range of loads, from the nano- to the micro range.

The obtained results shows that the additives undergo reactions during adsorption, and it takes only 10 minutes for the film to strongly adhere to the substrate. The lowest friction coefficient is observed for monoethanolamine oligomer, for di- and triethanolamines the friction coefficient was higher. The results show that differences in tribological behavior might be due to the orientation of hydroxyl groups on the surface. Detail analysis of angular resolved measurements of peaks Cu, Fe, O, C and N showed that the molecules of diethanolamine oligomer stand upright on the surface, bound to it by the nitrogen atom. Orientation of molecules and functional groups in this compounds have influence friction behavior. More detailed studies with all ethanolamines on steel and other surfaces shall be undertaken. Further detailed studies are necessary to link macrotribological results with information on structural chemistry obtained by XPS.

### 5.1.3 Tribological properties of additives for water-based lubricants

"*Tribological properties of additives for water-based lubricants*" [3] compares the friction, wear and corrosion performance in rolling/sliding tribological contact of additives for water lubricants with similar chemical structure such as ethanolamines, ethylamines and glycols. These studies established the mechanism how various individual additives influence tribological properties of the water system and selected the best compounds and concentrations for this purpose. XPS chemical analysis was performed before and after tribotesting to understand how the structure of the molecular film influences macroscopic tribological performance and how it changes under mechanical loading. It was concluded that in rolling contact ethanolamines do not perform as well as it was previously reported due to the formation of a thick oxidation layer, which prevent additives to penetrate it. Ethylamines - the additives which were used for comparison in rolling contact significantly improved tribological performance due to the molecules activation and formation of a mechanically durable boundary film. Glycols significantly reduced friction as it was expected, however the anti-wear and anti-corrosion behavior were unsatisfactory.

#### TRIBOLOGICAL PROPERTIES OF ADDITIVES FOR WATER-BASED LUBRICANTS

A. Tomala<sup>1</sup>, A. Karpinska<sup>2</sup>, W.S.M. Werner<sup>1</sup>, A. Olver<sup>2</sup>, H. Stoeri<sup>1</sup>

<sup>1</sup> Institut für Angewandte Physik, Vienna University of Technology, Wiedner Hauptstrasse 8-10/134, 1040 Wien

<sup>2</sup> Imperial College, Mechanical Engineering Department, Tribology Group, London SW7 2AZ

WEAR

Volume 269 , Issue 11-12, May 2010, Pages 804-810

#### ABSTRACT

Fully formulated metalworking fluids have been thoroughly described in literature. However, the influence of individual additives on tribological properties of these compositions is still not fully clear.

In this paper we present frictional, anti-wear and anti-corrosion properties for separate solutions of anti-corrosion, anti-foaming and anti-microbial agents - amines

(ethanolamine oligomers, ethylamine oligomers), friction modifiers - glycols (monoethylene glycol, 1,4-butylene glycol) and amine derivatives with longer hydrocarbon chains (3-amino-1-propanol, 4-amino-1-butanol). As a reference, we also performed some tests with pure water.

The results show that the additives used in the tests in particular concentrations significantly improve tribological properties of water. The best performance - the lowest friction and no traces of corrosion - was obtained for triethylamine. Ethylene glycol and 1,4-butylene glycol significantly reduced friction, however their anti-wear behavior was unsatisfactory. Ethanolamines, which combine properties of amines and alcohols showed an increase in friction and corrosion, but significantly reduced wear. The conclusion is that the examined additives can enhance one property of a tribosystem while adversely affecting another.

### INTRODUCTION

Water is a low cost lubricant with a high cooling capacity but its low viscosity and corrosive properties make it unacceptable for most tribological applications. In order to adjust the performance and improve the properties of water-based lubricants, high quality additives are used, such as surface/interface active molecules [99].

Applications of water-based lubricants include metalworking fluids (MWFs). Water acts as a coolant and a lubricant, thus reducing workpiece thermal deformation, improving its surface finish, assuring longer tool life and lower friction between the tool and the workpiece, and flushing away chips from the cutting zone. Depending on the application, MWFs contain additives used to perform different functions: reduce tool wear, prevent corrosion and adhesion between the tool and the workpiece. The other important issue is preventing fungal and microbial growth in MWFs, which can otherwise lead to health and safety hazards, filter plugging and other operational problems [100].

In this study, we are focusing on the series of additives such as ethanolamine oligomers, ethylamine oligomers and glycols. Ethanolamines combine properties of amines (amine group  $-NH_2$ ) and alcohols (hydroxyl group  $-OH$ ), ethylamines contain only amine groups, glycols are the compounds having OH groups on both ends of molecule. Most of them are liquid, which makes them easy to handle, and many are soluble in water, so they are suitable for water based lubricants. They may be used as emulsifying, wetting and anti-icing agents [16]. Some of them act also as anti-microbial agents. They reduce corrosion by either forming a protective coating on the metal surface or by neutralizing corrosive contaminants in the fluid by maintaining the pH in a suitable range. They are employed in a wide variety

of products such as hydraulic fluids and rolling oils, and very often as ingredients for cutting fluids [100].

Glycols are most commonly used in hydraulic applications. In metalworking fluids, they are used as friction modifiers and to stabilize concentrated MWFs, preventing the separation of their components [100].

## MATERIALS AND METHODS

In this paper, we present results for separate solutions of anti-corrosion, anti-foaming and anti-microbial agents - amines (ethanolamine oligomers, ethylamine oligomers), friction modifiers - glycols (ethylene glycol, 1,4-butylene glycol) and amine derivatives with longer hydrocarbon chains (3-amino-1-propanol, 4-amino-1-butanol, diethylamine, propylamine). As a reference, we performed some tests for the same high purity water ( $<1\text{ M}\Omega\text{m}$ , pH 7) that was used to prepare the solutions. Water purification was done by reverse osmosis and the use of purification cartridges. To ensure the repeatability of the results, multiple tests were done for each blend.

The frictional performance of the prepared solutions was measured using a Mini-Traction Machine (MTM) which creates a mixed rolling/sliding contact between a test ball and a disc [101]. Tests were performed at room temperature, under low speed (20 mm/s) and load (3 N), with SRR (Slide to Roll Ratio) 10% for a period of 1 hour. The initial disc and ball roughness was  $R_a = 0.01\ \mu\text{m}$ , and their diameters were 46 mm and 19.05 mm respectively. Specimens used were made of AISI 52100 steel (PCS instruments, London, UK). The test conditions were not meant to represent a real application but were chosen to enable a comparison of the additives within the limitations of the test rig.

Wear volume was measured using Wyko NT9100 Optical Profiler. Volume Analysis tool is included in the Vision Advanced Analysis Package, the operating software of the Wyko profiler. This method estimates the volume between the worn surface and a reference plane. The reference plane was set as the average height of the unworn area outside the wear track. The wear volume was calculated for the whole disc and only the area under the reference plane was considered.

In addition, corrosion traces were visually inspected using an optical microscope.

Fresh steel specimens with adsorbed additive layers were studied with Angle-Resolved X-ray Photoelectron Spectroscopy (AR-XPS). This adsorption method and equipment was described in the previous work [102]. XPS is an appropriate analytical method for chemical analysis of thin (less than 10 nm) films adsorbed on a surface, configuration of the molecules and chemical bindings to the substrate.

Analysis of AR-XPS data was performed using the ARCTIC software [103] using the stratification method, which allows easy calculation of the average depth and the relative quantity of material in each layer.

## RESULTS

The results show that additives used in the tests significantly improved tribological properties of water. Water caused severe corrosive pits on the track when no additive was present, as can be seen in Fig. 5.19

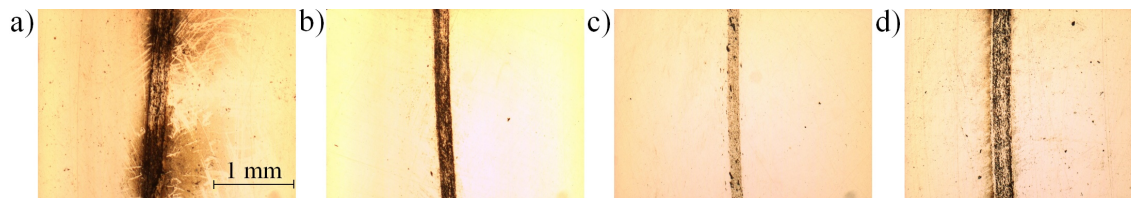


Figure 5.19: Optical microscope images of disc surface after 1 hour MTM test with (a) water (track width  $200\ \mu\text{m}$ ), (b) 0.025% monoethanolamine oligomer (MEA) solution (track width  $162\ \mu\text{m}$ ) (c) 0.05% triethylamine solution (track width  $115\ \mu\text{m}$ ) and (d) 0.05% ethylene glycol solution (track width  $176\ \mu\text{m}$ )

The concentration of the additives played a very important role. The average, stabilized, coefficient of friction for each test is shown in Fig. 5.20.

Further results presented in this paper are for the additives representing each group (ethanolamines- monoethanolamine oligomer (MEA), glycols- ethylene glycol, ethylamines- triethylamine) in selected concentrations, which gave the best performance from each group. Fig. 5.21 shows a time dependent measurement of friction coefficient for the selected additives. For triethylamine additive, at the beginning of the test friction was similar to that of pure water, but decreased with test time (after 30 min it reduced by 25%), while friction for water and MEA remained stable.

In Fig. 5.22 topography images of the disc wear tracks for water, glycol, triethylamine and monoethanolamine are shown. It is observed that the surface of the wear track is rough, and some corroded, plastically deformed or/and transferred material from the ball is present above the reference plane. For the wear volume calculation, only the area under the reference plane is considered.

Fig. 5.23 compares calculated wear volumes and measured disc wear track widths. Both Fig. 5.22 and Fig. 5.23 show that water without additives results in a high level of wear and corrosion. For ethylene glycol a considerable amount of wear and corrosion was still observed. For the additives containing amine groups (MEA and triethylamine) a significant reduction of wear was noticed, although

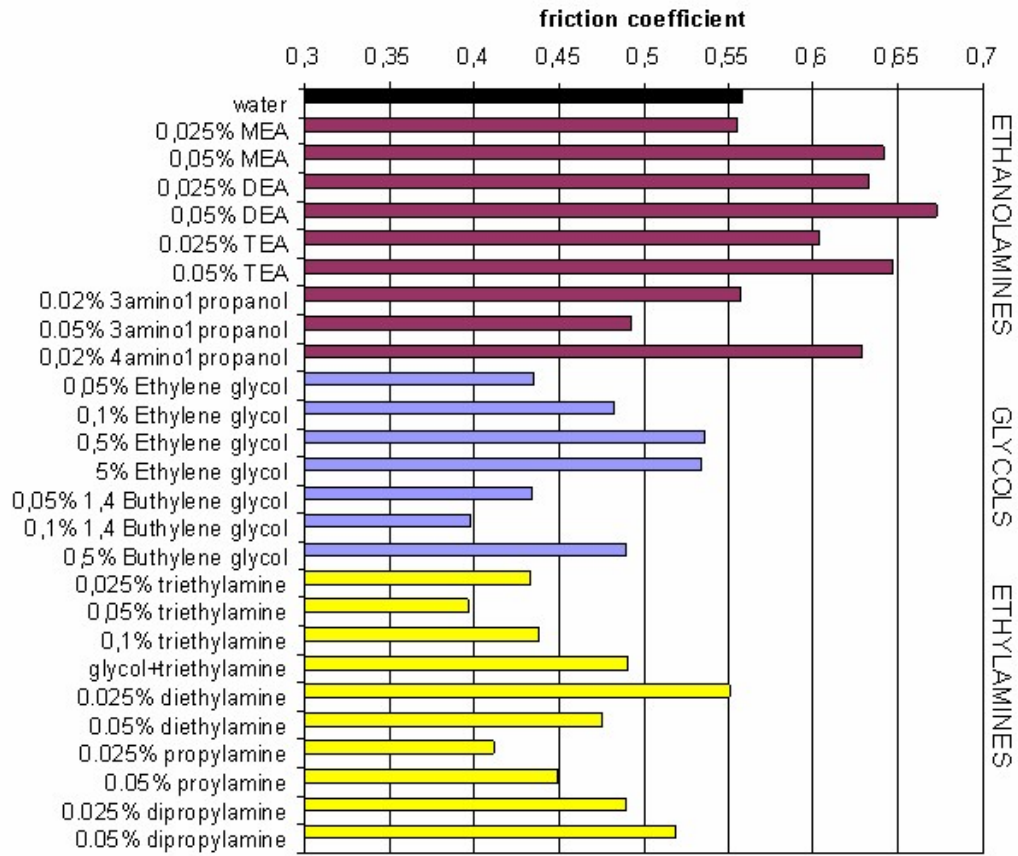


Figure 5.20: Friction results for chosen additives in different concentrations.

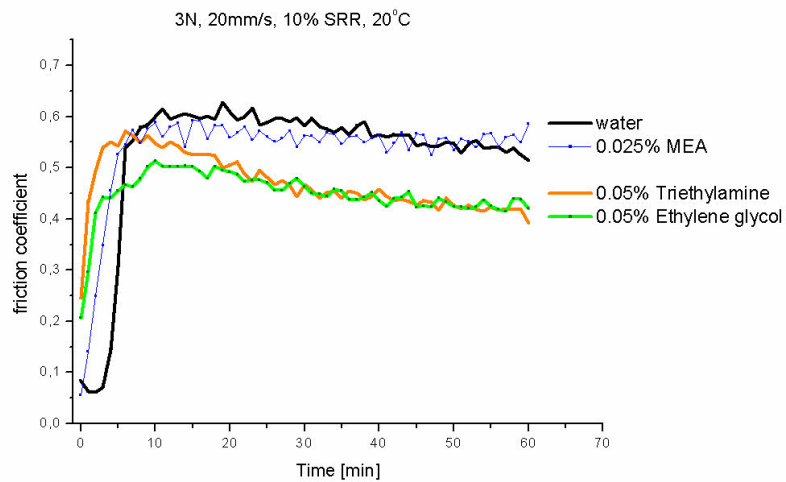


Figure 5.21: Friction results for the selected additives

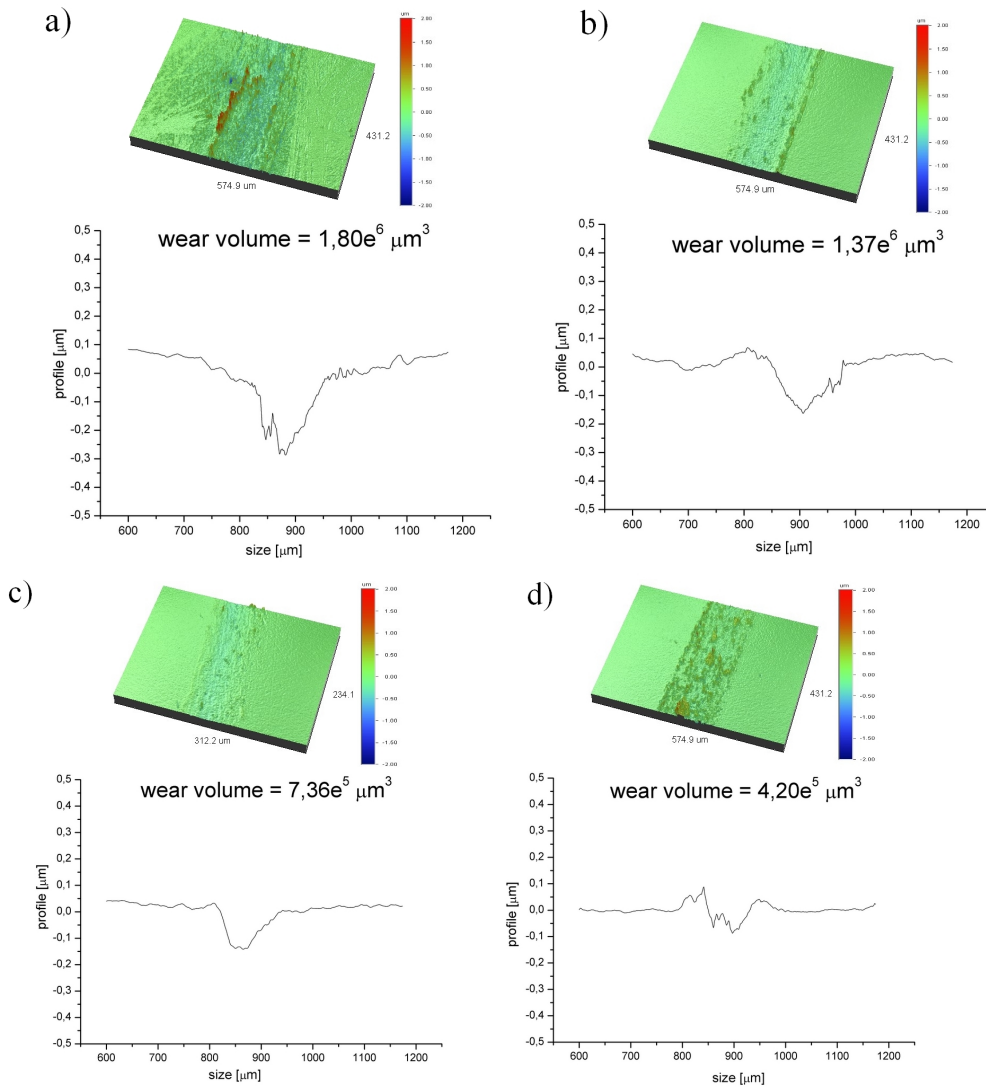


Figure 5.22: 3D topography images and profiles across the wear tracks for disc specimens after MTM tests with (a) water (b) 500ppm ethylene glycol (c) 500ppm triethylamine and (d) 250ppm MEA.

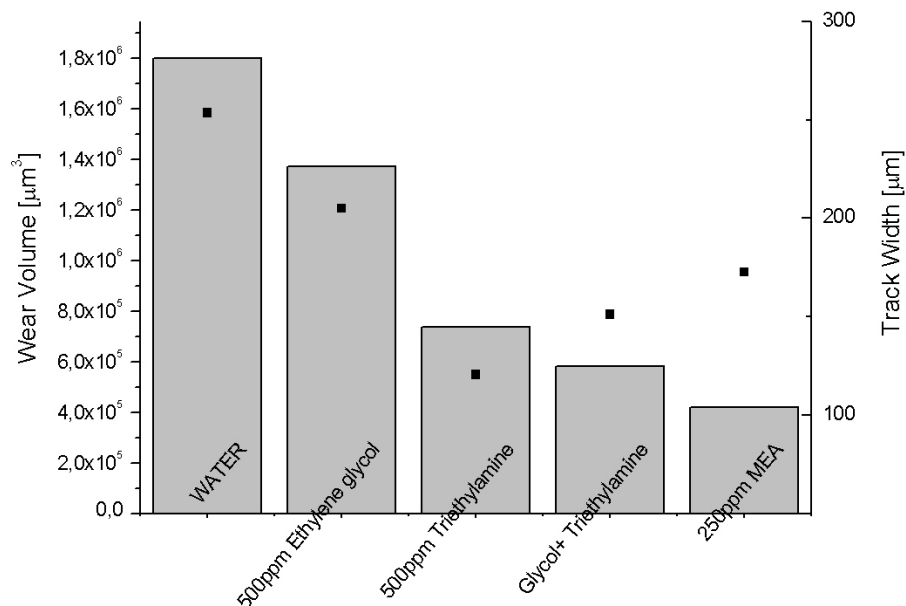


Figure 5.23: Wear results for selected additive solutions and pure water. Columns show calculated wear volume, dots indicate measured wear track widths.

for monoethanolamine a lot of corroded material was observed in the wear track. This fact is strictly linked with the pH of the tested solution. In case of aqueous systems, pH, concentration of oxygen and certain ions such as ammonium ( $\text{NH}_4^+$ ) and hydroxyl ( $\text{OH}^-$ ) ions influence corrosivity [104]. Table 5.3 lists the electrical conductivity and pH of the test fluids in those concentrations for which the best tribological results were obtained.

|                         | Electrical conductivity [MOhm] | pH   |
|-------------------------|--------------------------------|------|
| water                   | 0.9                            | 7.0  |
| 500 ppm ethylene glycol | 1.6                            | 7.5  |
| 500 ppm Triethylamine   | 0.7                            | 11.3 |
| 250 ppm MEA             | 0.8                            | 10.9 |

Table 5.3: Electrical conductivity and pH of the examined fluids.

The results of the chemical characterisation of adsorbed additives using Angular Resolved X-Ray Photoelectron Spectroscopy presented in Fig. 5.24 show that ethylamines and ethanolamines are chemisorbed on the steel surface. In case of ethanolamines the nitrogen atom from amine group is chemically bonded to the iron specimen, whereas OH groups comprise the top layer of the film, as shown

in previous work [102]. Ethylamines, which are also well known as anti-corrosion additives, adsorbed on the surface differently than ethanolamines. They are bonded to the iron oxide layer on the top of the steel substrate by the hydro-carbon chain, while the amine group stands on the top overlayer, as shown in Fig. 5.24.

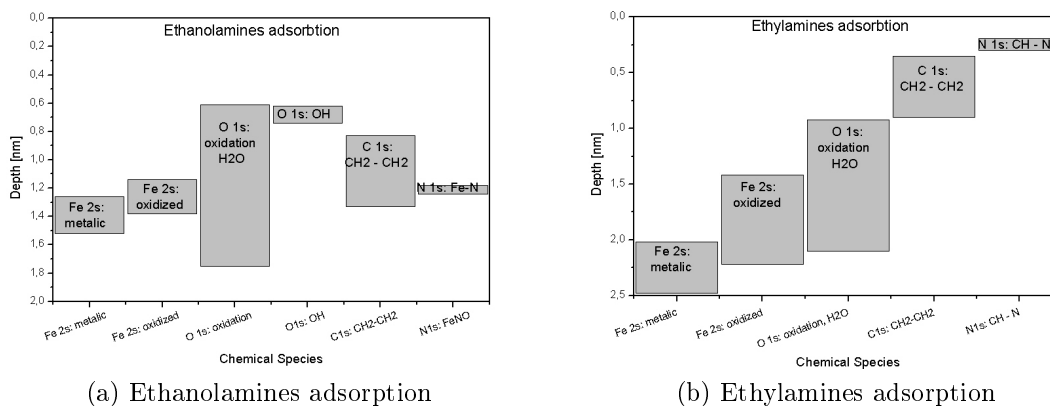


Figure 5.24: Stratification graph of chemisorbed additives. Bars indicate the depth range in which the specified chemical species are present.

An XPS chemical analysis of the wear tracks of the ball and disc specimens was conducted after the tribotests. More additive traces were detected on the ball surface, probably because the ball is subjected to more contact cycles than the disc. Additive content can be evaluated by the concentration of N 1s in the spectrum, as presented in Fig. 5.25.

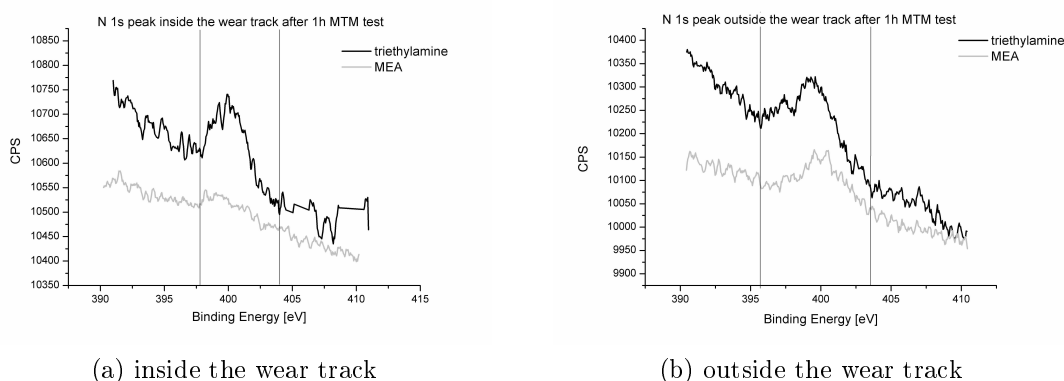


Figure 5.25: N 1s photoelectron peak as measured on the ball a) inside and b) outside the wear track for two tested additives - triethylamines - black line and monoethanolamine (MEA) - gray line.

For MEA tribotests, a lot of corrosion was observed in the wear track, indicating that the additive did not fulfil its role. Chemical analysis inside the wear track showed that almost no MEA was present, whereas for a triethylamine tribotest

a substantial amount of the additive was observed. Outside the wear track both additives were present in similar amounts.

### DISCUSSION

Ethanolamine oligomers, known for their lubricating and anti-corrosion properties [16], gave unsatisfactory results, in that the monoethanolamine oligomers did not affect the friction coefficient but the di- and triethanolamine oligomers increased it compared to pure water, as can be observed in Fig. 5.20. For these additives a lot of corrosion was observed in the wear track (Fig. 5.19). However, the wear volume in this case was very low (Fig. 5.23).

A characteristic advantage of ethanolamine oligomers is that they effectively protect steel surfaces from corrosion, that is why it was unexpected that for these additives the most corrosion was observed in the wear track, same as in case when both glycol and ethylamines were present in the solution. XPS chemical analysis in Fig. 5.25, showed that almost no additive was present on the wear track after the tribotest, while it was observed in higher concentration outside the track. On the basis of these observations, we can then propose that the additive indeed reacted with the surface but continued rolling/sliding scraped it off, leading to both wear and corrosion (tribocorrosion). A thick oxidation layer formed on the wear track, preventing ethanolamines from penetrating it. This mechanism could explain why the surface in the wear track could not be protected by the additives, whereas the clean surface outside the track stayed in perfect condition (Fig. 5.19). Thus, we can state that ethanolamines prevent corrosion in the absence of contact but are not good boundary lubrication additives.

As expected, ethylene glycol significantly reduced friction (Fig. 5.21). Even further reduction was observed for 1,4-buthylene glycol, a compound with a longer carbon chain. However, when compared to ethylamines and ethanolamines, the anti-wear and anti-corrosion behavior of the glycols is unsatisfactory. This can be seen in Fig. 5.22 and Fig. 5.23, which compare the wear results for water, ethylene glycol, triethylamine and monoethanolamine. These observations are also in good agreement with the results reported by Singh, Wan and Igari [105], [106], [107]. They stated that the use of a lubricant containing OH groups at both ends of the lubricant molecule increases the wear of aluminium, because it forms aluminium alkoxide, thus causing a decrease in the strength of the protective oxide layer.

Ethylamines gave the best overall performance, a very good corrosion protection inside and outside the wear track (Fig. 5.19), a low friction coefficient (Fig. 5.20 and Fig. 5.21) and a low wear volume (Fig. 5.22 and Fig. 5.23). Fig. 5.21 shows that ethylamines reduced friction coefficient with progressing test time. The

improved performance may be due to a better activation under rolling-sliding contact or to the formation of a more mechanically durable film. Both would be consistent with the thicker molecular film evident in the XPS results (Fig. 5.24).

### CONCLUSIONS

Various chemical compounds have been investigated as additives for water-based metalworking fluids.

The results suggest that in rolling/sliding contact hydroxyl groups (OH) present at both ends of the additive molecules increase corrosion and wear rate of the steel specimens, while amine groups on their own significantly improve tribological performance. Amine and hydroxyl groups presented together in a lubricant molecule reduced the wear rate, but corrosion within the wear scar remained substantial.

The more general conclusion is that the additives in a mixture can enhance one property while adversely affecting another. Furthermore, the presence of an amine group in additive molecules can have a big impact on a water lubricated tribosystem.

The mixture of 1,4-buthylene glycol (hydroxyl group alone) and triethylamine (amine group alone) increased friction and corrosion, while the wear rate reminded lower compared to both additives tested separately (Fig. 5.23). The mixture showed similar behavior to that of an ethanolamine solution (it combines properties of both amines and alcohols). Thus, mixing the additives, which separately gave very good friction results, did not give a better outcome.

### ACKNOWLEDGEMENTS

The work presented in this paper has been supported by the EC, Sixth Framework Programme, Marie Curie Action (WEMESURF research project entitled: "Characterization of wear mechanisms and surface functionalities with regard to life time prediction and quality criteria-from micro to nano range" under contract MRTN CT 2006 035589).

### 5.1.4 Behavior of corrosion inhibitors under different tribological contact

*"Behavior of corrosion inhibitors under different tribological contact"* presents the performance comparison of the additives for water lubricants in different tribological contact situations - rolling/sliding and severe pure sliding conditions. In this manuscript ethanolamines, ethylamines and glycols were investigated under static corrosion and tribologically induced corrosion conditions. A wide range of rolling and sliding tribocontact parameters was tested to show differences in behaviors. At the same time molecular processes which affect macrotribological performance were explained and graphically illustrated. From the experiments it was concluded that ethanolamines most efficiently reduce the static corrosion and tribocorrosion in severe sliding contact, however they do not perform well in rolling contact due to a thick oxidation layer which prevent the additives to react with the metallic surface. Ethylamines undergo filiform static corrosion, in pure sliding contact they do not perform well due to long adsorption time, thus continuous sliding shear off the molecules. Nevertheless in rolling/sliding contact, ethylamines undergoing activation causing the formation of an anti-wear boundary tribofilm. This manuscript also presents AR-XPS chemical characterization result and compare it with SESSA simulation result to confirm the accuracy and correctness of the analysis. The results showed that in both cases of ethanolamines and ethylamines the experimental results and simulation data were consistence.

#### BEHAVIOR OF CORROSION INHIBITORS UNDER DIFFERENT TRIBOLOGICAL CONTACT

A. Tomala<sup>1,2</sup>, A. Naveira-Suarez<sup>3,4</sup>, R. Pasaribu<sup>3</sup>, N. Doerr<sup>2</sup>, W.S.M. Werner<sup>1</sup>,  
H. Stoeri<sup>1</sup>

<sup>1</sup> Institute of Applied Physics, Vienna University of Technology, Wiedner  
Hauptstrasse 8-10/134, 1040 Wien, Austria

<sup>2</sup> AC2T Austrian Center of Competence for Tribology, Viktor Kaplan-Straße 2,  
2700 Wiener Neustadt, Austria

<sup>3</sup> SKF Engineering and Research Centre, Kelvinbaan 16, 3439 MT Nieuwegein,  
The Netherlands

<sup>4</sup> Division of Machine Elements, Lulea University of Technology, SE-971 87,  
Lulea, Sweden

Under submission in TRIBOLOGY LETTERS

### **Abstract**

Additives in lubrication technology perform by physically or chemically adsorbed films of tribological surface or by neutralizing pH of contaminants in the fluid. These processes are especially important in water lubricated tribosystems when the environment is very corrosive.

Ethanolamines and ethylamines are known as ligands which can form chelate bonds with metals via their amino, hydroxyl and deprotonated hydroxyl-groups. In tribology they are widely accepted, as corrosion inhibitors and detergents especially for water based lubricants. This study inquires static corrosion behavior of the solution as well as tribological performance in two types of tribotesters which represent different contact situations.

Understanding the performance of the first chemisorbed layers of additives on the work piece yields important information for the optimization of lubrication in aqueous solutions. The structure of the adsorbed compounds based on amines on the tribological surfaces was studied with usage of Angle Resolved X-ray Photoelectron Spectroscopy (AR-XPS). Analysis of the AR-XPS results was performed using stratification method, which provides information of the depth and relative amount of each element in each layer. The experimental results were compared with simulations performed with Simulation of Electron Spectra for Surface Analysis software (SESSA). The objective was to confirm the accuracy of the performed analysis.

### **Introduction**

In most tribological systems lubricated with water, materials forming the tribological contact are exposed to a very corrosive environment and therefore they are subjected to both mechanical and chemical devastation. Typical examples are orthopedic implants, chemical pumps, mining equipment, or the well-known problem of erosion corrosion of pumps and pipes carrying slurries.

Corrosive wear is defined as the degradation of materials in which both corrosion and wear mechanisms are involved. The combined effects of wear and corrosion can result in total material losses that are much greater than the effects of each process taken alone, which indicates synergism between the two processes [29]. Corrosion and wear damage to materials, both directly and indirectly, costs hundreds of billions of dollars annually. Although corrosion can often occur in the absence of mechanical wear, the converse is rarely true. Under such conditions the rate of degradation of a tribological contact cannot be predicted simply from knowledge of the wear resistance in the absence of corrosion or from the corrosion resistance in the absence of friction. The reason is that in tribocorrosion systems

the chemical and mechanical degradation mechanism are not independent of each other and synergistic effects can result in accelerated material removal. In other words, tribocorrosion affects the friction, wear and lubrication behavior of the tribosystems [30]. Normally, tribocorrosion leads to degradation of the material, but in some applications tribocorrosion can be useful for example chemical-mechanical polishing (CMP) for surface planarization and smoothing.[31]

Materials degradation due to simultaneous chemical and mechanical effects may occur under a variety of conditions such as sliding, fretting, rolling and impingement. Two or three body contact between sliding surfaces can be unidirectional such as in pin-on-disc apparatus or it can be reciprocating. Fretting is special type of tribological contact involving a reciprocating motion of small amplitude. Tribocorrosion is also observed in rolling contacts typical for ball bearings. Particle impact can result in a combined mechanical and chemical attack of the material. From a physical point of view, tribocorrosion includes a variety of mechanical and chemical degradation phenomena referred in the literature as corrosive wear, wear accelerated corrosion, erosion corrosion, oxidative wear, fretting corrosion and impingement attack [30]. In the present work, corrosion under static condition as well as tribocorrosion in both sliding and rolling contacts will be discussed.

### **Objectives**

This manuscript focuses on representative additives from Ethylamines and Ethanolamines groups known from their anti-corrosion properties. Ethanolamines combine properties of amines (amine group  $-NH_2$ ) and alcohols (hydroxyl group  $-OH$ ), while Ethylamines contain only amine groups. Water and Glycols were used as references. Glycols are the compounds having hydroxyl groups on both end of the molecule. They are known friction modifiers in water lubricating tribosystem, however having high corrosive properties. [3] The aim of this studies was:

- to compare the behavior of anti corrosion additives in static conditions and under rolling and sliding tribological contact.
- to analyze the first chemisorbed layers of additives on work piece in order to understand the structure and molecular mechanism.
- to confirm the accuracy of the experimentally performed analysis with simulated result.

The last conclusion section explains how the adsorption mechanism of the additives on surfaces lead to differences in rolling and sliding tribological performance.

## MATERIALS AND METHODS

### Additives Solutions

All experiments were performed using distilled water as a solvent. The additives were at least 98% purity (GC) and used as obtained. Groups of additives were represented by selected single additives in order to demonstrate just the exemplary results. Ethanolamine group was represented by Monoethanolamine oligomer (MEA) -  $C_2H_7NO$ , it was dissolved in concentration 250 ppm, Ethylamines by Triethylamine -  $N(C_2H_5)_3$  in 500 ppm and Glycols by Monoethylene glycol -  $HOCH_2CH_2OH$  in 500 ppm. The representative additives and their concentrations were selected based on the results obtained in previous studies [3]. Concentrations of the additives were below saturation concentration, to prevent growth of additive crystals on the surface.

### Samples used for tribological and adsorption tests

#### MTM tests

Specimens used for MTM tribotests were made of AISI 52100 steel (PCS instruments, London, UK). The initial disc and ball roughness was  $R_a=0.01 \mu m$ . The disc diameter was 46 mm and ball diameter 19.05 mm. The specimens were cleaned in an ultrasonic bath of toluene for 10 min and then in ethanol for 10 min.

#### Ball on disc tests

The steel balls (20 mm diameter) were of AISI 52100 steel with hardness 59-66 HRC and an average roughness ( $R_a$ ) of 10 nm. The rings were washers (WS 81212) from SKF Cylindrical Thrust Roller Bearings of AISI 52100 steel with hardness 59-66 HRC and  $R_a=10nm$ . The specimens were cleaned prior to testing by successive immersion first in an ultrasonic bath of toluene for 10 min and then ethanol for 10 min.

#### Adsorption test

The samples for adsorption tests were cut from SKF standard roller bearing with a cutting machine. The final size of the samples was  $0.8 \times 10 \times 3 mm^3$  and slightly exceed the size of XPS sample holders. The sheets were grounded with silicon carbide abrasive paper with a grid size from 150 to 4000 on a Struers LaboPol-4 grinding machine. Afterwards the sheets were polished with DP-Spray containing polycrystalline diamond grains until a roughness of  $R_a=10 nm$  was reached. The samples were cleaned in ultrasonic bath with toluene for 10 min and than with ethanol for 10 min.

### Methods

Tribological tests were performed using Mini-Traction Machine (MTM) to represent rolling conditions, and ball on disc to represent pure sliding conditions.

The frictional performance of fluids was measured using a Mini-Traction Machine (MTM) in which a steel ball (3/4 inch diameter) was rotated on a steel plate. MTM provides a mixed sliding/rolling contact through the independent control of the ball and disc velocities. The slide/roll ratio, SRR, is defined as the percentage ratio of the difference and the mean of the ball velocity ( $v_{ball}$ ) and disc velocity ( $v_{disc}$ ). Thus, SRR=0% ( $v_{ball}=v_{disc}$ ), represent pure rolling contact, and SRR=200% (either  $v_{ball}$  or  $v_{disc}=0$ ), represent pure sliding contact, while the values between 0 and 200% represent a mixed sliding/rolling contact. Traction coefficients were measured at room temperature (20 °C), using a slide-roll ratio (SRR) of 10%, with a speed of 20 mm/s, under loads of 3 and 10 N. One hour tests were performed with and without additives.

In ball on disc experiment a fixed 6mm ball was loaded against circulating disc. This experimental setup represents pure sliding contact between ball and a disc. Friction coefficients were measured at room temperature (20 °C), with speed 20 mm/s, under loads of 1 N (what effects in contact pressure regimes of 960 MPa). One hour test were performed for solutions with additives and some only for distilled water as a reference. Test conditions for MTM and ball on disc experiments are listed in table 5.4.

Setup of the corrosion experiments consisted of 100Cr6 steel plates completely covered with additives solutions in 20 ml glass tubes. The ratio between the metal surface (area) and the amount of solution (weight), was kept at 1:1 for all experiments, to assure the comparability between the individual results. The glass containers where kept for 65h in the oven set for 40°C.

Surface topography, section profiles and wear volume was measured using Wyko NT9100 Optical Profiler. The operating software of the Wyko profiler called Vision Advanced Analysis Package was used for graphs preparation and volume analysis. Volume analysis method estimates the volume between the worn surface and a reference plane. The reference plane was set as the average height of the unworn area outside the wear track. The wear volume was calculated for the whole disc and only the area under the reference plane was considered. In addition, corrosion traces were visually inspected using an optical microscope.

Fresh steel specimens with adsorbed additive layers were studied with Angle-Resolved X-ray Photoelectron Spectroscopy (AR-XPS). This adsorption method and equipment was described in the previous work [108]. XPS is an appropriate analytical method for chemical analysis of thin (less than 10nm) films adsorbed on a surface and the configuration of the molecules and chemical bindings to the substrate.

| Technical specification                 | Experimental Parameters  |  |
|---|--|--|
|   | Mini Traction Machine (MTM)  | Ball on disc   |
| Type of movement                        | rolling/sliding - SRR=10%  | pure sliding - SRR=200%  |
| Contact geometry                        | Non-conformal: point   | Non-conformal: point   |
| Spatial configuration                   | Horizontal disc rotation axis  | Horizontal disc rotation axis  |
| Ball diameter (mm)                      | 19.05  | 6  |
| Disc diameter (mm)                      | 46   | 40   |
| Sliding velocity ( <i>mm/s</i> )        | 20   | 20   |
| Normal load (Hertzian contact pressure) | 3 N (290 MPa)  | 1 N (960 Mpa)  |
| Track radius (mm)                       | 20   | 5  |
| Solutions                               | distilled water,<br>250 ppm<br>ethanolamine oligomer,<br>500 ppm<br>ethylamine oligomer,<br>500 ppm glycol | distilled water,<br>250 ppm<br>ethanolamine oligomer,<br>500 ppm<br>ethylamine oligomer,<br>500 ppm glycol |

Table 5.4: Technical specifications of MTM and ball-on-disc tribometers with parameters used for the tests.

Analysis of AR-XPS data was performed using the ARCTIC software [109] using the stratification method, which allows easy calculation of the average depth and the relative quantity of material in each layer.

Simulations of AR-XPS data was performed with the SESSA software (Simulation of Electron Spectra for Surface Analysis). The objective of SESSA is to help with the interpretation of AES and XPS electron spectra, and to improve the accuracy in quantification in analysis [110].

## RESULTS AND DISCUSSION

### Static corrosion studies

Corrosion tests were performed in 40 °C for 65 hours. Polished steel plates with a roughness of  $R_a \approx 10$  nm were placed in a mixture of water solution with additives. The most corrosive as we expected was pure distilled water (Fig. 5.26a), however also excessive corrosion took place in solution of Ethylene Glycol and 1,4 Buthylene Glycol as it can be seen on Fig. 5.26b. This properties of glycols was not surprising and previously reported by other researchers [111].

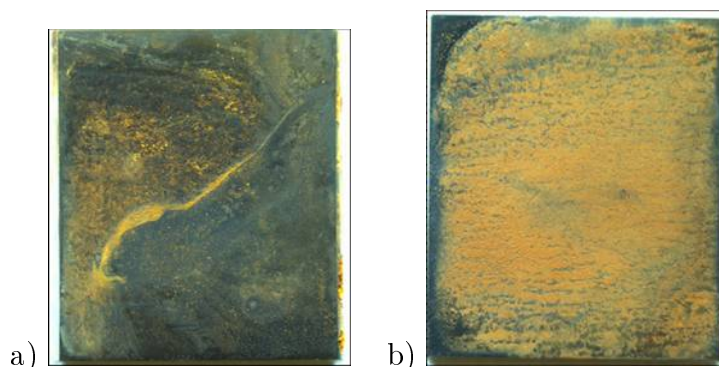


Figure 5.26: Static corrosion test performed in a)double distilled water and b)solution of double distilled water with Ethylene Glycol

For additives with amine group in the chemical structure only very small traces of corrosion were observed. For all Ethanolamines solutions (MEA, DEA and TEA) no visible corrosion was noticed in the optical microscope as can be seen on Fig. 5.27a. For all Ethylamines solutions a visible pattern on the surface was observed as on Fig. 5.27b but no traces of yellowish corrosion. This pattern represents a filiform corrosion which usually occurs on metallic surfaces coated with organic films, it starts in bulk and with time it expands to the whole surface. From the optical images presented above it can be clearly seen that Ethanolamines present best anti-corrosion protection. Additional corrosion tests for ethanolamines were performed where samples were left in solution of water with ethanolamine for

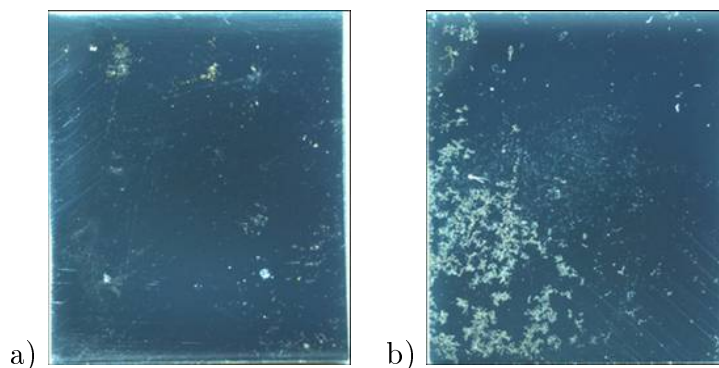


Figure 5.27: Static corrosion test performed in a) solution of double distilled water with MEA (monoethanolamine oilgomer) and b) solution of double distilled water with Triethylamine

seven days at 70 °C, they did not show any corrosion traces, however ethylamines undergo filiform corrosion all over the sample surface after 3 days. Samples which represent the lowest corrosion rates were analyzed with SEM-EDX. Ethanolamines which presented no corrosion on optical microscope images with SEM showed only very small local spots as can be observe in Fig. 5.28a. For Ethylamines, SEM images were acquired to have a closer look on filiform corrosion spots (Fig. 5.28b).

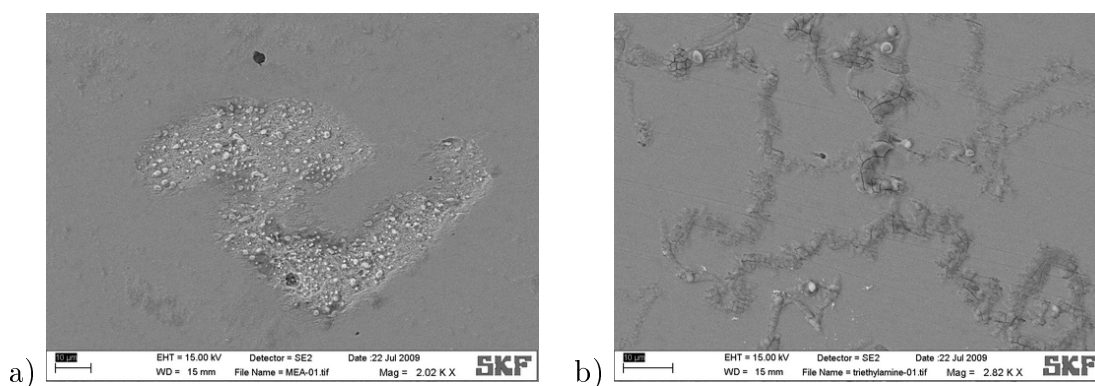


Figure 5.28: Scanning Electron Microscope images after static corrosion in distilled water solutions with a) Ethanolamines b) Ethylamines.

From the corrosion results we can assume that the ethanolamines perform as best anti corrosion additives among tested solutions, also ethylamines present good corrosion protection, however after long time filiform corrosion occurs. The SEM images show that in case of ethanolamines a few corrosive pits with approx 50  $\mu\text{m}$  diameter are presented on the surface. Inside the corrosive pits grainy structures consisting of small amount of CrC and iron oxide species are present (Fig.5.30a spectrum 3). The EDX analysis of samples after corrosion test with ethylamines show that the filiform tracks mainly consist of C and variety of iron oxide species (Fig.5.30b spectrum 1).

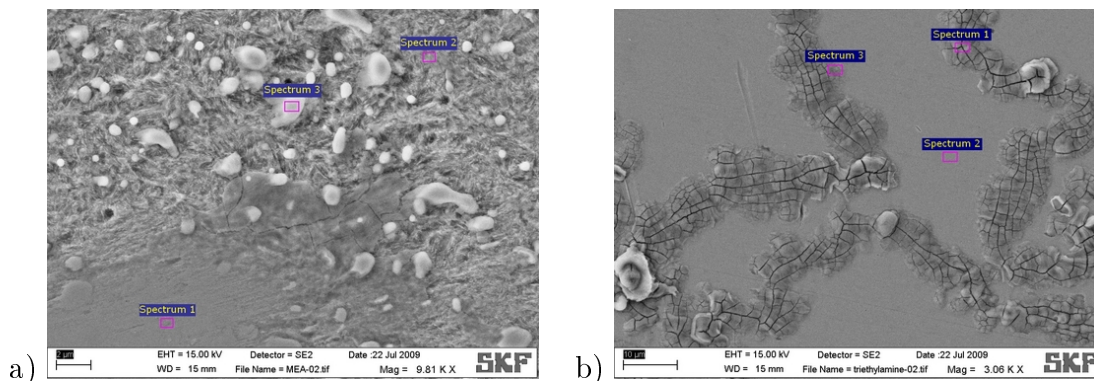


Figure 5.29: Scanning Electron Microscope  $10\mu\text{m}$  images after static corrosion tests in distilled water solutions with a) Ethanolamines b) Ethylamines.

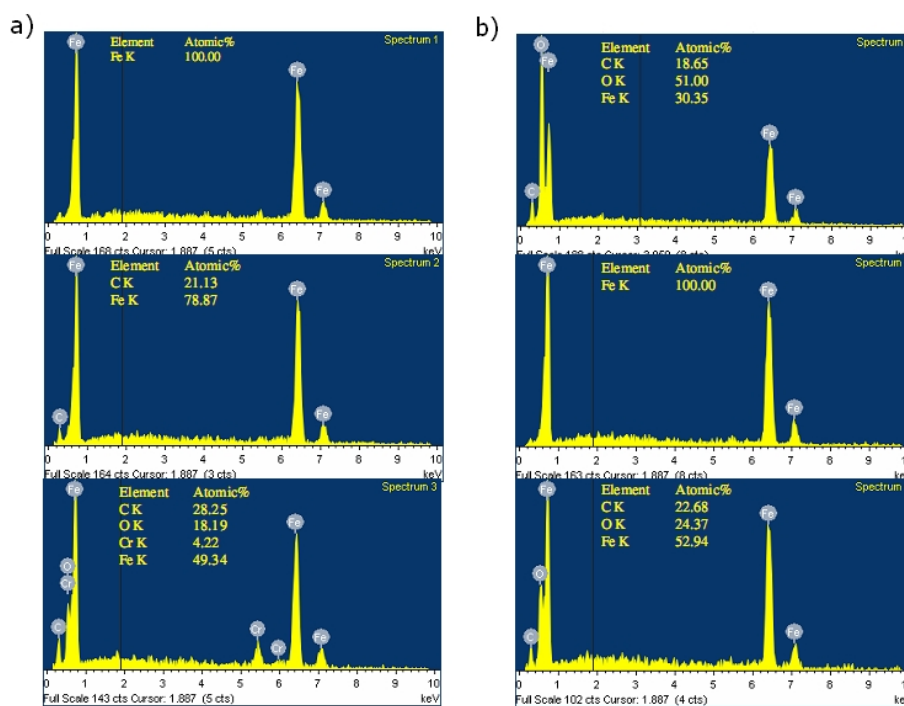


Figure 5.30: Magnified Scanning Electron Microscope images after static corrosion tests in distilled water solutions with a) Ethanolamines b) Ethylamines.

### Adsorption of Additives on Specimens - Comparison of Experimental Results with Simulated Spectra (SESSA)

One of the methods to achieve quantitative results on the near-surface structure of the material is to vary the detection angle in electron spectroscopy for depth dependent analysis. This method is known as Angle Resolved X-ray Photoelectron Spectroscopy. AR-XPS is an appropriate analytical method for chemical analysis of thin (less than 10 nm) films adsorbed on surfaces. It allows one to investigate the bondings to the substrate and configuration of the molecules by measurements of composition of different species with depth [112]. In ARXPS experiments, measurements of the intensities of selected photoelectron peaks as a function of electron emission angle are done in the range from 0 °C to 60 °C with respect to the surface normal. The measurements can be done either by simply tilting the sample or in a parallel acquisition mode (without sample tilting). In the present paper simulation of the angular distribution of the excited photoelectron lines from the steel sample covered with monomolecular layer of adsorbed corrosion inhibitors were compared with experimental data obtained from Vacuum Generators MicroLab MKII. The intensities of Fe, O, C and N species were experimentally determined for emission angles of 15°, 22°, 35°, 49° and 63° and for excitation with AlK $\alpha$ . Row area under the measured peaks was exported, next a spectrometer and sensitivity factors were extracted from these data. The angular distribution of photoelectrons distributed from samples were calculated using the NIST database for the simulation of Electron Spectra for Surface Analysis (SESSA). Calculated data were normalized in order to be able to compare it with experimental results. C 1s photoelectron peak was used as a reference peak to calculate reference ratio between measured and simulated peaks. This ratio was next used to normalize calculated SESSA results. The ratios between peak intensities measured and calculated with SESSA were compared in order to present the consistency between these results.

The results showed that the SESSA model is very close to reality. The consistency achieved in this way for major peaks of Fe, O, C and N is high. On the Fig. 5.31 a and 5.31 b comparison between experimental results (a) and SESSA simulation results (b) is shown for adsorbed Ethylamines molecules.

For Ethylamines it took about 20 minutes to adsorb on the surface to have measurable photoelectron signal from additives elements (N,C,O). Fig. 5.32 shows comparison between experimental points (points on the graphs) and simulation lines (lines on graphs) for each chemical species is presented.

On the Fig. 5.33 comparison between a) experimental results and b) SESSA simulation results for ethanolamine oligomers is shown.

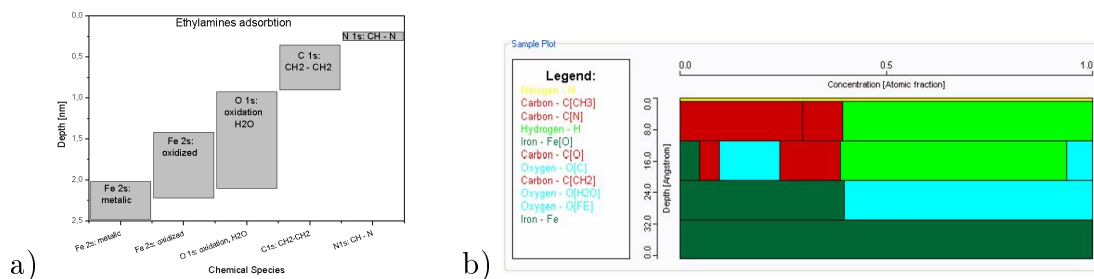


Figure 5.31: Comparison between a) molecular layers obtained from experimental result and b) user defined layer sample structure

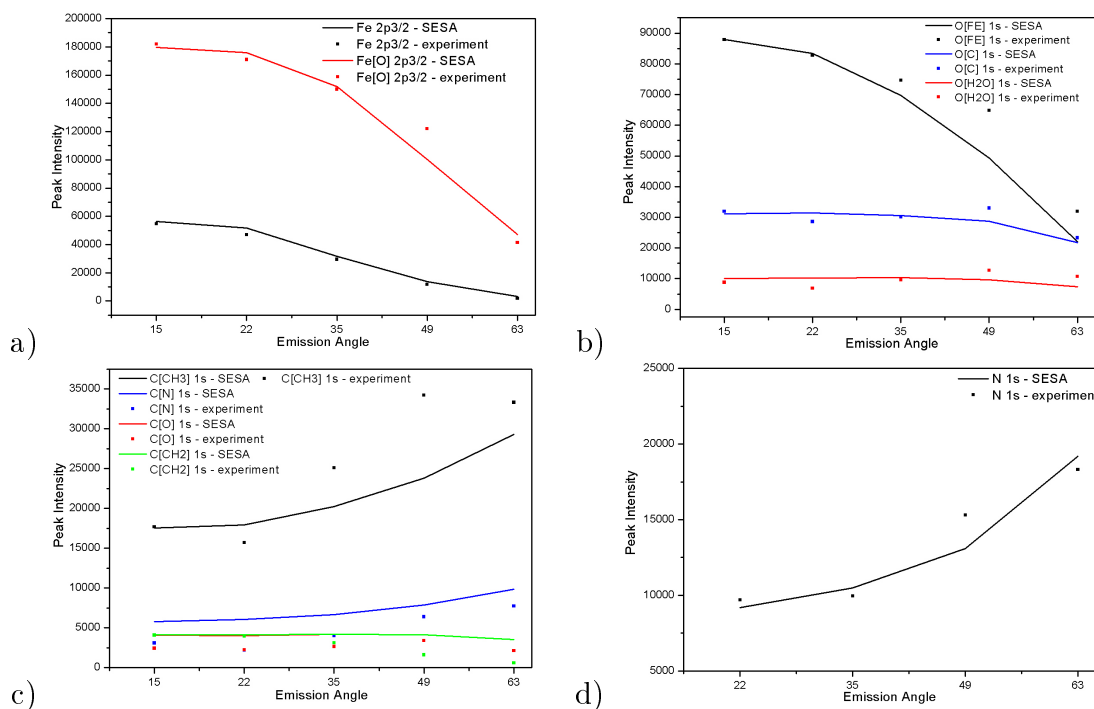


Figure 5.32: Comparison between experimental points (points on the graphs) and simulated angular distribution of the photoelectron intensity (solid curves) for each chemical element - a)Fe b)O c)C and d)N. As it can be seen the SESSA model is very close to reality. The consistency achieved in this way for major peaks of Fe, O, C and N is high.

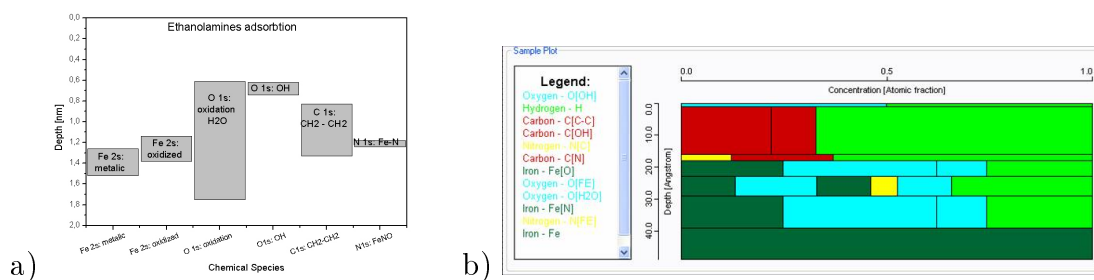


Figure 5.33: Comparison between a) molecular layers obtained from experimental result and b) user defined layer sample structure

On the Fig. 5.34 comparison between experimental points (points on the graphs) and simulation lines (lines on graphs) for each chemical species is presented.

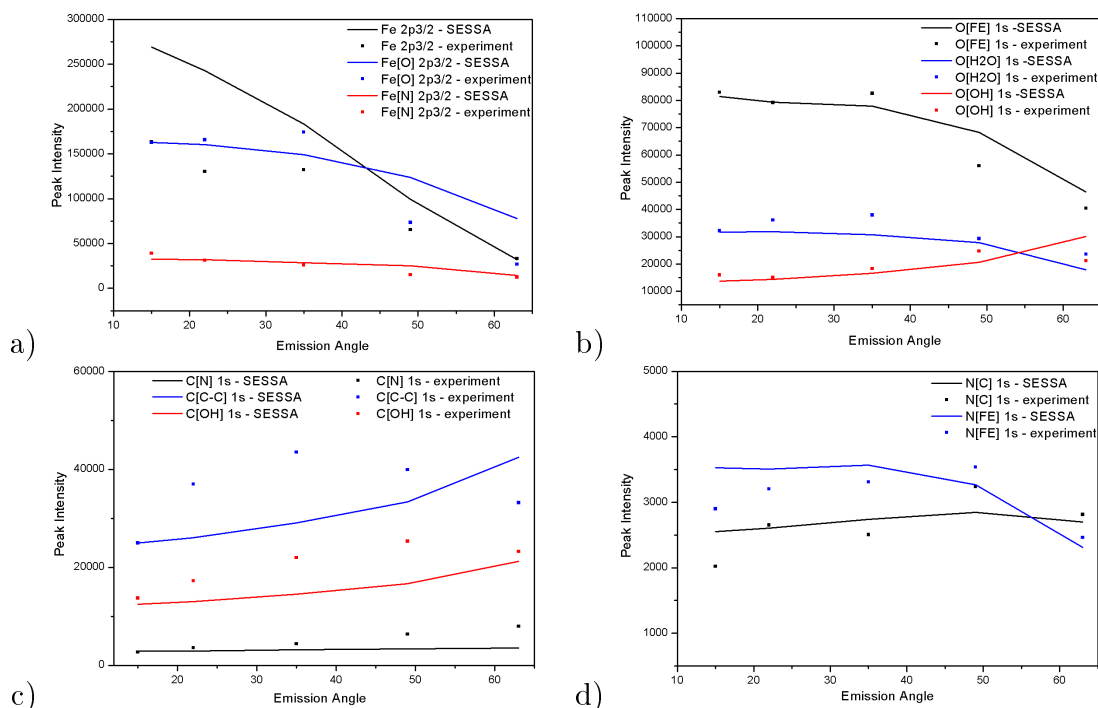


Figure 5.34: Comparison between experimental points (points on the graphs) and simulation lines (lines on graphs) for each chemical species - a)Fe b)O c)C and d)N. As it can be seen the SESSA model is very close to reality. The consistency achieved in this way for major peaks of Fe, O, C and N is high.

For both corrosion inhibitors - ethanolamines and ethylamines, experimental and simulated distributions generally agree for all analyzed detection angles. In both cases the intensities of Fe 2p and O 1s gradually decreased with the increase of emission angle (Fig. 5.32a b and 5.34 a b), indicating that they were mainly under organic species. The intensity of C 1s in case of ethylamines clearly increase (Fig. 5.32 c) and give a hint concerning the orientation of molecules. Based on the analyzed ARXPS results and SESSA simulation an adsorption mechanism can be propose like on Fig. 5.35a. The molecules ethylamines are bonded to the iron oxide layer on the top of the steel substrate by the hydro-carbon chain, while the amine group stands on the top overlayer. In case of ethanolamines the intensity change of C 1s with emission angle was not clear (Fig. 5.34 c), indicating the distribution of organic molecules is rather complicated than only one adsorbed layer. We propose that the nitrogen atom from amine group is chemically bonded to the iron specimen, whereas OH groups comprise the top layer of the film (also proved by XPS in [108]). The direct chemical reaction between Fe

and N is the reason for very good corrosion protection of this types of additives. Next layers of the molecules has the same orientation as first one, the N atom and C chain are directed towards the surface. In the literature there are available references confirms the complicated mechanism of action of ethanolamines [113, 114]. Proposed mechanism for Ethanolamines is not easy to prove with ARXPS method and SESSA simulation technique where only single monomolecular layers, which do not overlap can be easily analyzed.

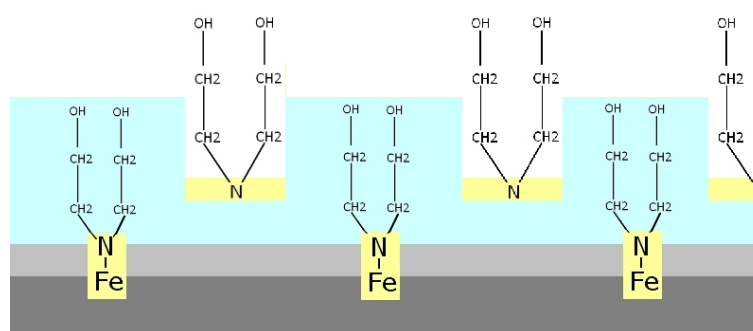
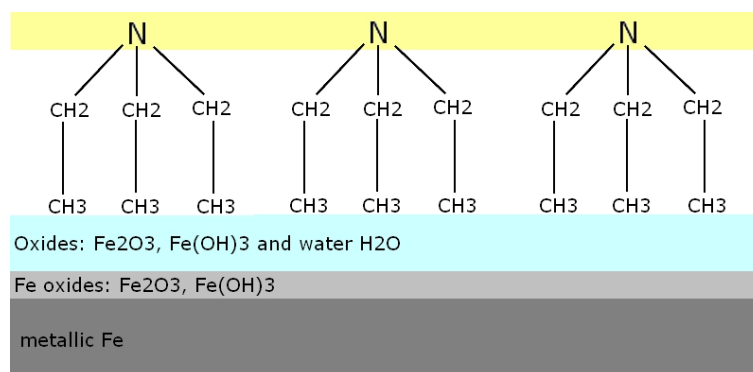


Figure 5.35: Proposed mechanism of adsorption of the a)Ethylamines and b)Ethanolimes additives on steel surface based on ARXPS experimental results and SESSA simulation results.

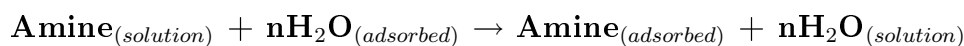
From the surface analysis data of the ethanolamines and ethylamines, it can be concluded that the adsorption of additives on the iron surface inhibits corrosion. Generally, four types of adsorption may take place involving organic molecules at the metal- solution interface [115]:

- electrostatic attraction between charged molecules and the charged metal
- interaction of unshared electron pairs in the molecules with the metal
- interaction of  $\pi$  electrons with the metal and

- a combination of the above

Inhibition efficiency depends on the number of adsorption sites and their charge density, molecular size, heat of hydrogenation, mode of interaction with the metal surface and the formation of metallic complexes [116].

The action of amine inhibitor molecules is due to the adsorption of the inhibitor molecules on an exposed metal surface. Amines may be adsorbed on the metal surface in the form of neutral molecules involving replacement of water molecules from the metal surface as:



and sharing of electron between the "N" atom of the inhibitor molecule and metal surface [117] or by the electrostatic interaction between the positively charged "N" atom and negatively charged metal surface [118, 119]. The inhibitive properties of amines are mainly dependent on the electron densities around the nitrogen atoms; the higher the electron densities at the nitrogen atom, the more effect is inhibitor. Due to adsorption, inhibitor molecules block the reaction sites and reduce the rate of corrosion reaction [120, 121].

#### **Tribological experiments**

Tribological experiments were performed with two different tribometers. Mini Traction Machine (MTM) was used to represent rolling/sliding conditions (SRR = 10%), whereas Ball on Disc was used to apply more severe pure sliding contact. Frictional behavior of tested additives is shown on Fig. 5.36. The results show that additives used in the tests significantly improved water tribological properties mainly in MTM tribological tests. High adhesive properties of water cause severe corrosive pits on the track when no additive is present. The concentration of the additives plays very important role. Most additives gave good results for concentration range of 250-1000 ppm, while higher concentrations increased friction and corrosion.

In the rolling/sliding contact the effect of additives is more pronounced than in case of pure sliding contact (Fig. 5.36). Additionally the results obtained with MTM tribometer where rolling/sliding conditions were applied were repeatable, what was not the case with ball on disc experiments. We assume that the conditions applied with ball on disc (pure sliding contact) were too severe for water lubricated system. As can be seen from Fig. 5.36 a in rolling contact Ethanolamines gave almost no reduction of friction compared to water, however Ethylamines and Glycols show visible reduction of friction coefficient. In case of sliding conditions - Fig. 5.36 b where test were not reproducible none of additives gave a significant friction reduction.

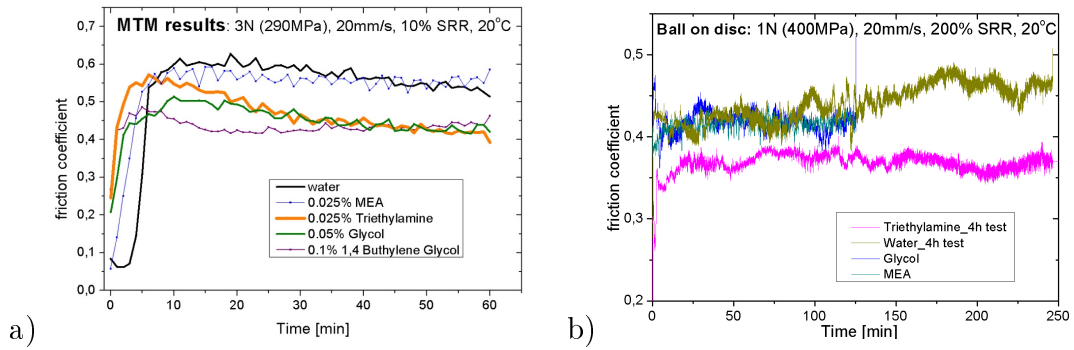


Figure 5.36: Frictional performance of additives in water lubricated system a) rolling/sliding contact with Mini Traction Machine and b) pure sliding contact with Ball on Disc.

As can be observed from Fig. 5.36 the frictional performance of the additives is highly dependent on the applied conditions, mainly on type of tribocontact situation.

Figure 5.37 shows optical profilometer scans of the worn surfaces of the steel discs that resulted from Mini Traction Machine tests. The specimens were exposed for 1 h tribotests in a) ethanolamine solution b) ethylamine solution c) pure water d) glycol solution. The profiles show beside many fine grooves also buildup tribocorrosive clues over entire wear track surface, typical of rolling corrosive wear.

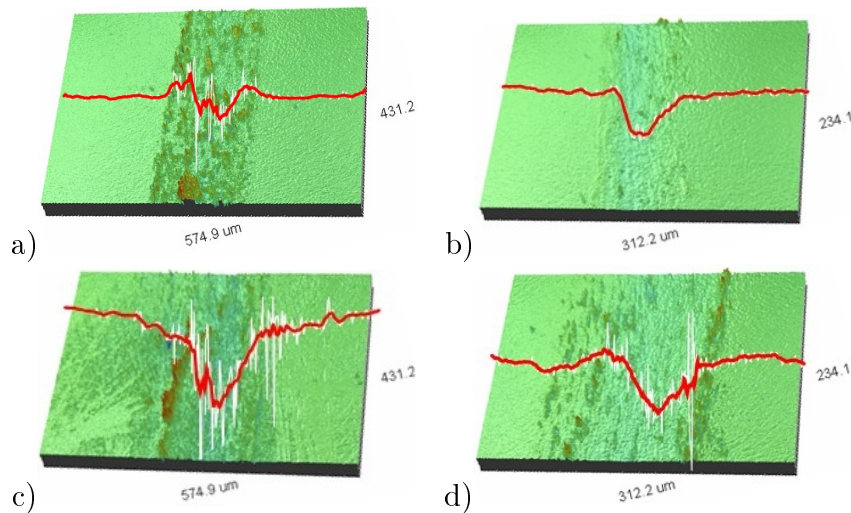


Figure 5.37: Wear track Wyko profiles after tribotest with Mini Traction Machine (rolling/sliding tribocontact) in water environment with additives. The wear volume for the solution of a) ethanolamine is  $V=2.5e^4 \mu\text{m}^3$  b) ethylamine is  $V=6.6e^3 \mu\text{m}^3$  c) pure water is  $V=1.5e^5 \mu\text{m}^3$  d) glycol is  $V=4.5e^5 \mu\text{m}^3$ .

In rolling conditions **ethanolamine oligomers**, which are known for their anti-corrosion properties, gave unsatisfactory results (increase of friction coefficient (5.36a), and tribocorrosion on wear track (5.37a) was observed). As expected, ethylene glycol significantly reduced friction (5.36a). However, when comparing to ethylamines, which gave the best overall performance, their anti-wear behavior is unsatisfactory.

For **ethylamines** continuous rolling-sliding on Mini Traction Machine improved additive activation what resulted in lower friction, wear and no corrosion traces (5.36a and 5.37b). Previous studies [3] showed that ethylamines form a mechanically durable tribofilm in mild rolling contact due to molecules activation.

Figure 5.38 shows the worn discs after ball on disc tests in a) ethanolamine b) ethylamine c) pure water and d) glycol environment. The specimens exposed for 1 h in the water with additives test present many fine grooves over its entire wear track surface, typical of cutting wear. Figures 5.38 indicate a deformation wear mechanism and wear acceleration due to tribocorrosion.

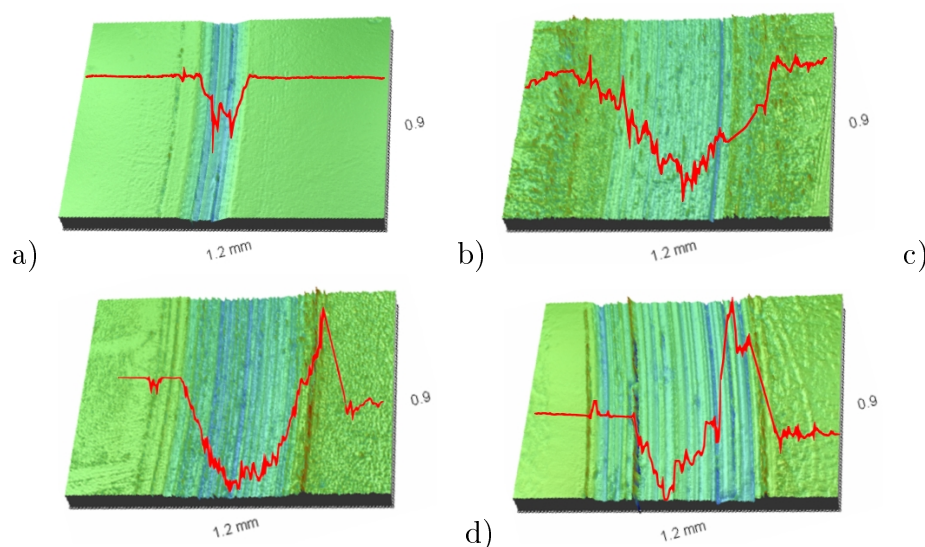


Figure 5.38: Wear track Wyko profiles after tribotest with Ball on disc (pure sliding condition) in water environment with additives. The wear volume for the solution of a) ethanolamine is  $V=1.2e^5 \mu\text{m}^3$  b) ethylamine is  $V=5.3e^5 \mu\text{m}^3$  c) pure water is  $V=6.8e^5 \mu\text{m}^3$  d) glycol is  $V=4.5e^5 \mu\text{m}^3$ .

In sliding conditions with ball on disc apparatus the additives are sheared off from wear track during continuous sliding operation, and their performance on the surface depend on their adsorption time. From ball on experiment on Fig. 5.36b it can be seen that none of additives gave significant reduction of friction coefficient. Only ethanolamines gave visible reduction of corrosion and wear on steel specimen

on Fig. 5.38a. This fact can be explained based on above described studies: we know that ethanolamines very easily adsorb on fresh steel surface. During ball on disc experiment the oxidation layer is sheared off and the ethanolamines immediately adsorb on the fresh iron surface, thus protect it from corrosion and wear.

For ethylamines additive it takes approximately 20 min to adsorb on the specimens, thus in sliding contact once the ethylamines are removed from substrate they have no time to re-adsorb and perform their role again. That is why extensive tribocorrosion is presented on the wear track (5.38b).

### CONCLUSION AND SUMMARY

Within these studies the additives for water lubricating tribosystems were analyzed under static corrosion and tribologically induced corrosion conditions. Wide range of rolling and sliding tribocontact parameters were tested to show differences in behaviors. At the same time a molecular processes which affect macrotribological performance were explained and graphically illustrated.

#### Corrosion and adsorption mechanism:

Ethylamines and ethanolamines show very good corrosion protection, however ethylamines have a tendency to grow filiform corrosion, which can also lead to failure of tribological system. Chemical analysis with AR-XPS showed that for ethylamines it takes approximately 20 min to absorb on metals surface (detectable signal), however ethanolamines adsorb immediately after placing sample in solution. Analysis of molecular structure with AR-XPS and SESSA showed that the molecules of ethylamines are bonded to the iron oxide layer on the top of the steel substrate by the hydro-carbon chain, while the amine group stands on the top overlayer. In case of ethanolamines, the distribution of organic molecules is not homogeneous and not only one adsorbed layer is presented on the surface. The nitrogen atom from amine group is chemically bonded to the iron specimen, whereas OH groups comprise the top layer of the film.

#### Tribological performance:

As a most general conclusion we can state that good performance of additives in water lubricated tribosystems depends on tribotesting conditions. Ethylamines give best tribological performance in rolling contact, however under sliding conditions they do not affect friction, additionally corrosion and wear is higher compare to rolling conditions. Ethanolamines in sliding and rolling conditions do not affect

friction compare to water, otherwise it gave most reduction of corrosion and wear for steel specimens in sliding, but not in rolling contact. Glycol does not reduce friction in sliding, like it did in rolling contact, corrosion and wear behavior are comparable to pure water.

Chemical analysis after tribotests and explanation of the mechanism:

Chemical analysis on specimens after rolling tribotesting showed that ethylamines concentration increased compare to adsorption test. The amount of ethylamines on the wear track is higher than outside the wear track - this indicates that a better activation under rolling-sliding contact or to the formation of a more mechanically durable film takes place what also leads to the improved performance of these additives under rolling contact.

During ball on disc experiments due to severe sliding conditions the ethylamine adsorbed molecules are scrapped off from the surface after first circle. Continuous sliding does not let the molecules to re-adsorb again on the wear track because for ethylamines it takes 20 min to adsorb. This process leads to extensive wear and tribocorrosion on the wear track, and no additive effect on friction. Inside the wear track the amount of ethylamines is lower than outside the wear track, what proves above described mechanism explanation.

Ethanolamines very easily adsorb on fresh steel surface (bonded to Fe with N group) which protects the surface from corrosion. After MTM rolling tribotests it was unexpected that for these additives the most corrosion was observed in the wear track. XPS chemical analysis, showed that almost no additive was present on the wear track after the tribotest, while it was observed in higher concentration outside the track. On the basis of these observations, we can then propose that the additive indeed reacted with the surface but continued rolling/sliding scraped it off, leading to both wear and corrosion (tribocorrosion). A thick oxidation layer formed on the wear track, preventing ethanolamines from penetrating it. This mechanism could explain why the surface in the wear track could not be protected by the additives, whereas the clean surface outside the track stayed in perfect condition. Thus, we can state that ethanolamines prevent corrosion in the absence of contact but are not good boundary lubrication additives.

In case of tribotests with ball on disc and pure sliding conditions iron oxide is removed from the track after first cycle and exposing pure metallic surface. The Ethanolamines additives very easily adsorb on the exposed surface of the track, thus protecting it from corrosion and reducing the tribocorrosion on wear track.

SESSA simulations:

We can certainly state that SESSA is an efficient tool for the simulation of ARXPS data for adsorbed molecular layers of additives on surface. We found excellent agreement of calculated and measured photoelectron signals from homogeneous monolayers of ethylamine additives. In case of ethanoloamines additives the layer is not monomolecularly thin and it is not homogeneously distributed, thus data analysis is more difficult however as we showed still possible.

#### **ACKNOWLEDGEMENTS**

The work presented in this paper has been supported by the EC, Sixth Framework Programme, Marie Curie Action (WEMESURF research project entitled: "Characterization of wear mechanisms and surface functionalities with regard to life time prediction and quality criteria-from micro to nano range" under contract MRTN CT 2006 035589). The authors are grateful to Ghazala Tasneem and Werner Smekal from the Institute für Angewandte Physik, Vienna University of Technology, for their valuable help with SESSA simulations.

## 5.2 Effect of ZDDP Additives on Rolling Bearings

Work presented in this subsection is based on collaboration with SKF - the market leading bearing company in particular with Engineering and Research Center engaged in research on improvements of the bearing performance.

### 5.2.1 Effect of Base Oil Polarity on Micro and Nano Friction Behavior of Base Oil + ZDDP Solution

*"Effect of Base Oil Polarity on Micro and Nano Friction Behavior of Base Oil + ZDDP Solution"* [4] presents the effect of base oil polarity on the ZDDP molecular behavior (boundary film formation) and friction performance of steel-steel contacts lubricated with two reference base oils (hexadecane - non polar and diethyleneglycol - polar) blended with different concentrations of the ZDDP (zinc dialkyldithiophosphate). The results showed that non polar base oil (HeD) ZDDP solutions generates a reaction layer more rapidly and thicker than that of polar base oil (DEG) ZDDP solutions. This fact is related with the molecular polarity - polar ZDDP molecule will compete with polar oil molecules to get a place on substrate, thus the probability that ZDDP molecule reach and react with steel surface is smaller than in case when it is dissolved in non-polar base oil. It was also concluded that AFM scanning in base oil containing ZDDP with high loads and high speeds did not lead to the build-up of an anti-wear film. The reason is that the single asperity contact temperatures during AFM scans are much lower compare to those presented in real machine parts.

#### EFFECT OF BASE OIL POLARITY ON MICRO AND NANO FRICTION BEHAVIOR OF BASE OIL + ZDDP SOLUTION

A. Tomala<sup>1</sup>, A. Naveira-Suarez<sup>2,3</sup>, I.C. Gebeshuber<sup>1,4,5</sup> and R. Pasaribu<sup>2</sup>

<sup>1</sup> Institut für Angewandte Physik, Vienna University of Technology, Wiedner Hauptstrasse 8-10/134, 1040 Wien, Austria

<sup>2</sup> SKF Engineering and Research Centre, Kelvinbaan 16, 3439 MT Nieuwegein, The Netherlands

<sup>3</sup> Division of Machine Elements, Lulea University of Technology SE-971 87, Lulea, Sweden

<sup>4</sup> Institute of Microengineering and Nanoelectronics, Universiti Kebangsaan Malaysia, 43600 UKM Bangi, Malaysia

<sup>5</sup> AC<sup>2</sup>T Austrian Center of Competence for Tribology, Viktor Kaplan-Straße 2,

2700 Wiener Neustadt, Austria

TRIBOLOGY - Materials, Surfaces & Interfaces

Nano-tribology Special Issue

Volume 3, Number 4, December 2009, Pages 182-188

KEY WORDS: ZDDP, base oil polarity, friction

### ABSTRACT

Ball-on-disc tribometer and atomic force microscopy were used to analyze the effect of base oil polarity on the friction behavior of steel-steel contacts lubricated with base oil + zinc dialkyldithiophosphate (ZDDP) solutions. Understanding the lubrication properties of the first chemisorbed layer of additives on work pieces yields important information for the optimization of lubricant formulation, in particular with regard to the type of additive and amount needed. To characterize the influence of base oil polarity, two reference base oils (hexadecane - non polar and diethyleneglycol - polar) were blended with different concentrations of C4-ZDDP, and the solutions were tested. A monolayer of base oil/additive solution was deposited on an AISI 52100 steel plate and scanned in AFM contact mode under various rubbing times and applied load conditions. An AFM technique was developed to estimate the microscopic values of friction coefficients showing how the oil polarity contributes to the differences in friction behavior of the solution due to the addition of ZDDP. With different base oils (hexadecane - non polar base oil and diethyleneglycol - polar oil) we observed significant different friction behaviors (in micro scale and nano scale) due to the addition of ZDDP compared to the base oil alone. This observation may be attributed to the contribution of base oil to transport the ZDDP additive onto the surface which will be discussed in more details in the paper. This results display the importance of base oil polarity on the friction behavior of formulated lubricants containing additives.

### INTRODUCTION

Commercially available lubricants are formulated products composed of a base oil (or base stock), which is either mineral or synthetic, and a functional additive package designed to achieve a required performance for a specific application [122]. Zinc dialkyldithiophosphates (ZDDP) have been widely used in the past decades as additives in engine lubrication oil. ZDDP was initially used as an antioxidant, but their excellent antiwear properties were quickly recognized. They can also act as mild extreme pressure agents and corrosion inhibitors. ZDDP additives have also been the object of a great deal of research due to their multifunctional performance and the complexity of the mechanisms that lead to it. The antiwear properties of

ZDDP additives arise from their ability to interact chemically with rubbing metal surfaces to form a protective layer. The additive decomposes under certain conditions and that decomposition products react to generate a 50-150 nm thick layer [123–125]. The structure and chemical composition of the layer has been analysed using advanced spectroscopy techniques such as X-ray photoelectron spectroscopy (XPS) [126–129], Auger electron spectroscopy (AES) [130, 131], and X-ray absorption near-edge spectroscopy [132, 133] and found to be dependent on temperature and tribological conditions. The layers are composed of a mixture of short- and long- polyphosphates [134, 135] with the presence of sulfides and oxides in the in the layer bulk [136]. A two-layer structure for the ZDDP-derived reaction layers has also been proposed, where a thin long-chain zinc poly(thio)phosphate layer is superimposed on a thicker short-chain mixed Fe/Zn polyphosphate layer, containing embedded nanocrystallites of ZnO and ZnS [137]. However several studies have proved ZDDP to have detrimental effects on wear under certain operation conditions [138], and to enhance friction when the system is operating in mixed and boundary lubrication regimes [139, 140].

Friction and wear of tribological systems depend strongly on the chemical and physical properties of atoms and molecules of the interface between the contacting surfaces in lubricated contacts [141], therefore it is necessary to study the surfaces at the atomic level to understand the effect of ZDDP additives on tribological performance. Atomic force microscopy (AFM) allows the study of surfaces at the nanoscale, providing a method of measuring ultra small forces between a single asperity probe tip and the surface of the sample. AFM has become a widely-used tool in tribology to study dry lubricant films (i.e. coatings) and also films formed by liquid lubricants. Concerning the latest, AFM can provide information of the morphology and topography [142–144] of reactions films formed by lubricant. Recording simultaneously lateral and height signals from the scanning tip, topography and friction can be obtained in the same time. By recording pull off forces, adhesion, elastic and viscoelastic properties of the additive-derived layer can be investigated [145]. However the technique has not been previously used to provide an insight on the initial stage of additive molecules attaching to the surface and their friction behavior. The base oil polarity has proven to play an important role in the formation [146] and characteristics [147] of ZDDP-derived reaction layers. The present study explores the use of atomic force microscopy to provide information on the relation between the friction behavior of ZDDP derived reaction layers formed on tribological specimens under conditions matching the real conditions in bearing applications (macrotribological tests) and the fric-

tion resulting from using the AFM tip as a simulation for an asperity contact [148]. The objective is to characterize the origin of the differences observed in friction behavior for tribological tests when ZDDP is blended in oils with different polarity.

## EXPERIMENTAL

### Macro-tribological test

#### *WAM5 ball-on-disc test rig*

WAM5 ball-on-disc test rig (Wedeven Associates Inc., Edgmont, PA, USA) was utilized to evaluate the tribological performance of additive-base oil blends at controlled temperature, load, entrainment speed and slide-roll ratio (SRR). The ball and the ring are driven independently by motors allowing controlled slide-roll ratio.

#### *Test samples*

The steel balls (20 mm diameter) were of AISI 52100 steel with hardness 59-66 HRC and an average roughness (Ra) of 10 nm. The rings were washers (WS 81212) from SKF Cylindrical Thrust Roller Bearings (CRTB) of AISI 52100 steel with hardness 59-66 HRC and Ra=100 nm. The rings are assembled in a holder to attach them to the rotating shaft of the test rig. The specimens were cleaned prior to testing by successive immersion first in an ultrasonic bath of petroleum ether for 10 min and then acetone for 10 min. In order to study the influence of base oil polarity on tribological performance two low-viscosity model base oils were selected: one polar oil, diethyleneglycol diethyleter (DEG) and one non polar oil, n-hexadecane (HeD), both by Acros Organics, NJ, USA. Iso-butyl-zinc dithiophosphate (ZDDP), 99% purity by A&S Chemie, Tübingen, Germany, was employed in simple solution in both base oils without other additives present.

#### *Test conditions*

Base oil polarity effect on ZDDP behavior was studied in mixed rolling/sliding contact. The tribological tests were carried out at applied normal loads of 100 and 600N, resulted in a maximum Hertz contact pressure of 1.34 GPa (contact diameter 0.38  $\mu\text{m}$ ) and 2.43 GPa (contact diameter 0.69  $\mu\text{m}$ ). The slide-roll ratio (SRR) was set constant at 0.05. (The slide-roll ratio is defined as sliding speed, or entrainment speed,  $US = UB - UR$  divided by the rolling speed,  $U = (UB + UR)/2$  where UB and UR are the ball and ring surface speed in contact respectively). The entrainment speed was set at 0.5 m/s. Temperature for all the tests was set constant at 90°C. The tests were conducted for 1 hour rubbing time. Pure base oil and two different concentrations, 2 and 5 wt% ZDDP, were tested. Under these conditions the elastohydrodynamic film thickness is calculated at the centre of the contact to be  $\approx 10\text{nm}$  for the different systems which indicates that the system is

operating in the boundary lubrication regime.

### Nano-tribological test

#### *Atomic Force Microscopy*

Measurements were performed with an AFM MFP-3D atomic force microscope (by Asylum Research, Santa Barbara, CA, USA) in contact, constant force mode using non conductive silicon nitride cantilevers with a spring constant  $k = 0.2 \text{ N/m}$  and a resonant frequency  $f_0 = 38 \text{ kHz}$  (Veeco Instruments, Santa Barbara, CA, USA). Cantilever specification are given in Tab. 5.5

|                             |                           |
|-----------------------------|---------------------------|
| Material                    | Silicon Nitride           |
| Thickness (t)(Nom)          | 0.6 $\mu\text{m}$         |
| Thickness (t)(RNG)          | 0.59 - 0.61 $\mu\text{m}$ |
| Bottom Layer Back           | 15 nm of Cr               |
| Tip Specification           |                           |
| Geometry                    | Cast                      |
| Tip Height (h)              | 2.5 - 3.5 $\mu\text{m}$   |
| Tip Radius (Nom)            | 20 nm                     |
| Length (L)( $\mu\text{m}$ ) | 140                       |

Table 5.5: Cantilever Specification

#### *Test samples*

The steel plates used were of AISI 52100 steel with hardness 59-66 HRC and an average roughness (Ra) of 10 nm. The same base oils and additives used for the macro-tribological were tested.

#### *Test conditions*

The main measurement parameters were: a scan size from  $5 \times 5$  to  $80 \times 80 \mu\text{m}^2$  (512 scan points and 512 scan lines), a scan rate from 0.5 to 2 Hz, scan angle of  $90^\circ$ , and a set point from 10 nN to 50 nN in contact mode. The recorded data was both trace/retrace of height, deflection, and lateral force. Force curves (cantilever spring force as a function of z-piezo extension) were also determined at fixed positions on the specimens. Away from the specimen the lever maintains its free deflection, and first makes a surface contact at S ("snap-in"). In air, this initial contact is frequently with a surface layer of adsorbed water vapour or other contaminants, and is accompanied by formation of a meniscus around the tip-surface contact. Retraction of the lever results in an increasing cantilever spring force acting against the meniscus-related and other adhesive forces, until the "pull-off" force (P) is reached, when the cantilever jumps back to its free deflection position. Hysteresis during contact indicates that some plastic deformation has

occurred whilst load was applied to the surface, due to the presence of a relatively soft surface film. In order to compare the conditions in the AFM tests with ball on disc experiments, we estimate AFM single asperity contact pressure. For the tip we used for these measurements the radius is 20 nm and the maximum applied load of 50 nN, therefore the range of contact pressure is in the order 100 MPa.

*Friction calculations* Bhushan introduced two methods to measure friction [149]. For the present measurements the lateral force technique was used since it is described as more reliable and objective. The sample is scanned perpendicularly to the long axis of the cantilever beam and the lateral force signals in trace and retrace ( $LT, LRT$ ) are recorded. In this arrangement, as the sample moves under the tip, the friction force will cause the cantilever to twist. Therefore the signal intensity between the left and the right detectors will be different, denoted as FFM signal  $[(L - R)/(L + R)]$ . This signal can be related to the degree of twisting, hence to the magnitude of friction force. By changing the set point parameter in the feedback loop, the normal force applied between probing tip and sample surface can be changed. The scan sizes were  $5\mu\text{m}$  by  $5\mu\text{m}$ , consisting of 512 scan lines with 512 scan points each. First, the average value of all of the 512 lines with 512 points for Lateral Trace ( $LTV_{avg}$ ) and Lateral Retrace ( $LRTV_{avg}$ ) from every scan were calculated. To obtain the friction force value ( $FFV$ ), these two mean values have to be subtracted from each other, and divided by two [149], see equation 5.6.

$$FFV = \frac{|LTV_{avg} - LRTV_{avg}|}{2} \quad (5.6)$$

The measurements of the friction force values were repeated ten times in every environment to obtain representative and repeatable results. Assuming that the friction in nanoscale follows Amonton's law, the friction force is given by equation 5.7

$$FFV = \mu(SP + F_0) \quad (5.7)$$

Where  $\mu$  is the friction coefficient, the set point (SP) is the applied load and  $F_0$  is a force constant. Following the procedure suggested by Beake et al.[150], the force constant is nearly equal to the pull off force determined from the force distance curves, therefore the friction coefficient can be calculated using equation 5.8.

$$\mu = \frac{FFV}{(SP + F_0)} \quad (5.8)$$

Usually, the FFV and SP values are given in [V] Volts as acquired from lateral force measurements. However, the results can be easily compared with each other

because findings in Volts are connected with the forces between tip and surface. In order to obtain commonly used units (newton), the lateral force needs to be calibrated by the determination of the slope of deflection vs. LVDT. The calibration delivers an accurate value of the inverse optical lever sensitivity (InvOLS) describing the sensitivity of the detector-cantilever combination. With the knowledge of the accurate value of InvOLS, it is possible to calculate FFV and SP in Newton as follows:

$$FFV(V) \times InvOLS(nm/V) \times springconstant(nN/nm) = FFV(nN) \quad (5.9)$$

$$SP(V) \times InvOLS(nm/V) \times springconstant(nN/nm) = SP(nN) \quad (5.10)$$

## RESULTS AND DISCUSSION

### Friction

A series of ball-on-disc tests with different base oil/additives blends were conducted under the conditions described before. In the beginning of each test, the coefficient of friction was decreasing as a function of time for a period of time and stayed constant afterwards. The coefficients of friction of the different solutions at different normal load are showed in table 5.6 As can be seen from Table 5.6 the

|          | n-hexadecane |           | Diethylenglycol dibutyl ether |           |
|----------|--------------|-----------|-------------------------------|-----------|
|          | P=1.3 GPa    | P=2.4 GPa | P=1.3 GPa                     | P=2.4 GPa |
| 0 % ZDDP | 0.080        | 0.060     | 0.125                         | 0.100     |
| 2% ZDDP  | 0.120        | 0.080     | 0.140                         | 0.105     |
| 5% ZDDP  | 0.110        | 0.085     | 0.135                         | 0.110     |

Table 5.6: Steady state coefficient of friction after 1 hour rubbing time for polar base oil diethylenglycoldiethyleter (DEG) and non polar oil hexadecane (HeD) with different content of ZDDP.

coefficient of friction increases when ZDDP is present in the lubricant. However, one can notice that the degree of friction increase is higher for the case of hexadecane base oil.

### Surface analysis

Scanning Electron Microscopy (SEM) and Energy-Dispersive X-Ray Spectroscopy (EDS) analysis performed on the balls after tribological tests showed that the traces of elements present in the additives are only found inside the rubbing track. No traces of additive reaction could be found outside the rubbing track. Further analysis revealed that the traces of additive are only found at the asperity tip

where the real contact is occurred. An example of SEM-EDS analysis is presented in Fig. 5.39.

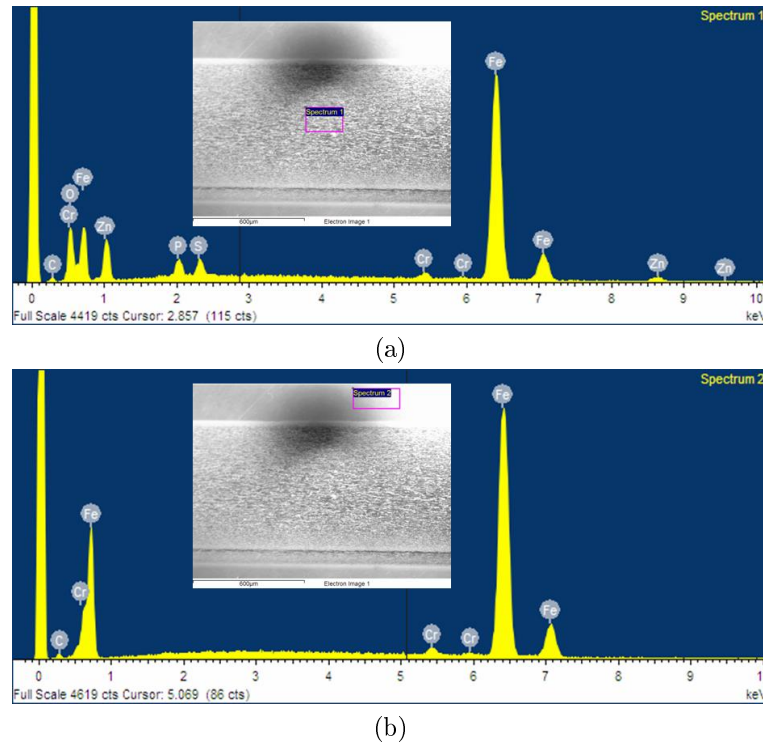


Figure 5.39: EDS spectra and SEM images (a) inside and (b) outside the rubbing track of specimen tested with DEG + 2% wt ZDDP.

Surface roughness of the rubbing track after each experiment was analysed using WYKO optical profilometer and the results are shown in the Fig. 5.40. It is apparent from Fig. 5.40 that the addition of ZDDP increases surface roughness in both base oils, however the roughening of the layer is more prominent when ZDDP is blended in the polar base oil. Our investigations using an adapted interferometry technique [146, 147] suggest that the reaction layer formed when ZDDP is blended in a non-polar base oil is thicker than the reaction layer derived from polar base oil-ZDDP solution. The interaction of the base oil molecules with the additive molecules determine the reaction layer formed and it is in the origin of the different tribological behavior observed. The different characteristics of the ZDDP-derived layer formed on rubbing surfaces are thought to be responsible for the difference in the measured coefficient of friction.

### AFM results

The objectives of the experiments under oil were to establish the feasibility of imaging and friction force measurement, and to investigate the possibility of using the AFM tip to simulate a single asperity contact in a tribological situation, thereby

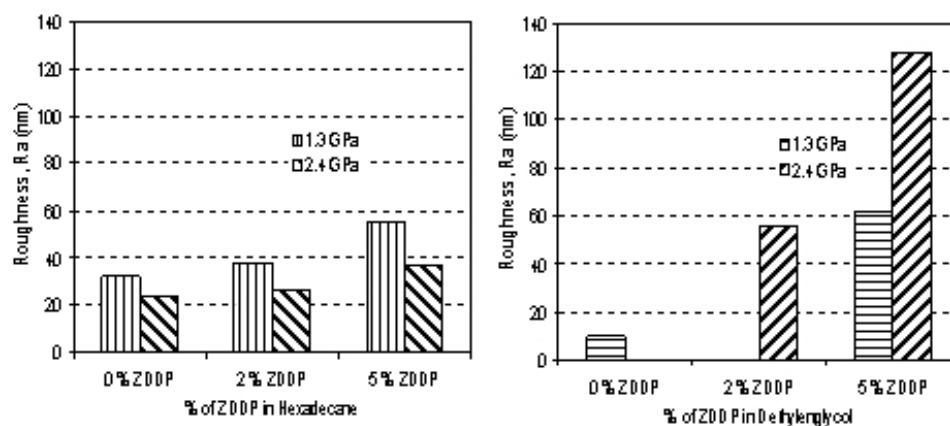


Figure 5.40: Comparison of roughness after the tribo tests

providing a route to study additive-derived layer formation processes [149] and explain the differences observed in the macro-tribological tests. To understand the nature of interaction between the cantilever tip and the surface, the deflection displacement curves were recorded, before every measurement. Fig. 5.41 shows the deflection of the cantilever tip as a function of the distance from the film surface. In all cases, a full line indicates the tip approach to the surface and a dashed line represents the tip being pulled away from the surface. The vertical separation between the point where the tip was touching the film (A) and the point where the tip was pulled off the film (B) together with the spring constant of the cantilever (0.22 nN/nm) were used to calculate the pull off (adhesive) force [151]. The pull off forces for samples with DEG+0% ZDDP, DEG+5%ZDDP, DEG+90% ZDDP were 16.8nN, 70.4nN and 66.7nN, respectively. It can clearly be seen that the pull off force decreases significantly with the addition of ZDDP, with respect to the value obtained for pure base oil. The pull off forces values when ZDDP was added to the base oil were very similar for any additive concentration. This fact is related to some plastic deformation that occurred due to the presence of a relatively soft surface film.

Additionally, pull of force comparisons between pure DEG and pure HeD base oils were carried out. Fig. 5.42 shows the deflection of the cantilever tip as a function of the distance from the surface.

The pull off force values of these samples are similar indicating that under these rubbing conditions there is no layer formation in the absence of ZDDP additive.

In the table 5.7 detailed information about AFM measurements and calculation are summarized.

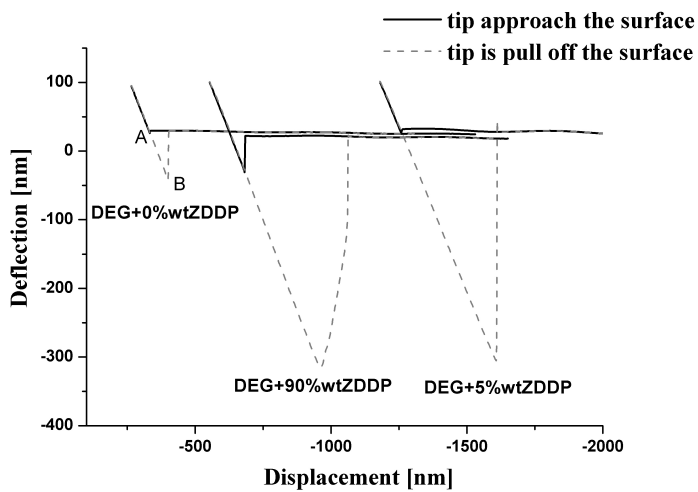


Figure 5.41: Pull of force curves of investigated samples

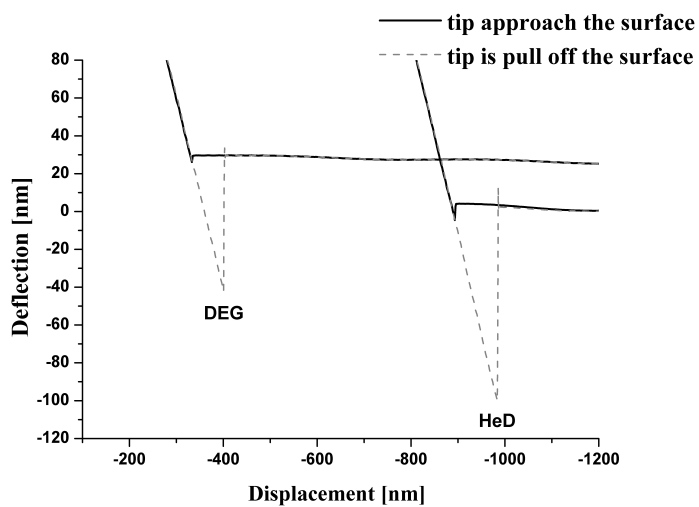


Figure 5.42: Pull of force curves of surface with DEG and HeD oil

| DEG + 0% ZDDP  |                |                                |         |          |                         |                     |               |                            |
|----------------|----------------|--------------------------------|---------|----------|-------------------------|---------------------|---------------|----------------------------|
| Set point [V]  | Set point [nN] | Scan speed [ $\mu\text{m/s}$ ] | FFV [V] | FFV [nN] | Spring constant [nN/nm] | Defl. InvOLS [nm/V] | Distance [nN] | $\mu$ friction coefficient |
| 1              | 10.405         | 12.52                          | 0.0042  | 0.044    | 0.235                   | 44.18               | 16.863        | 0.002                      |
| 1              | 10.405         | 37.56                          | 0.0041  | 0.042    | 0.235                   | 44.18               | 16.863        | 0.002                      |
| 3              | 31.215         | 12.52                          | 0.0110  | 0.114    | 0.235                   | 44.18               | 16.863        | 0.002                      |
| 3              | 31.215         | 37.56                          | 0.0181  | 0.188    | 0.235                   | 44.18               | 16.863        | 0.002                      |
| 5              | 52.025         | 12.52                          | 0.0156  | 0.163    | 0.235                   | 44.18               | 16.863        | 0.003                      |
| 5              | 52.025         | 37.56                          | 0.0245  | 0.255    | 0.235                   | 44.18               | 16.863        | 0.004                      |
| DEG + 5% ZDDP  |                |                                |         |          |                         |                     |               |                            |
| 1              | 9.105          | 12.52                          | 0.0058  | 0.05     | 0.224                   | 40.60               | 74.779        | 0.001                      |
| 1              | 9.105          | 37.56                          | 0.0075  | 0.07     | 0.224                   | 40.60               | 74.779        | 0.001                      |
| 3              | 27.314         | 12.52                          | 0.0145  | 0.13     | 0.224                   | 40.60               | 74.779        | 0.001                      |
| 3              | 27.314         | 37.56                          | 0.0145  | 0.13     | 0.224                   | 40.60               | 74.779        | 0.001                      |
| 5              | 45.523         | 12.52                          | 0.0208  | 0.19     | 0.224                   | 40.60               | 74.779        | 0.002                      |
| 5              | 45.523         | 37.56                          | 0.0185  | 0.17     | 0.224                   | 40.60               | 74.779        | 0.001                      |
| DEG + 90% ZDDP |                |                                |         |          |                         |                     |               |                            |
| 1              | 9.556          | 12.52                          | 0.0801  | 0.76     | 0.229                   | 41.63               | 66.71         | 0.010                      |
| 1              | 9.556          | 37.56                          | 0.0876  | 0.83     | 0.229                   | 41.63               | 66.71         | 0.012                      |
| 3              | 28.670         | 12.52                          | 0.0688  | 0.66     | 0.229                   | 41.63               | 66.71         | 0.007                      |
| 3              | 28.670         | 37.56                          | 0.1169  | 1.11     | 0.229                   | 41.63               | 66.71         | 0.012                      |
| 5              | 47.783         | 12.52                          | 0.0840  | 0.80     | 0.229                   | 41.63               | 66.71         | 0.007                      |
| 5              | 47.783         | 37.56                          | 0.0919  | 0.87     | 0.229                   | 41.63               | 66.71         | 0.008                      |

Table 5.7: Atomic force microscopic data

Fig. 5.43 shows the dependency of Friction Force Value (representative of friction coefficient) versus Set point (representative of load) for DEG mineral oil without and with additives is different concentrations. Since results for HeD were very similar to those for DEG and they are presented in the following figures.

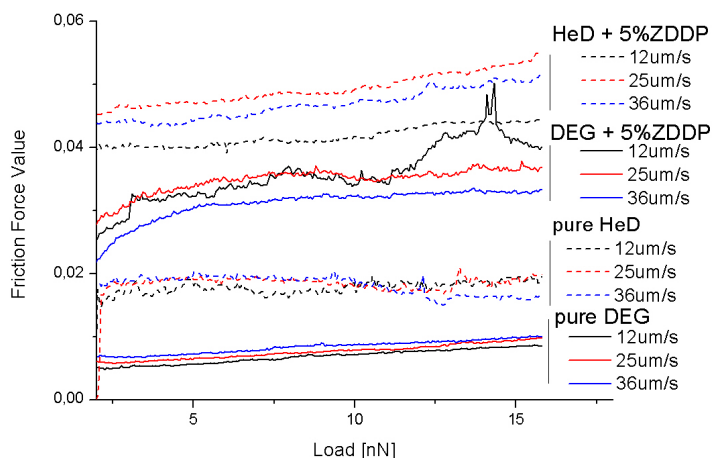


Figure 5.43: Friction Force Value (representative of friction coefficient) versus Load [nN] for DEG and HeD mineral oils without and with ZDDP additives for three different scan speeds

The friction-additive concentration relation observed in the nanoscale measurements shows the same tendency as observed in the macro-tribological tests, i.e. increase in friction by addition of ZDDP. It also can be seen that the scanning speed does not significantly influence friction force values, just when ZDDP are presented in the oils friction vary more with scanning speed.

Additional experiments were performed to study the effect of rubbing time on friction for DEG base oil with and without the additive and for HeD. Fig. 5.44 present behavior of friction force values with number of scans. It can be assumed from Fig. 5.44 that in nanonewton load range there is no influence of rubbing time on friction force values. There is no evidence for the build-up of an anti-wear film.

In order to compare conditions in the AFM wear test with those in the ball on disc test, we may a crude estimation of the peak AFM local contact pressure, assuming an elastic Hertzian contact with a tip radius of 10-50 nm and an applied load of 500 nN, to be of the order of 1 GPa. In the WAM ball running at 100 and 600 N load, the calculated Hertzian contact of 1.34 GPa (contact diameter 0.38  $\mu\text{m}$ ) and 2.43 GPa (contact diameter 0.69  $\mu\text{m}$ ). In case of single asperity contact with AFM tip and sample, there does not appear to be evidence for the presence of a reacted ZDDP-based layer in the AFM images. This is perhaps not surprising

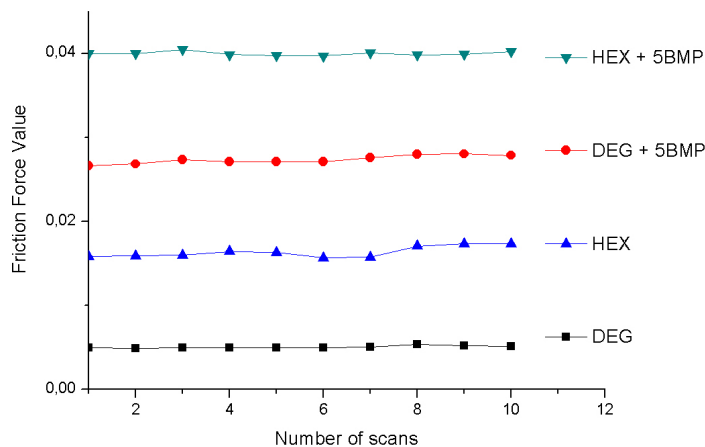


Figure 5.44: Friction force value vs set point for scanning speed  $12 \mu\text{m/s}$

given that the AFM test is carried out at room temperature with a maximum scan speed of  $30 \mu\text{m/s}$ , whereas in a pin on disc experiment the parts may move with peak relative velocities of the order of several metres per second over several hours with oil temperatures in the range  $80 - 120^\circ\text{C}$ .

## CONCLUSION

The results presented here clearly show that base oil polarity changes the tribological behavior and the effect it makes when ZDDP is added. Non-polar base oil (HeD)-ZDDP solution generates a tribofilm more rapidly and thicker than that of polar base oil (DEG)-ZDDP solutions. The nature of ZDDP as polar molecules will of course make ZDDP to have higher probability to reach the steel surface when dissolved in non polar oil compared to the case when dissolved in polar base oil. Furthermore, since it is known that the reaction layer formed by ZDDP increases friction, the amount of the ZDDP reaction layer on the rubbing track will also determine the degree of friction increase. Therefore, since we observed that for the case of non-polar base oil the reaction layer is thicker compared with that of polar base oil, the increase of the degree of friction is also expected to be higher. The same tendency was observed for the test carried out using atomic force microscopy (AFM), for different additive concentration and applied load, showing the connection between the phenomena occurring at the atomic level and the overall macroscopic behavior. AFM force-distance curves indicate the existence of soft surface layer when ZDDP is added to the base oil for any additive concentration. Micromechanical properties of this layer are important in relation to the formation action of anti-wear film during severe tribological stresses. Un-

fortunately AFM scanning in base oil containing ZDDP, at high load and scan rate did not lead to the build-up of an anti wear film. This fact shows that single asperity contact temperatures during AFM scans are much lower compare to those presented in real machine parts [148]. However this technique is perfect choice for investigation of already built-up layers after tribological tests, their morphology, topography and micromechanical properties, additionally deflection-displacement measurements allow to understand adhesion, elastic and viscoelastic characteristics.

The polarity of the base oil molecules determines the way the additive molecules can reach and attach to the surface, influencing the final structure and characteristics of the ZDDP-derived reaction layer.

#### **ACKNOWLEDGEMENT**

The authors wish to thank Prof. Stathis Ioannides (Product R&D Director of SKF at SKF Engineering & Research Centre in The Netherlands) for permission to publish this work. The work presented in this paper has been supported by the EC, Sixth Framework Programme, Marie Curie Action (WEMESURF research project entitled: "Characterization of wear mechanisms and surface functionalities with regard to life time prediction and quality criteria-from micro to nano range" under contract MRTN CT 2006 035589).

### 5.2.2 Evolution of ZDDP-derived reaction layer morphology with rubbing time

*"Evolution of ZDDP-derived reaction layer morphology with rubbing time"* [5] reports on growth of tribological film within tribotesting time until reaching a limiting thickness. The tribotests were conducted with a low polarity commercial base oil, poly- $\alpha$ -olefin (PAO), blended with C<sub>4</sub> Zinc Dialkyl DithioPhosphates (ZDDP). An adapted in-situ interferometry technique was continuously used to monitor the additive derived reaction layer formation. The evolution of the topography and mechanical properties of the ZDDP-derived reaction layer with rubbing time were studied using Atomic Force Microscopy. From this experiments it was concluded that initially a thin and soft ZDDP reaction layer is formed (after 5 min rubbing test) and than very quickly it develops, after 30 min it becomes harder and thicker. After 60 min test stable, rough and hard layer is developed with a limited thickness of 70 nm.

#### EVOLUTION OF ZDDP-DERIVED REACTION LAYER MORPHOLOGY WITH RUBBING TIME

A. Naveira-Suarez<sup>1,2</sup>, A. Tomala<sup>3,5</sup> R. Pasaribu<sup>1</sup>, R. Larsson<sup>2</sup> and I.C. Gebeshuber<sup>3,4,5</sup>

<sup>1</sup> SKF Engineering and Research Centre, Kelvinbaan 16, 3439 MT Nieuwegein, The Netherlands

<sup>2</sup> Division of Machine Elements, Lulea University of Technology, SE-971 87, Lulea, Sweden

<sup>3</sup> Institute of Applied Physics, Vienna University of Technology, Wiedner Hauptstrasse 8-10/134, 1040 Wien, Austria

<sup>4</sup> Institute of Microengineering and Nanoelectronics, Universiti Kebangsaan Malaysia, 43600 UKM Bangi, Malaysia

<sup>5</sup> AC<sup>2</sup>T Austrian Center of Competence for Tribology, Viktor Kaplan-Straße 2, 2700 Wiener Neustadt, Austria

SCANNING

Volume 31, September 2010, Pages 1-10

#### Abstract

Functional additives, particularly extreme-pressure and antiwear additives, in formulated oil will compete to adsorb and function in tribological contacts. A low

polarity commercial base oil, poly- $\alpha$ -olefin (PAO), blended with zinc dialkyl dithiophosphates has been studied. The tribological performance was evaluated using a ball-on-disc test rig under mixed rolling-sliding conditions in the boundary lubrication regime at 90 °C. An adapted in-situ interferometry technique was used to monitor the additive derived reaction layer formation. The thickness of the reaction layer evolves with rubbing until reaching a limiting thickness value of approximately 70 nm. The evolution of the topography and mechanical properties of the ZDDP-derived reaction layer with rubbing time were studied using Atomic Force Microscopy. A constant roughening and hardening of the additive-derived layer with rubbing time is observed and related to the different tribological performance of the layer at different rubbing times.

Keywords: additives, AFM, atomic force microscopy, boundary layers formation, boundary lubrication, morphology, nanowear, reaction layer, ZDDP.

## INTRODUCTION

Extreme-pressure (EP) and antiwear additives (AW) control the performance of lubricants in the mixed and boundary lubrication regimes. Performance enhancing properties of these additives are very important since, if oil lacks lubricating ability, excessive wear and friction can occur (American Society for Metals 1992). The main elements, which are responsible for the extreme-pressure and antiwear action, are sulfur and phosphorus respectively [152]

Metal dialkyl dithiophosphate compounds (MDTPs) have been used in lubricating oils due to their multifunctional performance as antiwear, extreme-pressure, friction modifying, antioxidant and corrosion inhibiting additives. Dialkyl dithiophosphates of different metals such as molybdenum (Sarin et al 1994), cadmium [153], copper [154], titanium, gadolinium [155], iron, antimony and other metals have been introduced in lubricants, albeit zinc dialkyl dithiophosphates (ZDDP) are the most widely used ([156], [157], [158], [159]).

ZDDP reacts with the surface in contact to form protective reaction layers. A variety of mechanisms have been proposed [160] for the formation of the ZDDP derived reaction layers, involving oxidative (by reaction with hydroperoxides or peroxy radicals) [161], catalytic (chemisorption on metal, hydrolytic, [158], and thermal [162] decomposition of the ZDDP. The additive decomposes under certain conditions and the decomposition products react to generate a 50-150 nm thick layer [163], [164], [165]. The resulting reaction layers have a heterogeneous composition with the chemical structure of the starting materials dictating their chemical composition [166], [167]. The structure and chemical composition of the layer have been analyzed using advanced spectroscopy techniques, such as X-ray

photoelectron spectroscopy [168], [169], [170], [171], [172], Auger electron spectroscopy [173] and X-ray absorption near edge spectroscopy [166], [174] and found to be dependent on temperature and tribological conditions. The layers are composed of a mixture of short and long polyphosphates [160], [175] with the presence of sulphides and oxides in the layer bulk [176]. A two-layer structure for the ZDDP derived reaction layers has also been proposed, where a thin long chain zinc poly(thio)-phosphate layer is superimposed on a thicker short chain mixed Fe/Zn polyphosphate layer, containing embedded nanocrystallites of ZnO and ZnS [177].

However, several studies have proven ZDDP to have detrimental effects on wear under certain operation conditions [178] and to enhance friction when the system is operating in mixed and boundary lubrication regimes [179], [180].

Atomic Force Microscopy (AFM) allows the study of surfaces at the nanoscale, providing a method of measuring ultra small forces between a single asperity probe tip and the surface of the sample. Therefore it is a suitable instrument to study engineering surfaces under dry or wet conditions with atomic resolution. Thus, the atomic-scale origins of friction could be observed with this technique. Transition from single (nanoscale) asperity to multiple asperity contacts holds the promise to predict tribological behavior. AFM was previously used to address the nano-scale origins of the effect of base oil polarity on friction and wear behavior of ZDDP-derived reaction layers [4] using low viscosity model base oils. Force vs. distance plots are often used to measure the interaction forces between the tip and the surface, by pushing the tip against the surface, and then separating the tip and surface. From this data adhesion, indentation and layer elasticity can be studied. It was found that base oil polarity determines the transport of additives to the surface thereby controlling the maximum reaction layer thickness, friction and wear, as well as the morphology of the additive-derived reaction layer. However the reaction layer chemical composition is not strongly influenced by the base oil polarity [181]. The same behavior was observed when using ZDDP in solution with commercial base oils of different polarities and among the operating conditions, shear was identified as a fundamental parameter on the activation of additives on rubbing steel surfaces and the properties of the derived reaction layer [182]. In this paper we study the evolution of the reaction layer with rubbing time and its nano-friction and nano-wear behavior, to further understand the differences observed in the friction and wear performance.

## MATERIALS AND METHODS

### Test samples

The  $\varnothing$  20 mm steel balls were AISI 52100 steel with hardness 59-66 HRC and an average roughness (Ra) of 10 nm. The rings were washers (WS 81212) from SKF Cylindrical Thrust Roller Bearings (CTRB) of ASI 52100 steel with hardness 59-66 HRC and Ra=100 nm. The specimens were cleaned prior to testing by successive immersion first in an ultrasonic bath of petroleum ether for 10 min and then acetone for 10 min.

### Lubricant

The lubricant selected as the base oil was poly- $\alpha$ -olefin (PAO), a synthetic non-polar oil. PAO was chosen over mineral oil due to its purity, as mineral oil has a relatively high concentration of sulfur which might interfere with the additives. The physical properties, sulfur and phosphorus content, obtained by X-ray fluorescence (XRF) analysis of the base oil samples before testing, are summarized in Table 5.8.

| Code | Kinematic viscosity at 40 °C [mm <sup>2</sup> /s] | Kinematic viscosity at 100°C [mm <sup>2</sup> /s] | Sulfur content [wt%] | Phosphorus content [wt%] |
|------|---|---|----------------------|--------------------------|
| PAO  | 24.6  | 5.1   | 0.00055              | <0.00030                 |

Table 5.8: Base oil properties.

It is assumed that the addition of the additives does not significantly change the viscosity of the bulk solution.

A fully formulated iso-C<sub>4</sub>-zinc dialkyl dithiophosphate (ZDDP), with 99 % purity is employed in simple solution in both base oils without other additives present. 2 wt% ZDDP solutions were prepared using an ultrasonic bath to dissolve the additives in the base oils. The temperature of the lubricant solution remained below 40 °C during the dissolving procedure.

### Macro-tribological tests

SKF-WAM5 ball-on-disc test rig (Wedeven Associates, Inc., Edgmont, PA, USA) enables the performance of a variety of tests to evaluate the tribological performance of additive/base oil blends under controlled contact conditions. The ball and the disc are independently driven giving the possibility to simulate pure rolling and various slide-roll ratios. The slide-roll ratio (SRR), or slip ratio, is defined as the sliding speed  $US = UB - UR$  divided by the entrainment speed, or rolling speed,  $U = (UB + UR)/2$  where UB and UR are the ball and ring surface speed in contact, respectively.

The effect of rubbing time in the morphology and properties of the ZDDP-derived reaction layer is studied in a mixed rolling/sliding contact, with wear evenly distributed in the tracks of both specimens. The tribotests were carried out at an applied load of 300 N which resulted in a maximum Hertzian contact pressure of 1.9 GPa (contact diameter 540  $\mu\text{m}$ ) at a SRR = -10 %. The temperature was set constant at 90 °C for all the tests. The specific film thickness or lambda ratio (the ratio of the central film thickness to the composite surface roughness of the two surfaces in contact) was set constant at 0.4<sup>1</sup> and the entrainment speed was set accordingly to 0.25 m/s. The system was operating in the boundary lubrication regime.

### **Spacer Layer Interferometry**

Spacer layer interferometry imaging principle [183] is used as an in-situ (inside the tribometer, out of the contact) and post-mortem (after friction) method [184] to monitor reaction layer formation [164]. Tests are carried out by rolling/sliding a steel ball on a lubricated steel disc, to produce a wear track on both ball and disc. Motion is halted and a spacer layer and chromium-coated glass disc are loaded against the wear track on the steel ball. The lubricant is squeezed out from the contact, but any solid-like reaction layer remains. A contact is formed between the reflective steel ball and the flat surface of a glass disc, which is coated with a thin chromium layer and a thicker silica spacer layer. White light is shown through the glass disc into the contact, where some of the light is reflected from the semi-reflecting chromium layer while the rest passes through the spacer layer and any transparent reaction layer present. Because the two beams have traveled different distances, they interfere constructively and destructively at wavelengths dependent upon the path difference, to produce a colored interference image [183]. The interference image produced is frame-grabbed and the color of each pixel analyzed to determine the corresponding path difference and thus layer thickness, based on a calibration procedure. The interference images are a map of the reaction layer present in the contact. Once the image of the reaction layer formed at the rubbing steel ball is taken, the glass disc is then removed and the sliding/rolling of the steel ball on the steel disc continues.

### **Nanotribological tests: Atomic Force Microscopy**

AFM and Lateral Force Microscopy (LFM) images of the wear track after the tribotests were obtained with an AFM MFP-3D (Asylum Research, Santa Barbara, CA) in ambient conditions. Silicon nitride tips (supplied by Veeco) on a V shaped

---

<sup>1</sup>calculated using Dowson Hamrock equation, according roughness and tribotesting parameters in order to be sure that the system is operating in the boundary lubrication regime

triangular cantilever with a low spring constant were used for nanotribological tests (friction measurements). Silicon tips on an aluminium coated cantilever (OLYMPUS OMCL-HA) were used to perform nanowear tests. The important features of both cantilever types used for the study are listed in Table 5.9. The cantilevers were calibrated for topography mode and pull off force mode using a silicon chip. The value of spring constant for silicon nitride tips was 0.1 N/m, and for silicon tips was 42 N/m. The scan area was  $5 \times 5 \mu\text{m}^2$ . Images were recorded in the contact mode, i.e. the feedback electronics and the corresponding software was used to keep the cantilever at constant deflection measuring the sample topography. In order to obtain the maximum LFM signal (torsion motion), the sample was scanned along the direction perpendicular to the cantilever long axis. The lateral force was evaluated from the difference in the torsional signals (displayed as output voltage) at forward and reverse scans on the lateral force (friction) loop. For each applied force, 512 lateral force loops on an area of  $5 \mu\text{m}^2$  were obtained from different regions. For wear measurement, all samples were scratched 40 times using a silicon tip on an aluminium coated cantilever with a very high spring constant (42 N/m). The load applied to cantilever was 22  $\mu\text{N}$  (equal to set point of 8 V), the scratching speed was 25  $\mu\text{m/s}$ , scanning direction was perpendicular to the cantilever long axis and perpendicular to the wear track direction. After the scratching, topography of the scratched area was measured. The extent of wear was estimated by determining the average depth and width of the scratched area.

|                              | Cantilever V type VEECO<br>(Topography & LFM) | Cantilever OLYMPUS<br>OMCL-HA (Scratching,<br>nano-wear test) |
|------------------------------|---|---|
| Material                     | $\text{Si}_3\text{N}_4$                       | Si coated with Al   |
| Cantilever spring constant   | 0.1 N/m                                       | 42 N/m  |
| Cantilever arm length, width | 140 $\mu\text{m}$ , 18 $\mu\text{m}$          | 160 $\mu\text{m}$ , 50 $\mu\text{m}$                          |
| Resonance frequency          | 38 kHz  | 300 kHz   |
| Full tip opening angle       | 35°   | -   |
| Tip radius                   | 10 nm   | <10 nm  |

Table 5.9: Major features of the cantilever used for AFM study.

## RESULTS AND DISCUSSION

### Macrotribological tests

A series of interference images of the center of the wear track derived from the PAO+ZDDP solution (low polarity base oil) from the rubbing times are shown in Fig. 5.45<sup>2</sup>. In all the images the sliding direction is from bottom to top. It can be seen that a reaction layer, evidently from the color scale in the images, develops differently due to the increase on rubbing time.

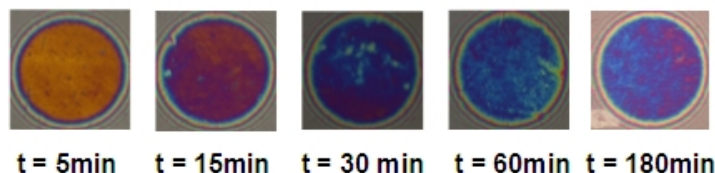


Figure 5.45: Series of interference images from different positions of the wear track for PAO+ZDDP at rubbing times  $t=5, 15, 30, 60$  and  $180$  minutes.

From the interference images, reaction layer thickness values were determined at each position across a horizontal profile of the contact. From those values the mean reaction layer thickness at the center of the contact was calculated. The antiwear properties and average friction coefficient of the reaction layers derived from PAO + ZDDP solutions at different rubbing times were also investigated. The wear track width (WTW) was measured from the balls using a calibrated optical microscope. The friction coefficient is continuously recorded during the tribological tests and from these data the average friction coefficient is calculated. The results are summarized in Table 5.10

| SAMPLE | Rubbing time [min] | Parameters                         |                                    |                               |
|--------|--------------------|------------------------------------|------------------------------------|-------------------------------|
|        |                    | Average friction coefficient $\mu$ | Wear track width [ $\mu\text{m}$ ] | Reaction layer thickness [nm] |
| ZDDP1  | 5 min              | $0.086 \pm 0.002$                  | $540.1 \pm 4.4$                    | $13.3 \pm 2.3$                |
| ZDDP2  | 15 min             | $0.092 \pm 0.001$                  | $503.7 \pm 2.5$                    | $53.3 \pm 1.2$                |
| ZDDP3  | 30 min             | $0.089 \pm 0.002$                  | $508.3 \pm 2.6$                    | $70.8 \pm 2.1$                |
| ZDDP4  | 60 min             | $0.083 \pm 0.005$                  | $574.3 \pm 2.5$                    | $79.4 \pm 1.2$                |
| ZDDP5  | 180 min            | $0.098 \pm 0.003$                  | $589.9 \pm 2.0$                    | $72.7 \pm 1.5$                |

Table 5.10: Wear track width, friction coefficient and reaction layer thickness.

The evolution of the ZDDP-derived reaction layer thickness shows how initially a thick layer quickly develops with rubbing time, before stabilizing at a 'limiting

<sup>2</sup>Color of each pixel can be converted, via a suitable layer thickness/colour calibration [183], to a map of the reaction layer thickness present on the ball. Blue color indicates thick layer.

thickness'. It is possible to identify an initial activation stage when the additive molecules are activated by the tribological energy and approach the surface. The growth mechanism begins with distinct reaction events on micro-asperity contact at the steel surfaces, leading to distinct segregated pads. The reaction layer develops initially very rapidly with the rate of formation being higher than the rate of removal. This suggests that the layer formation may be strongly catalysed by chemical species generated or released during rubbing [164], such as soluble  $\text{Fe}^{2+}$  or  $\text{Fe}^{3+}$ . By ligand exchange, the iron ion replace the zinc in ZDDP to form a less thermally stable metal dithiophosphate, that subsequently decomposes [170] at lower temperatures to form iron phosphate glass in a reaction similar to that which occurs for ZDDP at higher temperatures. The formation of an iron phosphate layer on the steel surface predominantly occurs at the beginning of the experiment were there is substantial steel-steel contact as no, or hardly any, protective layer has formed. This would also establish the autocatalytic reaction so that ZDDP can subsequently decompose directly [164]. The process can also be triggered by triboelectronic processes such as exoelectron emission and a subsequent negative ion reaction. The reaction layer rapidly develops until reaching saturation. At this point the steel surface is completely covered by the reaction layer, which slows the rate of reaction layer formation. The next stage involves a wearing-out of the layer, being the rate of formation lower than the rate of removal. Due to the reaction layer thickness, primarily the iron (rich) phosphate layer is worn, and as there is no supply of iron ions anymore the new layer formed will have  $\text{Zn}^{2+}$  as counter ion. ZDDPs are more thermally stable, thus the rate of formation is smaller than the wear of the iron rich layer leading to a decrease in the layer thickness until a final stage of equilibrium, between the rate of formation and removal, is reached. At this equilibrium stage the layer reaches a constant thickness value or limiting thickness. The reaction layer will have an iron gradient being richer in iron close to the steel surface and richer in zinc at the layer/oil interface. At this stage, primarily the zinc rich top layer will be worn during rubbing and as there are few (or none) iron ions available the new reaction layer will be formed with zinc as counter ion, leading to a an equilibrium in the rates of formation and removal [182]. The initial wear track width measured in sample ZDDP1, after 5 min rubbing, corresponds with the Hertzian contact diameter. The continuous rubbing leads to lower WTW values that indicate how the formation of a reaction layer protects the steel surface. However the rubbing progression leads to a later increase of the wear track width, as observed in sample ZDDP4, which also stabilizes with rubbing time.

### Nanotribological tests

In order to understand the nature of the interaction between the cantilever tip and the formed reaction layer, the deflection displacement curves were recorded. Fig. 5.46 shows the deflection of the cantilever tip as a function of the distance from the reaction layer formed in the rubbing steel surfaces. The solid line indicates the tip approach to the surface, while the dashed line represents the tip being pulled away from the surface. The vertical separation between the point where the tip was touching the layer and the point where the tip was pulled away from it together with spring constant of the cantilever (0.1 nN/nm) were used to calculate the pull off (adhesive) force [58], see Table 5.11.

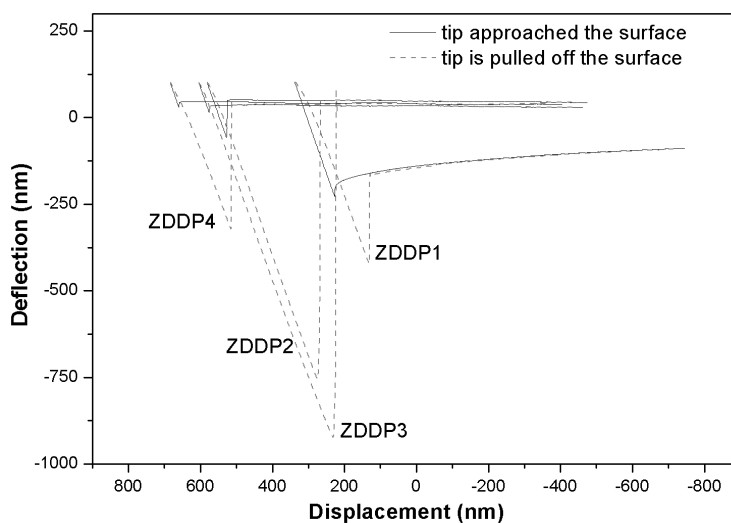


Figure 5.46: The deflection of the cantilever tip as a function of the distance from the wear track surface for all the investigated samples.

| SAMPLE | Deflection [nm] | Pull-off force [nN] |
|--------|-----------------|---------------------|
| ZDDP1  | 199.10 ± 0.23   | 19.35               |
| ZDDP2  | 697.84 ± 0.86   | 67.83               |
| ZDDP3  | 951.82 ± 0.72   | 92.51               |
| ZDDP4  | 360.28 ± 0.41   | 35.01               |

Table 5.11: Pull-off force values.

Fig. 5.46 shows that with increasing the ZDDP-derived reaction layer thickness, the force needed to pull off the cantilever from the surface also increases. This fact is related to high adhesion and plastic deformation, due to the presence of a soft surface layer formed by ZDDP. For sample ZDDP1 the reaction layer is thin (13.3 nm) and does not cover the surface homogenously. Short deflection displacement curve is due to contact of the cantilever with asperities from steel surface

while engaging. For sample ZDDP4, after 1 h test, the additive-derived reaction layer becomes stable and harder, as suggested by the nanowear results (Figs. 5.47b, 5.48b, 5.49b, 5.50b), as the adhesion forces are subsequently reduced. The three-dimensional AFM images showing the topographies of the ZDDP-derived layers are illustrated in Figs. 5.47a, 5.48a, 5.49a, 5.50a. Section graphs attached to the AFM images show the height distribution across the scan. Section graphs have the same scale as the color scale on the right side of the AFM images.

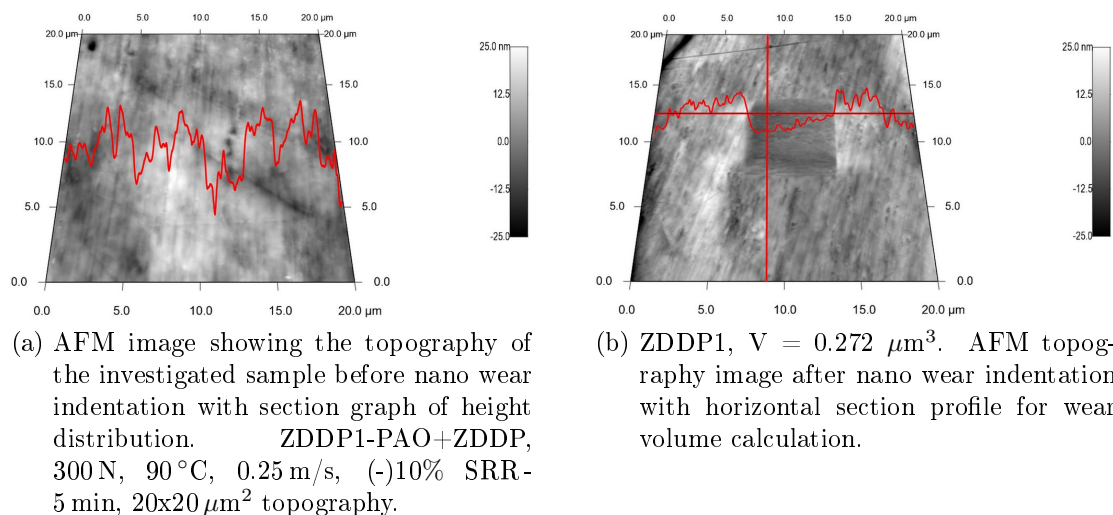
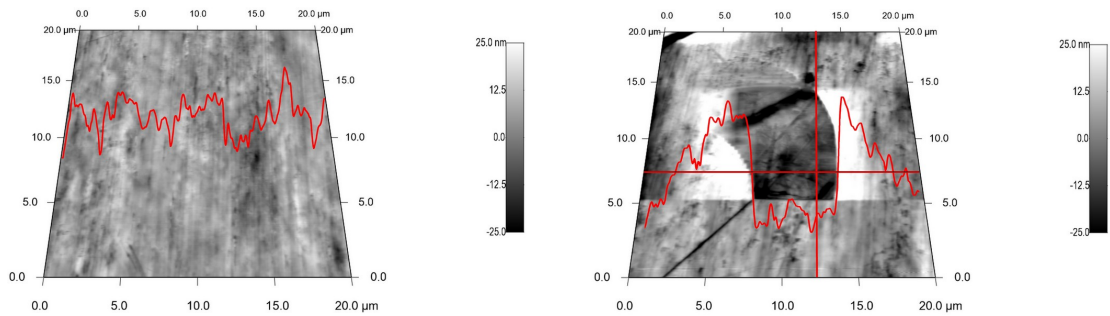


Figure 5.47: ZDDP1-AFM images showing the topographies of the investigated samples before (a) and after (b) nanowear indentation with section graphs of height distribution for wear volume calculation.

Various topographical parameters such RMS, minimum and maximum spot heights on the surface are given in Table 5.12. Parameters describing surface roughness include the autocorrelation function that compares surface heights between different points along the surface. The autocorrelation length gives a full description of roughness spacing, analogous to the height distribution for roughness height. Strictly related to the autocorrelation function is the roughness exponent  $\alpha$ , also called Hurst parameter. It reveals how jagged a surface with a given rms roughness and lateral correlation length is.  $\alpha$  usually ranges between 0.5 (exponential decay of  $C(r)$ -more jagged surface) and 1 (Gaussian  $C(r)$ -less jagged) [155]. For sample ZDDP4 the Hurst parameters are close to 0.5, which is therefore the most jagged surface. This is expected because from Figs. 5.47a, 5.48a, 5.49a, 5.50a. and Table 5.12 it can be observed that sample ZDDP4 appears rougher and shows more spikes compared to the other layers.

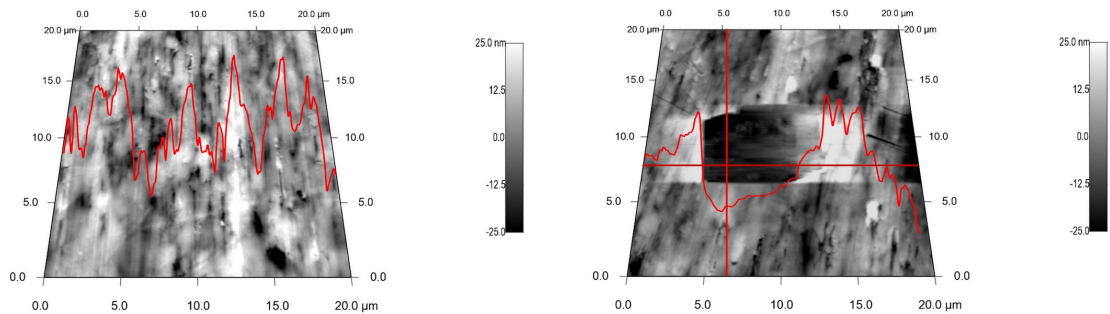
The RMS values displayed in Table 5.12 show how, in the initial stage of layer formation, a slight smoothening of the layer occurs. This process can be attributed



(a) AFM image showing the topography of the investigated sample before nano wear indentation with section graph of height distribution. ZDDP2-PAO+ZDDP, 300N, 90 °C, 0.25 m/s, (-)10% SRR-15 min, 20x20  $\mu\text{m}^2$  topography.

(b) ZDDP2,  $V = 0.425 \mu\text{m}^3$ . AFM topography image after nano wear indentation with horizontal section profile for wear volume calculation.

Figure 5.48: ZDDP2-AFM images showing the topographies of the investigated samples before (a) and after (b) nanowear indentation with section graphs of height distribution for wear volume calculation.



(a) AFM image showing the topography of the investigated sample before nano wear indentation with section graph of height distribution. ZDDP3-PAO+ZDDP, 300N, 90 °C, 0.25 m/s, (-)10% SRR-30 min, 20x20  $\mu\text{m}^2$  topography.

(b) ZDDP3,  $V = 0.475 \mu\text{m}^3$ . AFM topography image after nano wear indentation with horizontal section profile for wear volume calculation.

Figure 5.49: ZDDP3-AFM images showing the topographies of the investigated samples before (a) and after (b) nanowear indentation with section graphs of height distribution for wear volume calculation.

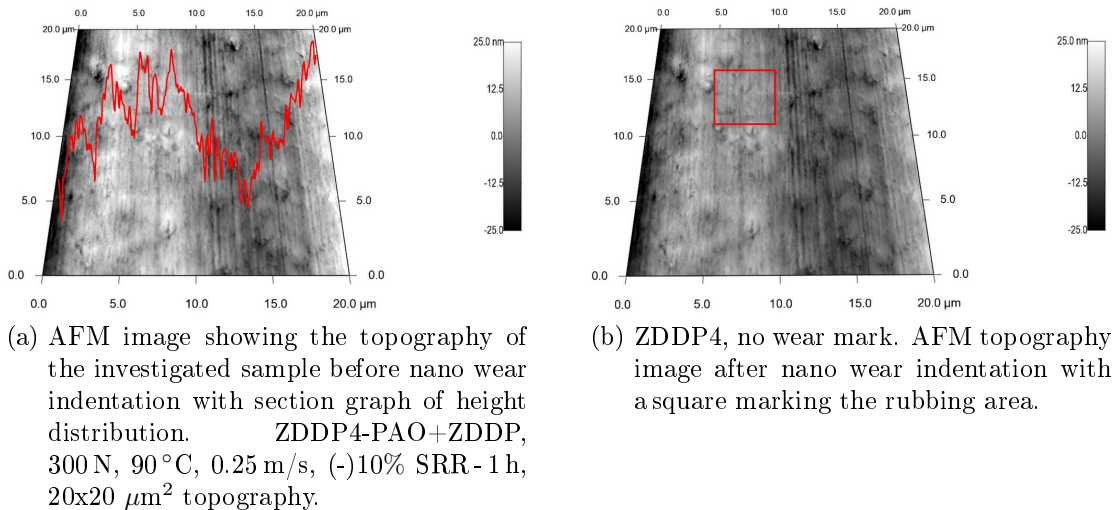


Figure 5.50: ZDDP4-AFM images showing the topographies of the investigated samples before (a) and after (b) nanowear indentation with section graphs of height distribution for wear volume calculation.

| SAMPLE | Rubbing time [min] | Parameters           |                     |                     |                |
|--------|--------------------|----------------------|---------------------|---------------------|----------------|
|        |                    | R.M.S Roughness [nm] | Minimum Height [nm] | Maximum Height [nm] | Hurst $\alpha$ |
| ZDDP1  | 5 min              | 16.774               | -279.403            | 138.731             | 0.778          |
| ZDDP2  | 15 min             | 14.910               | -109.366            | 49.423              | 0.761          |
| ZDDP3  | 30 min             | 10.010               | -211.205            | 45.665              | 0.774          |
| ZDDP4  | 60 min             | 34.974               | -372.240            | 154.989             | 0.564          |
| ZDDP5  | 180 min            | 48.037               | -138.251            | 216.618             | 0.815          |

Table 5.12: Topographical parameters of the reaction layer formed at different rubbing times.

to the gradual coverage of the first initial nucleation on asperity-asperity contacts. Sample ZDDP1, after 5 min rubbing time, presents higher roughness values than samples ZDDP2 and ZDDP3, after 15 and 30 min rubbing respectively. The topography images show a partial coverage of the steel surface, as no surface finishing marks from the original steel surface are visible, by a very thin reaction layer from sample ZDDP1, therefore having an important influence in the roughness from the initial steel surface. When rubbing progresses, a thicker layer develops, growing from distinct reaction events on micro-asperity contacts at the steel surfaces, leading to the formation of segregated pads, as seen in the topographical images of sample ZDDP2. Further rubbing causes the pads grow and coalesce to form a complete reaction layer and a consequent smoothing of the layer, as observed for sample ZDDP3. The roughening observed when rubbing continuous is due to evolution of the reaction layer morphology, with further development of distinctive features [185].

Following the procedure suggested by Beake and co-workers [186], the friction force ( $F_L$ ) is given by

$$F_L = 1/2(LF(f) - LF(r)) \quad (5.11)$$

where  $LF(f)$  and  $LF(r)$  are the signals in the forward and reverse direction of motion of the tip in LFM mode. This equation is based on the fact that when there is substantial variation in the surface topography, the LFM signal contains a component due to normal force acting through the local slope. Since lateral force is determined from the difference between signals reaching the left and the right halves of a four segment photo detector, the topographic contribution of the LFM image may be eliminated by subtracting signals recorded in opposite directions.

The variation of friction force as a function of load for all samples is presented in Fig. 5.51. The highest friction is observed for sample ZDDP4 (PAO+ZDDP, 300 N, 90 °C, 0.25 m/s, (-) 10% SRR, 1 h). This is in good agreement with previously reported studies [156], due to the formation of a rougher and thicker reaction layer on the steel surface, as can be observed in the topographical images, see Table 5.10 and Fig. 5.50a. The higher friction exhibited by sample ZDDP1, corresponding to the reaction layer formed after 5 min rubbing, may be caused by the elevated asperity friction due to the low thickness of the layer. Therefore the friction will arise mainly from the steel substrate, a less shearable material than the ZDDP-derived layers. This fact is in good agreement with pull-off force records where sample ZDDP1 exhibits short deflection displacement curve due to contact of the cantilever with the asperities from the steel surface while engaging.

When analysing these results one have to be aware of the limitation of the quali-

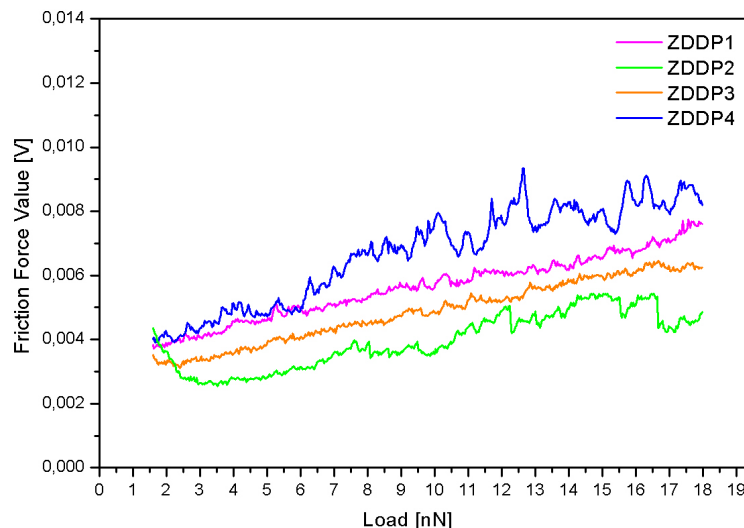


Figure 5.51: The variation of friction force as a function of applied load for the investigated samples.

tative AFM analysis. To provide nanometer spatial resolution, a very sharp tip of nanometer-scale radius is used but the precise geometry of this tip is difficult to measure and can vary with use, which lead to poor repeatability from experiment to experiment. In this study, a fresh cantilever was used for every sample, however the possible variations in the original geometry of the tips were not considered. Wear test for the ZDDP4 and ZDDP5 samples did not show any point of indentation after 40 scans of  $5 \times 5 \mu\text{m}^2$  area using a cantilevers with very high spring constant at Set point 8 V ( $22 \mu\text{N}$ ). Samples ZDDP1, ZDDP2 and ZDDP3 showed clear indentation areas as can be observed on Figs. 5.47b, 5.48b and 5.49b. The average wear volume was calculated using the average height of the horizontal and vertical profiles of the unworn area outside the indentation region (plane). Volume Analysis estimates the volume occupied by the space between a surface and a plane parallel to the reference plane of the surface that intersects the maximum height of the surface. This parameter can be seen as the volume of water that the surface must hold in order to completely "submerge it". The wear volume calculations contain a measurement error due to the roughness of the layers, however despite this fact, it can be seen from the line profiles that the indentation caused by the nanowear tests is greater than the initial roughness. Therefore nanowear measurements enable a valid comparison among the ZDDP samples.

The wear volume calculations indicate that the ZDDP-derived layer is initially softer, undergoing a hardening process with rubbing time. The indentation reaches the steel substrate for sample ZDDP1, according to the reaction layer thickness

values presented in Table 5.10. The wear values calculated for samples ZDDP2 and ZDDP3 are very similar, showing the same tendency as presented in the macroscopic measurements, despite the existing difference in layer thickness. For both samples the indentation created by the nano-wear tests was between 20-30nm in depth, and despite the uncertainty on layer base line, none of the indentations have reached the substrate. The results obtained for ZDDP4, where no indentation was observed after the nano-wear test, indicate a possible hardening process parallel to the roughening process of the layer that has also been observed, with the development of pad-like features [182]. Previous studies [58], [185] have shown how those features are higher than the surroundings and present a higher hardness and elastic modulus, which is attributed to the load carrying capacity of the layer.

## CONCLUSIONS

The formation and evolution of ZDDP-derived reaction layer with rubbing time were studied using a ball-on-disc test rig, spacer layer interferometry and atomic force microscopy. The macrotribological tests results showed that initially a thin ZDDP-derived layer formed after a 5 min rubbing test (sample ZDDP1) and then quickly develops on the rubbing surfaces with increasing rubbing time. After 15 min and 30 min test (samples ZDDP2 and ZDDP3) the reaction layer thickness increased while the wear track width (WTW) values were reduced. That indicates how the formation of an additive-derived reaction layer protects the steel surface. The rubbing progression leads to a later increase of the WTW until a stable, rough and hard layer develops (sample ZDDP4), reaching a 'limiting thickness' of approximately 70 nm (sample ZDDP5).

The topography of the layer at different rubbing times, analyzed using Atomic Force Microscopy, evolves from an initial slight coverage of the surface, to the growth of a thick layer over the wear track, verifying the interferometry findings.

Sample ZDDP1 (after 5min test) exhibits a thin reaction layer, the cantilever has alternate contact with asperities from steel surface and the layer. This results in short pull-off values when tip engages the elevated asperities and high lateral respond.

Sample ZDDP2 (15 min test) and ZDDP3 (30 min test) present a thick and soft reaction layer that covers entirely the steel surface. The cantilever interact only with the soft layer covering the surfaces resulting in long distance curves, low friction however high wear volume in nanoscale. Higher adhesive properties of the soft layer are caused by the molecular interactions between the molecules attached to the tip and the molecules on the layer.

When rubbing progresses further, the additive-derived layer experiences a constant roughening and hardening with rubbing time, as indicated by the nano-wear tests, which show no indentation for the layers ZDDP4 after 1h rubbing time. These processes may be responsible for the observed increase in friction and wear protection with rubbing time of the additive-derived reaction layers, in both the macro and the nano scale.

#### **ACKNOWLEDGEMENT**

The authors are grateful to the European Commission for supporting this work through their WEMESURF Training and Mobility of Researchers Network. The authors wish to thank Alexander de Vries, SKF Engineering and Research Centre Managing Director, for permission to publish this work.

## 5.3 Solid Lubrication

Work presented in this section is based on collaboration with AC<sup>2</sup>T Austrian Center of Competence for Tribology. Nanotribological investigations of miscellaneous hard coatings with variance properties were carried out in order to find the best structure desired for application in microelectromechanical systems (MEMS).

### 5.3.1 Micro- and Nanomechanical Properties of Diamond Films with Various Surface Morphologies

*"Micro- and Nanomechanical Properties of Diamond Films with Various Surface Morphologies"* [6] concerns the influence of the morphologies of chemically vapour deposited (CVD) diamond films on their micro- and nanomechanical properties. Diamond films having coarse ballas, fine ballas and faceted morphologies were characterized with the help of Scanning Electron Microscopy (SEM) and Raman spectroscopy. Hardness of the films was evaluated using nano indenter. Force spectroscopy, topographies and lateral force values of these films were estimated by means of Atomic Force Microscopy (AFM). Results indicate that diamond films deposited with faceted morphology (contains  $sp^3$  bonds) gives best combination of morphological and topographical parameters. The friction forces of diamond film are governed by adhesion force and it is minimal for film having fine ballas morphology (contains microcrystalline graphite). Film with coarse ballas morphology possesses highest relative elastic modulus and maximal friction coefficient.

#### MICRO- AND NANOMECHANICAL PROPERTIES OF DIAMOND FILMS WITH VARIOUS SURFACE MORPHOLOGIES

A. Bogus<sup>1</sup>, I.C. Gebeshuber<sup>1,2</sup>, A. Pauschitz<sup>2</sup>, Manish Roy<sup>2</sup> and R. Haubner<sup>3</sup>

<sup>1</sup> Institute for Applied Physics, Vienna University of Technology, Wiedner Hauptstrasse 8-10/134, 1040 Wien

<sup>2</sup> Austrian Center of Competence for Tribology, Viktor Kaplan-Strasse 2, 2700 Wiener Neustadt, Austria

<sup>3</sup> Institute of Chemical Technologies and Analytics, Vienna University of Technology, Vienna, Austria

DIAMOND & RELATED MATERIALS

Volume 17, June 2008, Pages 1998-2004

## ABSTRACT

The morphologies of chemical vapour deposited (CVD) diamond films can be changed over a wide range by controlling the process parameters of the deposition. The surface morphologies of the film in turns, govern the micro- and nanomechanical properties of the film. In view of these, diamond films having three different types of morphologies namely coarse ballas, fine ballas and faceted, have been deposited using micro wave chemical vapour deposition (MWCVD) technique. The morphology, and nature of bonds of these films are characterised with the help of scanning electron microscopy (SEM) and Raman spectroscopy. Hardness of the films is evaluated using nanoindenter. Force spectroscopy, topographies and lateral force values of these films are estimated by means of atomic force microscopy (AFM). Results indicate that films having fine ballas morphology exhibit the minimum roughness whereas film with faceted morphology has highest relative hardness. The friction force was found to be minimum with the film having fine ballas morphology and the friction force was maximum with film having coarse ballas morphology.

## INTRODUCTION

Diamond film is one of the hardest materials and is well known for several extraordinary features such as high mechanical strength [187], excellent thermal conductivity [188], outstanding wear and friction properties [189, 190], high chemical inertness [191] etc. These films exhibit high surface roughness because of their columnar growth [192] making it unsuitable for many applications such as in microelectronics and as optical components [193, 194]. However, end use tends to favour a particular crystallographic surface texture, purity and thickness matched to the surface that offers the most compatible properties. Thus, properties e.g. broad optical transparency, high refractive index, wide band gap, low or negative electron affinity, transparency to light from deep ultra violet to far infrared and low thermal expansion make these films suitable for numerous industrial applications[195].

Consideration of desired properties of microelectromechanical systems (MEMS) reveals chemical vapour deposited (CVD) diamond as a candidate materials. Development of "flatland" technology has seen diamond MEMS in the form of seismic mass membrane accelerometer, microspot heater for a liquid ejector [196] and electrostatically actuated microswitch [197]. Amorphous diamond is also used to produce a comb drive actuator [198]. Development of selective deposition micropatterning of diamond on Si and SiO<sub>2</sub> has given movable microgrippers, V-shaped cantilevers and tips for an atomic force microscopy (AFM) [199]. Further,

diamond is micromachined by pulsed excimer laser irradiation [200]. Patterning of diamond film by reactive ion etching has given beam like and turning fork like resonators [201].

Deposition of diamond by CVD process has extensively been studied in the last decade [202, 203]. Yugo et al. [204] developed a method to enhance growth rate of diamond by applying a bias enhance nucleation (BEN). This method has also helped in overcoming the difficulties of heteroepitaxial nucleation of diamond on Si substrates with substantial lattice mismatch of 52 % between the bulk lattice constant of diamond and Si. Subsequently several studies were conducted employing this method [205, 206, 206]. Synthesis of diamond film aims at faceted diamond layers even though hemispherical polycrystalline diamonds (ballases) are also found under non optimal growth conditions [207, 208]. The CVD ballas films are also known as cauliflower-like, ball-shaped diamond layers. Faceted diamond layers can be obtained for a wide range of depositing parameter. These methods are based on activation of CH<sub>4</sub>/H<sub>2</sub> gas mixtures in order to generate large amounts of atomic hydrogen and carbon radicals [209]. If there is super saturation of carbon in the gas phase, growth conditions of faceted diamond becomes poor and a high density of twins and stacking faults is introduced [210]. This finally, leads to radial growth of polycrystalline unfaceted diamonds of "ballas-type" [211].

In this paper, the influence of surface morphologies such as faceted, fine ballas and coarse ballas on the micro- and nanomechanical properties of microcrystalline diamond film deposited by microwave plasma chemical vapour deposition (MWCVD) process has been evaluated.

## EXPERIMENTAL DETAILS

### Deposition of the film

Diamond films were deposited using an ASTEX microwave plasma CVD apparatus. The system has a stainless steel chamber and it operates at 2.45 GHz, 1.5 kW. It is equipped with a heated graphite substrate holder. Silicon (100) substrates scratched with diamond powders<sup>3</sup> were used for deposition of film. Si was scratched with 0.25 mm diamond powders for 30 min and then cleaned ultrasonically. The substrate temperatures were measured with the help of an optical pyrometer. Deposition parameters such as gas pressure, gas flow and microwave power were kept constant. The ratio of CH<sub>4</sub> to H<sub>2</sub>, substrate temperature and deposition time were varied.

---

<sup>3</sup>Most substrates used for diamond growth are preliminary scratched with diamond powder(roughening) in order to enhance nucleation kinetics.

### Characterization of the film

The morphologies of the films were examined using a scanning electron microscopy (SEM). Raman spectra were obtained by an integrated confocal micro-Raman system. LabRam Aramis (Horiba Jobin Yvon) spectrometer equipped with a BXFM confocal microscope and a charge-couple device (CCD) multichannel detector was used for this purpose. The excitation source was a diode pumped solid state (DPSS) laser emitting green light at 532 nm with 50 mW power. On the incoming path, the laser beam was reflected towards the microscope, and the parallel laser beam was then focused onto the sample by a 10x microscope objective. The Raman signal was collected by the same microscope objective and followed the return path to the spectrograph. The backscattered laser light was filtered out. The spectrometer hole and slit widths were set to 1000  $\mu\text{m}$  and 100  $\mu\text{m}$ , respectively and the grating to 1800 grooves/mm.

### AFM measurement

AFM and lateral force microscopy (LFM) images of the films were obtained with an AFM MFP-3D (Asylum Research, Santa Barbara, CA) in air at ambient condition. Silicon nitride tips, a triangular cantilevers with a spring constants of 0.1 N/m were used, the scan area was 5 x 5  $\mu\text{m}^2$ . Images were recorded in the 'constant-force' mode, that is, feedback electronics and the corresponding software were used to keep the cantilever at constant deflection and to measure the sample topography. In order to obtain the maximum LFM signal (torsion motion), the sample was scanned along the direction perpendicular to the cantilever long axis. The lateral force was evaluated from the difference in the torsional signals (displayed as output voltage) at forward and reverse scans on the lateral force (friction) loop. For each applied force, 512 lateral force loops over a distance of 5  $\mu\text{m}$  were obtained from different regions. The important features of the cantilever used for AFM study are listed in Table 5.13. Force calibration was performed for each sample.

|                            |                         |
|----------------------------|-------------------------|
| Material                   | $\text{Si}_3\text{N}_4$ |
| Cantilever spring constant | 0.1 N/m                 |
| Cantilever arm length      | 140 $\mu\text{m}$       |
| Cantilever arm width       | 18 $\mu\text{m}$        |
| Resonance frequency        | 38 kHz                  |
| Full tip opening angle     | 35°                     |
| Tip radius                 | 10 nm                   |

Table 5.13: The important features of the cantilever used for AFM study.

### Nanohardness measurement

The hardness and the elastic modulus of these films were determined with the help of an instrumented indentation tester equipped with a Berkovich three sided pyramidal diamond indenter with a nominal angle equal to  $63.5^\circ$ . The instrument was placed inside a vibration free isolated chamber. This was a depth sensing indenter. The applied load was 4 mN. The load was selected so as to keep the deformation confined within the film. The load and displacement resolution of the instrument was 50 nN and 0.1 nm respectively<sup>4</sup>. The holding time of indentation was 5 s in all cases. Both loading and unloading time was 10 s. The experimental results were corrected for the thermal drift of the equipment, and for the uncertainty in the zero position. The reported hardness and elastic modulus has average of 10 indentations for each sample on different surface position separated by 50  $\mu\text{m}$ . The elastic modulus was determined using a procedure enumerated elsewhere [212]. Elastic modulus was calculated employing equation Eq. 5.12 as given below.

$$\frac{1}{E_r} = \frac{(1 - \nu^2)}{E} + \frac{(1 - \nu_i^2)}{E_i} \quad (5.12)$$

where  $E_r$  is given by:

$$E_r = \frac{0.89S}{\sqrt{A}} \quad (5.13)$$

where  $S$  is the slope of the initial part of the unloading curve (in N/m),  $A$  is the contact area between the indenter and the substrate (in  $\text{m}^2$ ).  $E$  and  $E_i$  are the elastic moduli and  $\nu$  and  $\nu_i$  are the Poisson ratios of the film and the indenter respectively. The nanoindenter was calibrated by indenting on a fused silica sample and measuring the hardness and elastic modulus of fused silica with hardness and elastic modulus approximately 10 and 73 GPa respectively. Measurement was performed at in a clean air environment with a relative humidity of approximately 40% while the temperature was around  $22^\circ\text{C}$ .

## RESULTS AND DISCUSSION

SEM images showing the morphologies of the diamond films are presented in Fig. 1. The morphologies and the structures of the films differ considerably. The film D1 grown at 2%  $\text{CH}_4$  consists of crystallites with faceted morphologies having cubo-octahedral and icosahedral symmetries. This crystallite faceted CVD grown diamond can contain many defects [213, 214]. Micro twins are mainly observed in (111) growth sectors, while dislocations are mainly observed in the (100) growth

---

<sup>4</sup>Vertical displacement of the tip is determined by measuring the displacement of the center plate relative to the two outer plates using the change in capacitance.

sector. Film D2 exhibits radially grown coarse ballas morphology. This morphology is obtained when diamond is grown under condition close to faceted diamond regions [213]. TEM observations of this ballas showed large single crystalline diamond areas in a micro-twined matrix. Film D3 is relatively featureless. In this film also fine ballas can be seen. This ballas morphology can be seen when the film is grown close to graphitic region. This type of morphology is characterised by homogenous microtwinned matrix.

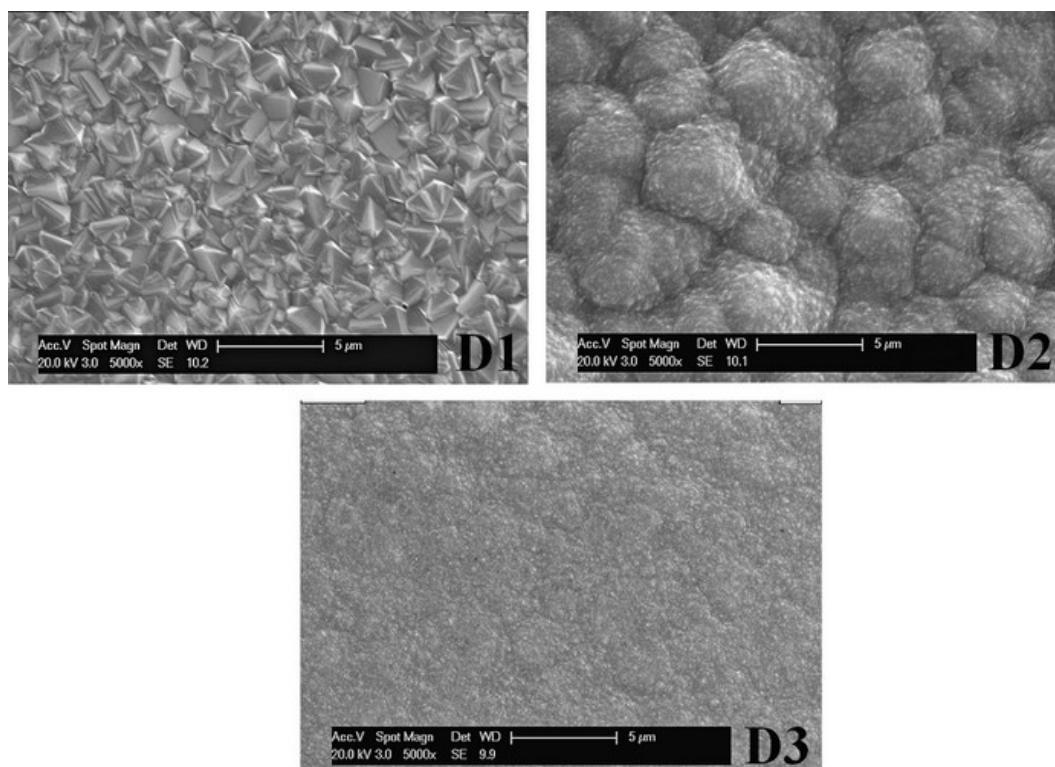


Figure 5.52: SEM images showing the morphologies of investigated films.

Raman spectra obtained from all the films are presented in Fig. 5.53. All three films show peaks at wave number ( $1340\text{ cm}^{-1}$ ) corresponding to  $\text{sp}^3$  bond. The corresponding bond for pure diamond is at  $1330\text{ cm}^{-1}$ . This peak is very prominent for the D1 and D2 film and very weak for the D3 film. Film D1 has only one peak. The spectra of the film D2 consists of a broad band between  $1400$  to  $1650\text{ cm}^{-1}$ . This can be deconvoluted in to two peaks at  $1470\text{ cm}^{-1}$  and  $1560\text{ cm}^{-1}$ . The peak at  $1470\text{ cm}^{-1}$  is commonly observed in nanocrystalline diamond films [215–218]. Ferrari and Robertson [219] however, assigned this peak to transpolyacetylene situated at the grain boundaries of diamond nanocrystals. The peak at  $1560\text{ cm}^{-1}$  can be assigned to the G band of microcrystalline graphite. The presence of this band proves existence of  $\text{sp}^2$  bonded carbon within the film. At this point, it

should be stated that due to resonance effect [220, 221], Raman measurement with excitation at 532 nm is much more sensitive to  $sp^2$  carbon than  $sp^3$  carbon. Film D2 also exhibits the presence of a weak peak at wave number  $1160\text{ cm}^{-1}$ . This peak can also be assigned to diamond nanocrystal. The Raman spectra of the film D3 is characterised by a weak peak at  $1160\text{ cm}^{-1}$ , a weak and broad peak in the band of  $1300\text{ cm}^{-1}$  to  $1400\text{ cm}^{-1}$  and another broad peak in the band from  $1400\text{ cm}^{-1}$  to  $1650\text{ cm}^{-1}$ . These peaks at  $1160\text{ cm}^{-1}$  and in the band from  $1400\text{ cm}^{-1}$  to  $1650\text{ cm}^{-1}$  belong to diamond nanocrystals, G band of microcrystalline graphite and diamond nanocrystal respectively, as described for film D2. The broad peak in the band of  $1300\text{ cm}^{-1}$  to  $1400\text{ cm}^{-1}$  can be deconvoluted in to two peaks at  $1330\text{ cm}^{-1}$  and  $1370\text{ cm}^{-1}$ . While the peak at  $1330\text{ cm}^{-1}$  corresponds to diamond, the peak at  $1370\text{ cm}^{-1}$  will certainly pertain to the D band of microcrystalline graphite. Thus, film D1 is the best diamond film.

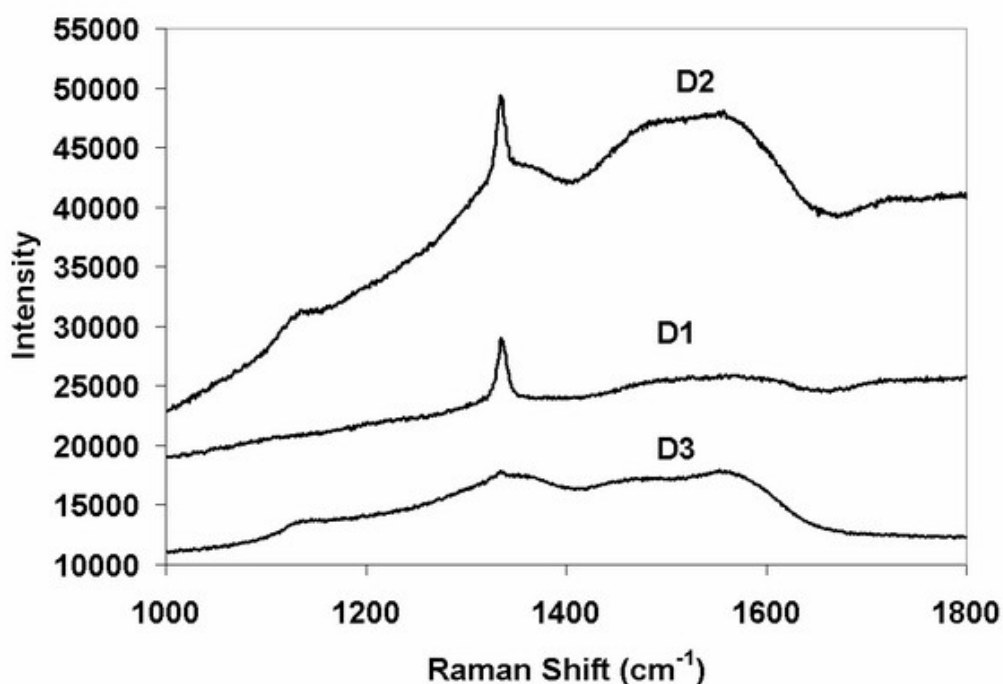


Figure 5.53: Raman spectra of investigated films.

To understand the nature of interaction between the cantilever tip and the coating, the deflection displacement curves are recorded. Figure 5.54 shows the deflection of the cantilever tip as a function of the distance from the film surfaces for all three films. In all cases, darker line indicates tip approach and lighter line represents the tip being pulled away. The vertical separation between point where the tip is touching the film and point where the tip is pulled off the film is

a measure of the pull off (adhesive) force. The product of this horizontal distance of separation and the spring constant of the cantilever (0.1 nN/nm) gives the pull off forces [222]. The pull off forces for film D1, D2 and D3 are 21.3 nN, 81.5 nN and 13.1 nN respectively. It can clearly be seen that the pull off force for film D2 is significantly larger than the pull off forces for film D1 and D3. This fact may be related to increase of surface energy due to oxygen adsorption of the surface. These values are substantially lower than the pull off force calculated to be 445 nN for Ti/a-C : H film and comparable to the pull off force of 76.4 nN PECVD diamond film reported previously [223].

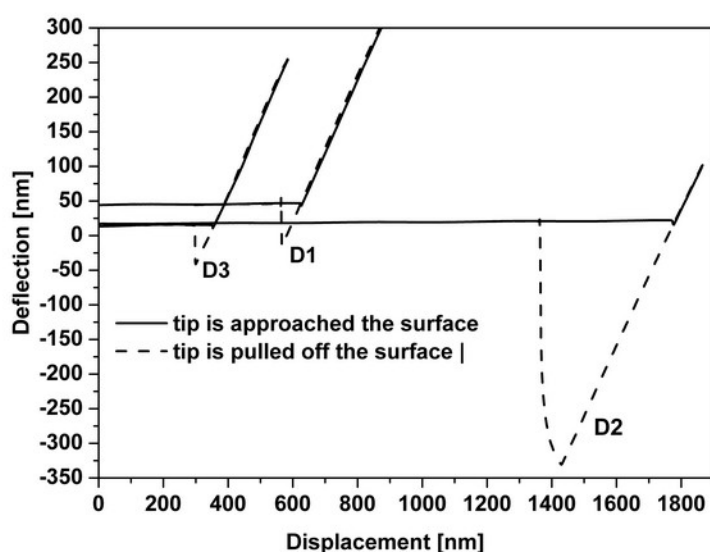


Figure 5.54: Force spectroscopy of the investigated films.

The three dimensional AFM images showing the topographies of all the films are illustrated in Fig. 5.55. Film D2 can be characterized with faceted topographical feature. Film D1 exhibits presence of several small peaks on relatively big dome like peak. Film D3 has sharp conical deep but small peaks uniformly distributed. Various topographical parameters are summarized in Table 5.14. The root mean square (RMS) value of film D2 is higher than that of films D1 and D3. This RMS value is quite high as compared to Ti/a-C:H film and PECVD diamond film [223]. However, the maximum height of film D1 and film D3 are comparable with the maximum height of Ti/a-C:H film and PECVD diamond film [223].

The load vs. displacement curves for all three films are provided in Fig. 5.56. The load vs. displacement curves of these films are obtained essentially by superposition of 10 different curves. It should be mentioned here that the depth of penetration is quite low as compared to the roughness of diamond surfaces. Thus,

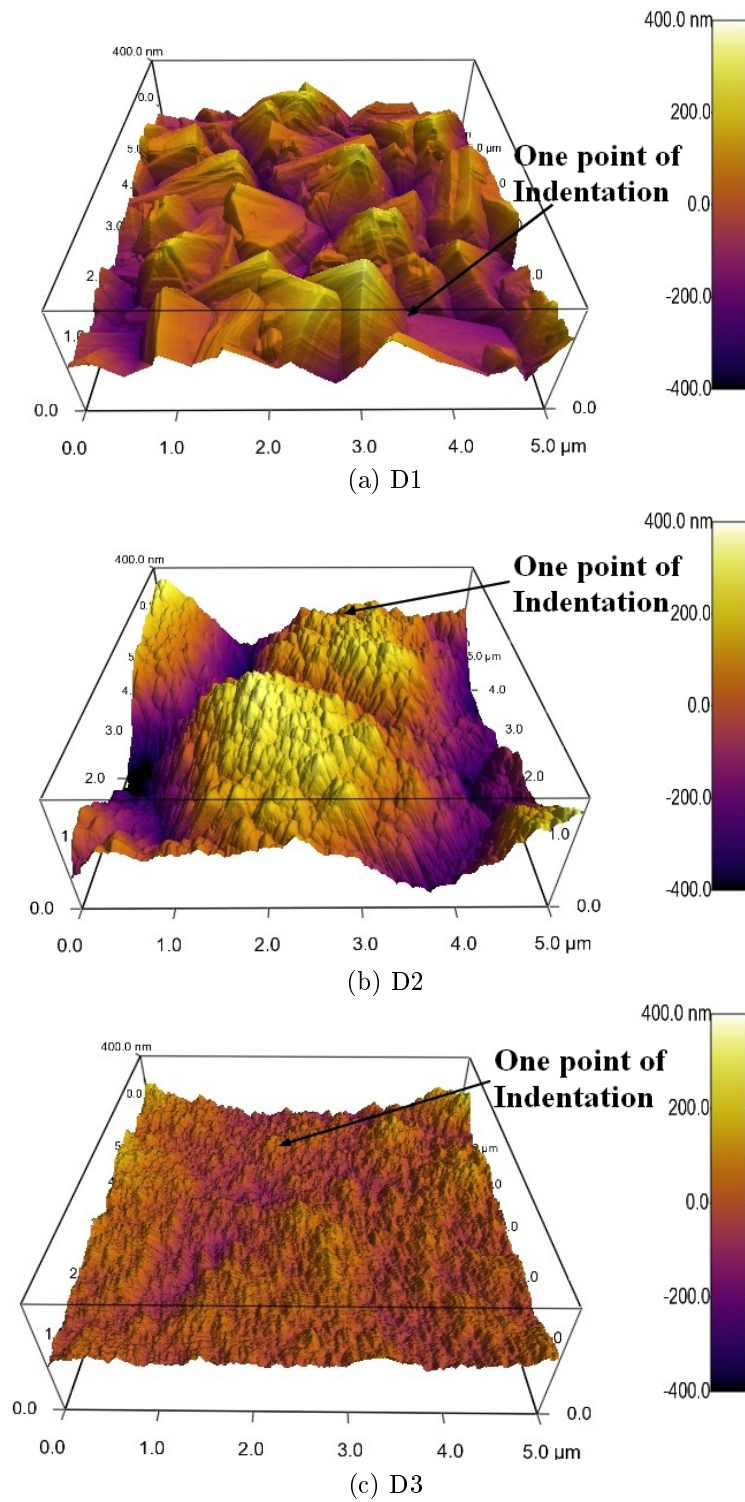


Figure 5.55: Topographies of the investigated films.

| Films | Parameters          |                 |                     |                     |
|-------|---------------------|-----------------|---------------------|---------------------|
|       | Average Height (nm) | R.M.S (nm)      | Minimum Height (nm) | Maximum Height (nm) |
| D1    | $-66.0 \pm 1.6$     | $66.0 \pm 1.3$  | -67.6               | -64.3               |
| D2    | $151.0 \pm 9.2$     | $151.4 \pm 7.8$ | 209.6               | 152.2               |
| D3    | $29.9 \pm 2.4$      | $30.0 \pm 1.7$  | 27.9                | 33.0                |

Table 5.14: Topographical parameters of the films.

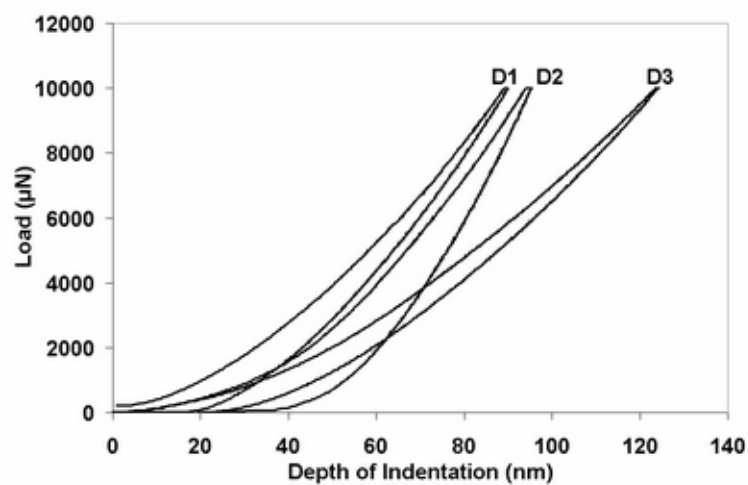


Figure 5.56: Load vs. displacement curves of the investigated films.

the roughness criteria is not fulfilled in this case. As higher depth of penetration will result is influence of the substrate, a higher depth of penetration is not possible. However, indentation points are selected carefully. The selected indentation areas for one indentation for each film are marked by arrow in Fig. 5.55. Given the fact that each curve (load vs. displacement) is super imposition of 10 different curves and given the reproducibility of the data, the load vs. displacement curves can be considered to be at least relative representation of the film properties even though a valid indentation test can not be performed on such rough films. Very high elastic deformation is evident for these films. The maximum depth of penetration and the residual depth of penetration of all these films are summarized in Table 5.15. The relative elastic modulus and relative hardness of these films are also given in Table 5.15. The film D3 has the maximum depth of penetration. Film D1 exhibits the minimum depth of penetration and the minimum elastic recovery, as this film has the minimum depth of penetration and the moderate residual depth. The relative elastic modulus of film D1 and D2 are comparable and higher than the elastic modulus of film D3. Among all these films, the maximum relative hardness is exhibited by film D1 having faceted morphology.

| Films | Maximum Depth of Penetration (nm) | Residual Depth of Penetration (nm) | Elastic Modulus (GPa) | Relative Hardness (GPa) |
|-------|-----------------------------------|------------------------------------|-----------------------|-------------------------|
| D1    | 90                                | 16                                 | $535.5 \pm 22.0$      | $82.9 \pm 3.4$          |
| D2    | 95                                | 20                                 | $563.5 \pm 35.0$      | $58.5 \pm 4.8$          |
| D3    | 124                               | 20                                 | $379.2 \pm 38.0$      | $59.3 \pm 6.1$          |

Table 5.15: Elastic Modulus and Hardness of various films.

Two dimensional AFM images of the friction force values of all three films are displayed in Fig. 5.57. These images were obtained for an applied load of 4.5 nN and a scan speed of  $10 \text{ ms}^{-1}$ . Clearly film D2 has significantly higher friction force than the other two films. The peaks are more prominent in forward scan than in reverse scan, signifying that the friction force on the film is quite high, especially when the film traverses the top of the grain during forward scanning. Furthermore, the average friction force during forward scanning is higher than that during reverse scanning. The friction force of various films are evaluated from the friction force values following the procedure suggested by Beake et al. [224], the friction force( $F_L$ ) is given by:

$$F_L = 1/2(LF(f) - LF(r)) \quad (5.14)$$

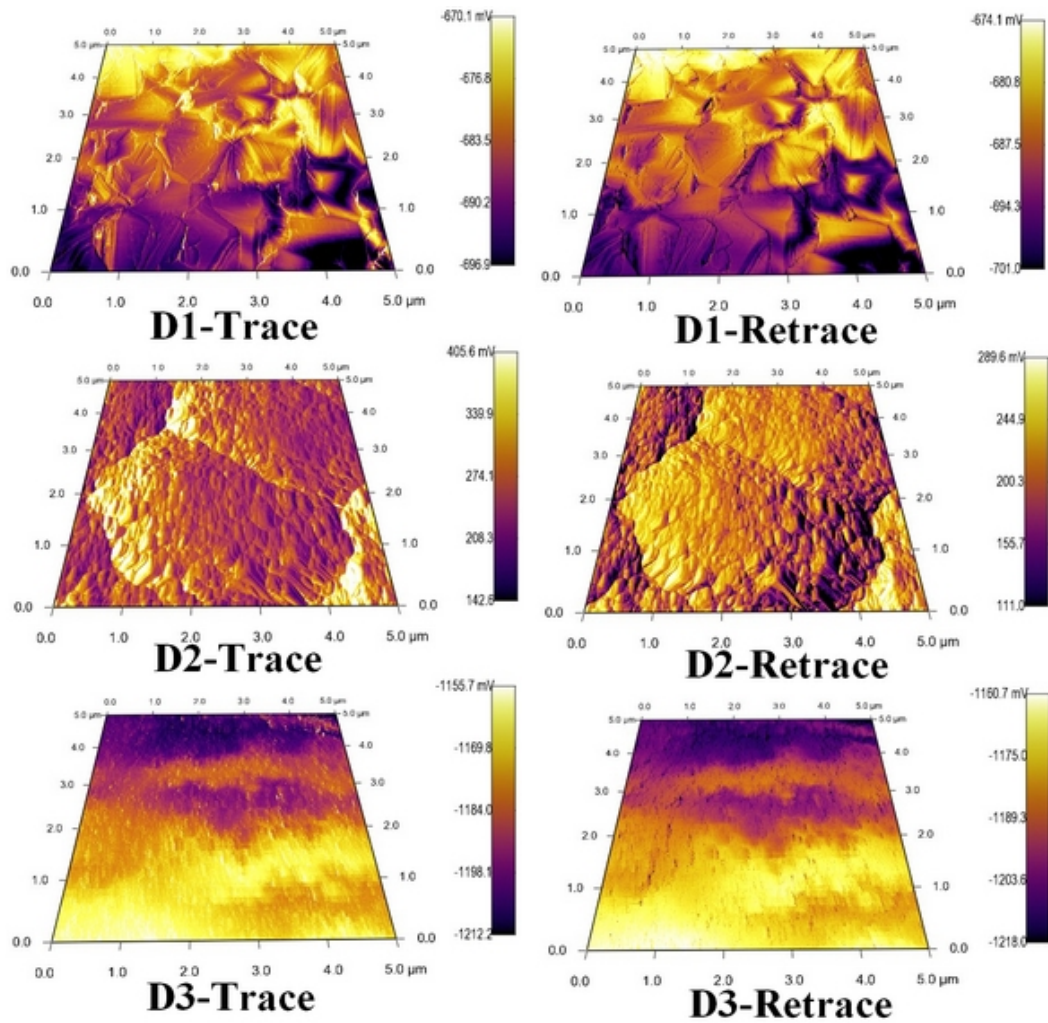


Figure 5.57: Lateral force images of the investigated films.

where  $LF(f)$  and  $LF(r)$  are the signals in the forward and reverse direction of motion of the tip in LFM mode.

This is based on the fact that when there is substantial variation of the surface topography, the LFM signal contains a component due to normal force acting through the local slope. Since lateral force is determined from the difference between signals reaching the left and the right halves of a four segments photo detector, the topographic contribution of the LFM image may be eliminated by subtracting signals recorded in opposite directions.

The variation of friction force as a function of scan speed for all the films at two different applied loads is presented in Fig. 5.58. Clearly film D2 has a higher friction force than film D1 and film D3. A higher surface roughness of film D2 compared to films D1 and D3 may be responsible for this behavior. In general, friction force is independent of scan speed for film D1 and D3. In contrast, friction force decreases with increase of scan speed for film D2. The influence of applied

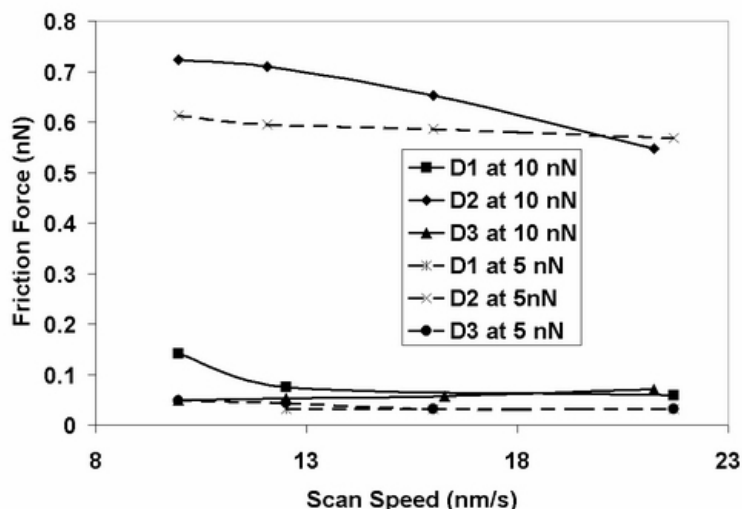
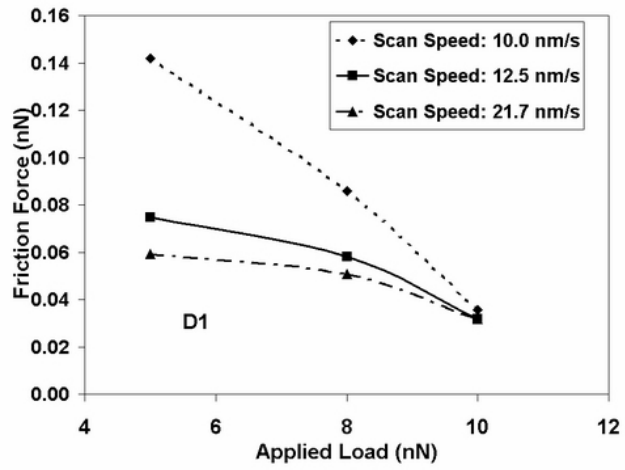
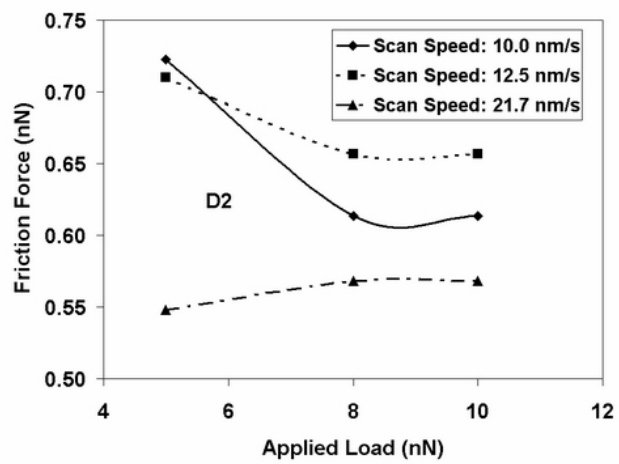


Figure 5.58: The influence of scan speed on the friction force of the investigated films.

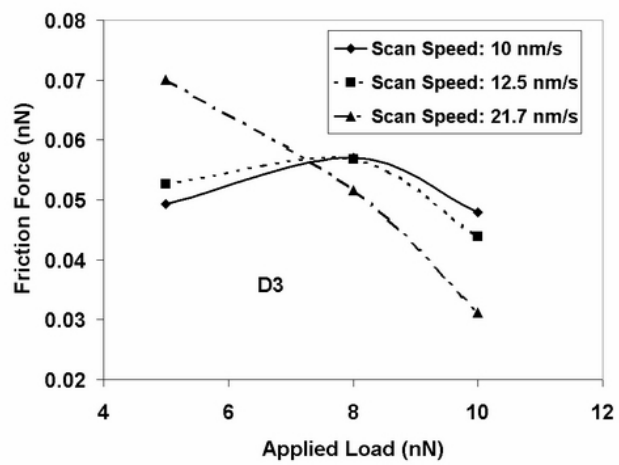
load on the friction force is depicted in Fig. 5.59. In most of the cases investigated, the friction force decreases with increase of applied load. This suggests that friction force is not governed by ploughing mechanism since in this case, the friction force would increase with increase of applied load when ploughing plays important role. Rather it is controlled by surface force. Friction can be described as dissipation of energy at the sliding interface. In order to evaluate the possible friction dissipation mechanism, adhesion can be considered to play an important role. Since experiments are conducted in ambient condition the pull off force is



(a) D1



(b) D2



(c) D3

Figure 5.59: The influence of applied load on the friction force of the investigated films.

a measure of adhesion induced friction force. Perusal of pull off force and friction force indicates that pull off force increases in the order  $D3 < D1 < D2$ . Similarly the friction force also follows the trend  $D3 < D1 < D2$ . Thus adhesion force influences friction force appreciably.

In the wear under nN load, two additional friction dissipation mechanisms besides adhesion become important. The first mechanism is by emission of photons [225, 226]. The second mechanism is energy dissipation by electron-hole pair mechanism [227]. Generally, phononic mechanism is considered to be the dominant mechanism [228, 229] in diamond film. In the present investigation, film D1 and D2 are rich in  $sp^3$  hybridisation whereas film D3 is poor in  $sp^3$  hybridisation. Thus, different energy dissipation mechanisms can be considered for these films. If phononic mechanism can be considered to be the dominant mechanism, then the friction force should be either high for both D1 and D2 film and low for D3 film or vice versa. The present observation on friction force indicates completely different behavior and they are independent of  $sp^3$  hybridisation. Thus in the present work, phononic mechanism does not play influencing role.

It is reported [230] that friction and wear of diamond films can be reduced on the macroscopic scale by adding  $sp^2$  bonds. This observation is valid partially in the present investigation. The friction force is less for D3 having  $sp^2$  bond than film D1 without  $sp^2$  bond. However, the friction force of D2 film having  $sp^2$  bond is higher than the friction force of D1 film. This may possibly be related to the higher roughness of D2 film than D1 film.

At this stage, it should be mentioned that use of microcrystalline films are limited because of their high roughness. In present days, variety of processes are available for depositing nanocrystalline diamond film having low roughness and smooth diamond film [231]. The friction behavior of nanocrystalline diamond is characterised by roughness independent low friction coefficient and friction coefficient is governed by transfer of carbonaceous film [232]. The wear mechanism in nanocrystalline diamond film is primarily microabrasion [233]. This wear mechanism gives rise to ultra smooth surface and wear coefficient characteristics of mild wear regime [234]. The friction coefficient mostly show high initial friction followed by running in period of low friction coefficient [233]. Unfortunately nanotribology of nanocrystalline diamond film is not yet reported and it appears to be an interesting area of future study. Hitherto no report has been found in relation to transfer of materials in nanotribological study [235]. Thus possibility of carbonaceous transfer layer reducing friction coefficient can be ruled out for the time being. Further, as is the case with most of the materials, nanocrystalline diamond

film is expected to have higher hardness than microcrystalline diamond film with similar morphology. However, during nanotribological process, it is the surface force rather than applied load that governs the friction behavior. Thus increased hardness due to fine grains is unlikely to contribute towards improvement of wear and friction behavior of nanocrystalline diamond film in nanotribological regime.

**CONCLUSIONS:**

1. The micro and nanomechanical properties of MWCVD diamond films having faceted, fine ballas and coarse ballas morphologies are evaluated.
2. Study with Raman spectroscopy reveals that diamond films with ballas morphologies contain microcrystalline graphite.
3. Diamond film with faceted morphology exhibit highest relative hardness and film having coarse ballas morphology possesses highest relative elastic modulus.
4. The diamond film deposited with faceted morphology gives best combination of morphological, topographical parameters.
5. The friction forces of MWCVD diamond film are governed by adhesion force. The friction force is the minimum with the film having fine ballas morphology.

**Acknowledgement:**

Authors are grateful to European Commission for supporting this work through their program 'WEMESURF' and through their project No. MIF1-CT-2006-039220. Authors are also grateful to Dr. Thomas Koch from Institute of Materials Science and Technology, Vienna University of Technology, for carrying out the nanoindentation study.

### 5.3.2 Nanotribology of Mo-Se-C Films

"*Nanotribology of Mo-Se-C Films*" [7] examines topography, lateral force and pull off force of transition metal dichalcogenides film at an applied load in the range of nanonewton. The effect of carbon content, applied load and scanning speed on the friction coefficient was evaluated. Observed nanotribological behavior of these films was analyzed in the light of their nanohardness. Chemical analysis showed that these films consist of very fine MoSe<sub>2</sub> grains embedded in a carbon matrix. The conclusion state that carbon content has significant influence on all investigated parameters. With increasing carbon content of the films tested, the hardness increases and wear volume decreases. The friction force of all the films is very low and in general dependent on surface pull-off forces. The film having the highest carbon content exhibits the maximum friction force.

#### NANOTRIBOLOGY OF MO-SE-C FILMS

A. Tomala<sup>1</sup>, Manish Roy<sup>2</sup> and F. Franek<sup>3,4</sup>

<sup>1</sup> Institute for Applied Physics, Vienna University of Technology, Wiedner Hauptstrasse 8-10/134, 1040 Vienna, Austria

<sup>2</sup> Defence Metallurgical Research Laboratory, PO: Kanchanbagh, Hyderabad: 500058, India

<sup>3</sup> Austrian Center of Competence for Tribology, Viktor Kaplan-Strasse 2, 2700 Wiener Neustadt, Austria

<sup>4</sup> Institute of Sensor and Actuator Systems, Vienna University of Technology, 1040 Vienna, Austria

PHILOSOPHICAL MAGAZINE

Volume 90, Number 29, October 2009, Pages 3827-3843

#### ABSTRACT

Transition metal dichalcogenides having layered structure are well known for their self-lubricating properties, particularly in vacuum or dry atmosphere. The macrotribological properties of these films have been studied extensively. However, the tribological behavior of these films in the nanonewton load range has hardly been reported. Study of tribological properties with load in the nanonewton range is required for applications related to micro electro mechanical systems or nano electro mechanical systems. In view of the above, the present work is undertaken to examine hardness, surface force, friction force etc. of Mo-Se-C film at an applied

load in the range of nanonewton using nanoindenter and atomic force microscopy. The effect of carbon content, applied load and scanning speed on the friction coefficient is presented. Data pertaining to topography, lateral force and pull off force of various surfaces are illustrated. The observed nanotribological behavior of these films is analyzed in the light of their nanohardness. The results indicate that friction force of all the films are very low and in general dependent on surface force. However, film having highest carbon content exhibits the maximum friction force. With increasing carbon content of the films tested, the hardness increases and wear decreases. The above results pertain to investigation at ambient condition.

### INTRODUCTION

Transition metal dichalcogenides (TMD) are compounds of hexagonal layered structures. In these compounds a hexagonal sheet of metal atoms is sandwiched between two hexagonally packed chalcogen layers. The bonding between metal and chalcogens is covalent, whereas the sandwiches themselves are held together by weak von der Waals forces. Therefore, easy slip between lamellae takes place during sliding particularly when the basal planes are parallel to the sliding surfaces. In addition, other tribological phenomena such as transfer of layers to the counterface etc. take place during sliding of TMD. Having basal planes parallel to the sliding surface is very important as friction forces increase when the basal planes are perpendicular to the sliding surfaces.

Among various TMD, MoSe<sub>2</sub> layers have received considerable attention for photoelectrochemical solar energy conversion due to their well-matched band gap with the solar spectrum [236]. In tribological applications, MoSe<sub>2</sub> offers a lower friction coefficient compared to WS<sub>2</sub> and the friction coefficient is almost independent of humidity [237]. Molybdenum diselenoid is more resistant to oxidation in humid ambient than molybdenum sulphide [238]. Although, a variety of films are deposited by several techniques [239–244], deposition by magnetron sputtering has become increasingly popular. In this method, the deposition parameters can empirically be optimised by changing discharge power, gas pressure, position of the substrate relative to the sputtered target, bias voltage and substrate temperature [245–248]. Comparing molybdenum disulphides and diselenides, the metal to chalcogen mass ratio is closer to 1 in the latter case [239], and this limits the re-sputtering of selenium from the coating. Therefore, a higher chalcogen-metal ratio compared to sputtered Mo-S could be expected.

The macrotribological properties of MoSe<sub>2</sub> film have already been studied to a limited extent [237, 239]. The more promising results have been achieved by doping Mo-Se coating with carbon and this significantly improved load-bearing

capacity and frictional behavior in humid air [53, 249]. However, tribological studies at very low load for applications related to microelectromechanical systems (MEMS) or micro mechanical assembly (MMA) have received little attention. The friction of cleaved MoS<sub>2</sub> surface sliding against Si<sub>3</sub>N<sub>4</sub> in a LFM test has been studied [250]. Nanotribological studies of metal dichalcogenides using scanning probe microscopy have revealed excellent lubricating properties even in atomic scales [251, 252]. Santos et al. [253] noted a wide range of friction coefficients due to surface contamination of the MoS<sub>2</sub> film. Cohen et al. [254] found fullerene-like nanoparticles or nanotubes of dichalcogenides exhibited significantly low friction coefficients against Si, mica and quartz. Zhang and Celis [255] reported the transfer of materials from MoS<sub>2</sub> film to the Si<sub>3</sub>N<sub>4</sub> tip, the wear of the MoS<sub>2</sub> film and the independency of the friction coefficient on the frequency of oscillation during the nanotribological study of MoS<sub>2</sub> film under oscillating nano and micro sliding test.

Moving parts of micro electro mechanical systems (MEMS) or micro mechanical assemblies (MMA) having very high surface to volume ratio are subjected to undesirable effects such as sticking or high friction force leading to operational failures. Under ambient condition various carbon films offer reasonable solution. However, when different atmosphere is required, such as vacuum, dry and humid air, elevated temperature up to 200 °C, the Mo-Se films doped by carbon (Mo-Se-C) could be considered to be potential substitute for carbon films. The present study analyses the influence of carbon content on the nanotribological behavior of Mo-Se-C film deposited by non reactive magnetron sputtering.

## EXPERIMENTAL DETAILS

### Deposition of the films:

The Mo-Se-C coatings were deposited by r.f. magnetron sputtering of a carbon target with pellets of MoSe<sub>2</sub> in a basic ESM 100 Edwards unit in an argon atmosphere following a similar procedure as presented in a previous research [256]. The pellets (99.8% pure) with dimensions of 1.5 × 3 × 4 mm were distributed uniformly in the circular erosion zone of the carbon target; their number varied between 16 and 72. Before deposition, the substrates were cleaned for 30 min by establishing the plasma close to the substrate electrode. A thin titanium interlayer (≈300 nm) was deposited in order to improve the adhesion of the coatings to the substrate. The discharge pressure and the power density were 0.75 Pa and 8 W/cm<sup>-2</sup>, respectively. The deposition time was 1 h giving rise to a final thickness of the coatings in the range of 2 μm. No substrate bias was applied during the deposition.

### Characterization of the films:

The chemical composition and the cross-section morphologies of these films were analysed by a Cameca *SX50* electron probe microanalysis (EPMA) apparatus and a *Jeol* scanning electron microscope (SEM) respectively. X-ray diffraction patterns were obtained from the coated surfaces using *Philips PW1830* diffractometer in glancing mode to examine the structure of these films. The X-ray diffractometer was set at 40 KV and 30 mA with  $CoK_{\alpha}$  radiation target and a nickel filter. The diffraction patterns were recorded at a speed of  $0.01^{\circ}s^{-1}$ . Raman spectra were obtained by an integrated confocal microRaman system, *LabRam Aramis* (Horiba Jobin Yvon) spectrometer equipped with a BXFM confocal microscope and a charge-couple device (CCD) multichannel detector. The excitation source was a diode pumped solid state (DPSS) laser emitting green light at 532 nm with 50 mW power. The Raman signal was collected by the same microscope objective and followed the return path to the spectrograph. The backscattered laser light was filtered out. The spectrometer hole and slit widths were set to 1000  $\mu\text{m}$  and 100  $\mu\text{m}$ , respectively and the grating to 1800 grooves/mm.

**Nanohardness measurement:**

The hardness and the elastic modulus of these films were determined with the help of an instrumented indentation tester equipped with a Berkovich three sided pyramidal diamond. The instrument was placed on a vibration free isolated chamber. The applied load was 2 mN. The load was selected so as to keep the deformation confined within the film. The load and displacement resolution of the instrument was 50 nN and 0.1 nm respectively. The holding time of indentation was 5 sec in all cases. Both loading and unloading time were 10 sec. The experimental results were corrected for the thermal drift of the equipment and for the uncertainty in the zero position. The reported hardness and elastic modulus is the average of 10 indentations for each sample on different surface positions separated by 50  $\mu\text{m}$ . The elastic modulus was determined using a procedure enumerated elsewhere [257]. The nanoindenter was calibrated by indenting on a fused silica sample and measuring the hardness and elastic modulus of fused silica having hardness and elastic modulus approximately 10 and 73 GPa respectively. Measurements were performed in a clean air environment with a relative humidity of approximately 40% while the temperature was around 22  $^{\circ}\text{C}$ .

**AFM measurement:**

AFM and LFM images of these films were obtained with a *AFM MFP-3D* (Asylum Research, Santa Barbara, CA) in ambient condition. Silicon nitride tips on a triangular cantilever *V* shaped with low spring constant were used for nanotribological tests. Silicon tips on aluminum coated cantilever (*OLYMPUS OMCL-HA*)

were used to perform nanowear tests. Silicon tips on aluminium coated cantilever (OLYMPUS OMCL-HA) were used to perform nanowear tests. The important features of both cantilever types used for the study are listed in Table 5.16. The cantilevers were calibrated for topography mode and pull off force mode using a silicon chip. After calibration, the accurate value of spring constant for silicon nitride tips was 0.175 N/m, and for silicon tips was 43.432 N/m. The scan area was  $5 \times 5 \mu\text{m}^2$ . Images were recorded in the contact mode, i.e. the feedback electronics and the corresponding software was used to keep the cantilever at constant deflection measuring the sample topography. In order to obtain the maximum LFM signal (torsion motion), the sample was scanned along the direction perpendicular to the cantilever long axis. The lateral force was evaluated from the difference in the torsional signals (displayed as output voltage) at forward and reverse scans on the lateral force (friction) loop. For each applied force, 512 lateral force loops on an area of  $25 \mu\text{m}^2$  were obtained from different regions. For wear measurement, all samples were scratched 20 times using a silicon tips on aluminum coated cantilever having very high spring constant. After the scratching, topography of the scratched area was measured. Wear amount was estimated by determining the average depth of the scratched area.

|                            | <b>Cantilever-1</b> (Topography and LFM) | <b>Cantilever-2</b> (Scratching) |
|----------------------------|--|----------------------------------|
| Material                   | Si <sub>3</sub> N <sub>4</sub>           | Si coated with Al                |
| Cantilever spring constant | 0.1 N/m                                  | 42 N/m                           |
| Cantilever arm length      | 140 $\mu\text{m}$                        | 160 $\mu\text{m}$                |
| Cantilever arm width       | 18 $\mu\text{m}$                         | 50 $\mu\text{m}$                 |
| Resonance frequency        | 38 kHz                                   | 300 kHz                          |
| Full tip opening angle     | 35°                                      | -                                |
| Tip radius                 | 10 nm                                    | <10nm                            |

Table 5.16: Major features of the cantilever used for AFM study.

## RESULTS AND DISCUSSION

### Structure and composition of the films:

The chemical compositions of all these films are summarised in Table 5.17. In addition to Mo, Se and C, contamination O arising either from the residual atmosphere (particularly water vapour) in the chamber and the target or from surface adsorption from the atmosphere after deposition was also detected. Figure 5.60 shows the evolution of the cross section morphology of Mo-Se-C coatings with increasing C content. SEM micrograph of the cross-section of the coating with

the lowest carbon content shows a columnar structure perpendicular to substrate, which is typical for pure transition metal dichalcogenides [258]. However, this structure exhibits a very small number of pores compared to pure TMD deposited by magnetron sputtering [237]. The columns length decreases with increasing carbon content and columns start to grow in a dendritic way. The coating with 55 at.% C is amorphous-like with no clear visible columns. There is a progressive densification of the coatings with a significant decrease of the number of pores, which results in a increase in hardness with increasing carbon content.

| Film Designation | at % Mo | at % Se | at % C | at % O |
|------------------|---------|---------|--------|--------|
| F1               | 21.7    | 38.6    | 36.9   | 2.8    |
| F2               | 18.9    | 35.7    | 42.9   | 2.4    |
| F3               | 16.5    | 29.7    | 48.5   | 5.4    |
| F4               | 13.6    | 25.8    | 55.2   | 5.4    |

Table 5.17: Chemical compositions of the test materials.

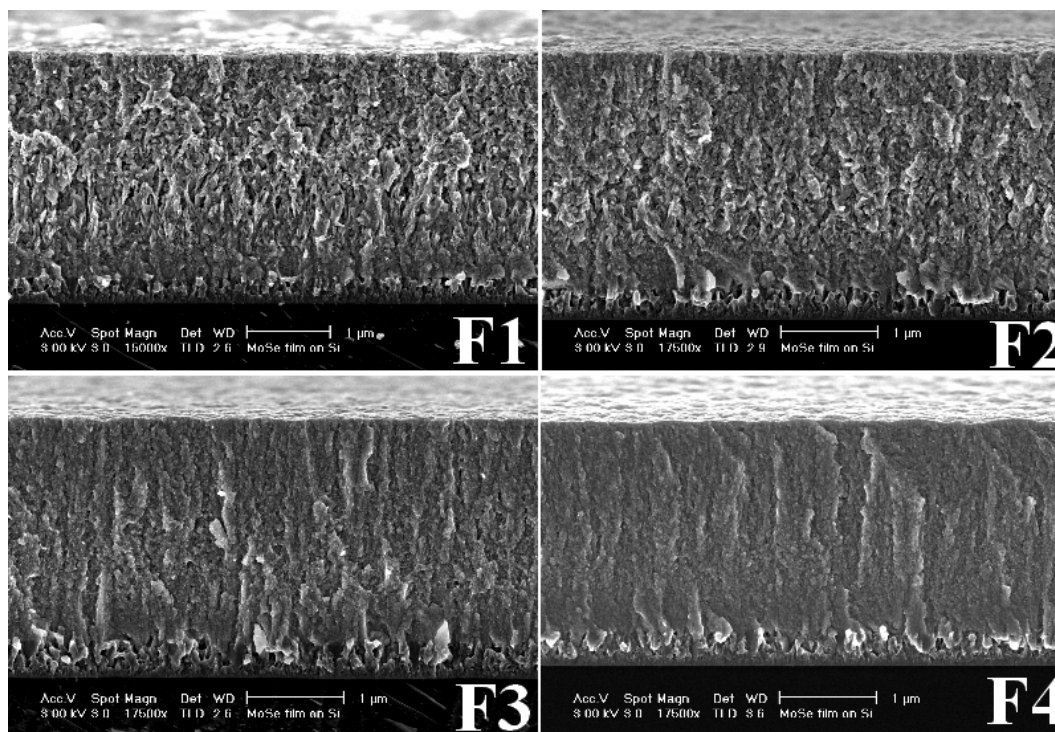


Figure 5.60: Evolution of the cross section morphology of Mo-Se-C coatings with increasing C content.

The XRD patterns of these films are illustrated in Fig. 5.61. The XRD diffractograms of Mo-Se-C coatings shows a peak close to  $2\theta \approx 37.5^\circ$  ( $\text{MoSe}_2$  phase with (100) orientation) followed by a second peak at  $2\theta \approx 44.5^\circ$ . The latter is highly

asymmetric with a long tail towards higher  $2\theta$ . Finally a last peak positioned at  $2\theta \approx 70^\circ$  can be indexed as (110). Weise et al. [259] demonstrated that the extended shoulder of the sputtered  $\text{MoS}_2$  peak positioned close to  $2\theta \approx 40^\circ$  corresponded to a turbostratic stacking of (10L) planes ( $L = 0, 1, 2, 3$ ). XRD patterns then could be explained by a 2D organization of the basal planes which could have several tenths of unit cells dimension. With the progressive decrease of the lateral dimensions of the basal planes, either broadening or drops in the intensity of the (10L) plane occurred until a unique low intensity and broad peak typical of an amorphous structure was detected. This situation would arise when the lateral order of the basal planes did not exceed a couple of lattice parameters [259]. As demonstrated in Fig. 5.61, the presence of molybdenum carbide phases could not be detected by XRD. Furthermore, Mo-C bonds were not observed by XPS in previous study [256]. Therefore, it may be suggested that Mo-Se-C coatings consist of small  $\text{MoSe}_2$  grains embedded in an amorphous carbon matrix. Careful examination of the X-ray diffraction patterns shows slight peak broadening with the increase of the carbon content in the coatings.

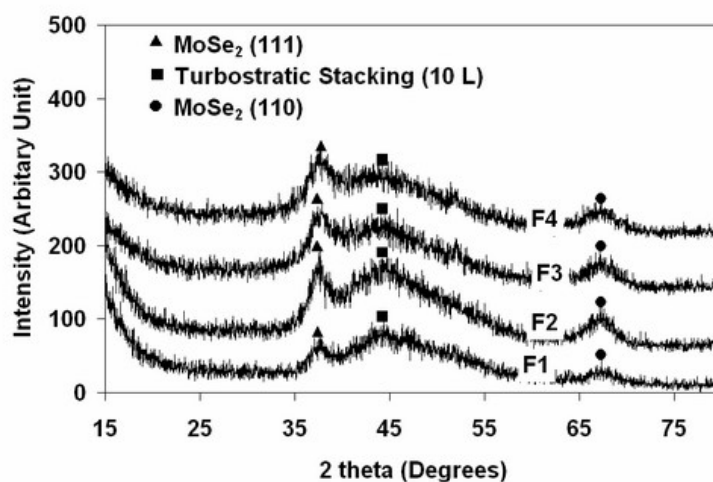


Figure 5.61: The XRD patterns of the investigated films.

Raman spectra obtained from the film surface is presented in Fig. 5.62. A typical spectrum of Mo-Se-C coatings can be divided into two parts: (i) a group of peaks belonging to molybdenum diselenide phases in the range of  $200\text{-}700\text{ cm}^{-1}$ , and (ii) peaks representing D and G bands of microcrystalline graphite in the range  $1100\text{-}1800\text{ cm}^{-1}$ . As stated earlier [256]  $\text{MoSe}_2$  peak appears to be even broader in the case of Mo-Se-C films compared to pure sputtered  $\text{MoSe}_2$ . It confirms the result obtained by XRD and supports Wiese's interpretation, i.e. the presence of Mo-Se grains with dimensions significantly lower than 10 nm. Some mild peaks can

be seen at  $700\text{-}900\text{ cm}^{-1}$  corresponding to molybdenum oxide. The molybdenum oxide peak is identified as  $\text{MoO}_3$  [260].

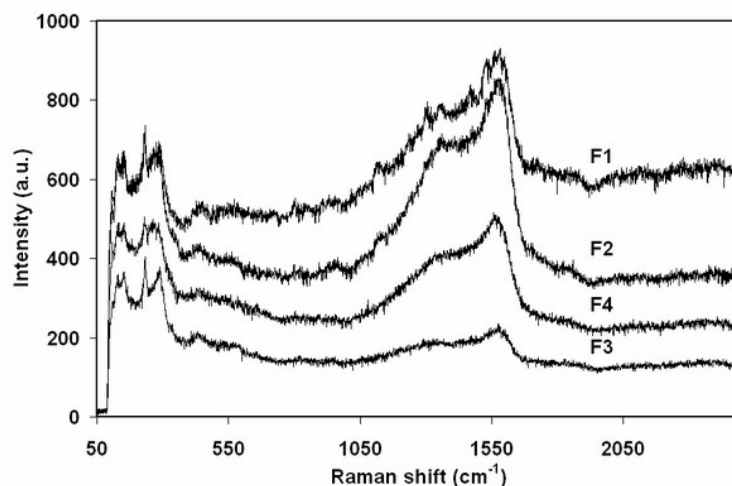


Figure 5.62: Raman spectra obtained from the surfaces of the films investigated.

#### Hardness:

The load vs. displacement curves of these films obtained at an applied load of 2 mN are smooth and none of the curves shows the presence of pop in or pop out events indicating no evidence of fracture of the film. It is clear that, films with lower carbon content exhibit higher depth of penetration. Table 5.18 summarizes the total depth of penetration, residual depth of penetration and % of plastic deformation as ratio of residual depth of penetration to total depth of penetration of various films studied in the present work.

| Films | Maximum Depth of Penetration (nm) | Residual Depth of Penetration (nm) | % of plastic deformation | Elastic Modulus (GPa) | Hardness (GPa) |
|-------|-----------------------------------|------------------------------------|--------------------------|-----------------------|----------------|
| F1    | 264.1                             | 147.1                              | 55.7                     | $26.0 \pm 1.1$        | $1.4 \pm 0.11$ |
| F2    | 226.7                             | 108.0                              | 47.6                     | $13.0 \pm 1.4$        | $2.2 \pm 0.2$  |
| F3    | 187.6                             | 62.7                               | 33.2                     | $39.0 \pm 2.8$        | $4.0 \pm 0.44$ |
| F4    | 176.4                             | 62.3                               | 35.5                     | $40.0 \pm 2.1$        | $4.0 \pm 0.35$ |

Table 5.18: Mechanical properties of various films.

Thus film F4 exhibit very low % of plastic deformation. During the hold at the maximum load, the displacement increases in all the films indicating drift due to the creep as the load vs. displacement curves are plotted after incorporating the

correction due to thermal drift. The extent of this drift decreases with increasing carbon content, being minimal at 55.2 at % carbon. It is also noted that the hardness of these films increases with carbon content. Such trend can partly be attributed to interstitial hardening. The films become denser with increasing carbon content and this densification is partly responsible for increase in hardness.

#### Friction behavior:

To understand the nature of interaction between the cantilever tip and the coating, the deflection displacement curves were recorded. Figure 5.63 shows the deflection of the cantilever tip as a function of the distance from the film surfaces for all these films. In all cases, darker line indicates tip approach to the surface and lighter line represents the tip being pulled away from the surface. The vertical separation between the point where the tip was touching the film and the point where the tip was pulled off the film together with spring constant of the cantilever (0.1 nN/nm) were used to calculate the pull off (adhesive) force [261]. The pull of forces for film F1, F2, F3 and F4 are 26.0 ( $\pm 3.0$ )nN, 28 ( $\pm 3.0$ )nN, 18 ( $\pm 2.0$ )nN, and 10 ( $\pm 1.0$ ) nN respectively. It can clearly be seen that the pull off force decreases with increasing carbon content except for F2. Diamond like carbon film exhibited long time hydrophobic properties [262]. As the carbon content in the film decreases the films become more hydrophilic resulting in tendency to adsorb water. Higher adsorbed water by films containing lower amount carbon causes higher pull off force due to higher surface tension. Consequently pull off forces increases with decrease of carbon content.

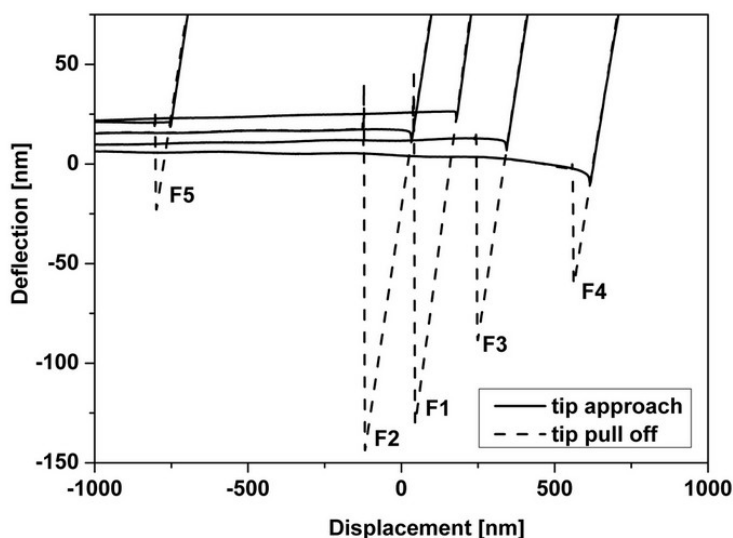


Figure 5.63: The deflection of the cantilever tip as a function of the distance from the film surfaces for all the films investigated.

The three dimensional AFM images showing the topographies of these films are illustrated in Fig. 5.64. Film F1 and film F3 exhibit presence of sharp peaks. Various topographical parameters are summarized in Table 5.19. The root mean square (RMS) roughness value of these films initially increases with increasing C content. Film F3 exhibits the highest RMS roughness value. On further increase of carbon content these parameters decrease. This RMS roughness value is minimum with film F4. Such decrease in roughness can be attributed to near amorphous structure of film F4. However, the RMS value of film F1 is comparable to the RMS value of Ti/a-C : H film and PECVD diamond film [263].

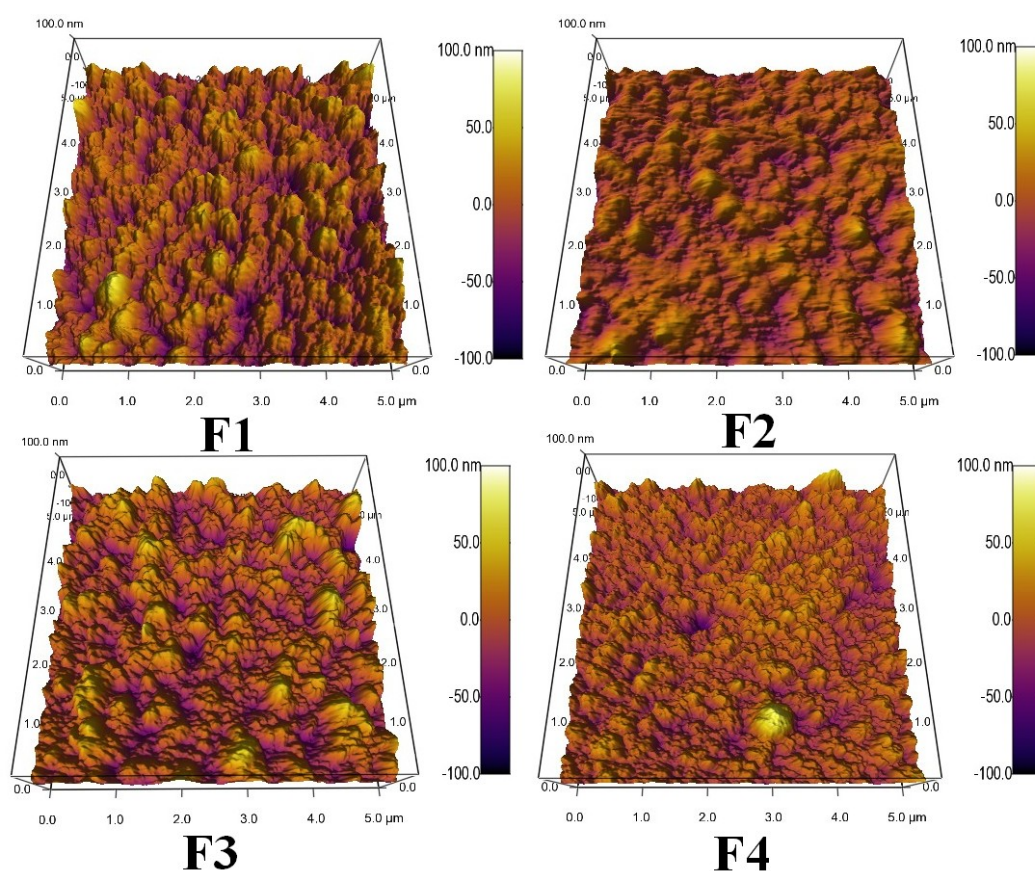


Figure 5.64: The three dimensional AFM images showing the topographies of the films investigated.

The surface morphology of thin film can generally be described by a Gaussian self-affine fractal with a long wavelength cutoff. Such a model gives a surface height-height correlation function [264] of

$$C(r) = \lambda^2 \exp[-(|r|/\zeta)^{2\alpha}] \quad (5.15)$$

| Films | Parameters          |                |                     |                     |
|-------|---------------------|----------------|---------------------|---------------------|
|       | Average Height (nm) | R.M.S (nm)     | Minimum Height (nm) | Maximum Height (nm) |
| F1    | $-3.4 \pm 0.8$      | $3.5 \pm 0.7$  | -2.5                | -4.2                |
| F2    | $-8.8 \pm 0.3$      | $8.8 \pm 0.3$  | -8.4                | -9.1                |
| F3    | $-14.8 \pm 1.4$     | $14.8 \pm 1.0$ | -13.2               | -15.5               |
| F4    | $0.4 \pm 0.8$       | $0.8 \pm 0.7$  | 1.2                 | -0.3                |

Table 5.19: Topographical parameters of the films.

where  $\lambda$  is the root mean square amplitude of the surface or interface roughness. Parameter  $\zeta$  is called lateral correlation length. The correlation length is a measure of and denotes the average length for which the heights between two surface points are correlated.  $\zeta$  is a measure for the lateral fluctuations of the roughness. The third parameter is the roughness exponent  $\alpha$ , also called Hurst parameter, which is related to the local fractal dimension  $d$  of the surface through  $\alpha=3-d$ . It tells how jagged a surface with a given rms roughness and lateral correlation length is.  $\alpha$  usually ranges between 0.5 (exponential decay of  $C(r)$ -more jagged surface) and 1 (Gaussian  $C(r)$ -less jagged). These parameters as determined from the investigated surfaces and listed in Table 5.20. These parameters do not follow the same trend as that of the R.M.S values. The statistical roughness is comparable for all films even though AFM roughness are widely different. As the Hurst parameters are close to 0.5, the surfaces are highly jagged. Film F1 is least jagged. The lateral fluctuation is the highest for film F2.

| Sample | AFM measure RMS [nm] | $\sigma$ - statistical RMS [nm] | $\zeta$ - lateral correlation length [nm] | $\alpha$ - Hurst parameter) |
|--------|----------------------|---------------------------------|---|-----------------------------|
| F1     | $3.5 \pm 0.7$        | $7.9 \pm 0.1$                   | $117.9 \pm 3.8$                           | 0.78                        |
| F2     | $8.8 \pm 0.3$        | $7.9 \pm 0.13$                  | $141.5 \pm 5.8$                           | 0.48                        |
| F3     | $14.8 \pm 0.1$       | $7.8 \pm 0.11$                  | $140.6 \pm 5.0$                           | 0.52                        |
| F4     | $0.8 \pm 0.7$        | $7.4 \pm 0.11$                  | $135.8 \pm 5.3$                           | 0.69                        |

Table 5.20: RMS, Lateral correlation length and Hurst parameters of the investigated films.

The friction force values of these films were obtained for an applied load of 9 nN and a scan speed of  $12.5 \mu\text{m s}^{-1}$ . The friction force surfaces show peaks more prominent in forward scan than in reverse scan, signifying that the friction force on the film is quite high, especially when the film traverses the top of the grain during forward scanning. Furthermore, the average friction force during forward

scanning is higher than that during reverse scanning. Following the procedure suggested by Beake et al. [265], the friction force ( $F_L$ ) is given by

$$F_L = 1/2(LF(f) - LF(r)) \quad (5.16)$$

where  $LF(f)$  and  $LF(r)$  are the signals in the forward and reverse direction of motion of the tip in LFM mode. This equation is based on the fact that when there is substantial variation in the surface topography, the LFM signal contains a component due to normal force acting through the local slope. Since lateral force is determined from the difference between signals reaching the left and the right halves of a four segments photo detector, the topographic contribution of the LFM image may be eliminated by subtracting signals recorded in opposite directions.

The variation of friction force as a function of applied load for all the films is presented in Fig. 5.65. In general, friction force marginally increases with increasing the applied load. The load dependences of friction forces of film F4 and F2 are identical and increase marginally with applied load. This trend is expected when ploughing mechanism is operative. As the applied load increases deeper grooves are formed and higher friction coefficient is noted. From Fig. 5.65, it is also clear that friction force exhibit the minimum value at an intermediate carbon content (F2, 42.9 at% C). The influence of scan speed on the friction force

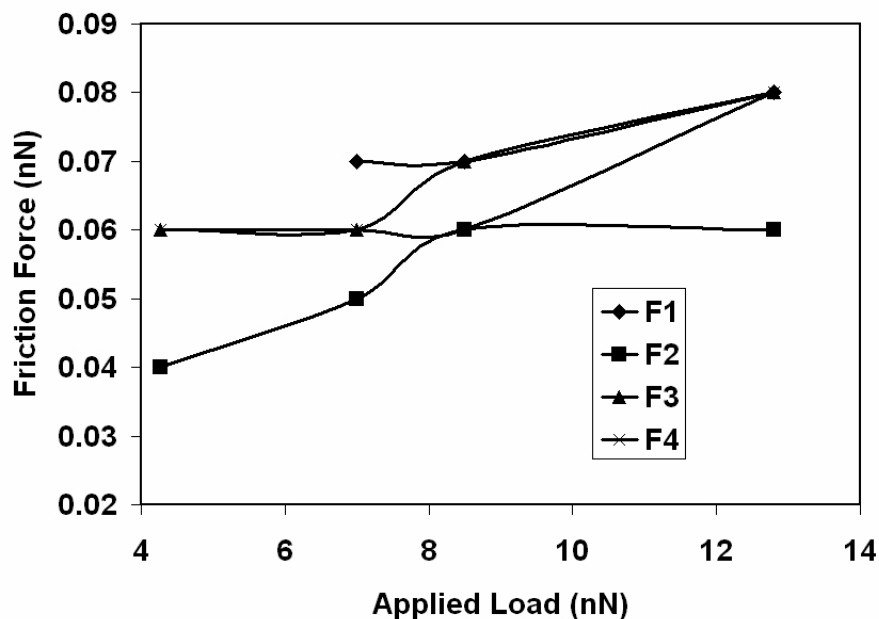


Figure 5.65: The variation of friction force as a function of applied load for all the films.

is depicted in Fig. 5.66. In most of the cases investigated, the friction force can be considered to be independent of scan speed. The friction force of film containing minimum carbon (F1) decreases with scan speed. The reason for this is not clear and needs further investigation.

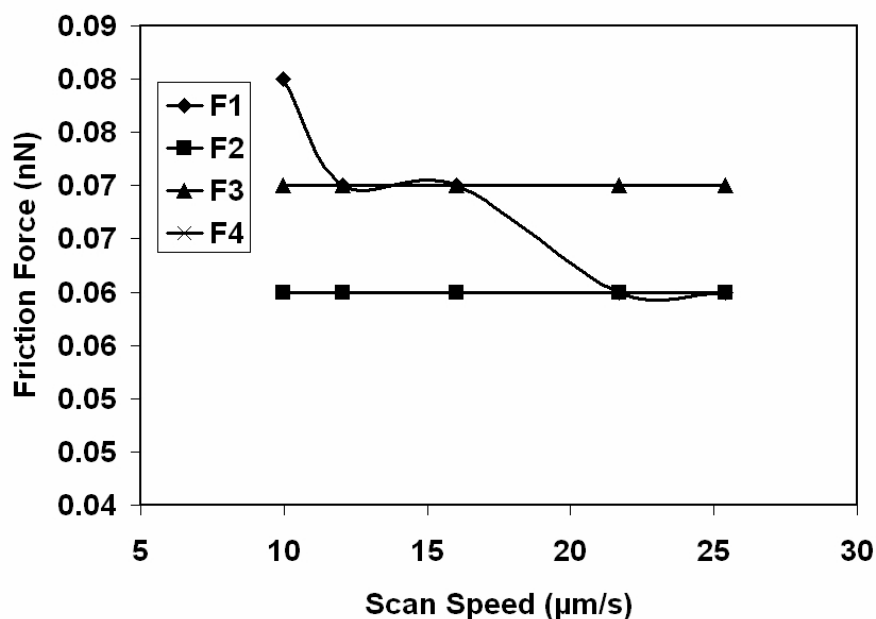
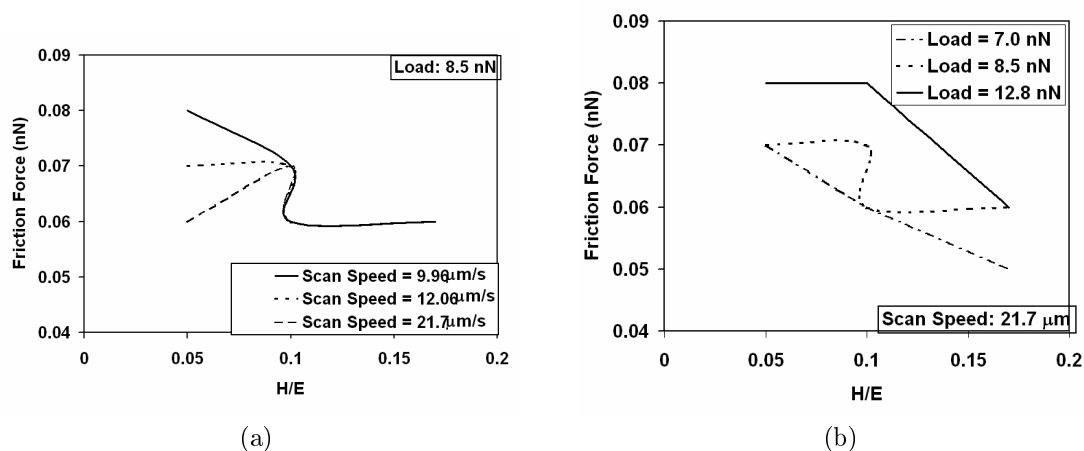


Figure 5.66: The influence of scan speed on the friction force.

In recent time, it is demonstrated that not only hardness (H) or elastic modulus (E) but also the ratio H/E is very important materials property [266]. The ratio H/E multiplied by geometric factor, which is ratio of the diameter of plastic zone to total deformed zone, gives the plasticity index. The plasticity index describes the deformation properties of contacting surfaces. This quantity also appears in various expressions for fracture toughness. The variation of friction force as function of H/E is presented in Fig. 5.67a and Fig. 5.67b for different scan speed and different applied load. Friction force tends to decrease with increase of H/E. at different scan speed and different applied load. Thus although friction force is not related clearly with hardness, it is related with H/E ratio signifying the fact that deformation properties of contacting surfaces govern friction force.

Although R.M.S. surface roughness does not carry any information about slopes, sizes or frequencies of asperities, it is still an important parameter for predicting and understanding the properties of tribological systems. Earlier investigations indicated that friction coefficient of diamond film increases with increase of roughness [267], [268]. Higher roughness increases the asperities slope angle, which in turn increases friction coefficient [267]. There are two mechanisms, which govern

Figure 5.67: Variation of friction force with  $H/E$  ratio.

the roughness dependence of friction coefficient. The first mechanism is known as ratchetting mechanism where relative motion between two surfaces is achieved by asperities riding over each other. The second possible mechanism is related to energy loss mechanism where asperities push each other. In the initial stage of sliding, there can be other operative mechanisms. The influence of roughness on the friction force is shown in Fig. 5.68a and Fig. 5.68b for different scan speed and for different applied load. No direct relationship between the roughness and friction force can be established. Thus the mechanisms mentioned above do not hold good for the present investigation. This may be related to different friction mechanisms. Further, in present investigation the counter body act as single asperity contact. In such system, stress distribution as obtained under multiple asperity contact is altered significantly. Moreover, mechanical interlocking does not play any important role under single asperity contact. As noted in Fig. 5.68a and Fig. 5.68b, friction force is minimum at the highest roughness. The roughness is highest for film F3 having low pull off force. Thus, surface force plays dominant role in determining friction force at this low load tribological study.

These films were subjected to rubbing for 20 times using a cantilever having very high spring constant. The topography of the worn surface was measured after rubbing the surfaces. The amount of wear estimated by measuring the average depth of the rubbed area in nm for different films are shown as bar diagram in Fig. 5.69. The amount of wear decreases with increase of carbon content of the films. This is expected as the hardness of the films also increases with increase of carbon content. The topographies of the worn area of film F3 and film F4 are given in Fig 5.70. Pull off forces are also measured from the worn area of these samples. The representative pull off force curves measured from a worn area and an unworn

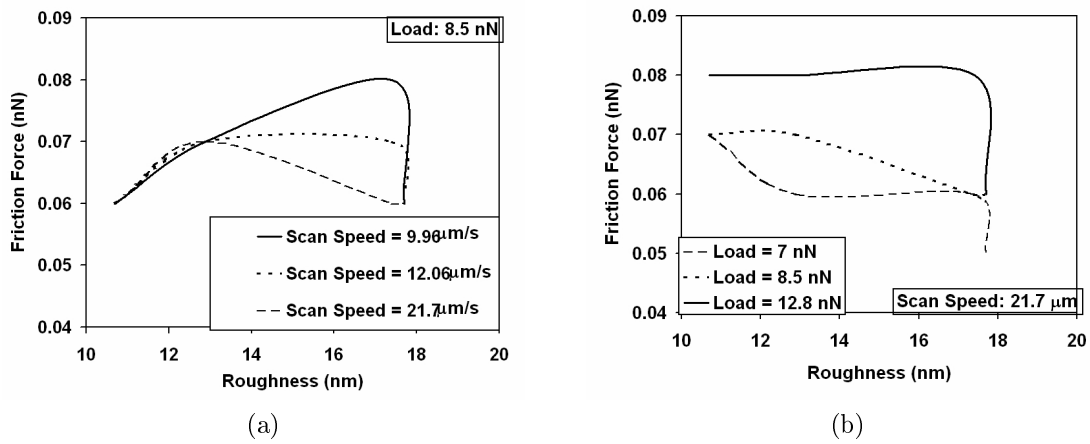


Figure 5.68: Influence of roughness on the friction force.

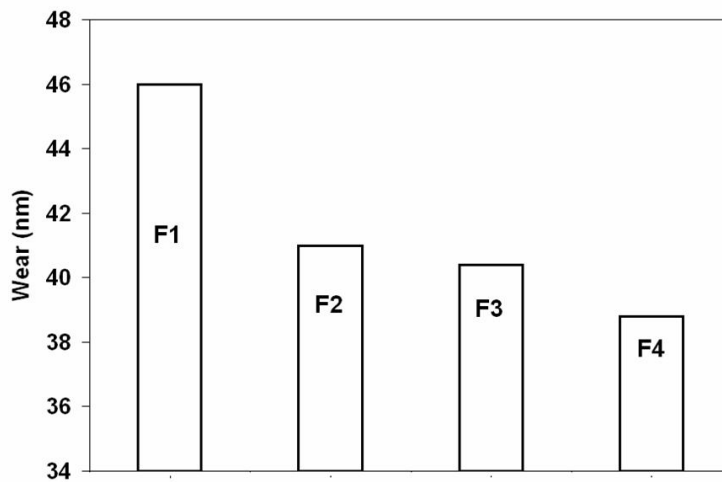


Figure 5.69: The amount of wear estimated by measuring the average depth of the rubbed area in nm for different films.

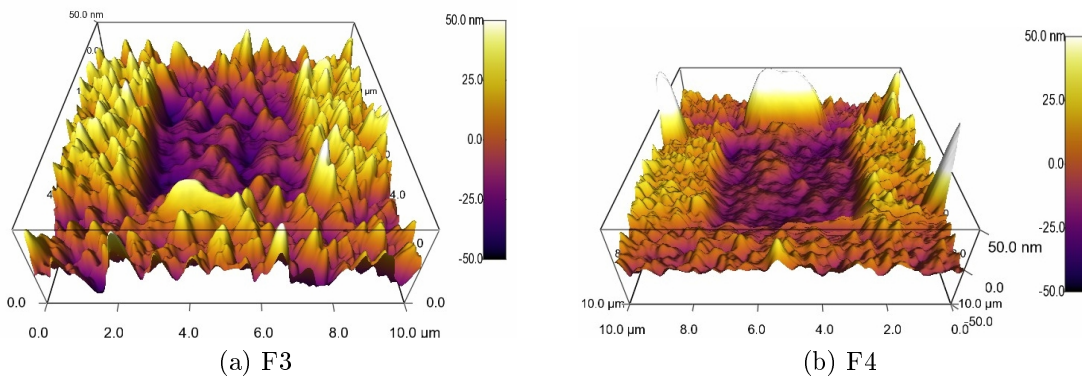


Figure 5.70: AFM images showing topographies of the worn area of film F3 and film F4.

area of film F3 and F4 are illustrated in Fig. 5.71. The shape of the curves and magnitudes of pull off forces are changed significantly for film F3 but not so much for film F4. This indicates that there is transfer of layers during wear even at this low load for films F3 or films with lower carbon content. In contrast, film F4 or film having higher carbon content there is no transfer film. The friction response of these films is related to the phenomenon of alteration of surface layer for film with low carbon content. The wear rate of these films decreases with carbon content. Further, it was noted that the friction coefficient of carbon alloyed TMD decreases with increasing carbon content [269]. In this system, such a trend is not noted due to alteration of the surface properties at lower carbon content.

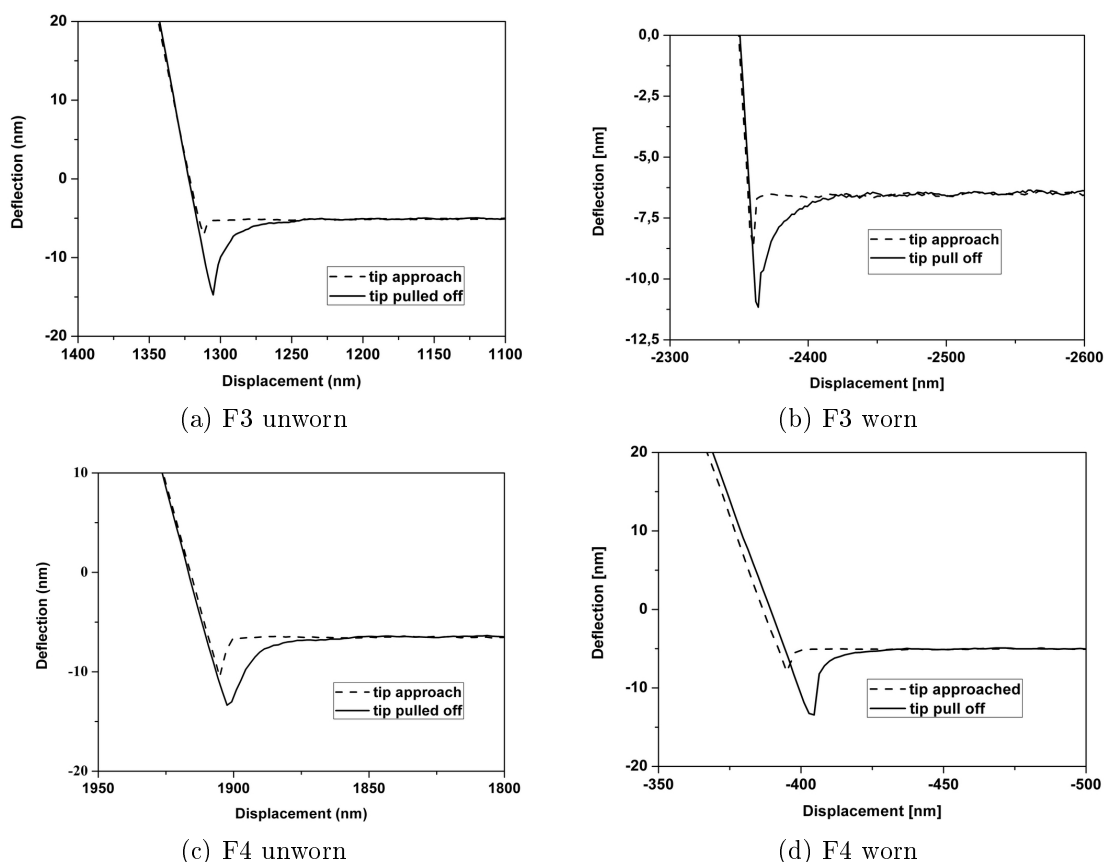


Figure 5.71: The representative pull off force curves measured from a worn area and an unworn area of film F3 and F4.

Valuating the frictional processes, it can be described as dissipation of energy at the sliding interface. In order to evaluate the possible friction dissipation mechanism, adhesion can be considered to play an important role. Since experiments are conducted in ambient condition the pull off force is a measure of adhesion induced friction force. The pull off forces of films F1 to F4 are 26.0, 28.0, 18.0 and 10.0. Examination of pull off force and friction force indicates that pull off force

increases in the order  $F_4 < F_3 < F_2 < F_1$ . In contrast the friction forces of these films do not follow similar trend. Thus, adhesion force does not influence friction force appreciably for these films.

In the wear under very low (nN) load, two additional friction dissipation mechanisms become important. The first mechanism is by emission of photons [270], [271]. The second mechanism is energy dissipation by electron-hole pair mechanism [272]. The films investigated in present work will have increasing amount of sp<sup>2</sup> bond with increasing carbon content. If electron mechanism were governing mechanism a specific trend in friction force would have been noted with increasing carbon content. Since no such trend is noted electronic mechanism is unlikely dominating mechanism. Generally, the phononic mechanism is considered to be the dominant mechanism [273] in insulating film. Carbon alloyed TMD can very much be considered as insulating film. Diamond films are rich in sp<sup>3</sup> hybridisation. In the present investigation as noted from Raman spectra, all the films are poor in sp<sup>3</sup> hybridisation but rich in sp<sup>2</sup> hybridisation, Thus, different energy dissipation mechanisms can be considered for these films when compared with diamond film. If electron-hole pair mechanism can be considered to be the dominant mechanism for diamond films, then phononic mechanism can be dominant for the films investigated in present work.

### CONCLUSIONS:

1. Based on XRD and Raman spectroscopy study, it can be stated that the films consist of very fine MoSe<sub>2</sub> grains embedded in carbon matrix.
2. The pull of force of the films tested decreases with increase of carbon content.
3. The hardness of Mo-Se-C films increases and wear rate decreases with increase of carbon content.
4. The friction force decreases with H/E ratio. No direct relation between friction force and roughness or between friction force and carbon content can be established.
5. In general, friction force for all the films tested, increases with applied load. The friction force is independent of scan speed except for film F1. The friction force decreases with scan speed for film F1.

**Acknowledgement** Authors are grateful to Prof. A. Cavaleiro and his group, University of Coimbra for providing the test materials. Authors are also grateful

to the European Commission for supporting this work through their project no MIMO1-CT-2006-039220 and WEMESURF research-training network. Authors are also grateful to Dr. Thomas Koch from Institute of Materials Science and Technology, Vienna University of Technology, for carrying out the nanoindentation study. Part of the work was financed by the Austrian Kplus programme via the Austrian Center of Competence for Tribology, AC2T research GmbH, Wiener Neustadt.

## 6 SUMMARY

The purpose of this research work was to investigate how the lubricant additive molecules perform on the surface and how the molecular processes are leading to the macroscopic lubricity. In this study a wide range of lubricants and additives were considered. The main attention was focused on additives for water based lubricants, because the influence of individual additives on tribological properties of fully formulated water based lubricants compositions is still not clear. A first consideration were corrosion inhibitors and their tribocorrosion behavior. Thus solutions of anti-corrosion, anti-foaming and anti-microbial agents - amines (Ethanolamine oligomers, Ethylamine oligomers), friction modifiers - glycols (monoethylene glycol, 1,4-butylene glycol) and amine derivatives with longer hydrocarbon chains (3-amino-1-propanol, 4-amino-1-butanol) were investigated.

To summarize this work we can state:

- The friction measurement method under nano Newton load range using AFM close fluid cell was developed, thus the atomic-scale origins of friction can be observed with this technique to characterize behavior of the additives in aqueous media (Chapter 5.1.1 on page 69).
- This research work showed that in nanometer load range the most efficient additive - monoethanolamine oligomer (representant of ethanolamine group) reduced friction by 76% in respect to reference friction measurements performed in double distilled water. Investigated additives showed a comparable tribological performance for a wide range of loads (nano and micro Newtons). Ethanolamines also turned out to be best anti-corrosion agent in static conditions (Chapter 5.1.1 on page 77).
- The improvements of nanofrictional behavior might be due to the orientation of amine and hydroxyl groups on the surface. Detail XPS analysis showed that ethanolamine molecules stand upright on the surface, bound to it by the nitrogen atom. Direct bonding between iron and nitrogen strongly affects anti-corrosion performance. Number of hydroxyl groups in chemical com-

pound have influence on friction and compromise on the top layer of the film (Chapter 5.1.2 on page 89).

- Macrotribological studies showed that in rolling contact ethanolamines do not perform as well as it was founded in nanoscale due to the formation of a thick oxidation layer, which prevents the additives to penetrate it. Surprisingly ethylamines - the additives which were used for comparison - significantly improved tribological performance in rolling contact due to the molecules activation and formation of a mechanically durable boundary film. Glycols - used as reference friction modifiers significantly reduced friction, however the anti-wear and anti-corrosion behavior was unsatisfactory (Chapter 5.1.3 on page 96).
- Ethylamines, also known as corrosion inhibitors undergo filiform corrosion on metallic surfaces. They adsorb on the surface different than ethanolamines - bond to iron oxide layer by the hydrocarbon chain, while amine group stands on the top overlayer (Chapter 5.1.3 on page 100).
- Macrotribological tests in pure severe sliding contact showed that none of the additives influenced the friction coefficient compared to distilled water, however significant differences in wear and tribocorrosion on the wear track were observed. From the experiments it was concluded that ethanolamines most efficiently reduce the tribocorrosion in severe sliding contact. Ethylamines performed very well in rolling contact, however in pure sliding conditions significant tribocorrosion was present. This can be explained based on additive adsorption time. Continuous sliding sheared off the molecules, ethanolamines which immediately react with the surface continuously protect fresh exposed surface from corrosion, however ethylamines which need over 20 min to re-adsorb again, let the fresh surface to interact with water (Chapter 5.1.4 on page 109).
- All AR-XPS chemical characterization result were analyzed and compared with SESSA simulation result to confirm the accuracy and correctness of the analysis. The results showed that in both cases of ethanolamines and ethylamines the experimental data analysis was correct and consistency with simulation data was better than 5% (Chapter 5.1.4 on page 114).

Furthermore, lubricants for rolling bearing elements like polar and non polar oil with zinc dialkyldithiophosphate (ZDDP) solutions were examined. The main conclusions we can state as follows:

- Non polar base oil (HeD-hexadecane) ZDDP solutions generates a reaction layer more rapidly and thicker than that of polar base oil (DEG-diethyleneglycol) ZDDP solutions. This fact is related with the molecular polarity - polar ZDDP molecules will compete with polar oil molecules to get a place on the substrate, thus the probability that ZDDP molecule reach and react with the steel surface is smaller than in case when it is dissolved in non-polar base oil (Chapter 5.2.1 on page 129).
- In every type of oil, ZDDP addition always increases the friction coefficient, due to tribofilm formation causing roughening (Chapter 5.2.1 on page 128).
- AFM scanning in base oil containing ZDDP with high loads and high speeds did not lead to the build-up of an anti-wear film. The reason is that the single asperity contact temperatures during AFM scans are much lower compared to those presented in real machine parts (Chapter 5.2.1 on page 133).
- The evolution of the ZDDP-derived reaction layer with rubbing time progresses rapidly. Initially a thin and soft ZDDP reaction layer is formed (after 5 min rubbing test) and than very quickly it develops, after 30 min it becomes harder and thicker. After 60 min test stable, rough and hard layer is developed with a limited thickness of 70 nm (Chapter 5.2.2 on page 142).

The second part of this work was addressed on chemical vapor deposited (CVD) diamond films and transition metal dichalcogenides (TMD) in consideration of desired properties for micro electro mechanical systems (MEMS). In this study the influence of the morphology, topography and chemical composition of these films on the micro- and nanomechanical properties was presented. Taking into account these studies it can be concluded that:

- Diamond films having coarse ballas, fine ballas and faceted morphologies have significant differences in their nanotribological properties. Diamond films deposited with faceted morphology gives the best combination of morphological and topographical parameters. The friction forces of MWCVD diamond film are governed by the adhesion force and it is minimal for films having fine ballas morphology. Films with coarse ballas morphology possess the highest relative elastic modulus and maximal friction coefficient (Chapter 5.3.1 on page 157).
- Mo-Se-C films consist of very fine MoSe<sub>2</sub> grains embedded in a carbon matrix. Carbon content has significant influence on all investigated parameters.

With increasing carbon content of the tested films, the hardness increases and wear volume decreases. The friction force of all the films is very low and in general dependent on surface pull-off forces. The film having the highest carbon content exhibits the maximum friction force (Chapter 5.3.2 on page 181).

### **OUTLOOK - Suggestions for future work**

Keeping in mind the interest within industry to improve tribocorrosion resistance of fully formulated water based fluids it would be worthwhile to investigate oxidation evolution under tribological stress and its effect on tribocorrosion.

Further search for the additives, which undergo direct chemical bonding between nitrogen and iron should be carried out to establish its positive effects on corrosion protection in water lubricated systems.

From a more fundamental point of view a molecular dynamic simulation should be performed to show the effects of tribological parameters (contact situation, environment, polarity) on the molecular processes manners.

Concerning ZDDP derived reaction layer, it would be interesting to perform SESSA simulation to confirm the accuracy of the AR-XPS analysis, which was done by many researchers. There are many reaction layer models suggested but none of them verified by SESSA.

## 7 CONCLUSION

Various research in this work showed without any doubt that molecular processes, especially chemical bondings between lubricants, additives and surfaces strongly affect performance of tribological systems. Presented results in this thesis support this statement in many ways:

- Macroscopic behavior of the additives depend on the applied tribological parameters, particularly on the tribocontact situation (rolling, sliding, impacting, fretting). Thus the conditions used in the tests should represent variable conditions present in characteristic applications.
- Investigated additives only in specific concentrations can significantly improve desired properties of tribosystem, performing either as chemisorbed or chemically reacted layer.
- Mixing of the additives, which separately can enhance properties do not always give a better final outcome.
- The presence of amine group in additive molecules can have a tremendous impact on tribocorrosion in a water lubricated tribosystem.
- Polarity of the oil highly influences the topography and mechanical properties of the ZDDP-derived reaction layer.
- The friction behavior of nanocrystalline diamond is roughness independent and governed by transfer of carbonaceous film .

In this thesis it was clearly shown that the physical and chemical composition of surfaces determine important tribological properties of the solids such as corrosion, adhesion, friction, wear and finally the failure mechanism.

# REFERENCES

- [1] A. Tomala, C.A. Vasko, N. Dörr, H. Störi, and I.C. Gebeshuber. Oligomer specific lubrication. *Proceedings 34th Leeds-Lyon Symposium on Tribology*, 30:2–3, 2007.
- [2] A. Tomala, W.S.M Werner, I.C. Gebeshuber, N. Dörr, and H. Störi. Tribochemistry of monomolecular lubricant films of ethanolamine oligomers. *Tribology International*, 42:1513–1518, 2009.
- [3] A. Tomala, A. Karpinska, W.S.M. Werner, A.V. Olver, and H. Störi. Tribological performance of additives for water-based lubricants. *Wear*, 269 (11-12):804–810, 2010.
- [4] A. Tomala, A. Naveira-Suarez, I.C. Gebeshuber, and R. Pasaribu R. Effect of base oil polarity on micro and nanofriction behaviour of base oil + ZDDP solutions. *Tribology - Materials Surfaces and Interfaces*, 3(4):182–188, 2009.
- [5] A. Naveira-Suarez, A. Tomala, R. Pasaribu, R. Larsson, and I.C. Gebeshuber. Evolution of ZDDP-derived reaction layer morphology with rubbing time. *Scanning*, 31:1–10, 2010.
- [6] A. Bogus, I.C. Gebeshuber, A. Pauschitz, Manish Roy, and R. Haubner. Micro- and nanomechanical properties of diamond films with various surface morphologies. *DIAMOND & RELATED MATERIALS*, 17:1998–2004, 2008.
- [7] A. Tomala, Manish Roy, and F. Franek. *Philosophical magazine*, 90 (29):3827–3843, 2009.
- [8] D. Dowson. *History of Tribology*. PEP Ltd. Bury St Edmunds, 2<sup>nd</sup> edition, 1998.
- [9] F.P Bowden and D. Tabor. Mechanism of metallic friction. *Nature*, 150:197–199, 1942.
- [10] D. Tabor. Junction growth in metallic friction. *Proc. Roy. Soc. London*, A251:378–393, 1959.

- 
- [11] J.A Greenwood and J.B.P Williamson. Contact of nominally flat surfaces. *Proc. Roy. Soc. London*, A295:300–319, 1966.
- [12] G. W. Stachowiak and A.W. Batchelor. *Engineering Tribology*. Butterworth-Heinemann, 2<sup>nd</sup> edition, 2001.
- [13] B. Bhushan. *Handbook of Nanotechnology*. Berlin: Springer, 2<sup>nd</sup> edition, 2003.
- [14] [www.pcs-instruments.com](http://www.pcs-instruments.com).
- [15] M. Rojas-Campanur, J. Lara-Romero, F. Chinas-Castillo, and G. Alonso-Nunez. Tribological performance of rosin acid additives in water based lubricants. *Tribology Online*, 2:29–33, 2007.
- [16] C. Kajdas, S.S.K. Harvey, and E. Wilusz. *Encyclopedia of Tribology*. Elsevier Science, 4<sup>th</sup> edition, 1990.
- [17] A. Cambiella, J.M. Benito, and C. Pazos. Interfacial properties of oil-in-water emulsions designed to be used as metalworking fluids. *Colloids and Surfaces A: Physicochemical and Engineering Aspects*, 305:112–119, 2007.
- [18] K. Persson and R. Gahlin. Tribological performance of a dlc coating in combination with water based lubricants. *Tribology International*, 36(11):851–855, 2003.
- [19] L. Fang, Y. Gao, and Z. Zhang. Tribology of  $\text{Si}_3\text{N}_4$  with different glassy phase content sliding against grey cast iron lubricated with water. *Wear*, 225-229:896–904, 1999.
- [20] R. M. Gresham. The mysterious world of MWF additives. *Tribology and Lubrication Technology*, 2:29–33, 2006.
- [21] A. Tomala, A. Karpinska, W.S.M. Werner, A.V. Olver, and H. Störi. Tribological performance of additives for water-based lubricants. *Proceedings of the ASME/STLE International Joint Tribology Conference*, 2:29–33, 2009.
- [22] M. Haibing, L. Jing, Ch. Huan, Z. Guangzhi, Y. Yi, R. Tianhui, and Z. Yidong. XPS and XANES characteristics of tribofilms and thermal films generated by two P- and/or S- containing additives in water-based lubricant. *Tribology International*, 42(6):940–945, 2009.
-

- 
- [23] L. Tokarzewski, J. Zakrzewski, J. Wachowicz, and S. Szczepaniak. Phosphoryl tris (diethanolamide) (dap) - a new additive for water-based and ethylene-glycol-based hydraulic fluids and lubricants. *Wear*, 50(2):365–369, 1978.
- [24] W. Zhang, W.M. Liu, and L. Yu. Friction and wear behaviors of a (ca, mg)- sialon/sae 52100 steel pair under the lubrication of various polyols as water-based lubricating additives. *Tribology International*, 33(11):769–755, 2000.
- [25] H. Lei, W.C. Guan, and J.B. Luo. Tribological behavior of fullerene - styrene sulfonic acid copolymer as water-based lubricant additive. *Wear*, 252(3-4):345–350, 2002.
- [26] H. Lei, W.C. Guan, and J.B. Luo. Weldable corrosion resistant primer material. *US Patent*, 4.263.167, 1981.
- [27] W. Huang, J. Dong, F. Li, and B. Chen. Study of the tribological behavior of S-(carboxylpropyl)-N-dialkyl dithiocarbamic acid as additives in water-based fluid. *Wear*, 252:306–310, 2002.
- [28] K. Takahashia, Y. Shitaraa, T. Kaimaia, A. Kannob, and Sh. Mori. Lubricating properties of TR gel-lube-influence of chemical structure and content of gel agent. *Tribology International*, 232:250–256, 2010.
- [29] D.J. Dunn. Metal removal mechanisms comprising wear in mineral processing. *Wear of Materials*, 1:501–508, 1985.
- [30] D. Landolt, S. Mischler, and M. Stemp. Electrochemical methods in tribo-corrosion: a critical appraisal. *Electrochimica acta*, 46:3913–3929, 2001.
- [31] J.M. Steigerwald, S.P. Murarka, R.J. Gutmann, and D.J. Duquette. *Chemical Mechanical Planarization of Microelectronic Materials*. Wiley, 2<sup>nd</sup> edition, 1997.
- [32] S. Bec, A. Tonck, J.M. Georges, R.C. Coy, J.C. Bell, and G.W. Roper. A relationship between mechanical properties and structures of zinc dithiophosphate anti-wear films. *Proceedings - Royal Society. Mathematical, physical and engineering sciences*, 455:4181–4203, 1999.
-

- 
- [33] P.A. Willermet, D.P. Dailey, R.O. Carter, P.J. Schmitz, and W. Zhu. Mechanism of formation of antiwear films from zinc dialkyldithiophosphates. *Tribology International*, 28(3):177–187, 1995.
- [34] H. Spedding and R.C. Watkins. Antiwear mechanism of zddp's - 1. *Tribology International*, 15(1):9–12, 1982.
- [35] G.M. Bancroft, M. Kasrai, M. Fuller, and Z. Yin. Mechanism of tribochemical film formation: Stability of tribo- and thermally-generated zddp films. *Tribology Letters*, 3:47–51, 1997.
- [36] E.S. Forbes. The load carrying action of organic sulfur compounds - a review. *Wear*, 15:87–96, 1970.
- [37] C.H. Bovington and B.Dacre. The adsorption and reaction of decomposition products of zinc di-isopropyldithiophosphate on steel. *ASME Transactions*, 27:252–258, 1984.
- [38] H. Fujita, R.P. Glovnea, and H. Spikes. The formation of zinc dithiophosphate antiwear films. *Proceedings of the Institution of Mechanical Engineers. Part J, Journal of Engineering Tribology*, 218:265–277, 2004.
- [39] T.P. Debies and W.G. Johnston. Surface chemistry of some antiwear additives as determined by electron spectroscopy. *ASLE Transactions*, 23:289–297, 1980.
- [40] P.A. Willermet, D.P. Dailey, R.O. Carter III, P.J. Schmitz, W. Zhu, J.C. Bell, and D. Park. The composition of lubricant-derived surface layers formed in a lubricated cam/tappet contact II. effects of adding overbased detergent and dispersant to a simple ZDTP solution. *Tribology International*, 28:163–175, 1995.
- [41] P.J.M. Martin, C. Grossiord, Th. Lemogne, S. Bec, and A. Tonck. The two-layer structure of ZNDTP tribofilms, part I: AES, XPS and XANES analyses. *Tribology International*, 34(3):523–530, 2001.
- [42] L. Taylor and H. Spikes. Friction-enhancing properties of ZDDP antiwear additive: Part I - friction and morphology of zddp reaction films. *Tribology Transactions*, 46(3):303–309, 2003.
- [43] L. Taylor A., Dratva, and H.A. Spikes. Friction and wear behavior of zinc dialkyldithiophosphate additive. *Tribology Transactions*, 43(3):469–479, 2000.
-

- 
- [44] J.S. Sheasby and Z. Nisenholz Rafael. Antiwear characteristics of a commercial secondary ZDDP additives. *Tribology Transactions*, 36:399–401, 1993.
- [45] J.F. Graham, C. McCague, and P.R. Norton. Topography and nanomechanical properties of tribochemical films derived from zinc dialkyl and diaryl dithiophosphates. *Tribology Letters*, 6:149–157, 1999.
- [46] G.W. Canning, M.L. Suominen Fuller, G.M. Bancroft, M. Kasrai, J.N. Cutler, G. De Stasio, and B. Gilbert. Spectromicroscopy of tribological films from engine oil additives. part I. films from zddp's. *Tribology Letters*, 6 (3-4):159–169, 1999.
- [47] B. Bhushan. *Modern Tribology Handbook, Volume two: Material Coatings, and Industrial Applications*. CRC Press LLC, 1<sup>st</sup> edition, 2001.
- [48] T. Spalvins. Deposition of MOS<sub>2</sub> films by physical sputtering and their lubrication properties in vacuum. *ASLE Transactions*, 12:36–43, 1969.
- [49] R.S. Bhattacharya, A.K. Rai, A.W. McCormick, and A. Erdemir. High-energy (mev) ion-beam modifications of sputtered MOS<sub>2</sub> coatings on ceramics. *Tribology Transactions*, 36:621–626, 1993.
- [50] J.S. Zabinski, M.S. Donley, V.J. Dyhouse, and N.T. McDevitt. Chemical and tribological characterization of PBO-MOS<sub>2</sub> films grown by pulsed laser deposition. *Thin Solid Films*, 214:156–163, 1992.
- [51] J.M. Martin, H. Pascal, C. Donnet, T. LeMogne, J.L. Loubet, and T. Epicier. Superlubricity of MOS<sub>2</sub>: crystal orientation mechanisms. *Surface Coating Technology*, 68-69:427–432, 1994.
- [52] T. Polcar, M. Evaristo, M. Stueber, and A. Cavaleiro. Synthesis and structural properties of MO-SE-C sputtered coatings. *Surface and Coatings Technology*, 202:2418–2422, 2008.
- [53] T. Polcar, M. Evaristo, M. Stuebar, and A. Cavelrio. *Proceedings European Tribology Conference*, 12-15:613, 2007.
- [54] C.A. Brookes and E.J. Brookes. Diamond on perspective - A review of mechanical properties of natural diamond. *Diamond and Related Materials*, 1:13–17, 1991.
-

- 
- [55] A. Erdemir, O.L. Eryilmaz, and G. Fenske. Synthesis of diamond like carbon films with superlow friction and wear properties. *Journal of Vacuum Science Technology*, 18:1987–1992, 2000.
- [56] B. Bhushan. *Handbook of Nanotechnology*. Berlin: Springer, 2<sup>nd</sup> edition, 2003.
- [57] A.J. Mchohan. The mechanism of action of an oleic imidazoline based corrosion inhibitor for oilfield use. *Colloids and surfaces*, 59:187–208, 1991.
- [58] B. Bhushan. *Nanotribology and Nanomechanics - An Introduction*. Berlin: Springer, 2<sup>nd</sup> edition, 2005.
- [59] G. Binnig and H. Rohrer. Scanning tunneling microscopy from birth to adolescence. *Rev. of Mod. Phys*, 59:615, 1987.
- [60] R. Young, J. Ward, and F. Scire. The topografiner: An instrument for measuring surface microtopography. *Rev. Sci. Inst.*, 43:999, 1972.
- [61] G. Binnig, H. Rohrer, Ch. Gerber, and E. Weibel. Surface studies by scanning tunneling microscopy. *Rev. of Mod. Phys*, 49:57, 1982.
- [62] G. Binnig, C.F. Quate, and Ch. Geber. Atomic force microscope. *Phys. Rev. Letters*, 56:930, 1986.
- [63] Asylum Research. Understanding AFM. *Information brochure and CD*, 1:1–5, 2004.
- [64] R. Linnemann, T. Gotszalk, I.W. Rangelow, P. Dumania, and E. Oesterschulze. Atomic force microscopy and lateral force microscopy using piezoresistive cantilevers. *Journal of Vacuum Science and Technology*, 14:856–860, 1996.
- [65] V. Shahin, Y. Ludwig, C. Schafer, D. Nikova, and H. Oberleithne. Glucocorticoids remodel nuclear envelope structure and permeability. *Journal of Cell Science*, 118:2881–2889, 2005.
- [66] O. Marti, J. Colchero, and J. Mlynek. Nanosources and manipulation of atoms under high fields and temperatures. *Nanotechnology*, 1:253–260, 1991.
- [67] G. Mayer and N.M Amer. Simultaneous measurement of lateral and normal forces with an optical-beam-deflection atomic force microscope. *Appl. Phys. Lett.*, 57(20):2089, 1990.
-

- [68] B.D. Beake, I.U. Hassan, C.A. Rego, and W. Ahmed. Friction force microscopy study of diamond films modified by a glow discharge treatment. *Diamond & Related Materials*, 9:1421–1429, 2000.
- [69] D. F. Ogletree, R. W. Carpick, and M. Salmeron. Calibration of frictional forces in atomic force microscopy. *Review of Scientific Instruments*, 67(9):3298–3306, 1996.
- [70] E. Tocha, H. Schonherr, and G. Vancso. Calibration of frictional forces in atomic force microscopy. *Langmuir*, 22(5):2340–2350, 2006.
- [71] Y. Zhao, G. C. Wang, and T. M. Lu. *Characterization of amorphous and crystalline rough surface: Principles and application*. Elsevier Science, 1<sup>st</sup> edition, 2001.
- [72] Christian Teichert. Self-organization of nanostructures in semiconductor heteroepitaxy. *Physics Reports*, 365:335–432, 2002.
- [73] S.K. Sinha, E.B. Sirota, S. Garoff, and H.B. Stanley. X-ray and neutron scattering from rough surfaces. *Phys. Rev. B*, 38:2297–2311, 1988.
- [74] <http://www.falexint.com>.
- [75] J. de Vicente, J. R. Stokes, and H. A. Spikes. Rolling and sliding friction in compliant, lubricated contact. *Proc. I.Mech.E.*, J220:55–63, 2006.
- [76] A. Schneider, J. Böhm, and F. Franek. Tribologische analysen zur griffigkeit von waschbeton-fahrbahnoberflächen neue methoden in der oberflächenanalyse von waschbeton. *Kolloquium 2010: Forschung und Entwicklung für Zement und Beton*, 1, year = 2010, pages = 7 - 10.
- [77] John F. Watts and John Wolstenholme. *An Introduction to Surface Analysis by XPS and AES*. Wiley, 1<sup>st</sup> edition, 2003.
- [78] C. Jogl. Quasi-in-situ Photoelektronen-Spektroskopie an elektrochemisch hergestellten filmen. *PhD Thesis, Vienna University of Technology*, 2005.
- [79] Frank A. Settle. *Handbook of Instrumental Techniques for Analytical Chemistry*. Prentice Hall PTR, 1<sup>st</sup> edition, 1997.
- [80] H. Oechsner (Ed). Thin film and depth profile analysis. *Topics in Current Physics*, 37, 1984.

- 
- [81] R. Behrisch (Ed). Sputtering by particle bombardment. *Topics in Applied Physics*, 47, 1981.
- [82] D. Briggs and J.T. Grant (Ed.). *Surface Analysis by Auger and X-ray Photoelectron Spectroscopy*. IM Publications, 1<sup>st</sup> edition, 2003.
- [83] C.J. Cumpson. Arctic ARXPS-spreadsheet. *Crown Copyright*, 1998.
- [84] W. S. M. Werner, W.Smekal, and C. J. Powell. *NIST Database for the Simulation of Electron Spectra for Surface Analysis - Version 1.1*. National Institute of Standards and Technology, Gaithersburg, MD, 1<sup>st</sup> edition, 2006.
- [85] A.G. Olszak, J. Schmit, and M.G. Heaton. Interferometry: Technology and applications. *VECCO information brochure*, 2000.
- [86] <http://www.atomicforce.de>.
- [87] S. Kvasnica, J. Schalko, C. Eisenmenger-Sittner, J. Benardi, G. Vorlaufer, A. Pauschitz, and M. Roy. Nanotribological study of PECVD DLC and reactively sputtered Ti containing carbon films. *Diamond & Related Materials*, 15:1743–1752, 2006.
- [88] R. Kolm, I.C. Gebeshuber, E. Kenesey, A. Ecker A, A. Pauschitz, W.S.M. Werner, and H. Störi. Tribochemistry of mono molecular additive films on metal surfaces, investigated by XPS and HFRR. *Tribology and Interface Engineering Series*, 48:269–282, 2005.
- [89] P. J. Cumpson. Angle-resolved XPS and AES: Depth-resolution limits and a general comparison of properties of depth-profile reconstruction methods. *Journal of Electron Spectroscopy and Related Phenomena*, 73:25–52, 1995.
- [90] T. Schneider, G. Meier zu Köcker, and E. Santer. Topographic changes on the surfaces of PVD coatings in humid air: an AFM/LFM study. *Surface and Interface Analysis*, 24:7–14, 1996.
- [91] R. Kolm, I.C. Gebeshuber, E. Kenesey, A. Ecker A, A. Pauschitz, W.S.M. Werner, and H. Störi. Tribochemistry of mono molecular additive films on metal surfaces, investigated by XPS and HFRR. *Tribology and Interface Engineering Series*, 48:269–282, 2005.
- [92] R. Kolm, I.C. Gebeshuber, C. Jogl, W.S.M. Werner, H. Störi, and R. Kleiner. Characterisation of monomolecular lubricant films. *Technische Akademie Esslingen, Proc. 14th Int. Colloquium Tribology*, III:1663 – 1666, 2004.
-

- 
- [93] P. Mills and J.L. Sullivan. A study of the core level electrons in iron and its three oxides by means of X-ray photoelectron spectroscopy. *Journal of Physics D: Applied Physics*, cited in NIST XPS database, 16:723 – 732, 1983.
- [94] G. Ertl and K. Wandelt. Electron spectroscopic studies of clean and oxidized iron. *Surface Science*, cited in NIST XPS database, 50:479 – 492, 1975.
- [95] J.P. Riviere, M. Cahoreau, and P. Meheust. Chemical bonding of nitrogen in low energy high flux implanted austenitic stainless steel. *Journal of Physics D: Applied Physics*, 91(10):6361 – 6366, 2002.
- [96] B.M. Biwer and S.L. Bernasek. Electron spectroscopic study of the iron surface and its interaction with oxygen and nitrogen. *Journal of Electron Spectroscopy and Related Phenomena*, 40:339–345, 1986.
- [97] T.-C. Lin, G. Seshadri, and J.A. Kelber. A consistent method for quantitative XPS peak analysis of thin oxide films on clean polycrystalline iron surfaces. *Applied Surface Science*, 119:83–92, 1997.
- [98] S. Affrossman, R.F. Comrie, and S.M. MacDonald. Interaction of a model epoxy resin compound, diethanolamine, with aluminium surfaces studied by static SIMS and XPS. *Journal of the Chemical Society, Faraday Transactions*, 94:289 – 294, 1998.
- [99] M. Rojas-Campanur, J. Lara-Romero, F. Chinas-Castillo, and G. Alonso-Nunez. Tribological performance of rosin acid additives in water based lubricants. *Tribology Online*, 2(1):29 – 33, 2007.
- [100] R. M. Gresham. The mysterious world of MWF additives. *Tribology & Lubrication Technology, Business Publication*, 2006.
- [101] J. de Vicente, J. R. Stokes, and H. A. Spikes. Rolling and sliding friction in compliant, lubricated contact. *Proc. I.Mech.E. Part J*, 220:55 – 63, 2006.
- [102] A. Tomala, W.S.M Werner, I.C. Gebeshuber, N. Dörr, and H. Störi. Tribochemistry of monomolecular lubricant films of ethanolamine oligomers. *Tribology International*, 42:1513–1518, 2009.
- [103] C.J. Cumpson. ARCTIC ARXPS-spreadsheet. *Crown Copyright*, 1998.
-

- 
- [104] M.T. Mathew, E. Ariza, L.A. Rocha, A.C. Fernandes, and F. Vaz. TiCxOy thin films for decorative applications: Tribocorrosion mechanisms and synergism. *Tribology International*, 41:603 – 615, 2008.
- [105] T. Singh Mukul Jain, D. Ganguli, and K. Ravi. Evaluation of water glycol hydraulic fluids: a tribological approach. *J. Synthetic Lubrication*, 23:177 – 184, 2006.
- [106] Y. Wan, W. Liu, and Q. Xue. Effects of diol compounds on the friction and wear of aluminum alloy in a lubricated aluminum-on-steel contact. *Wear*, 193:99 – 104, 1996.
- [107] S. Igari, S. Mori, and Y. Takikawa. Effects of molecular structure of aliphatic diols and polyalkylene glycol as lubricants on the wear of aluminum. *Wear*, 224:180 – 184, 2000.
- [108] A. Tomala, W.S.M Werner, I.C. Gebeshuber, N. Dörr, and H. Störi. Tribochemistry of monomolecular lubricant films of ethanolamine oligomers. *Tribology International*, 42:1513–1518, 2009.
- [109] C.J. Cumpson. ARCTIC ARXPS - spreadsheet. *Crown Copyright*, 1998.
- [110] W. S. M. Werner, W. Smekal, and C. J. Powell. *NIST Database for the Simulation of Electron Spectra for Surface Analysis - Version 1.1*. National Institute of Standards and Technology, Gaithersburg, MD, 1<sup>st</sup> edition, 2006.
- [111] T. Singh Mukul Jain, D. Ganguli, and K. Ravi. Evaluation of water glycol hydraulic fluids: a tribological approach. *J. Synthetic Lubrication*, 23:177 – 184, 2006.
- [112] P.J. Cumpson, Eds: D. Briggs, and J. T. Grant. *Surface Analysis by Auger and X-ray Photoelectron Spectroscopy*. IM Publications, Chichester, 4<sup>th</sup> edition, 2003.
- [113] Chen-Hung Liao and Meng-Hui Li. Kinetics of absorption of carbon dioxide into aqueous solutions of monoethanolamine + N-methyldiethanolamine. *Chemical Engineering Science*, 57(21):4569–4582, 2002.
- [114] G. Vazquez, G. Antorrena, J. M. Navaza, and V. Santos. Absorption of CO<sub>2</sub> by water and surfactant solutions in the presence of induced marangoni effect. *Chemical Engineering Science*, 51(12):3317–3324, 1996.
-

- [115] C. Jeyaprabha, S. Sathiyarayanan, and G. Venkatachari. Corrosion inhibition of pure iron in 0.5 M H<sub>2</sub>SO<sub>4</sub> solutions by ethanolamines. *Applied Surface Science*, 246 (1-3):108–116, 2005.
- [116] A.S. Fouda, M.N. Moussa, F.I. Taha, and A.I. Elneanaa. The role of some thiosemicarbazide derivatives in the corrosion inhibition of aluminium in hydrochloric acid. *Corrosion Science*, 26(9):719–726, 1986.
- [117] A. C. Makrides and Norman Hackerman. Inhibition of acid dissolution of metals - some general observations. *The Journal of Physical Chemistry*, 59(8):707–710, 1955.
- [118] C.A. Mann. *Trans. Electrochem. Soc.*, 69:105, 1936.
- [119] B. Sanyal and K. Srivastava. Inhibitive effect of an onium compound on the dissolution of steel in hydrochloric acid. *British Corrosion Journal*, 9(2):103–107, 1974.
- [120] N. Hackerman, E. Snaveley Jr., and J.S. Payne. *J. Electrochem. Soc.*, 113:651, 1966.
- [121] T. Murekewa and N. Hackerman. *Corr. Sci.*, 4):381, 1964.
- [122] American Society of Metals. *ASM Handbook: Friction, Lubrication and Wear Technology v. 18*. ASM International, 10th edition edition, October 1992.
- [123] S. Bec, A. Tonck, J.M. Georges, R.C. Coy, J.C. Bell, and G.W. Roper. Relationship between mechanical properties and structures of zinc dithiophosphate anti-wear films. *Proceedings of the Royal Society A: Mathematical, Physical and Engineering Sciences*, 455(1992):4181–4203, 1999.
- [124] H. Fujita, R.P. Glovnea, and H.A. Spikes. Study of zinc dialkydithiophosphate antiwear film formation and removal processes, part I: Experimental. *Tribology Transactions*, 48(4):558–566, 2005.
- [125] C. Minfray, J.M. Martin, C. Esnouf, T. Le Mogne, R. Kersting, and B. Hagenhoff. A multi-technique approach of tribofilm characterisation. *Thin Solid Films*, 447-448:272–277, 2004.
- [126] R.J. Bird and G.D. Galvin. The application of photoelectron spectroscopy to the study of e. p. films on lubricated surfaces. *Wear*, 37(1):143–167, 1976.

- 
- [127] M. Eglin, A. Rossi, and N.D. Spencer. X-ray photoelectron spectroscopy analysis of tribostressed samples in the presence of ZnDTP: a combinatorial approach. *Tribology Letters*, 15(3):199–210, 2003.
- [128] F.M. Piras, A. Rossi, and N.D. Spencer. Combined in situ (ATR FT-IR) and ex situ (XPS) study of the ZnDTP-iron surface interaction. *Tribology Letters*, 15(3):181–192, 2003.
- [129] R. Heuberger, A. Rossi, and N.D. Spencer. XPS study of the influence of temperature on ZnDTP tribofilm composition. *Tribology Letters*, 25(3):185–196, 2007.
- [130] T.P. Debies and W.G. Johnston. Surface chemistry of some antiwear additives as determined by electrospectroscopy. *ASLE Transactions*, (79), 1979.
- [131] C. Minfray, T. Le Mogne, A.A. Lubrecht, and J.-M. Martin. Experimental simulation of chemical reactions between ZDDP tribofilms and steel surfaces during friction processes. *Tribology Letters*, 21(1):65–76, 2006.
- [132] Z. Yin, M. Kasrai, M. Fuller, G.M. Bancroft, K. Fyfe, and K.H. Tan. Application of soft X-ray absorption spectroscopy in chemical characterization of antiwear films generated by ZDDP part I: The effects of physical parameters. *Wear*, 202(2):172–191, 1997.
- [133] M. Fuller, Z. Yin, M. Kasrai, G.M. Bancroft, E.S. Yamaguchi, P.R. Ryason, P.A. Willermet, and K.H. Tan. Chemical characterization of tribochemical and thermal films generated from neutral and basic ZDDPs using X-ray absorption spectroscopy. *Tribology International*, 30(4):305–315, 1997.
- [134] G.M. Bancroft, M. Kasrai, M. Fuller, Z. Yin, K. Fyfe, and K.H. Tan. Mechanisms of tribochemical film formation: Stability of tribo- and thermally-generated ZDDP films. *Tribology Letters*, 3(1):47–51, 1997.
- [135] P.A. Willermet, R.O. Carter III, and E.N. Boulos. Lubricant-derived tribochemical films - An infra-red spectroscopic study. *Tribology International*, 25(6):371–380, 1992.
- [136] P.A. Willermet, D.P. Dailey, R.O. Carter III, P.J. Schmitz, W. Zhu, J.C. Bell, and D. Park. The composition of lubricant-derived surface layers formed in a lubricated cam/tappet contact II. effects of adding overbased detergent and
-

- dispersant to a simple ZDTP solution. *Tribology International*, 28(3):163–175, 1995.
- [137] J.M. Martin, C. Grossiord, T. Le Mogne, S. Bec, and A. Tonck. The two-layer structure of zndtp tribofilms, part I: AES, XPS and XANES analyses. *Tribology International*, 34(8):523–530, 2001.
- [138] A.A. Torrance, J.E. Morgan, and G.T.Y. Wan. An additive’s influence on the pitting and wear of ball bearing steel. *Wear*, 192(1-2):66–73, 1996.
- [139] L. Taylor, A. Dratva, and H.A. Spikes. Friction and wear behavior of zinc dialkyldithiophosphate additive. *Tribology Transactions*, 43(3):469–479, 2000.
- [140] L.J. Taylor and H.A. Spikes. Friction-enhancing properties of ZDDP antiwear additive: Part I - friction and morphology of ZDDP reaction films. *Tribology Transactions*, 46(3):303–309, 2003.
- [141] K. Topolovec-Miklozic, T.R. Forbus, and H.A. Spikes. Film thickness and roughness of ZDDP antiwear films. *Tribology Letters*, 26(2):161–171, 2007.
- [142] J.F. Graham, C. McCague, and P.R. Norton. Topography and nanomechanical properties of tribochemical films derived from zinc dialkyl and diaryl dithiophosphates. *Tribology Letters*, 6(3-4):149–157, 1999.
- [143] M. Aktary, M.T. McDermott, and G.A. McAlpine. Morphology and nanomechanical properties of ZDDP antiwear films as a function of tribological contact time. *Tribology Letters*, 12(3):155–162, 2002.
- [144] O.L. Warren, J.F. Graham, P.R. Norton, J.E. Houston, and T.A. Michalske. Nanomechanical properties of films derived from zinc dialkyldithiophosphate. *Tribology Letters*, 4(2):189–198, 1998.
- [145] K. Komvopolous, V. Do, E.S. Yamaguchi, and P.R. Ryason. Nanomechanical and nanotribological properties of an antiwear tribofilm produced from phosphorus-containing additives on boundary-lubricated steel surfaces. *Journal of Tribology*, 126(4):775–780, 2004.
- [146] A. Naveira Suarez, M. Grahn, R. Pasaribu, and R. Larsson. The influence of base oil polarity on the tribological performance of zinc dialkyl dithiophosphate additives. *Tribology International*, 43(12):2268–2278, 2010.

- [147] A. Naveira-Suarez, M. Zaccheddu, M. Grahn, R. Pasaribu, and R. Larsson. Parameters affecting the functionality of additives in tribological contacts - An experimental and molecular dynamics simulation study. In *World Tribology Congress 2009 - Proceedings*, page 66, 2009.
- [148] A.J. Pidduck and G.C. Smith. Scanning probe microscopy of automotive anti-wear films. *Wear*, 212(2):254–264, 1997.
- [149] Bharat Bhushan. *Nanotribology and nanomechanics: an introduction*. Berlin: Springer, 2008.
- [150] B.D. Beake, I.U. Hassan, C.A. Rego, and W. Ahmed. Friction force microscopy study of diamond films modified by a glow discharge treatment. *Diamond and Related Materials*, 9(8):1421–1429, 2000.
- [151] S. Kvasnica, J. Schalko, C. Eisenmenger-Sittner, J. Benardi, G. Vorlauffer, A. Pauschitz, and M. Roy. Nanotribological study of PECVD DLC and reactively sputtered Ti containing carbon films. *Diamond and Related Materials*, 15(10):1743–1752, 2006.
- [152] Sakamoto T, Uetz H, and Foehl J. Reaction layer formation on bronze with an S-P extreme pressure additive in boundary lubrication under increasing load.i. *Wear*, 105(4):307–321, 1985.
- [153] Jianqiang H, Huanqin Z, Li W, Xianyong W, Feng J, and Zhiming Z. Study on tribological properties and action mechanism of organic cadmium compound in lubricants. *Wear*, 259(1-6):519–523, 2005.
- [154] Zhang J, Liu W, Xue Q, and Wang Q. Investigation of the friction and wear behaviors of Cu(I) and Cu(II) dioctyldithiophosphates as additives in liquid paraffin. *Wear*, 216(1):35–40, 1998.
- [155] Boshui C, Junxiu D, and Guoxu C. Tribochemistry of gadolinium dialkyldithiophosphate. *Wear*, 196(1-2):16–20, 1996.
- [156] Georges JM, Martin JM, Mathia T, Kapsa P, Meille G, and Montes H. Mechanism of boundary lubrication with zinc dithiophosphate. *Wear*, 53(1):9–31, 1979.
- [157] Watkins RC and Spedding H. Antiwear mechanism of ZDDP's - 2. *Tribology International*, 15(1):13–15, 1982.

- [158] Spedding H and Watkins RC. Antiwear mechanism of ZDDP's - 1. *Tribology International*, 15(1):9–12, 1982.
- [159] Gellman AJ and Spencer ND. Surface chemistry in tribology. *Proceedings of the Institution of Mechanical Engineers - Part J: Journal of Engineering Tribology*, 216(6):433–461, 2002.
- [160] Bancroft GM, Kasrai M, Fuller M, and Yin Z. Mechanism of tribochemical film formation: stability of tribo- and thermally-generated zddp films. *Tribology Letters*, 3:47–51, 1997.
- [161] Willermet PA, Dailey DP, Carter RO, Schmitz PJ, and Zhu W. Mechanism of formation of antiwear films from zinc dialkyldithiophosphates. *Tribology international*, 28(3):177–187, 1995.
- [162] Coy RC and Jones RB. Thermal degradation and ep performance of zinc dialkyldithiophosphates additives in white oil. *ASLE Transactions*, 24(1):77–90, 1981.
- [163] Bec S, Tonck A, Georges JM, Coy RC, Bell JC, and Roper GW. Relationship between mechanical properties and structures of zinc dithiophosphate antiwear films. *Proceedings of the Royal Society A: Mathematical, Physical and Engineering Sciences*, 455:4181–4203, 1999.
- [164] Fujita H and Spikes HA. The formation of zinc dithiophosphate antiwear films. *Proceedings of the Institution of Mechanical Engineers - Part J: Journal of Engineering Tribology*, 218(4):265–277, 2004.
- [165] C. Minfray. A multi-technique approach of tribofilm characterisation. *Thin Solid Films*, 477:272–277, 2004.
- [166] Fuller M, Yin Z, Kasrai M, Bancroft GM, Yamaguchi ES, Ryason PR, Willermet PA, and Tan KH. Chemical characterization of tribochemical and thermal films generated from neutral and basic ZDDPs using x-ray absorption spectroscopy. *Tribology International*, 30(4):305–315, 1997.
- [167] Yin Z, Kasrai M, Bancroft GM, Laycock KF, and Tan KH. Chemical characterization of antiwear films generated on steel by zinc dialkyl dithiophosphate using x-ray absorption spectroscopy. *Tribology international*, 26(6):383–388, 1993.

- 
- [168] Bird R.J. and Galvin G.D. The application of photoelectron spectroscopy to the study of e. p. films on lubricated surfaces. *Wear*, 37(1):143–167, 1976.
- [169] Eglin M, Rossi A, and Spencer ND. x-ray photoelectron spectroscopy analysis of tribostressed samples in the presence of zndtp: A combinatorial approach. *Tribology Letters*, 15(3):199–209, 2003.
- [170] Piras FM, Rossi A, and Spencer ND. Combined in situ (ATR FT-IR) and ex situ (XPS) study of the ZNDTP-iron surface interaction. *Tribology Letters*, 15(3):181–191, 2003.
- [171] Heuberger R, Rossi A, and Spencer ND. Pressure dependence of zndtp tribochemical film formation: a combinatorial approach. *Tribology Letters*, 28(2):209–277, 2007.
- [172] Heuberger R, Rossi A, and Spencer ND. XPS study of the influence of temperature on ZNDTP tribofilm composition. *Tribology Letters*, 25(3):185–196, 2007.
- [173] C. Minfray. Experimental simulation of chemical reactions between zddp tribofilms and steel surfaces during friction processes. *Tribology Letters*, 21(1):65–76, 2006.
- [174] Yin Z., Kasrai M., Fuller M., Bancroft G.M., Fyfe K., and Tan K.H. Application of soft X-ray absorption spectroscopy in chemical characterization of antiwear films generated by ZDDP part II: the effect of detergents and dispersants. *Wear*, 202(2):192–201, 1997.
- [175] Willermet PA, Carter RO, Schmitz PJ, Everson M, Scholl DJ, and Weber WH. Formation, structure, and properties of lubricant-derived antiwear films. *Lubrication Science*, 9(4):325–348, 1997.
- [176] Willermet PA, Dailey DP, Carter RO, Schmitz PJ, Zhu W, Bell JC, and Park D. The composition of lubricant-derived surface layers formed in a lubricated cam/tappet contact II. Effects of adding overbased detergent and dispersant to a simple ZDTP solution. *Tribology international*, 28(3):163–175, 1995.
- [177] Martin JM, Grossiord C, Le Mogne T, Bec S, and Tonck A. The two-layer structure of ZNDTP tribofilms, part I: AES, XPS and XANES analyses. *Tribology International*, 34(8):523–530, 2001.
-

- 
- [178] Torrance AA, Morgan JE, and Wan GTY. An additive's influence on the pitting and wear of ball bearing steel. *Wear*, 192:66–73, 1996.
- [179] Taylor L, Dratva A, and Spikes HA. Friction and wear behavior of zinc dialkyldithiophosphate additive. *Tribology Transactions*, 43(3):469–479, 2000.
- [180] Taylor LJ and Spikes HA. Friction-enhancing properties of ZDDP antiwear additive: Part I - friction and morphology of zddp reaction films. *Tribology Transactions*, 46(3):303–309, 2003.
- [181] Naveira-Suarez A, Zaccheddu M, Grahn M, Pasaribu R, and Larsson R. Parameters affecting the functionality of additives in tribological contacts - an experimental and molecular dynamics simulation study. *Proceedings of the IV World Tribology Congress Kyoto, Japan*, 66:66–79, 2009.
- [182] Naveira-Suarez A, Zaccheddu M, Grahn M, Pasaribu R, and Larsson R. The influence of base oil polarity and slide-roll ratio on additive derived reaction layer formation. *Proceedings of the 14th Nordic Symposium in Tribology (NordTrib 2010) Storforsen Sweden*, Submitted to Proceedings of the Institution of Mechanical Engineers - Part J: Journal of Engineering Tribology:23–29, 2010.
- [183] Cann PM, Hutchinson J, and Spikes HA. The development of a spacer layer imaging method (slim) for mapping elastohydrodynamic contacts. *Tribology Transactions*, 39(4):915–921, 1996.
- [184] Donnet C. *Handbook of surface and interface analysis - Methods for problem-solving*. Marcel Dekker, Basel, 2<sup>nd</sup> edition, 1998.
- [185] Aktary M, McDermott MT, and McAlpine GA. Morphology and nanomechanical properties of ZDDP antiwear films as a function of tribological contact time. *Tribology Letters*, 12(3):155–162, 2002.
- [186] Beake BD, Hassan IU, Rego CA, and Ahmed W. Friction force microscopy study of diamond films modified by a glow discharge treatment. *Diamond and Related Materials*, 9(8):1421–1429, 2000.
- [187] K.A. Dean and B.R. Chalamala. *Applied Physics Letter*, 76:375, 1999.
- [188] eds. I. Sigals and R.J. Caveney. *Diamond Materials and Their Applications*. Willey, 1<sup>st</sup> edition, 2008.
-

- [189] C. Donnet. *Surface Coating Technology*, 80:139, 1996.
- [190] T. Zehnder and J. Patscheider. *Surface Coating Technology*, 133-134:138, 2000.
- [191] L.C. Wu, K. Miyoshi, R. Vuppuladhadium, and H.E. Jackson. *Surface Coating Technology*, 54-55:576, 1992.
- [192] R. Haubner and B. Lux. *Diamond and Related Materials*, 2:1277, 1993.
- [193] M. Kohzaki, K. Higuchi, S. Noda, and K. Uccida. *Journal of Materials Research*, 7:1769, 1992.
- [194] K. Miyoshi, R.L.C. Wu, and A. Garscadden. *Surface Coating Technology*, 54/55:428, 1992.
- [195] J. Robertson. *Materials Science and Engineering*, R37:129, 2002.
- [196] E. Kohn, P. Gluche, and M. Adamschik. *Diamond and Related Materials*, 8:934, 1999.
- [197] S. Ertl, M. Adamschik, P. Schmid, P. Gluche, A. Flöter, and E. Kohn. *Diamond and Related Materials*, 9:970, 2000.
- [198] E. Kohn, M. Adamschik, P. Schmid, and S. Ertl. *Diamond and Related Materials*, 10:1684, 2001.
- [199] T. Shibata, Y. Kitamoto, K. Unno, and E. Makino. *Journal of Microelectromechanical Systems*, 9:47, 2000.
- [200] J.K. Park, V.M. Ayres, J. Asmussen, and K. Mukherjee. *Diamond and Related Materials*, 9:1154, 2000.
- [201] I.S. Forbes and J.I.B. Wilson. *Thin Solid Films*, 420-421:508, 2002.
- [202] W.A. Yarbrough and R. Messier. *Science*, 247:688, 1990.
- [203] J.C. Angus and C.C. Hayman. *Science*, 241:913, 1988.
- [204] S. Yugo, T. Kanai, T. Kimura, and T. Muto. *Applied Physics Letters*, 58:1036, 1991.
- [205] X. Jiang and C.P. Klages. *Diamond and Related Materials*, 2:1112, 1993.

---

REFERENCES

---

- [206] Y.K. Kim, K.Y. Lee, and J.Y. Lee. *Diamond and Related Materials*, 7:96, 1998.
- [207] S. Bühlmann, E. Blank, R. Haubner, and B. Lux. *Refractory Metals and Hard Materials*, 20:93, 2002.
- [208] R. Haubner and B. Lux. *Diamond and Related Materials*, 9:1154, 2000.
- [209] A. Lindlbauer. *Refractory Metals Hard Materials*, 11:247, 1992.
- [210] J. Michler, J. Stiegler, Y. von Kaenel, P. Moeckli, W. Dorsch, D. Stenkamp, and E. Blank. *Journal of Crystal Growth*, 172:404, 1997.
- [211] B. Lux, R. Haubner, H. Holzer, and R.C. DeVries. *Refractory Metals Hard Materials*, 15:263, 1997.
- [212] W.C. Oliver and G.M. Pharr. *Journal of Materials Research*, 7:1564, 1992.
- [213] M. Joksh, P. Wurzinger, P. Pongratz, R. Haubner, and B. Lux. *Diamond and Related Materials*, 3:681, 1994.
- [214] J. Michler, Y von Kaenel, J. Stiegler, and E. Blank. *Journal of Applied Physics*, 83:187, 1998.
- [215] D.M. Gruen, X. Pan, A.R. Krauss, S. Liu, J. Luo, and C.M. Foster. *The Journal of Vacuum Science and Technology A*, 12:1491, 1994.
- [216] R.J. Nemanich, J.T. Glass, G. Lucovsky, and R.E. Shroder. *The Journal of Vacuum Science and Technology A*, 6:1783, 1988.
- [217] S. Praver, K.W. Nugent, D.N. Jamieson, J.O. Orwa, L.A. Bursill, and J.L. Peng. *Chemical Physics Letters*, 332:93, 2000.
- [218] T. Sharda, M. Umeno, T. Soga, and T. Jimbo. *Journal of Applied Physics*, 89:4874, 2001.
- [219] A.C. Ferrai and J. Robertson. *Physical Review B*, 63:121405, 2001.
- [220] D.S. Night and W.B. White. *Journal of Materials Research*, 4:385, 1989.
- [221] K. Okada, K. Kanda, S. Komatsu, and S. Matsumoto. *Journal of Applied Physics*, 88:1674, 2001.
- [222] B. Bhushan. *Handbook of Nanotechnology*. Berlin: Springer, 2<sup>nd</sup> edition, 2003.

- 
- [223] A. Pauschitz, J. Schalko, T. Koch, C. Eissenmenger Sittner, S. Kvasnica, and M. Roy. *Bulletin of Materials Science*, 26:585, 2003.
- [224] B.D. Beake, I.U. Hassan, C.A. Rego, and W. Ahmed. *Diamond and Related Materials*, 9:1421, 2000.
- [225] M. Cieplak, E.D. Smith, and M.O. Robbins. *Science*, 265:1209, 1994.
- [226] J. Krim. *Langmuir*, 12:4564, 1996.
- [227] B.N.J. Persson. *Physical Review B*, 44:3277, 1991.
- [228] P.B. Merrill and S.S. Perry. *Surface Science*, 418:342, 1998.
- [229] S. Kavasnica, J. Schalko, C. Eisenmenger-Sittner, J. Bernardi, G. Vorlauffer, A. Pauschitz, and M. Roy. *Diamond and Related Materials*, 15:1743, 2006.
- [230] T.Le Huu, M. Schmitt, and D. Paulmier. *Surface Science*, 433-435:690, 1999.
- [231] E. Erdemir, G.R. Fenske, A.R. Krauss, D.M. Gruen, T. Macauley, and R.T. Csencsits. *Surface Coating Technology*, 120-121:565, 1999.
- [232] R.R. Chromik, A.L. Winfrey, J. Lüning, R.J. Nemanich, and K.J. Wahl. *Wear*, 265:477, 2008.
- [233] C.S. Abreu, M. Amaral, A.J.S. Fernandes, F.J. Oliveira, R.F. Silva, and J.R. Gomes. *Diamond and Related Materials*, 15:739, 2006.
- [234] M. Amaral, C.S. Abreu, A.J.S. Fernandes, F.J. Oliveira, R.F. Silva, and J.R. Gomes. *Diamond and Related Materials*, 16:790, 2007.
- [235] E. Reido, J. Chevrier, F. Comminand, and H. Brune. *Surface Science*, 477:25, 2001.
- [236] L. Assman, J.C. Bernede, A. Drici, C. Amory, E. Holgand, and M. Morsli. *Applied Surface Science*, 246:159, 2005.
- [237] T. Kubart, T. Polkar, L. Kopecky, R. Novak, and D. Novakova. *Surface And Coating Technology*, 193:230, 2005.
- [238] D.V. Shtansky, T.A. Lobova, V.Yu Fominski, S.A. Kulinich, I.V. Lyasotsky, M.I. Petrzlük, E.A. Levashov, and J.J. Moore. *Surface And Coating Technology*, 183:328, 2004.
-

- [239] V.Y. Fominsky, R.I. Romanov, A.V. Gusaraov, and J.P. Celis. *Surface And Coating Technology*, 201:7813, 2007.
- [240] A. Nossa and A. Cavaleiro. *Surface And Coating Technology*, 142-144:984, 2001.
- [241] A. Nossa and A. Cavaleiro. *Surface And Coating Technology*, 163-164:552, 2003.
- [242] M.C. Simonds, A. Savan, E. Pflüger, and H.V. Swygenhoven. *Surface And Coating Technology*, 126:15, 2000.
- [243] P. Cosemans, X. Zhu, J.P. Celis, and M.V. Stappen. *Surface And Coating Technology*, 174-175:416, 2003.
- [244] T.J.S. Anand, C. Sanjeeviraja, and M. Jayachandran. *Vacuum*, 60:431, 2001.
- [245] R. Bichsel and F. Levy. *Thin Solid Film*, 116:376, 1984.
- [246] A. Mallouky and J.C. Bernede. *Thin Solid Film*, 158:285, 1988.
- [247] X. Zhang, R.G. Vitchev, W. Lauwerens, L. Stals, J. He, and J.P. Celis. *Thin Solid Film*, 396:69, 2001.
- [248] J. Wang, W. Lauwerens, E. Wieers, L. Stals, J. He, and J.P. Celis. *Surface And Coating Technology*, 139:143, 2001.
- [249] T. Polcar, M. Evaristo, M. Stuebar, and A. Cavelrio. *Proceedings European Tribology Conference*, 12-15:505, 2007.
- [250] T. Sumonmgi, K. Hieda, T. Endo, and K. Kuwahara. *Applied Physics A*, 66:229, 1998.
- [251] P.E. Sheehan and C.M. Lieber. *Science*, 272:1158, 1996.
- [252] Y. Kim, J.L. Huang, and C.M. Lieber. *Applied Physics Letters*, 59:3404, 1991.
- [253] L.V. Santos, V.J. Trava-Airoldi, K. Iha, E.J. Corat, and M.C. Salvatori. *Diamond and Related Materials*, 10:1049, 2001.
- [254] S.R. Cohen, Y. Feldman, H. Cohen, and R. Tenne. *Applied Surface Science*, 144-145:603, 1999.

- 
- [255] X. Zhang and J.P. Celis. *Applied Surface Science*, 206:110, 2003.
- [256] T. Polcar, M. Evaristo, M. Stueber, and A. Cavaleiro. *Surface And Coating Technology*, 202:2418, 2008.
- [257] W.C. Oliver and G.M. Pharr. *Journal of Materials Research*, 7:1564, 1992.
- [258] A. Nossa and A. Cavaleiro. *Journal of Materials Research*, 19:2356, 2004.
- [259] G. Weisse, N. Mattern, H. Hermann, A. Teresiak, I. Bacher, W. Bruckner, H.D. Bauer, H. Vinzelberg, G. Reiss, U. Kreißig, M. Mader, and P. Markschlager. *Thin Solid Film*, 298:98, 1997.
- [260] A.A. Voevodin and J.S. Zabinski. *Wear*, 261:1285, 2006.
- [261] B. Bhushan. *Principles and Applications of Tribology*. John Wiley and Sons, New York, USA, isbn 0-471-59407-5 edition, 1999.
- [262] A. Opitz, S. I. Ahmed, M. Scherge, and J. A. Schaefer. *Wear*, 254:924, 2003.
- [263] S. Kavasnica, J. Schalko, C. Eisenmenger-Sittner, J. Bernardi, G. Vorlaufer, A. Pauschitz, and M. Roy. *Diamond and Related Materials*, 15:1743, 2006.
- [264] H.N. Yang, Y.P. Zhao, A. Chan, T.M. Lu, and G.C. Wang. *Physical Review B*, 56:4224, 1997.
- [265] B.D. Beake, I.U. Hassan, C.A. Rego, and W. Ahmed. *Diamond and Related Materials*, 9:1421, 2000.
- [266] J. Musil and M. Jirout. *Surface Coating Technology*, 201:5143, 2007.
- [267] S.J. Bull, P.R. Chalkar, C. Johnston, and V. Moore. *Surface Coating Technology*, 68:603, 1994.
- [268] S.E. Grillo and J.E. Field. *Journal of Physics D: Applied Physics*, 30:202, 1997.
- [269] T. Koch, M. Evaristo, A. Pauschitz, M. Roy, and A. Cavaleiro. *Thin Solid Films*, 518:185, 2009.
- [270] M. Cieplak, E.D. Smith, and M.O. Robbins. *Science*, 265:1209, 1994.
- [271] J. Krim. *Langmuir*, 12:4564, 1996.
- [272] B.N.J. Persson. *Physical Review B*, 44:3277, 1991.
- [273] P.B. Merrill and S.S. Perry. *Surface Science*, 418:342, 1998.
-

# ACKNOWLEDGMENT

First of all I would like to thank my supervisor PROF. WOLFGANG WERNER for help, insightful hints, fruitful discussions and encouraging words. I also want to say a big thank you to my former supervisor PROF. ILLE GEBESHUBER for giving me a chance to work on thesis in WEMESURF project, for all her organization help at the beginning of my time in Austria, and for guidance within first year of my work. This thesis would never have taken shape without the inspired problem solving of PROF. HERBERT STÖRI, thanks for his invaluable help, scientific advices and encouragement to finish this work. I highly appreciate help of Prof. FRIEDRICH FRANEK for his accurate proofread of this thesis and many valuable comments and hints.

Thanks to all colleagues from the Surface & Plasma Technology Research Group, who could be bothered with questions at any time, and who generally created a very agreeable working atmosphere in the Institute für Angewandte Physik.

From WEMESURF project, I would like to thank project managers MR. MARTIN JECH and DR. THOMAS WOPELKA, for their beyond reproach management, special care of progress of all Early Stage Researchers especially in complementary skills. Additionally I would like to thank for giving me a chance to participate in this training network and providing me an access to a broad range of complementary, technological and scientific fields. Furthermore thanks to all project participants: committees, scientists in charge, students and post-docs for their collaborative work and fantastic time together. I am very grateful for being given the chance to present the results of my work at numerous conferences, workshops and meetings.

Last but not least I would like to thank my husband and my family for endless moral support and trust given throughout this project.

**The work presented in this thesis has been supported by the EC, Sixth Framework Programme, Marie Curie Action (WEMESURF research project entitled: "*Characterization of wear mechanisms and surface functionalities with regard to life time prediction and quality criteria-from micro to nano range*" under contract MRTN CT 2006 035589).**